Effect of Additive Manufacturing Scanning Strategy on the Crystallographic Texture of NiTi Shape Memory Alloys

Master Thesis

Chrysoula Chatzopoulou

Delft University of Technology



TU Delft

Effect of Additive Manufacturing Scanning Strategy on the Crystallographic Texture of NiTi Shape Memory Alloys

Master Thesis

by

Chrysoula Chatzopoulou

A master's dissertation submitted in partial fulfillment of the requirement
for the award of Master of Science (MSc) degree in Materials Science and Engineering,
at the Delft University of Technology,
to be defended publicly on Tuesday, 19 December 2023 at 13:00.

Student Number:	5158982
Supervisors:	Dr V.A. Popovich, Dr J.-N. Zhu & Z. Yan
Project Duration:	September, 2022 - December, 2023
Thesis Committee:	Dr V.A. Popovich (3mE MSE), Dr J.-N. Zhu (3mE MSE), Dr Y. Tang (AE)
Department:	Materials Science & Engineering
Faculty:	Mechanical, Maritime & Materials Engineering, 3mE
Institution:	Delft University of Technology

TU Delft Delft University of Technology

Acknowledgements

I would like to express my sincere gratitude to Dr Vera Popovich for giving me the opportunity to work on this project for my MSc thesis. Her guidance, supervision and critical assessment of every aspect of the project were immensely helpful and crucial for the development of the project and the final outcome of my work.

This thesis would not have been possible without Dr Jianing Zhu, my day-to-day supervisor and mastermind behind the project. His tireless guidance and help throughout the duration of this work was truly invaluable, as was his uniquely extensive knowledge of the material and his kind and supportive spirit.

I am also grateful to Zhaorui Yan for this supervision, help and support throughout the duration of this project and for his critical input during various stages of the work.

I would also like to extend special thanks to Dr Ton Riemslag, Elise Reinton and Sean Scott for their indispensable help throughout the mechanical testing, their care and support. Special thanks are also due to Drs. Richard Huizenga for carrying out the XRD measurements and for his enthusiasm to discuss the results.

I would like to thank DP Mainali, Alice Dautezac and Sezen Kadir for the training and help in the polishing lab, as well as Roy Awater for his help with training and carrying out the DSC and TMA measurements. I would also like to acknowledge Tim Boot for his help with the Oxygen measurements.

Finally, I would like to thank my family for their unwavering support throughout this Masters degree, their understanding and love.

Chrysoula Chatzopoulou
Delft, December 2023

Abstract

Shape Memory Alloys (SMAs) are a class of metallic multi-functional materials which possess sensing and actuation capabilities, thanks to their unique ability to couple thermal and mechanical fields. NiTi-based Shape Memory Alloys exhibit properties which guarantee their high performance in adverse environments and, with the added benefit of two functionalities, the Shape Memory Effect and Superelasticity, these materials have become ideal candidates for a variety of applications. Spatial orientation of the NiTi crystals is crucial for achieving the superelastic functional response. According to studies on NiTi single crystals, when the grains adopt a [001] orientation along the direction of compression, slip is inhibited in the austenite phase and recoverable transformation strains similar to the theoretically estimated values of 5.3% are possible, defining the benchmark for superelastic responses.

Additive Manufacturing techniques, due to their inherent thermal processing conditions, have created unprecedented opportunities for fabrication of NiTi-based Shape Memory Alloys so that the thermo-mechanical behaviour of the material can be tailored to any application is intended for. During Laser-Powder Bed Fusion, the scanning strategy influences the thermal processing to which the alloy is subjected, affecting its solidification process as well as the heat fluxes and temperature gradients that arise during manufacturing. Meanwhile, it can play a decisive role in achieving epitaxial solidification of columnar grains extending over multiple deposition layers.

In this study, five different scanning strategies were employed during Laser-Powder Bed Fusion of a Ni-rich NiTi alloy and were evaluated with respect to the grain morphology and crystallographic texture that developed, as well as the superelastic response of the samples produced. It was found that a 67° interlayer rotation of the scanning vector promotes the fusion of neighbouring melt pools, resulting in columnar grains that solidify epitaxially along the build direction (BD) of the sample. Meanwhile, a strong $\langle 001 \rangle$ fibre texture emerges along the BD. The superelastic response was stabilised at 4.5% recoverable strain with 74.2% recovery ratio after 16 cycles of axial compression loading. When an island scanning pattern was incorporated into the 67° rotation scanning strategy, the crystallographic texture strengthened and the superelastic response improved, (5.0% stabilised recoverable strain and 84% recovery ratio). Furthermore, an increase in the volumetric energy density, achieved by using a flat top laser beam, produced a nearly single-crystalline microstructure, with the highest intensity of the $\langle 001 \rangle_{\parallel \mathrm{BD}}$ texture. The superelasticity in this case was stabilised at 5.5% recoverable strain with 91.5% recovery ratio. The effect of the loading direction on the superelastic response was also investigated, as was the nature of the residual strain left in the samples after their superelasticity stabilised.

Therefore, this study successfully demonstrated that the scanning strategy can be a vital tool in designing the crystallographic texture and the grain morphology of NiTi parts fabricated by L-PBF, and this way, effectively tailor the superelastic functional behaviour to specific requirements of potential applications.

Contents

Acknowledgements i

Abstract ii

1 Introduction 1

2 Literature Review 3

2.1 NiTi-based Shape Memory Alloys . . . 3

2.1.1 Phase Transformations in NiTi Shape Memory Alloys . . . 3

Shape Memory Effect . . . 4

Superelasticity . . . 5

Cyclic Behaviour of Shape Memory Alloys . . . 6

2.1.2 Factors influencing phase Transformations & Functional Properties . . . 8

Grain Size . . . 8

Chemical Composition . . . 8

Crystal Defects . . . 13

Crystal Orientation . . . 13

2.1.3 Applications . . . 16

2.2 Laser-Powder Bed Fusion Additive Manufacturing . . . 17

2.2.1 Process Parameters . . . 18

2.2.2 Effect of the scanning strategy on parts produced by Laser-Powder Bed Fusion . . . 21

2.3 Laser-Powder Bed Fusion of NiTi Shape Memory Alloys . . . 27

2.3.1 Microstructural evolution & defects . . . 27

2.3.2 Crystallographic texture . . . 29

2.3.3 Phase Transformations . . . 31

2.3.4 Mechanical Properties . . . 33

2.3.5 Functional Properties . . . 34

2.4 Conclusions & Research Objectives . . . 40

3 Materials & Methods 42

3.1 Material & Fabrication . . . 42

3.2 Characterisation Methods & Procedures . . . 44
3.2.1 Microstructure . . . 44
Optical Microscopy (OM) . . . 45
Electron Back-scatter Diffraction (EBSD) . . . 45
Scanning Electron Microscopy - Energy Dispersive X-ray Spectroscopy (SEM-EDS) . . . 46
3.2.2 Transformation & Phases . . . 46
X-Ray Diffraction (XRD) . . . 46
Differential Scanning Calorimetry (DSC) . . . 46
3.2.3 Functional Properties . . . 48
Mechanical Testing - Cyclic Axial Compression Tests . . . 48
Thermo-Mechanical Analysis (TMA) . . . 51

4 Results & Discussion **53**

4.1 Effect of Scanning Strategy on Crystallographic Texture & Functional Behaviour . . . 53
4.1.1 Microstructure & Phase Transformation Features . . . 53
4.1.2 Functional Behaviour . . . 65

4.2 Effect of Laser Power, Beam Size & Shape on the Crystallographic Texture & Functional Behaviour . . . 73
4.2.1 Microstructure & Phase Transformation Features . . . 73
4.2.2 Functional Behaviour . . . 79

4.3 Effect of the Loading Direction on the Functional Behaviour . . . 82
4.3.1 Microstructure & Phase Transformation Features . . . 82
4.3.2 Functional Behaviour . . . 85

4.4 Investigation of the Nature of Residual Strain . . . 90

5 Conclusions **97**

6 Recommendations for Future Research **99**

References **101**

A Differential Scanning Calorimetry **106**

B Scanning Electron Microscopy - Energy Dispersive X-Ray Spectroscopy **108**

C Cyclic Axial Compression Test for Superelasticity **110**

List of Figures

2.1 ***a)*** Schematic representation of the B2 austenitic phase of NiTi alloys. ***b)*** Schematic representation of the B19 crystal structure (orthorhombic). ***c)*** Schematic representation of the B19′ crystal structure (monoclinic). Large blue spheres are Ti atoms and small magenta spheres are the Ni atoms. Adapted from [3]. 3

2.2 Forward (top) and reverse (bottom) transformations occurring during the loading path where only temperature is imposed on the SMA. The sketches showcase the absence of any shape change during the process. Reproduced from [1]. 4

2.3 Phase diagram depicting an overview of the Shape Memory Effect using stress, σ, strain, ε, and temperature, T. Corresponding crystal structures of the alloy are shown in the side sketches. Reproduced from [5]. 5

2.4 Phase diagram depicting an overview of the superelastic behaviour of an SMA using stress, σ, and strain, ε. Corresponding crystal structures of the alloy are shown in the side sketches. Reproduced from [5]. 6

2.5 Temperature, T, [°C] versus strain, ε, [%] plot of the Two Way Shape Memory Effect, TWSME. Reproduced from [4]. 6

2.6 Strain, ε, [%] versus temperature, T, [°C] plot of the thermal cyclic loading of a NiTi wire under a constant applied stress of 150 MPa. The first and final cycles are noted. The accumulated strain saturation is also visible at the point where the cycles begin to overlap. Reproduced from [1]. 7

2.7 Stress, σ, [MPa] versus strain, ε, graph of the pseudoelastic response of a NiTi wire with A_f = 65°C tested at T = 70°C. The initial and final cycles are noted. The stabilised pseudoelastic hysteresis loop after 20 cycles is shown with thick black lines as the strain has become saturated at this point. Reproduced from [1]. 8

2.8 The phase diagram of the NiTi system. Reproduced from [14]. 9

2.9 ***a)*** Transformation temperature range dependence on the overall Ni content of NiTi alloys. The plot contains the variations of A_s in blue, A_f in black and M_s temperatures in green. For a specific alloy concentration the rhombohedral start temperature is also relevant, shown in red and marked as R_s. Reproduced from [11]. ***b)*** Variations of the M_s temperature (black squares) for Ni concentrations between 48-51 at.%. The depicted behaviour divides the plot in regions I and II. The slope of the decrease in Region II is marked on the graph. The open circles curve depicts the behaviour of the temperature of the thermodynamic equilibrium between austenite and martensite with respect to the Ni content. Reproduced from [15]. 10

2.10 Dependence of the M_s temperature on the Ni content of the NiTi SMA as well as on the Ni/Ti ratio of the material. The data shows a sharp drop which starts around the point of the stoichiometric composition, illustrating the heavy influence of composition on the thermal behaviour of the alloy. Reproduced from [17]. 11

2.11 ***a)*** Dependence of the width of the thermal hysteresis, ΔT_H, on the Ni content of the alloy. Region I corresponds to Ti-rich alloy concentrations, whereas Region II is associated with the Ni-rich NiTi. Reproduced from [15]. ***b)*** Concentration dependence of the heat of transformation, $|q|$, for the $B2 \rightleftharpoons B19'$ reactions. Again, Regions I and II are used to assist with data interpretation. Reproduced from [15]. 11

2.12 ***a)*** DSC curves (heat flow, $\dot{q}$, [W/g] versus temperature, T, [K]) for two NiTi samples of the same Ni content (50.7at.% Ni) showcasing the effect of O and C impurities pick-up. The solid black line corresponds to the sample melted four times and the dashed line to the sample melted 25 times. Reproduced from [15]. ***b)*** DSC curves (heat flow, $\dot{q}$, [W/g] versus temperature, T, [K]) for two NiTi alloys of different Ni contents illustrating the differences in terms of the M_s temperature, the width of the thermal hysteresis, ΔT_H, and the latent heat of the martensitic transformation, $q_{B2\rightarrow B19'}$. The thick black line corresponds to 49.6 at.% Ni sample and the light gray line to 50.1 at.% Ni sample. Reproduced from [15]. 12
2.13 Stress [MPa] versus temperature [°C] graph for NiTi-based SMAs. The five key temperatures for the functional behaviour of SMAs are marked on the x-axis, signifying the limits of occurrence of the SME, the SE and the plastic deformation of the material. The blue line represents the Critical Stress for Martensitic Variant Reorientation, which shows a declining trend with increasing temperature. The Critical Stress for Martensitic Transformation, σ_{SIM}, is given by the green line, exhibiting an increasing trend as temperature is raised. Finally, the red line represents the Critical Stress for Plastic Deformation, or σ_y, which follows a decreasing pattern with temperature as the Critical Stress for Martensite Reorientation. The shaded area named *"Superelastic Window"* indicates the possible stress and temperature state where the superelastic functionality can be realised. Reproduced from [27]. 14
2.14 Inverse pole figure mapping the superelastic capability of NiTi SMA to a number of crystallographic orientations. The so-called *Non-Superelastic Index* is given at the bottom of the figure providing guidance for the interpretation. Smaller index values and colours closer to blue indicate better material capability for the superelastic response. Reproduced from [26]. 15
2.15 Plastic slip initiation in the $\langle 001 \rangle \{110\}$ slip system of a B2 crystal. The cubes representing the unit crystal are oriented along ***a)*** the [0 0 1] direction, ***b)*** the [1 1 0] direction and ***c)*** the [1 1 1] direction. The slip planes are coloured green, the slip directions are marked by way of a green line and the loading directions are coloured red. The Schmid factor for each case is given above each schematic. Reproduced from [26]. 16
2.16 Schematic representation of the *Laser-Powder Bed System* process. Reproduced from [31]. 17
2.17 Process parameters involved in the L-PBF process. Reproduced from [31]. 19
2.18 Schematic illustration of layer thickness, laser power, scanning speed and hatch distance process parameters. Reproduced from [34]. 20
2.19 Schematic representation of different scanning strategies. ***a)*** Unidirectional scan, ***b)*** bi-directional scan (or zigzag), ***c)*** island scan, ***d)*** unidirectional scan with varied scanning sequences, ***e)*** bi-directional scan with varied scanning sequences, ***f)*** helix scan with square cross-section, ***g)*** contour scan, ***h)*** laser double-pass bi-directional scan, ***i)*** laser double-pass bi-directional scan with 90° interlayer rotation of the scan vector, ***j)*** cross scan, ***k)*** bi-directional scan with 90° interlayer rotation of the scanning vector, ***l)*** unidirectional scan with 90° interlayer rotation of the scanning vector, ***m)*** bi-directional scan with 45° interlayer rotation of the scanning vector, and, ***n)*** point melting scan. Reproduced from [36]. 22
2.20 ***a)*** Growth rate, R, versus temperature gradient, G, plot depicting their effect on the size and morphology of the crystals during solidification processes. Reproduced from [4]. . . 22
2.21 ***a)*** Schematic representation of the mechanism of competitive epitaxial grain growth in one melt pool during solidification process of L-PBF as the laser source moves away from the scanned area. The arrows in the crystals solidified indicate the easy-growth direction. Reproduced from [41]. ***b) and c)*** Schematic representation of the effect of the interlayer rotation of the scanning strategy. In b), there is no rotation between successive layers (0° interlayer scanning), the melt pools are superimposed on one another and the grains can attain any of the two orientations shown by the cubes on the side (namely, the $\langle 011 \rangle$ and the $\langle 001 \rangle$). In c), there is a 90° rotation between layers, and although the same orientations are possible, only the $\langle 001 \rangle$ is preferred and expressed as it minimises the misalignment with the previously deposited layer. Reproduced from [42]. 23

2.22 ***a) - i)*** Crystal orientation maps depicting the crystallographic texture resulted from different scanning strategies. Three different planes are shown for each scanning pattern followed. The corresponding scanning strategy is schematically shown at the top of the image and, for each strategy, the associated images are shown along a vertical line below the sketch (X-scan: *a), d), g) & j)*, XY-scan: *b), e), h) & k)*, Rot-scan: *c), f), i) & l)*). ***j) - l)*** At the bottom half of the image, the inverse pole figures for three families of planes are shown, illustrating the concentration intensity of the orientations observed directly above. Reproduced from [43]. 24
2.23 ***a), c) & e)*** SEM images with overlaid melt pool boundaries for the different scanning strategies. ***a'), c') & e')*** are higher magnification images of the SEM images shown in (a, c & e). ***b), d) & f)*** inverse pole figure maps of the corresponding areas analysed by SEM-EBSD. ***a), a') & b)*** correspond to the X-scan strategy, ***c), c') & d)*** are the samples fabricated using the XY-scanning and ***e), e') & f)*** show the Rot-scan samples. Black arrows noted in the SEM images denote the direction into which the columnar grains observed in the samples tend to grow. The samples are viewed along the building direction, on the yz-plane. Reproduced from [43]. 25
2.24 ***a), c) & e)*** SEM images with overlaid melt pool boundaries for the different scanning strategies. ***a'), c') & e')*** are higher magnification images of the SEM images shown in (a), c) & e)). ***b), d) & f)*** are inverse pole figure maps of the corresponding areas analysed by SEM-EBSD. ***a), a') & b)*** correspond to the X-scan strategy, ***c), c') & d)*** are the samples fabricated using the XY-scanning and ***e), e') & f)*** show the Rot-scan samples. Black arrows noted in the SEM images denote the direction into which the columnar grains observed in the samples tend to grow. The samples are viewed along the building direction, on the xz-plane. Reproduced from [43]. 26
2.25 Optical microscopy images of L-PBF fabricated NiTi alloy. The schematic on the right gives orientation information for the AM process. The top image is the side view, showing elongated columnar grains along the building direction. The bottom image is a top view of the associated x-y plane, showcasing the S-shaped grain morphology. Schematics on the side of the micrographs show the scanning direction. Reproduced from [16]. . . 28
2.26 ***a)*** Microstructure of NiTi alloy produced by L-PBF as found at the centre of the sample. Fine grain structure results in a homogeneous microstructure at this level of magnification. ***b)*** Microstructure of L-PBF-produced NiTi as found near the bottom region of the sample. The dark grey areas on the right-hand side micrograph are Ti_2Ni precipitates, combined with large NiTi grains arising due to the lower heat fluxes. Both micrographs together exhibit the variation found in the microstructure of NiTi parts produced by L-PBF. Reproduced from [16]. 29
2.27 Electron Backscatter Diffraction (EBSD) maps, inverse pole figure maps and pole figures of samples fabricated via L-PBF utilising ***a)*** a 45° build orientation , and ***b)*** a 90° build orientation, as obtained from the plane normal to the building direction. At the left of the maps a schematic insert shows the build orientation of the samples inside the L-PBF print bed, as well as the associated coordinate system. The plane normal to the building direction is also shown and is the plane normal to the loading direction of each sample. Reproduced from [49]. 30
2.28 ***a)*** Cross sectional view of the melt pool formed in Ti-rich NiTi fabricated by L-PBF using 950 W laser power and 500 μm laser beam diameter and corresponding schematic representation of the grain growth over several deposited layers. ***b)*** Cross sectional view of the melt pool formed in Ti-rich NiTi fabricated via L-PBF using 250 W laser power and 80 μm laser beam diameter with the corresponding schematic representation of the grain growth over several deposited layers. Reproduced from [26]. 31
2.29 Effect of the laser energy density, $[J/mm^3]$, on the transformation temperatures of three NiTi samples with ***a)*** Ti-rich (Ni49.7Ti), ***b)*** near equiatomic (Ni50.2Ti) and ***c)*** Ni-rich (Ni50.7Ti) compositions. ***a), b) & c)*** are the DSC graphs for various energy densities, see legend box below them. ***d) & e)*** Comparison between the phase transformation temperatures of the raw NiTi material (dashed lines) and the L-PBF final parts (solid lines) for each composition. Reproduced from [52]. 32

2.30 Stress, σ, [MPa] versus strain, ε, [%] curves until failure for Ti-rich NiTi alloy manufactured both conventionally and by L-PBF. The AM samples were also manufactured taken into account various orientations as shown on the graphic on the right. L-PBF NiTi parts fail earlier than their conventionally produced counterparts. Reproduced from [16]. 33
2.31 Stress, σ, [MPa] versus strain, ε, [%] curves until failure for Ni-rich NiTi alloy manufactured both conventionally and by L-PBF. The AM samples were also manufactured taken into account various orientations as shown on the graphic on the right. The parts fabricated by L-PBF all show similar behaviour, irrespective of fabrication orientation, but different to the behaviour of the conventionally manufactured sample. Reproduced from [16]. 34
2.32 ***a)*** Schematic representation of a single cycle of the testing procedure followed to evaluate the SME of NiTi samples. Values of importance concerning temperature, T, stress, σ, and strain, ε, are also noted on the graph for reference. ***b) &c)*** Stress, σ, [MPa] versus strain, ε, [%] curves showing the SME for NiTi alloys manufactured by ***a)*** AM and conventional methods respectively. ***d)*** The ratio between reversible and maximum strains plotted against the number of loading cycles for the two manufacturing methods. Reproduced from [52]. 35
2.33 ***a)*** True stress, σ_{true}, [MPa] versus true strain, ε_{true}, [%] versus temperature, T, [K] curves for the Ti-rich superelastic alloy developed by Zhu et al. in [26]. First cycle is marked in red, final cycle is shown in black. ***b)*** The same type of curve is given for the same composition alloy which has not been crystallographically designed as means of comparison. Blue line shows the first cycle and black line gives the last. For both cases, the mechanical portion of the loading occurred at room temperature. ***c)*** The recoverable strain measured for each material as a function of the loading cycles, and, ***d)*** the Two-Way SME as a function of the cycles. Reproduced from [26]. 36
2.34 ***a)*** Schematic representation of one cycle of the testing procedure followed to evaluate the SE behaviour of NiTi samples. Values of importance concerning temperature, T, stress, σ, and strain, ε are also noted on the graph for reference. ***b) & c)*** Stress, σ, [MPa] versus strain, ε, [%] curves showing the superelastic response for Ni-rich NiTi alloys manufactured by AM followed by heat treatments and conventional methods respectively. ***c)*** The ratio between reversible and maximum strains plotted against the number of loading cycles for the two manufacturing methods. Reproduced from [52]. 37
2.35 ***a)*** Cyclic compressive strain [%] versus stress [MPa] at temperature A_f + 10°C plot for sample manufactured by L-PBF with hatch distance 80 μm. ***b)*** Compressive strain [%] versus stress [MPa] at temperature A_f + 10°C for samples fabricated using different hatch distance values. These are as follows: A1 - 80 μm, A2 - 100 μm, A3 - 120 μm, A4 - 140 μm, A5 - 160 μm and A6 - 180 μm. Adapted from [57]. 38
2.36 Inverse pole figure map of a section of the sample fabricated using hatch distance of $80\ \mu m$ perpendicular to the building direction. The two black arrows indicate the scanning directions and the scale bar is equal to $300\ \mu m$. On the right, the pole figure texture plot of the sample is given, verifying the strong texture observed in the sample. Adapted from [57]. 39
2.37 True stress, σ_{true}, [MPa] versus true strain, $\varepsilon_{\text{true}}$, [%] curves as a function of the testing temperature for the Ti-rich NiTi alloy exhibiting high-temperature SE. Superelastic response is obtained for all temperatures shown, starting at 343 K up until 453 K. In the last two curves, the alloy shows yielding. Reproduced from [26]. 39

3.1 Scanning Electron Microscopy micrograph of the NiTi powder used for Laser-Powder Bed Fusion fabrication of the samples. 42
3.2 Schematic representations of the ***a)*** 0° rotation, ***b)*** 90° rotation and ***c)*** 30° rotation scanning strategies implemented for sample fabrication. 43
3.3 Schematic representations of the ***a)*** 67° rotation and ***b)*** the 67° rotation in island patterns scanning strategies implemented for sample fabrication. 44

3.4 ***a)*** Coordinate system defining the three dimensions associated with the L-PBF fabrication of the samples. It is customary to refer to the z-axis as the build direction (BD) and the y-axis as the scan direction (SD). The top, or xy, and side, or xz, faces of the cubic samples are also denoted. ***b)*** Schematic of the cubic sample fabricated by L-PBF for this thesis showing the dimensions after the EDM machining step. The intermittent lines outline one of the four cuboids into which each 10 × 10 × 10 mm is cut for further characterisation and testing. ***c)*** Schematic representation of the 8 × 4 × 4 mm cuboid sample used for the mechanical and TMA testing. A cut along the plane parallel to the xy plane of this cuboid produces the necessary sectioning to the sample for microstructural and phase characterisation. 45
3.5 Time [min] - Temperature [°C] profile for the DSC measurements. For simplicity, only the first two cycles are shown. 47
3.6 Typical DSC curve, Heat Flow [mW] versus temperature [°C] for a generic SMA. The four transformation temperatures are noted on the diagram together with the latent heat of transformation during both cooling and heating. The thermal hysteresis is also shown in blue, here taken as the difference between the peaks of the heat fluxes occurring during the two phase transformations. Adapted from [1]. 47
3.7 Time [min] versus strain [%] profile of the axial compression tests. For simplicity, only the first two cycles are shown. 49
3.8 The cuboid sample prepared for the mechanical test. The K type thermocouple is attached on two consecutive sample sides using arc welding in several spots along the wire lengths. 50
3.9 Close-up of the mechanical test set-up showing the induction coil, the air nozzles, the sample holder, the extensometer and the sample. 50
3.10 Stress versus strain diagram showing the deformation behaviour of single crystal NiTi subjected to compression at temperatures above the A_f. Strain definitions are also provided. Reproduced by [25]. 51
3.11 Time [min] versus temperature [°C] profile of the TMA test procedure. 52

4.1 ***a)*** Chemical composition of the 0, 90, 30, 67 and island_67 samples after the L-PBF fabrication measured by EDS. ***b)*** Oxygen content of the 0, 90, 30, 67 and island_67 samples measured after the L-PBF fabrication. 53
4.2 Optical micrographs obtained under visible light conditions of the samples 0 (***a***), 30 (***b***) and 67 (***c***). All images were taken along the BD of the samples. 55
4.3 OM images of the 0 sample obtained under polarised light conditions. ***a)*** Micrograph shows the xz plane of the sample (i.e. along the BD), ***b)*** xy view (i.e. perpendicular to the BD). 56
4.4 1D XRD spectra for the 0, 90, 30, 67 and island_67 samples. Additionally, the spectrum of the NiTi powder used for the L-PBF fabrication of the samples is also included for reference. The diffraction planes at 2θ values equal to 29.9°, 42.8°, 62.1° and 78.4° are also marked. 57
4.5 2D XRD spectra for the 0, 90, 30, 67 and island_67 samples showing the diffraction rings. The rings correspond to the diffraction angles in which peaks are measured in the 1D spectra. The spectrum of the NiTi powder utilised for the L-PBF fabrication of the samples is also included. In this case, rings appear in a discontinuous fashion, due to the fact that the powder consists of numerous crystallites. 57
4.6 EBSD map of the xz plane, ***a)***, and the xy plane, ***b)***, for sample 0. The associated Inverse Pole figures and the pole figures are also included. 58
4.7 EBSD map of the xz plane, ***a)***, and the xy plane, ***b)***, for sample 90. The associated Inverse Pole figures and the pole figures are also included. 59
4.8 EBSD map of the ***a)*** xz view and ***b)*** the xy view of sample 30. The Inverse Pole Figures and the Pole Figures are also included. 60
4.9 EBSD map of the ***a)*** xz view and ***b)*** the xy view of sample 67. The Inverse Pole Figures and the Pole Figures are also included. 61
4.10 EBSD map of the ***a)*** xz view and ***b)*** the xy view of sample island_67. The Inverse Pole Figures and the Pole Figures are also included. 61

4.11 ***a) - e)*** DSC curves (cycles 2 to 16) for the 0, 90, 30, 67 and island_67 samples respectively. For all specimens, the second cycle is depicted in blue, the 16^{th} cycle in red and the cycles in-between are given by black dotted lines. ***f)*** Detail of DSC heating segments, where the martensite to austenite phase transformation can be seen during heating. . . 64
4.12 Plot of the temperatures related to the forward phase transformation for each sample. The A_s is given in cyan, the A_f is given in magenta and the A_{peak} is given in wine red. The specific temperature values can be found in Table 4.2. 65
4.13 Mechanical response of the 0 sample for the HT, ***(a)***, and the LT, ***(b)***, groups. 66
4.14 Mechanical response of 90 sample for the HT, ***(a)***, and the LT, ***(b)***, groups. 67
4.15 Mechanical response of 30 sample for the HT, ***(a)***, and the LT, ***(b)***, groups. 67
4.16 Mechanical response of 67 sample for the HT, ***(a)***, and the LT, ***(b)***, groups. 67
4.17 Mechanical response of island_67 sample for the HT, ***(a)***, and the LT, ***(b)***, groups. . . . 68
4.18 First cycle of compression for all samples for the HT group, ***(a)***, and the LT, ***(b)***, groups. 68
4.19 Hardening rate for HT, ***a)***, and LT, ***b)***, groups. Sample 30 test produced only one compression cycle. 70
4.20 Recovery ratio for HT, ***a)***, and LT, ***b)***, groups. Sample 30 test produced only one compression cycle. 71
4.21 Stress hysteresis for HT, ***a)***, and LT, ***b)***, groups. Sample 30 test produced only one compression cycle. 71
4.22 Recoverable strain versus compression cycles for the samples of the HT group, ***a)***, and the LT group, ***b)***. 72
4.23 Recovery ratio versus compression cycles for the samples of the HT group, ***a)***, and the LT group, ***b)***. 72
4.24 SEM micrographs of the melt pools created by ***a)*** the low laser condition, i.e. samples of Section 4.1 and ***b)*** the high laser condition, i.e. the HLP_67 sample. The melt pool boundaries have been annotated for multiple melt pools as well as the dimensions of width, w_{MP} and depth, d_{MP}. 74
4.25 Chemical composition [at.%] of the 67, island_67 and HLP_67 samples after the L-PBF fabrication as measured by EDS. 75
4.26 1D XRD spectrum for HLP_67. Samples 67 and island_67 are shown for reference, as is also the spectrum of the NiTi powder. 76
4.27 2D XRD spectrum for HLP_67, diffraction rings. 76
4.28 EBSD map of the xz plane for samples HLP_67. The associated Inverse Pole figures and the pole figures are also included. 77
4.29 ***a), b) & c)*** Zoomed-in areas along a line of the EBSD map of the HLP_67 sample with a cubic lattice unit cell model showing the spatial orientation of the various grains. ***d)*** The positions of those zoomed-in areas with respect to the entire map. 77
4.30 ***a)*** DSC curves for HLP_67 sample, and ***b)*** close-up of the forward phase transformation as captured in the DSC measurements for samples 67, island_67 and HLP_67 b). . . . 78
4.31 Plot of the temperatures associated with the forward phase transformation for the 67, island_67 and HLP_67 samples. The A_s is given in cyan, the A_f in magenta and the A_{peak} in wine red. 79
4.32 Cyclic axial compression test for HLP_67, showing the full superelastic response of the sample. 80
4.33 1st compression cycle for HLP_67, island_67 and 67 samples. 81
4.34 ***a)*** Hardening rate and ***b)*** recovery rate plots for samples HLP_67, island_67 and 67. . . 81
4.35 Stress hysteresis plot for sample HLP_67. Samples 67 and island_67 are also included for reference. 82
4.36 Cyclic stability plots for sample HLP_67. ***a)*** Recoverable strain versus cycles, and, ***b)*** Recovery ratio versus cycles. Samples 67 and island_67 are also included for reference. 82
4.37 EBSD map of the xz plane, ***a)***, and the xy plane, ***b)***, for sample 0-R. The associated Inverse Pole figures and the pole figures are also included. 83
4.38 EBSD map of the xz plane, ***a)***, and the xy plane, ***b)***, for sample 90-R. The associated Inverse Pole figures and the pole figures are also included. 84
4.39 EBSD map of the xz plane, ***a)***, and the xy plane, ***b)***, for sample 67-R. The associated Inverse Pole figures and the pole figures are also included. 84

4.40 EBSD map of the xz plane, ***a)***, and the xy plane, ***b)***, for sample island_67-R. The associated Inverse Pole figures and the pole figures are also included. 85
4.41 EBSD map for the xz plane view of the HLP_67 sample. The associated Inverse Pole figures and the pole figures are also included. 85
4.42 ***a) - e)*** Cyclic axial compression test for the 0-R, 90-R, 67-R, island_67-R and HLP_67-R samples respectively. For all specimens, the first compression cycle is depicted in blue, the 16^{th} cycle in red and the cycles in-between are given by black dotted lines. ***f)*** First cycle of the compression test for all samples of the Rot group. 86
4.43 Plots of the hardening rate, ***a)***, and the recoverability, ***b)*** for the samples of the Rot group. 87
4.44 Plot of the stress hysteresis measured for the samples of the Rot group. 88
4.45 Cyclic stability plots for the samples of the Rot group. ***a)*** shows the recoverable strain as function of the cycles and ***b)*** depicts the recovery ratio versus the cycles. 88
4.46 EBSD map for the xz plane view of sample 90 after the end of the cyclic compression. The associated Inverse Pole figures and the pole figures are also included. 91
4.47 EBSD map for the xz plane view of sample 30 after the end of the cyclic compression. The associated Inverse Pole figures and the pole figures are also included. 91
4.48 EBSD map for the xz plane view of sample 67 after the end of the cyclic compression. The associated Inverse Pole figures and the pole figures are also included. 92
4.49 EBSD map for the xz plane view of sample island_67 after the end of the cyclic compression. The associated Inverse Pole figures and the pole figures are also included. 93
4.50 EBSD map for the xz plane view of sample HLP_67 after the end of the cyclic compression. The associated Inverse Pole figures and the pole figures are also included. 93
4.51 ***a)*** Plot depicting the superelastic response of sample 0, and, ***b*** sample 90. The plots include the amount of strain recovered during the high temperature heating during the TMA test. 94
4.52 ***c)*** Plot depicting the superelastic response of sample 30, and, ***d*** sample 67. The plots include the amount of strain recovered during the high temperature heating during the TMA test. 94
4.53 ***e)*** Plot depicting the superelastic response of sample island_67, and, ***f*** sample HLP_67. The plots include the amount of strain recovered during the high temperature heating during the TMA test. 95
4.54 Comparison between the residual strain left after the stabilisation of the superelastic behaviour, ε_{res}^{SE}, and the strain recovered by the high temperature heating during TMA, ε_{rec}^{TMA}. Samples discussed in Section 4.1 are shown in ***a)*** and samples 67, island_67 and HLP_67 are shown in ***b)***. 96
4.55 Percentage of strain recovery achieved by the TMA test procedure for all samples. Values are given in the last column of Table 4.10 96

C.1 Superelastic response for specimen no 2 of sample 0,***a)*** for the HT test and ***b)*** for the LT test. 110
C.2 Superelastic response for specimen no 2 of sample 90,***a)*** for the HT test and ***b)*** for the LT test. 110
C.3 Superelastic response for specimen no 2 of sample 30 for the LT test. 111
C.4 Superelastic response for specimen no 2 of sample 67,***a)*** for the HT test and ***b)*** for the LT test. 111
C.5 Superelastic response for specimen no 2 of sample island_67,***a)*** for the HT test and ***b)*** for the LT test. 111

List of Tables

2.1 A selection of post-process heat treatments used for achieving SE in Ni-rich NiTi SMAs together with the stabilised values of recoverable strain achieved 38

3.1 Scanning strategies and sample labels 43
3.2 Process parameters employed for the fabrication 44
3.3 Temperature conditions for the cyclic compression mechanical tests along the build direction 48
3.4 Rotated (Rot) group samples for the cyclic mechanical tests 49

4.1 Chemical composition of the fabricated 0, 90, 30, 67 and island_67 samples 54
4.2 Forward transformation temperatures 65
4.3 Details of the superelastic response of the HT group 70
4.4 Details of the superelastic response of the LT group 73
4.5 Recoverable strain and recovery ratio values from various publications. All values correspond to the stabilised behaviour unless stated otherwise. 74
4.6 Chemical composition for the fabricated HLP_67, island_67 and 67 samples 75
4.7 Forward transformation temperatures for the 67, island_67 and HLP_67 samples 78
4.8 Details of the superelastic response of the HLP_67 sample 80
4.9 Details of the superelastic response of the samples of the Rot group 89
4.10 Details of strain values associated with the high temperature recovery 95

A.1 Phase transformation temperatures and thermal hysteresis for sample 0. All values in °C.106
A.2 Phase transformation temperatures and thermal hysteresis for sample 90. All values in °C. 106
A.3 Phase transformation temperatures and thermal hysteresis for sample 30. All values in °C. 106
A.4 Phase transformation temperatures and thermal hysteresis for sample 67. All values in °C. 107
A.5 Phase transformation temperatures and thermal hysteresis for sample island_67. All values in °C. 107
A.6 Phase transformation temperatures and thermal hysteresis for sample HLP_67. All values in °C. 107

B.1 Titanium and Nickel content measured by SEM-EDS for sample 0. All values in at.%. . 108
B.2 Titanium and Nickel content measured by SEM-EDS for sample 90. All values in at.%. . 108
B.3 Titanium and Nickel content measured by SEM-EDS for sample 30. All values in at.%. . 108
B.4 Titanium and Nickel content measured by SEM-EDS for sample 67. All values in at.%. . 109
B.5 Titanium and Nickel content measured by SEM-EDS for sample island_67. All values in at.%. 109
B.6 Titanium and Nickel content measured by SEM-EDS for sample HLP_67. All values in at.%. 109

1

Introduction

The ever-growing challenges faced by humanity in the 21^{st} century in terms of technological advancement, tied with the ever-present needs for reducing the associated costs and limiting the environmental impact have highlighted the importance and necessity of developing materials whose capabilities extend beyond their traditional load-bearing capacity. Innovations in materials science and engineering during the 20^{th} and the 21^{st} centuries led to the development of materials which combine both structural capabilities as well as tailored properties and functionalities of various sorts. These materials became known as *multi-functional materials* and an important class of these are the so-called *active materials*. This specialised subgroup has the ability to possess sensing and actuation capabilities, or, in other words, exhibit a mechanical response when subjected to a non-mechanical field and vice versa. [1]

Shape Memory Alloys (SMAs) as one category of active materials are able of directly coupling thermal and mechanical fields. Depending on the situation, these metallic alloys can use either the mechanical or the non-mechanical field as the input and produce a specific response. The three key characteristics of SMAs are their ability to achieve shape recovery upon heating, even under high applied stresses, providing them with high actuation densities; to demonstrate cyclic behaviour by absorbing and dissipating mechanical energy in a reversible hysteretic manner involving a shape change, and, lastly, to exhibit various levels of frequency responses, which are crucial for their applications [1]. Their unique nature, which combines structural and functional properties, can have direct implications on a variety of aspects in any application they may be implemented; from reducing weight in aircraft and space equipment, to creating more compact assemblies of sensor-actuation systems, to providing responses mimicking that of natural tissues.

NiTi-based Shape Memory Alloys first came under the spotlight during the late 1950s, when William J. Buehler and Frederick E. Wang began to carefully exploring and studying the unique behaviour of the equiatomic NiTi alloy, which they named NiTiNOL [2]. Over the course of the last 80 years, NiTi-based alloys have become the most extensively researched Shape Memory Alloys, as they manage to bring together a set of properties that ensure their high performance even under extreme conditions, such as high resistance to fatigue, exceptional resistance against corrosive environments and excellent thermal conductivity [1]. Along with these come, of course, the two functionalities of these alloys; their ability to "remember" and recover their shapes and to withstand very high recoverable elastic strains. These two functional properties, suitably named *Shape Memory Effect* and *Superelasticity*, are what has triggered the interest of scientists and engineers and have resulted in this intensive research that continues to this day.

Nevertheless, this high performance nature of these alloys has had dire consequences on their manufacturability. For many years, these properties which are so coveted during service, resulted in the material being available in a very limited selection of shapes and forms, adversely affecting its applicability.

The advent of Additive Manufacturing during the last decades of the 20^{th} century brought about a revolution in the manufacturing of NiTi-based Shape Memory Alloys, and consequently in their availability

and use. The incredible flexibility and design freedom provided by Additive Manufacturing techniques has resulted in NiTi-based Shape Memory Alloys being now fabricated in any shape, size or form, attaining complex geometrical features and structures which were simply impossible with traditional manufacturing.

The most promising of the Additive Manufacturing methods employed for fabrication of NiTi-based Shape Memory Alloys is Laser-Powder Bed Fusion. In addition to the typical advantages of any Additive Manufacturing technique , it also allows for a unique opportunity; in-situ microstructural control of the material. This has made a critical breakthrough in the history of this metal, as it has allowed for the precise design of the functional behaviour of the alloy to be possible for the first time. By manipulating and optimising the parameters which govern the process, features such as the grain morphology and crystal spatial orientation can be tailored to produce desired thermomechanical responses.

As one can imagine, the interest surrounding the fabrication of NiTi-based Shape Memory Alloys by Laser-Powder Bed Fusion has intensified during the last 20 years. Significant efforts have been dedicated in studying how certain microstructural characteristics affect the two functionalities exhibited by NiTi-based Shape Memory Alloys, and then, how these characteristics can be bestowed upon the metal during its manufacturing. Nonetheless, the research is far from complete. The effect of several process parameters on the characteristics of the alloy still remains ambiguous and this offers great opportunities for fruitful and impactful research.

One of the process parameters which is known for significantly influencing the fabrication of metallic parts by Laser-Powder Bed Fusion is the scanning strategy followed during the deposition process. The choice of the scanning strategy is central for the result of the fabrication process, as it controls the thermal profile and history of the procedure. Aspects such as the solidification process, the laser beam energy and heat dispersion and dissipation throughout the build volume and the possible development of internal stresses and strains are determined by the features comprising the scanning strategy. Therefore, the need for deep understanding of the way that the scanning strategy employed during Laser-Powder Bed Fusion affects the process and the material is of paramount importance if successful manipulation of the thermomechanical behaviour of NiTi parts is to be realised.

The main goal and motivation behind this report is to present the research conducted on Ni-rich NiTi Shape Memory Alloy parts manufactured by Laser-Powder Bed Fusion implementing a variety of scanning strategies. The effect and influence of the scanning strategy on the microstructure of the alloy was studied and then linked to the resulting crystal structure, with respect to both the grain morphology and the crystallographic texture created. Afterwards, the functional behaviour of the material was evaluated in order to gain insight into how the superelastic response is affected by the scanning strategy employed during manufacturing. Finally, in the process of evaluating the ability of the material to showcase the Two-Way Shape Memory Effect, the nature of the unrecovered strain measured after the stabilisation of superelasticity was also investigated.

The structure of this report is as follows. Chapter 2 provides an in-depth discussion of the relevant theory behind the material being studied, together with an account of the relevant literature. Chapter 3 presents the methodology of the experimental work performed during this project. The results of the research are presented in Chapter 4, where they are also discussed and critically evaluated. Finally, Chapter 5 summarises the conclusions which are drawn by the study and Chapter 6 lists the various recommendations for future studies and research endeavours on this topic.

2

Literature Review

This Chapter provides an introduction into the theoretical aspects related to NiTi-based Shape Memory Alloys, as well as a concise overview of relevant research publications.

2.1 NiTi-based Shape Memory Alloys

2.1.1 Phase Transformations in NiTi Shape Memory Alloys

The ability of NiTi SMA, and of course of all SMAs that exist, to alternate between two forms, either this concerns a shape or a size, is rooted in the fact that in the range of operational temperatures of the material two phases with different crystal structures and properties exist. The high temperature phase, also referred to as the parent phase, is known as austenite (A) and it adopts a cubic B2 lattice structure, see a representation in Figure 2.1 a). The low temperature phase of the alloys is known as martensite (M), and can attain the tetragonal, orthorhombic (B19) or monoclinic (B19$'$) crystal structures, the latter two can be viewed in Figure 2.1 b) and c). Martensitic crystals tend to assemble in two forms when growing inside the grains; the first is the twinned martensite, M^t, a set of self-accommodated martensitic variants, and the second is the detwinned martensite, M^d, where one variant is dominant. The shape memory behaviour is essentially the ability of the alloy to transform between the above two phases, changing crystal structures in the process via a mechanism of shear lattice distortion. [1]

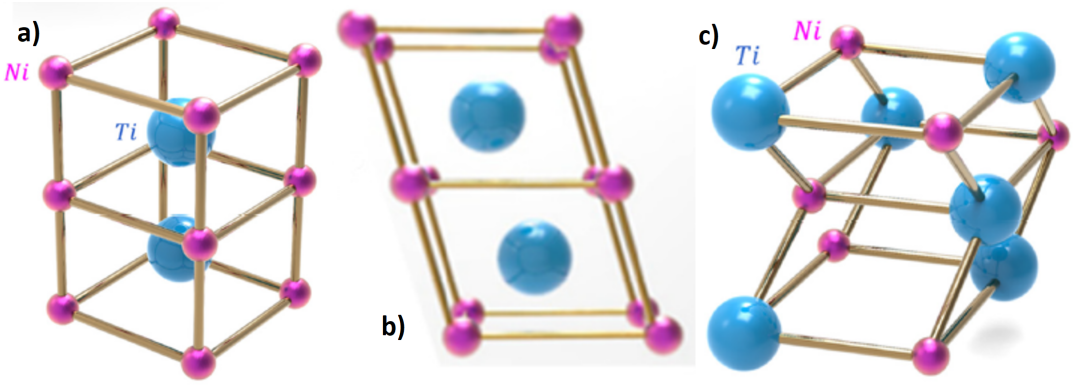


Figure 2.1: ***a)*** Schematic representation of the B2 austenitic phase of NiTi alloys. ***b)*** Schematic representation of the B19 crystal structure (orthorhombic). ***c)*** Schematic representation of the B19$'$ crystal structure (monoclinic). Large blue spheres are Ti atoms and small magenta spheres are the Ni atoms. Adapted from [3].

In general, SMAs couple thermal and mechanical fields, meaning that they can be loaded using thermal and/or mechanical loads. As a consequence, the two variables which determine their equilibrium state

are temperature and stress. For example, the temperature-induced martensite phase transformation can be seen in Figure 2.2, whereby the temperature is the variable determining the state of the alloy. During the forward transformation (top of Figure 2.2), the austenite transforms into the twinned martensite, in a process which starts at the martensite start temperature, M_s, and is completed at the martensite finish temperature, M_f, whereby it is considered the the entire volume of the material has adopted the B19' crystal lattice. In a similar process, the austenite transforms back to the twinned martensite phase, in what is known as the reverse transformation, see the bottom diagram of Figure 2.2. Accordingly, the process starts at the austenite start temperature,A_s, and is completed at the austenite finish temperature, A_f. During the phase transformations, phases are present and also disappear, which inevitably gives rise to phase interface energy as well as stored elastic energy [4]. These act as barriers causing the emergence of hysteresis, experienced as a delay between the occurrence of the transformations during the cooling and the heating cycles, see the differences between the temperature readings in Figure 2.2 [4]. All in all, three possible ways of loading arise for this type of materials; thermal loading alone, involving only changes in the temperature as seen above, mechanical loading alone through the action of forces, stress and strains, and combined thermal and mechanical loading. The apparent consequence of this coupling capability is that the thermomechanical behaviour of these materials becomes of the utmost importance.

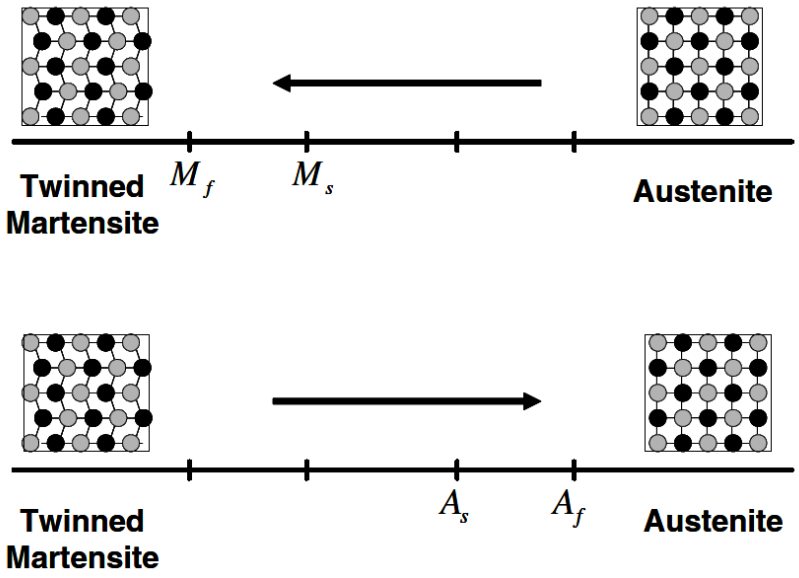


Figure 2.2: Forward (top) and reverse (bottom) transformations occurring during the loading path where only temperature is imposed on the SMA. The sketches showcase the absence of any shape change during the process. Reproduced from [1].

Shape Memory Effect

The term *Shape Memory Effect (SME)* describes the behaviour of the SMA when is deformed from the twinned martensite phase to the detwinned one and then unloaded while at temperatures below the A_s temperature. Shape recovery is then achieved by heating the alloy to temperatures above the A_f temperature, thus also recovering its austenitic parent phase. This load path and the associated behaviour is the *One-Way SME, (OWSME)* and is a behaviour induced by means of mechanically and thermally loading the material. [1]

Following along the curve depicted in Figure 2.3, the *Shape Memory Effect* of a SMA wire can be fully understood. Starting at point 1, the wire is at low temperature without any history of prior loading, either stress or strain. At this moment, a tensional load is applied to it, increasing the stress and strain values, see "loading" marking on the $\sigma - \varepsilon - T$ plot. This elastic loading segment ends at point 2, where the martensite starts to reorient itself and detwinn until point 3 by following a response which, up to this point, resembles plastic behaviour. At point 3 the reorientation is complete and the martensite is fully detwinned, and from this point onwards, loading results in an elastic response, again until point 4. From

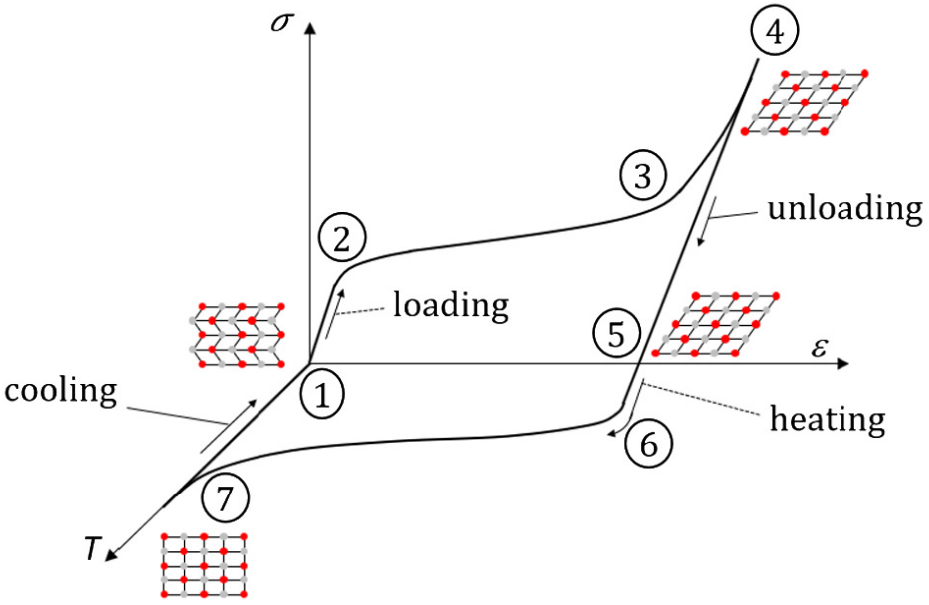


Figure 2.3: Phase diagram depicting an overview of the Shape Memory Effect using stress, σ, strain, ε, and temperature, T. Corresponding crystal structures of the alloy are shown in the side sketches. Reproduced from [5].

the point of maximum stress, point 4, the unloading begins, elastically at first until point 5, where stress levels fall to zero and strain remains in the material as residual deformation. Then, heating starts for the first time since the loading path began, reaching point 6 where the phase transformation to austenite is triggered and the residual strains begin being recovered by means of thermal loading. At point 7, the $M^d \rightarrow A$ transformation is completed, with the alloy being fully austenitic and having recovered all the residual strain. Finally, a cooling step is included, where, although no shape change is observed, the alloy returns to its twinned martensite state following the transformation $A \rightarrow M^t$. [5]

A few useful notes on this topic are in order at this point. Firstly, the stress required for the martensite variants of the twinned phase to be reoriented to the detwinned phase is far lower than the stress required for plastic yielding of the martensitic crystal, and this is the reason why the transformation takes place. Secondly, as expected, if no plastic strain is produced during the detwinning transformation, then the shape recovery reaches levels equal to 100%. Finally, in the context of the SME the transformation strain, ε^t, can be defined as the strain recovered due to the transformation from the detwinned martensite to the austenite parent phase. [1]

Superelasticity

When the SMA is solely mechanically loaded at temperatures above A_f, it initially undergoes a shape change due to the transformation to detwinned martensite, a process which generates large inelastic strains, and subsequently, during the unloading part of the path, the alloy returns to austenite, recovering its shape and partially the strain. This phenomenon, called *Superelasticity*, is usually combined with the *Rubber-like Behaviour* of martensite, which allows it to reorient reversibly, resulting in what is known as the *Pseudoelastic Effect*. [1]

The Pseudoelastic Effect results in a *hysteresis* corresponding to the amount of energy lost during a complete transformation cycle. The martensite created by such a transformation, which is strictly stress-induced, is known as *Stress-Induced Martensite, (SIM)*. [1] Usually, of particular interest for SMAs is the superelastic part of the Pseudoelastic Effect rather than the entire behaviour. This has lead to the two terms being used interchangeably to some extend, even though what is of significance and interest for the SMA class of materials is their superelasticity. [1].

Figure 2.4 shows the phase diagram of the superelastic response of an SMA wire loaded in tension. Following along the curve, starting at point 1 the material is found to be in its initial undeformed and unloaded state, i.e. $\sigma = \varepsilon = 0$. Elastic loading leads to point 2, where the transformation $A \rightarrow M^d$ starts,

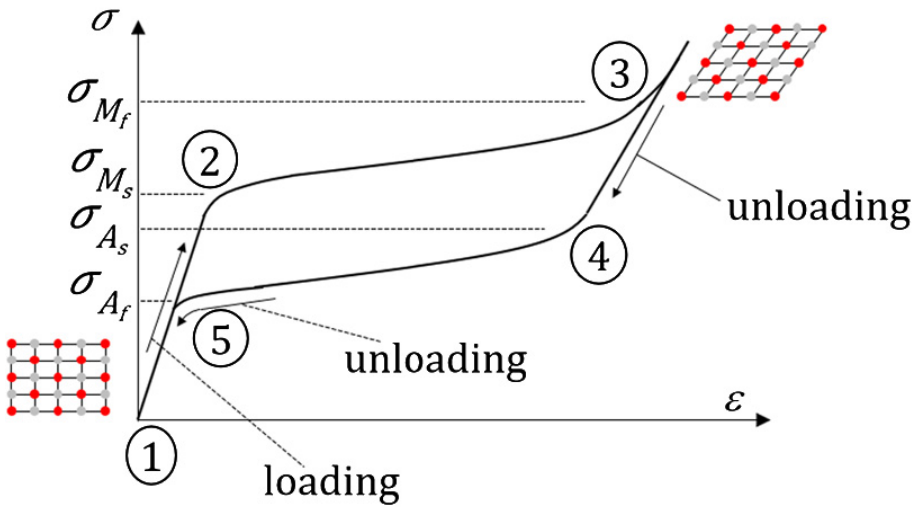


Figure 2.4: Phase diagram depicting an overview of the superelastic behaviour of an SMA using stress, σ, and strain, ε. Corresponding crystal structures of the alloy are shown in the side sketches. Reproduced from [5].

triggered at the stress values known as the cirtical stress for the Martensite transformation, $\sigma_{\text{crit}}^{\text{M}}$. At point 3 the transformation is completed and the shape change has taken place, as can be seen by the lattice sketch on the figure. Further loading until the maximum stress value shown on the plot results in the elastic deformation of the M^d. Subsequently, elastic unloading of the wire takes place, until point 4 is reached, where the reverse phase transformation from M^d to A begins. At point 5 the transformation is completed, and from this point onwards, i.e. until closing the curve again at point 1, the unloading of the wire continues elastically in the austenitic phase until the load is fully removed and the strain recovered. Full strain recovery is only possible if, after point 3, the deformation was not plastic. [5]

Cyclic Behaviour of Shape Memory Alloys

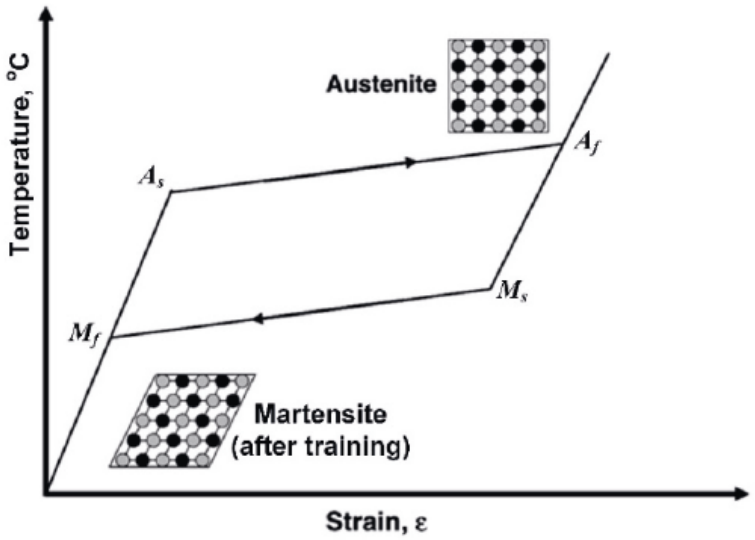


Figure 2.5: Temperature, T, [°C] versus strain, ε, [%] plot of the Two Way Shape Memory Effect, TWSME. Reproduced from [4].

Shape Memory Alloys are able of exhibiting cyclic behaviour, more commonly referred to as the *Two-*

Way Shape Memory Effect, (TWSME). This effect can be observed in SMAs which have been subjected to a repeated thermomechanical cyclic loading along a specific path, or in other words, have undergone *training* until their hysteretic response has been stabilised and the plastic strain is saturated [1]. The manifested behaviour of TWSME consists of repeatable shape changes between a high temperature (i.e. $T > A_f$) geometrical shape and a lower temperature (i.e. $T < M_f$) shape under a cyclic thermal loading alone without any stress application [6]. An schematic representation of the behaviour can be seen in Figure 2.5.

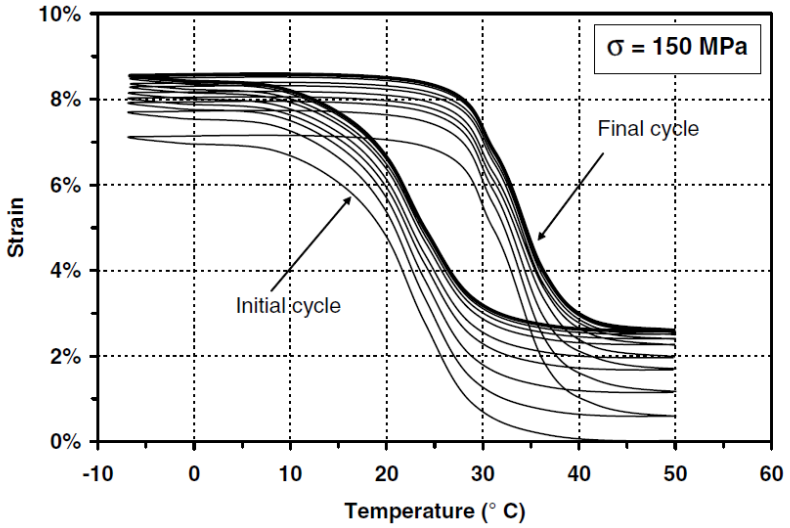


Figure 2.6: Strain, ε, [%] versus temperature, T, [°C] plot of the thermal cyclic loading of a NiTi wire under a constant applied stress of 150 MPa. The first and final cycles are noted. The accumulated strain saturation is also visible at the point where the cycles begin to overlap. Reproduced from [1].

This macroscopically observed behaviour is due to permanent defects introduced in the crystal lattice of the alloy during the training process. These permanent defects, structures of dislocations which are specifically oriented inside the lattice[4], arise due to the repeated nature of the mechanical loading to the martensitic phase and result in stabilising the configuration of the plates, thus giving rise to an internal residual stress state [6]. During the heating part of the cycle the martensite plates disappear, however, the defects remain in the matrix as do the residual stresses. The presence of this particular stress state promotes the formation of preferred martensitic variants during cooling of the austenite phase under no external loads [1], in order for the stresses to be accommodated within the crystal.

Training is a thermomechanical treatment in nature [1] [6]. Many training processes have been proposed to induce the TWSME in SMAs. Of the most classic options is to thermally train the SMA by means of subjecting it to a thermal loading cycle under constant applied stress, as can be seen in Figure 2.6. In this case, during each cycle the strain generated during the cooling part of the cycle is only partially recovered upon heating, resulting to an amount of permanent strain left in the lattice. As the training process progresses, the plastic unrecovered strain generated during each cycle begins to gradually decrease until it ceases to accumulates and the response of the material stabilises. The other typical training process for obtaining TWSME is to isothermally train the SMA by subjecting it to a repeated mechanical loading between zero stress and a certain strain value within its pseudoelastic regime (i.e. $T \geq A_f$) until, again, the strain saturation occurs [1] [6]. This training route can be seen in Figure 2.7.

As can be inferred, the TWSME is heavily dependent on the internal residual stress state of the material [1], meaning that any changes or modifications to it would disrupt it, because the defects essentially make the product phase of the metal to become more stable as more energetically favourable variants of martensite are promoted to grow in each cycle due to their presence [6].

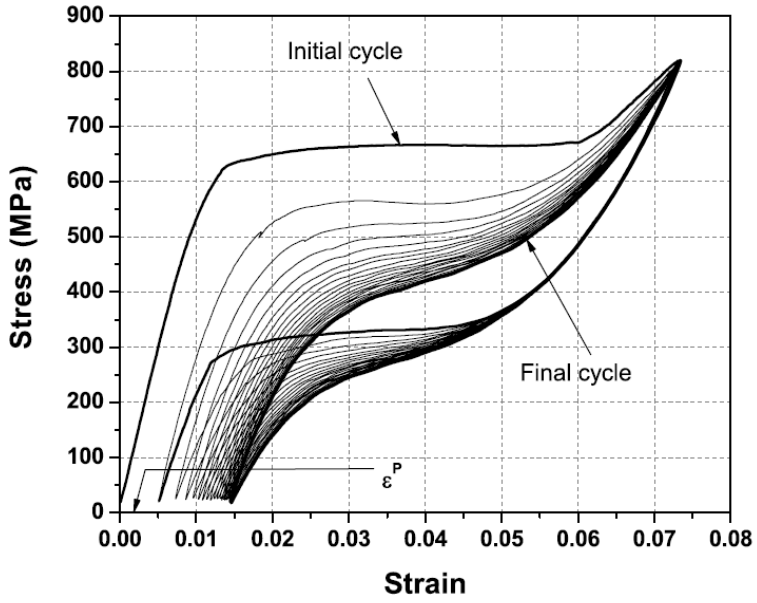


Figure 2.7: Stress, σ, [MPa] versus strain, ε, graph of the pseudoelastic response of a NiTi wire with A_f = 65°C tested at T = 70°C. The initial and final cycles are noted. The stabilised pseudoelastic hysteresis loop after 20 cycles is shown with thick black lines as the strain has become saturated at this point. Reproduced from [1].

2.1.2 Factors influencing phase Transformations & Functional Properties

Grain Size

Grain size is one of the factors which influence the functional behaviour of NiTi SMAs, affecting aspects as the phase transformations, their paths, the temperature at which these occur, the morphology of the martensite crystals that form, as well as the stability and degradation of the functional properties.

In general, decreasing the size of the grains below 100 nm results in a strong suppression of the transformation of the austenite phase to the martensite, which for grains smaller than 50 nm totally fades [7]. This is due to the increasing energy barrier of the transformation to the martensite which increases as the grain size diminishes [7]. Consequently, the temperature at which the transformation takes place also decreases with decreasing grain size as do the volumetric fraction of the material undergoing the transformation [7]. Additionally, both the morphology of the martensite crystals and the paths that these transformations follow are different for different grain sizes. For example, in nanocrystals of NiTi SMA, it is easier for the R-phase to arise when the metal transforms from the B2 austenite lattice and, in turn, is not so susceptible to the influence of the decreasing grain size compared to the $B19'$ phase [7].

As far as the functional behaviour degradation is concerned, modelling and experimental work has shown that as the size of the crystals of polycrystalline NiTi decreases, the functional degradation and fatigue is attenuated [8]. Moreover, for the cases when the grain size falls below 10 nm, simulations showed that no functional degradation occurs [8].

However, it is important to stress here that for the scope of this thesis the grain size effects on the behaviour of NiTi SMAs are rather not so vital. As Zhu et al. showed, NiTi parts fabricated by L-PBF normally consist of grains with sizes within the μm range [9], well above the level at which size effects are found to become crucial for the material.

Chemical Composition

As is the case with all materials, composition plays a significant role in determining the properties and controlling the final performance of NiTi SMAs, and hence, it dictates the applications in which they can be used. As explained by J.M. Jani et al. in [10], the transition temperature of NiTi-based SMAs and the behaviour of the hysteresis loop they exhibit are strongly influenced by the composition of the alloy, together with the thermomechanical (post-) processing employed and the specific working environment

of a given application, since stress levels for these materials can become crucial. As usual when metals are involved, alloying elements also create substantial differences in the properties and the performance of the material, and, lastly, of course, impurities can come into play and affect various parameters of their behaviour. In this section, all three are going to be discussed with respect to how they may affect the transformation temperature ranges of the Ni-rich NiTi alloy, and specifically the martensite start temperature, M_s, its thermal hysteresis, ΔT_H, and the latent heat of the transformations, ΔH. The impact on the alloy's mechanical properties, such as its fatigue and corrosion resistance and its manufacturability are also going to be viewed under this light.

In order to facilitate understanding of the way that the chemical composition of the NiTi alloy affects its applicability it is important to raise a few points here. All properties of interest showcased by SMAs are determined and controlled by the martensitic transformation which evolves through a series of temperatures, as it is not an instantaneous transition. These transition temperatures essentially define the temperature range at which the SME and superelasticity will be observed in service, making it the primary parameter taken into consideration when deciding on exploiting the two characteristic behaviours of NiTi alloys. A key point is that the lower this temperature range is, the stronger the manifestation of the SME will be in any given application [11]. Applications utilising the thermal memory of the alloy, or, in other words, the One Way SME for actuation and coupling purposes require that the formation of the martensite is completed above the operating temperature, i.e. M_f [12]. Considering superelasticity, also known as the mechanical memory of the material exploited for flexible medical and engineering applications, the austenite is required to be fully formed below the operating temperature for successful applications [12]. For instance, a component exploiting superelasticity at ambient temperature would require subzero transformation temperatures, which of course, cannot be too low, as in this case inducing the phase transition would be very hard [13].

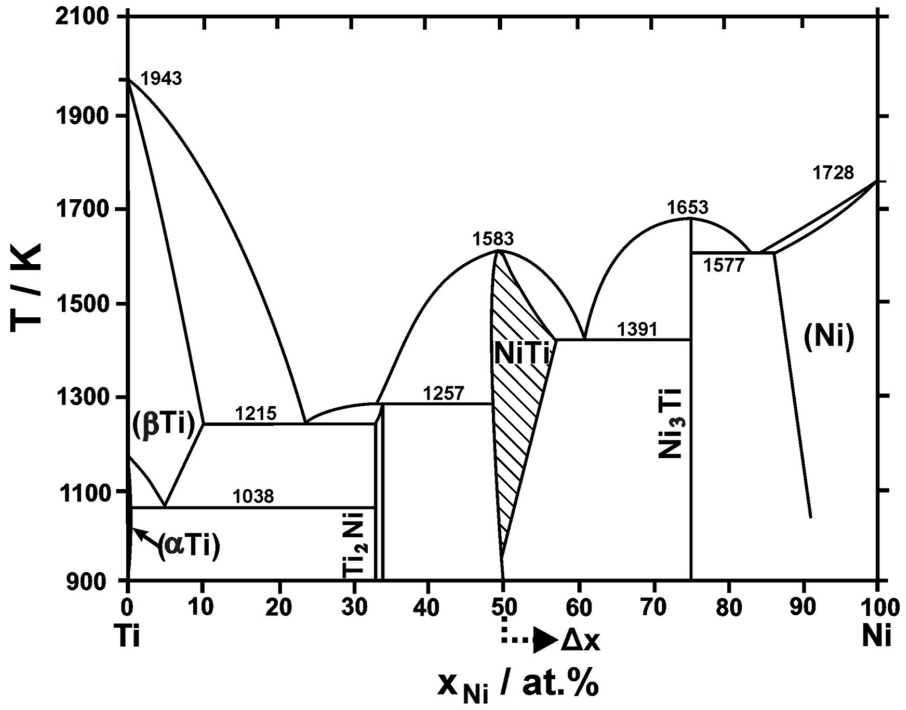


Figure 2.8: The phase diagram of the NiTi system. Reproduced from [14].

A look at the phase diagram of the Ni-Ti system, given in Figure 2.8, reveals that NiTi exists as an alloy in the neighbourhood of the equiatomic composition (the shaded area of the phase diagram), explaining why, when examining the effect of the alloy's composition, the interest is mainly focused in the range around 48.0-52.0 at.% Ni, occasionally extending up to concentrations of 55.0 at.% Ni. The border to the left of the alloy phase appears to be vertical to the concentration axis, implying that there is no possibility of dissolving excess Ti into the system. However, the border line to the right hand side of the NiTi phase, at approximately 1223 K, appears to have a positive slope denoting the increasing solubility of excess

Ni in the austenitic phase with increasing temperature [15]. A large variety of precipitates which can arise in the system at various conditions of temperature and composition can also be identified on the phase diagram.

Starting at the composition of the original NiTi alloy (equiatomic NiTiNOL), i.e. 50 at.% Ni and 50 at.% Ti, there exist two options for modifying it. The first follows the arrow on the phase diagram marked "Δx"; the content of Ni is increased at the expense of Ti, creating Ni-rich NiTi. Going towards the opposite direction of the "Δx" arrow the binary alloy becomes Ti-rich, achieved through introduction of other alloying elements in the matrix which substitute for the Ni atoms.

Decreasing the atomic percentage of Ni in NiTi has been found to have no effect on the transition temperature of the material [1], with the general behaviour of Ti-rich NiTi being similar to this of the equiatomic alloy [13]. This can be clearly seen on both graphs presented in Figure 2.9 as, for Ni concentrations below 50 at.%, the M_s temperature seems to follow a constant trend lying around 60°C. Regarding the effect of increasing Ti content of the binary alloy on the width of the thermal hysteresis, ΔT_H, as can be seen on Figure 2.11 a), for compositions up to and including the stoichiometric, there is no significant change (Region I marked on the plot), although the data does show some degree of scatter [15]. On Figure 2.11 b) one can see the effect of the Ni content of the alloy on the heat of both the forward (open circles, B2 → B19′) and the reverse (black squares, B19′ → B2) martensitic transformations as were reported in [15]. Notable is the fact that the heats are identical in many cases between the forward and the reverse transformations. The data also shows scatter, but, in general, there is a slightly increasing trend for the heats of transformation for the Ti-rich alloys as the composition approaches the stoichiometric.

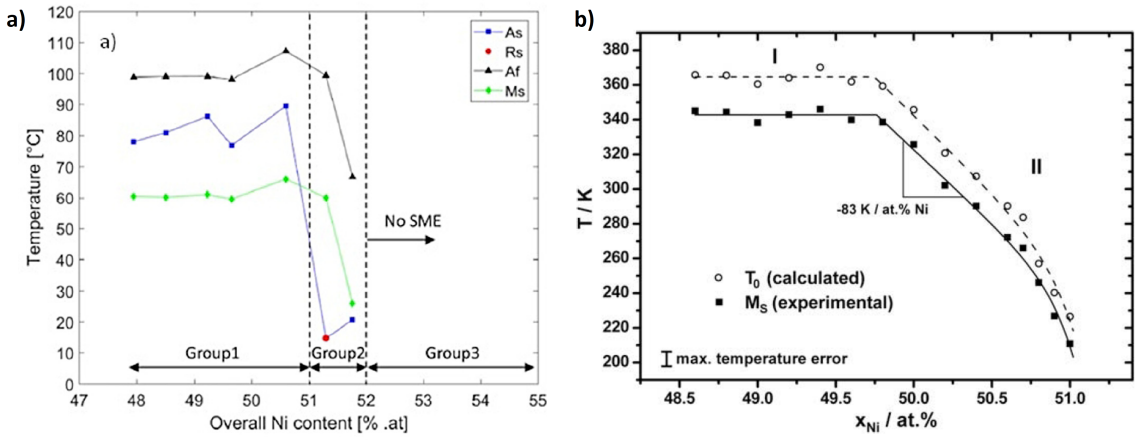


Figure 2.9: ***a)*** Transformation temperature range dependence on the overall Ni content of NiTi alloys. The plot contains the variations of A_s in blue, A_f in black and M_s temperatures in green. For a specific alloy concentration the rhombohedral start temperature is also relevant, shown in red and marked as R_s. Reproduced from [11]. ***b)*** Variations of the M_s temperature (black squares) for Ni concentrations between 48-51 at.%. The depicted behaviour divides the plot in regions I and II. The slope of the decrease in Region II is marked on the graph. The open circles curve depicts the behaviour of the temperature of the thermodynamic equilibrium between austenite and martensite with respect to the Ni content. Reproduced from [15].

Contrary to the situation regarding Ti-rich NiTi alloys, increases in the Ni content of the metal above the equiatomic composition yield tremendous effects, deducing that the most effective way of manipulating the thermal behaviour of the material is through altering the Ni/Ti ratio [13] [15]. In fact, it has been established that for Ni concentrations between 50.0 at.% and 51.2 at.%, the M_s temperature evolves from 339 K to 211 K [12]. This translates to a decrease of the phase transition temperature of the alloy equal to 10 K per 0.1 at.% of added Ni. This behaviour can be readily visualised in both Figures 2.9 and 2.10, where a considerable drop in all related transformation temperatures and especially M_s can be observed. Particularly, in Figure 2.10 the plot presents the added viewpoint of the Ni/Ti ratio in the alloy, a crucial factor in the exhibited functional behaviour of the material. Compositions of NiTi which tend to the Ti-rich side, are able of showcasing the SME response, whereas Ni-rich NiTi alloys are employed for their superelastic functional responses [16]. This further strengthens the statement made at the beginning of the paragraph regarding the impact of the Ni/Ti ratio on the properties and the realised functionalities of the metal.

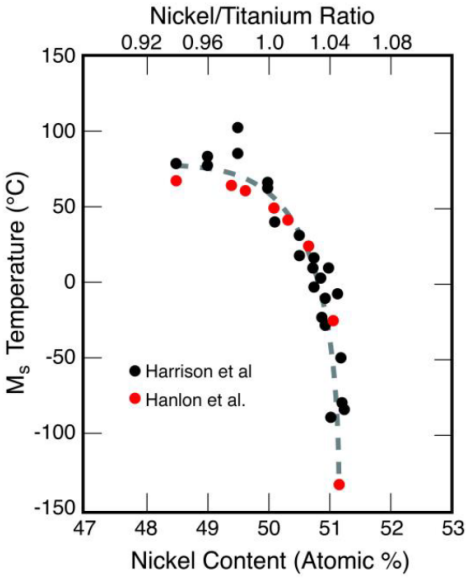


Figure 2.10: Dependence of the M_s temperature on the Ni content of the NiTi SMA as well as on the Ni/Ti ratio of the material. The data shows a sharp drop which starts around the point of the stoichiometric composition, illustrating the heavy influence of composition on the thermal behaviour of the alloy. Reproduced from [17].

A special Ni-rich NiTi composition worth mentioning concerns the metal when its Ni contents reach 55 at.%. At this point, the transition temperature range extends from - 10°C to + 60°C [1]. This particular composition of NiTi possesses superior corrosion resistance even at harsh environments, such as salt-water baths, as well as showcases excellent thermomechanical stability, a trait which enhances the metal's processablity and manufacturability [1].

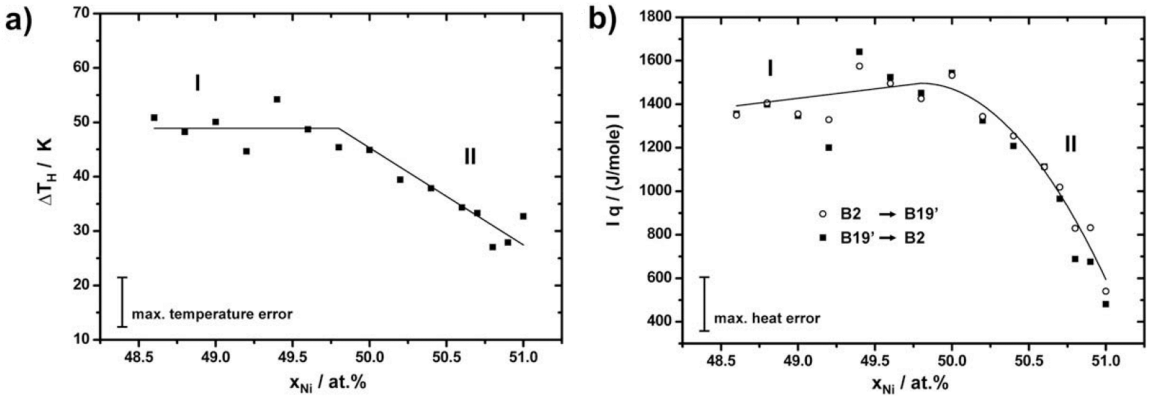


Figure 2.11: ***a)*** Dependence of the width of the thermal hysteresis, ΔT_H, on the Ni content of the alloy. Region I corresponds to Ti-rich alloy concentrations, whereas Region II is associated with the Ni-rich NiTi. Reproduced from [15]. ***b)*** Concentration dependence of the heat of transformation, $|q|$, for the $B2 \rightleftharpoons B19^{'}$ reactions. Again, Regions I and II are used to assist with data interpretation. Reproduced from [15].

As far as the width of the thermal hysteresis, ΔT_H, and the latent heat of the transformation, ΔH, for the Ni-rich alloys are concerned, a look at Figure 2.11 can be enlightening. For both quantities a decrease is observed with increasing Ni contents , which for the case of ΔT_H is linear. The explanation behind such a behaviour, which is also the reason behind this extremely strong dependence of the M_s temperature on the Ni concentration, has been proposed to be the following. The higher Ni content in the alloy increases the compatibility between the crystal lattices of the austenite and the martensite by means of stabilising the B2 austenitic crystal structure through the formation of anti-site defects, i.e. Ni atoms occupying positions in the Ti lattice. These defects are accompanied by large lattice relaxations occurring locally which aid in relieving the elastic strain energy of the structure leading to a decrease

of the height of the nucleation barrier for the martensite [12]. In other words, the phase transformations are better facilitated in alloys with high Ni contents resulting to a decrease of the width of the thermal hysteresis, ΔT_H, the latent heat associated with the transformations, ΔH, and, consequently, the temperature at which the reactions take place, primarily the M_s.

Both the processing itself, as well as any post-processing methods have a great effect on the material's behaviour. Additive Manufacturing (AM) techniques for example, tend to produce NiTi parts with high transformation temperature ranges, even higher than those of the initial material provided for printing [11]. This is attributed to the evaporation of Ni taking place during the printing process, leaving the matrix in a Ti-rich state, which, as explained at the start of this Section, is characterised by higher temperatures of transformation. Furthermore, when printing Ni-rich NiTi feedstock materials, secondary phases arise at temperatures around 200-700°C (most commonly Ni_4Ti_3, Ni_3Ti_2 and Ni_3Ti) which, due to being rich in Ni, deplete the matrix of its contents forcing it to become Ti-rich [11]. The consequence of this is that, again, the temperature at which the phase transformations occur at the finished parts is increased. Post-processing treatments implementing diffusional precipitation reactions have also been found to be a very effective and easy-to-control way for adjusting the transformation temperatures in Ni-rich NiTi after production. Aging of the NiTi SMA results in decreasing the transformation temperature range in a process where the final phase transition temperature seems to be solely controlled by the temperature at which the alloy is aged [13]. In particular, higher aging temperatures lead to greater decreases of the transformation temperature of interest, either this is the M_s or the R_s [13].

Lastly, impurities also play a significant role in the behaviour exhibited by NiTi alloys. The elements of interest are mainly Oxygen and Carbon which, in general, can affect the transformation temperatures as well as alter various mechanical and functional properties. In more detail, impurities have been known to decrease the temperatures at which the phase transitions take place and to incite the formation of various precipitates which, in occasions, tend to embrittle the austenitic matrix of the alloy [18]. The reason behind the effect of Oxygen and Carbon on the transition temperatures lies on the formation of Ti-rich secondary phases in the NiTi matrix, including Ti_4Ni_2O, $Ti_2Ni \cdot O_{1/2}$ and TiC, which arise from the combined events of the high reactivity of the Ti and the increased pick-up of the impurity elements occurring during processing [15]. These secondary phases end up stripping the NiTi matrix of its Ti, turning the alloy into a Ni-rich metal for which the phase transition temperatures are lowered. Particularly for Ni-rich NiTi alloys, the effect of the Oxygen-stabilised Ti_2Ni particles is very important [15].

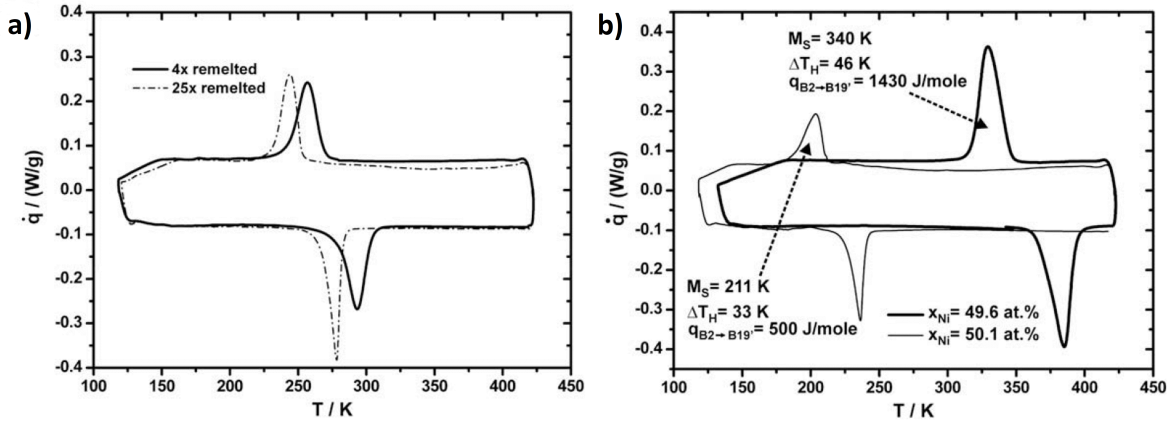


Figure 2.12: ***a)*** DSC curves (heat flow, $\dot{q}$, [W/g] versus temperature, T, [K]) for two NiTi samples of the same Ni content (50.7at.% Ni) showcasing the effect of O and C impurities pick-up. The solid black line corresponds to the sample melted four times and the dashed line to the sample melted 25 times. Reproduced from [15]. ***b)*** DSC curves (heat flow, $\dot{q}$, [W/g] versus temperature, T, [K]) for two NiTi alloys of different Ni contents illustrating the differences in terms of the M_s temperature, the width of the thermal hysteresis, ΔT_H, and the latent heat of the martensitic transformation, $q_{B2\rightarrow B19'}$. The thick black line corresponds to 49.6 at.% Ni sample and the light gray line to 50.1 at.% Ni sample. Reproduced from [15].

The recurring melting cycles to which the NiTi alloys are subjected to during fabrication, a characteristic of AM processes, lead to increased pick-up of impurities which have a strong effect on the thermo-mechanical behaviour of the final metallic part [15]. The significance of such an event is evident in the

Differential Scanning Calorimetry (DSC) plots shown in Figure 2.12 a), where two NiTi samples with 50.7 at.% Ni content were subjected to a different number of consecutive melting cycles (four versus 25 cycles). The effect of remelting is obvious; the curve corresponding to the sample melted 25 times has shifted to considerably lower temperatures, with the difference between the two curves being approximately 20 K attributed to the increased pick-up of both Oxygen and Carbon impurities [15]. Additionally, differences can be spotted between the corresponding peaks associated to the phase transformations of the two DSC curves on the plot.

For concluding this section, it can be said that the effect of the composition of the NiTi SMA on the properties of the material and its performance is tremendous. In fact, it has been noted that it is extremely unusual for a functional engineering material to have such heavy dependency on its constituents and their concentrations, to such an extend that it resembles the cases of materials employed in the electronics industry [12]. The DSC plots presented in Figure 2.12 b) illustrate the tremendous effect of Ni contents on the thermal behaviour of the alloy. The black line represents the DSC curve for a NiTi sample with 49.6 at.% Ni, whereas the gray line corresponds to a NiTi sample with 50.1 at.% Ni content. For such small differences in the Ni content between the two samples, the differences in all three quantities shown on the plot are massive; for the Ti-rich alloy, the M_s temperature is 340 K, the ΔT_H equals 46 K and the heat of the transformation to martensite reaches 1430 J/mol. For the Ni-rich NiTi, on the other hand, the M_s temperature lies at 211 K, the ΔT_H is given as 33 K and the heat of the martensitic transformation is 500 J/mol. As the alloy constituents have such a great effect on the properties and, hence, the behaviour of NiTi SMAs, the need for precise control of their combination is imperative, however, it is very difficult to actually achieve this level of compositional control in practice. Aspects of processing, including impurities introduced during manufacturing, secondary phases arising due to stress or temperature conditions, or potential post-processing treatments are yet another way for altering the thermomechanical behaviour of NiTi in a more accessible manner. Finally, alloying with a third element opens up an entirely new world of possibilities for NiTi-based SMAs, including alloys which exhibit their functionalities at temperatures up to 800°C known as High Temperature SMAs (HTSMAs) [1].

Crystal Defects

A variety of crystal defects has been reported to influence the behaviour exhibited by NiTi SMAs. Dislocations and dislocation structures, such as loops, arise during the martensitic transformation in order to accommodate it [19] and they have been found to play a role in both decreasing the M_s temperature, hence hindering the transformation during the SME cycling and in decreasing the σ^{M}_{crit} for the forward transformation during superelastic cycling of the metal, hence promoting the functionality [19].

Precipitates of various kinds are also common to arise in the material, as can be seen in the phase diagram of the Ni-Ti system shown in Figure 2.8. The formation of these precipitates influences the chemical composition of the NiTi matrix, as it can deplete from or enrich it to either of the two elements [20]. Concurrently, the presence of these precipitates inside the lattice introduces various kinds of strain fields leading to distortions which also affect the transformations, both in terms of the products and the paths [20].

Finally, crystal defects are reported to be responsible for the degradation of the functional behaviours, including the One Way SME, the superelasticity and the TWSME. Most notably, dislocations are named as a crucial parameter in the degradation of the superelastic response of NiTi alloys, as they participate in the accumulation of residual strain in the austenite phase during mechanical cycling of the material [21]. However, it is noted in the same publication that the steady-state structure of the dislocations in the metal lattice results in the degradation of the superelastic functionality to saturate as the number of loading cycles progresses beyond a certain point [21]. Regarding the One Way SME, the interplay between the reorientation of the martensite grains, the martensite transformation and the movement of dislocations is what results in the degradation of the functionality with repeated cycling of the NiTi alloy [22].

Crystal Orientation

Taking into account the fact that the entire behaviour of SMAs is based on phase transformations between different crystal lattices, one can easily infer that that behaviour of the material must be strongly dependent on the crystallographic orientation. Evidences of such dependency have been reported for

both the SME and the superelastic functionalities but they also extend to the mechanical properties of the alloy. Differences in the crystallographic texture have been proposed as being the reason behind differences in the shape memory behaviour and the tensile properties showcased by cold-rolled NiTi sheets [23] and equiatomic NiTi wires and sheets [24].

Similarly, the superelastic response is heavily dependent on the crystallographic orientation of single crystals of NiTi, as shown by Sehitoglu et al. [25]. Since this functional property is the focus of this thesis, an in-depth discussion of this topic will take place in the following lines.The stress, σ, versus strain, ε, plots given in Section 2.1.1 highlight the dependence of the functional behaviour of NiTi SMAs on the applied stress state, but as can be seen in Figure 2.13, this stress itself is a function of temperature for this metallic material. When the goal is to realise the superelastic behaviour, the deciding stress value is the critical stress for the Stress-Induced Martensitic Transformation (SIMT), denoted as σ_{SIM} [26]. As can be seen in Figure 2.13, this stress value follows an increasing trend as temperatures rise (green line), and is competing against the critical stress for plastic deformation or yield, σ_y, given by the red line, which shows a tendency to decrease as temperatures get higher. For the temperature range where superelasticity is possible ($A_f < T < M_d$, as shown in Figure 2.13), if σ_{SIM} is lower that σ_y, then the functional property will emerge, as the applied stress state will lie inside the superelastic window. As soon as the two lines of stress intersect and the red one lies beneath the green, the superelasticity disappears and the alloy will yield and plastically deform under the applied stresses [26].

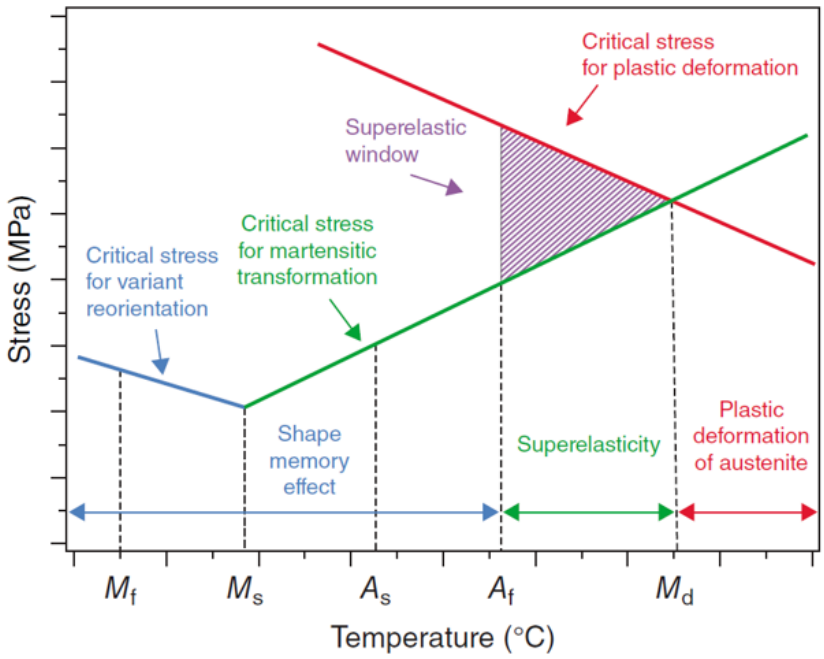


Figure 2.13: Stress [MPa] versus temperature [°C] graph for NiTi-based SMAs. The five key temperatures for the functional behaviour of SMAs are marked on the x-axis, signifying the limits of occurrence of the SME, the SE and the plastic deformation of the material. The blue line represents the Critical Stress for Martensitic Variant Reorientation, which shows a declining trend with increasing temperature. The Critical Stress for Martensitic Transformation, σ_{SIM}, is given by the green line, exhibiting an increasing trend as temperature is raised. Finally, the red line represents the Critical Stress for Plastic Deformation, or σ_y, which follows a decreasing pattern with temperature as the Critical Stress for Martensite Reorientation. The shaded area named *"Superelastic Window"* indicates the possible stress and temperature state where the superelastic functionality can be realised. Reproduced from [27].

Crystallographic considerations and texture come into play when taking into account that anisotropy is inherent in the crystal lattice of the NiTi alloy. Therefore, at least theoretically, there should exist crystallographic orientations which would promote the stress situation to remain within the superelastic window. These orientations, desirable for promoting superelastic responses in NiTi SMAs, shall produce, when compared to the rest of the crystal orientations, lower values of the critical stress for SIMT, σ_{SIM}, large recoverable strains, as well as low hardening rates during the phase transformation, which can be thought of as the slope of the green stress line on the stress versus temperature, $\sigma - T$, plot [26]. In other words, desirable crystallographic orientations would not permit plastic slip and would max-

imise the lattice correspondence between the austenite and the martensite, so that the alloy, under a given stress state would prefer to accommodate the stress by transforming, and, thus, showcasing superelastic and shape memory behaviour, rather than continuing its deformation within the plastic regime.

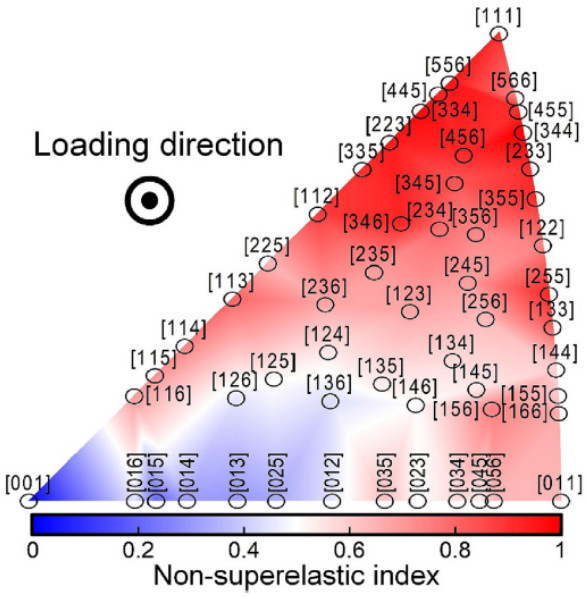


Figure 2.14: Inverse pole figure mapping the superelastic capability of NiTi SMA to a number of crystallographic orientations. The so-called *Non-Superelastic Index* is given at the bottom of the figure providing guidance for the interpretation. Smaller index values and colours closer to blue indicate better material capability for the superelastic response. Reproduced from [26].

Figure 2.14 presents in the form of an inverse pole figure multiple crystallographic orientations of NiTi SMAs ranked with respect to their superelastic capability. The reference bar placed at the bottom of the pole figure gives what was named by the authors of the particular study as the *"Non-Superelastic Index"*. This index resulted from an equal summation-based normalisation process of the σ_{SIM}, the hardening rate and the irrecoverable strain values calculated for each orientation using molecular dynamics simulations [26]. Orientations whose score lies closer to zero are viewed as desirable in terms of their capability of showcasing superelasticity. As can be seen from Figure 2.14, crystal orientations close to $\langle 001 \rangle$ score the lowest on the *"Non-Superelastic Index"* of the study, lending themselves to further investigation with respect to their ability to realise the desired functional properties.

Indeed, experimental investigations have proven the idea that the superelastic functionality is closely related to specific crystallographic orientations within NiTi single crystals [25], in the sense that the alloy's performance can be optimised if desired orientations have been selected for its fabrication. Zhu et al. managed to expand this conclusion to polycrystalline samples, showing that samples which contained columnar grains that grew adopting the $\langle 001 \rangle$ orientation along their building direction exhibited improved superelastic behaviour [26].

The reasons behind this particular orientation's ability to boost the superelastic response of NiTi alloys are described in the following lines. Initially, it shall be noted that as can be deduced from the schematic representations of the B2 phase crystal given in Figure 2.1 a), the occurrence of slip is strongly dependent on the crystal orientation [25]. Another important point for the discussion is the prevailing slip system in the austenite phase of NiTi SMAs; this being the $\langle 001 \rangle \{110\}$ slip system [25] [26] . Calculations of the Schmid factor of various crystallographic orientations of interest has shown that the $\langle 001 \rangle$ orientation possesses the lowest amongst them, which equals zero [25]. The significance of this is great as it effectively means that, theoretically, there is no chance of plastic slip and no yielding taking place along this direction. For a visualisation of the Schmid factor and the associated points concerning crystal slip see Figure 2.15. The practical consequence of these points is that deformations along this direction is possible to be recovered and, since the Schmid factor in the [001] single crystal is the lowest of all others, these recoverable strains are the highest of all [25]. Moreover, the Resolved Shear Stress

Factor of $\langle 001 \rangle$ grains is high, which, when taken into account in molecular dynamics studies, resulted in showing that the stress-induced martensitic transformation in this type of crystals is prompted at relatively low values of stress, another aspect which favours superelastic behaviour [26]. In short, the existence of a prevailing slip system which inhibits dislocation motion in the austenitic phase has allowed the alloy to exhibit recoverable strains which reach the theoretically estimated values of 4.2% in single crystal specimens [25].

Taking a look into the matter from the point of view of the reverse phase transformation which is crucial to occur if superelasticity is to be manifested, a few more words can be added to the above points. Firstly, in the $\langle 001 \rangle$-oriented NiTi grains, the transformation from the Stress-Induced Martensite back to the austenitic parent phase is promoted during the unloading of the material under a constant temperature [26]. This means that the resistance of the alloy to the transformation that allows it to return to its original form is low, hence increasing the compatibility between the austenitic parent phase and the martensite that has resulted from the stress application. The imposed elastic and interfacial energy resistance is decreased in the crystals that have assumed the $\langle 001 \rangle$ orientation [26], allowing the transformation to proceed more easily than in the other crystal orientations, and thus gifting the material with the best possible superelastic response.

Finally, a special note about the $\langle 001 \rangle$ crystallographic orientation in NiTi is that the yield stress continues to increase as the temperature of the material increases, and so, as the temperature rises, the slip deformation of the material is further restricted, a point that can be verified by Figure 2.13 as well [25]. Furthermore, beyond the point of 86°C, the flow stress of the alloy continuously increases with temperature, which is yet another aspect that sets this orientation apart from all the rest [25].

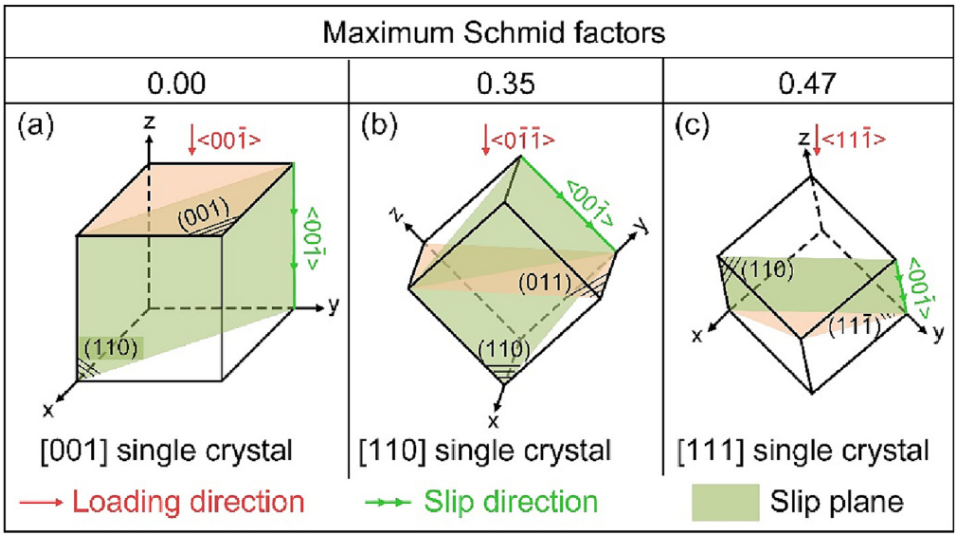


Figure 2.15: Plastic slip initiation in the $\langle 001 \rangle \{110\}$ slip system of a B2 crystal. The cubes representing the unit crystal are oriented along ***a)*** the [0 0 1] direction, ***b)*** the [1 1 0] direction and ***c)*** the [1 1 1] direction. The slip planes are coloured green, the slip directions are marked by way of a green line and the loading directions are coloured red. The Schmid factor for each case is given above each schematic. Reproduced from [26].

2.1.3 Applications

Since the early days of its development it became apparent that NiTi possesses a great potential for use in a diverse range of applications. Indeed, since the 1970s the alloy has found its way in numerous applications, from the aerospace and the automotive industries to medical applications and consumer goods. Although one might intuitively presume that NiTi may only be implemented in several applications for its sensing and actuation capabilities, it is actually true that many other functions can be benefited by the unique behaviour of this alloy.

Noteworthy applications of NiTi-based SMAs by industry are given below:

- ***Aerospace:*** "shrink-to-fit" pipe couplings for the F-14 fighter jets in the 1970 [1], wire tendons for hinge-less aileron actuation [1], variable geometry airfoils [1], variable geometry chevrons for

aircraft engine noise reduction [1], applications for turbulent aerodynamic drag reduction [1], rotor engine blade twisting actuators [1], shape wing morphing technologies [28], actuation and release systems at zero gravity conditions [10], vibrational damping for spacecraft launching operations [1] and solar panel actuators [1].

- ***Medical:*** pulmonary embolism filters [2], atrial septal occlusion devices [1], self-expanding cardiovascular stents [1], orthodontic bridge wires [2], palatal arches [2], drills for root canal surgery [1], cast substitutes [1], artificial bone implants [1], spinal vertebrae spacers [1], skeletal scoliosis correction devices [29] and tools for Minimally Invasive Surgery [1].
- ***Transport & Automotive:*** sensing, actuation, impact damping and absorption in vehicle engine room applications, drivetrain assemblies, suspension and steering systems, body, car exterior and passenger cabin applications [1] [10].
- ***Civil Engineering & Infrastructure:*** vibration control systems as dampeners and seismic protection applications [1] [30].
- ***Marine & Oil:*** high pressure and corrosion resistant seals [2], release devices for protection systems in downhole drilling equipment [1] and solid-state heat engines [2].
- ***Consumer goods:*** safety mechanisms for household appliances [1], eyeglass frames [2] and sports equipment [1] [2].

2.2 Laser-Powder Bed Fusion Additive Manufacturing

In this type of systems, the metal, in a powder form, is spread across the work area creating a powder bed. The power source, in the form of a scanning lased beam delivers its energy to the powder bed where it melts or sinters the metallic powder particles into one layer of the desired shape. As soon as one layer is deposited, the bed is lowered by a distance equal to the predetermined layer thickness [31] and the powder is raked across the bed to ensure than a new, fresh layer is evenly spread before the energy source scans the powder again to fabricate another layer [32]. By repeating the process multiple times a 3D object is created. The loose powder surrounding the part during construction acts as support for the subsequent layers, abolishing the need for extensive secondary supports which perplex the design and the process. A schematic illustration of such a system and the fabrication process can be seen in Figure 2.16.

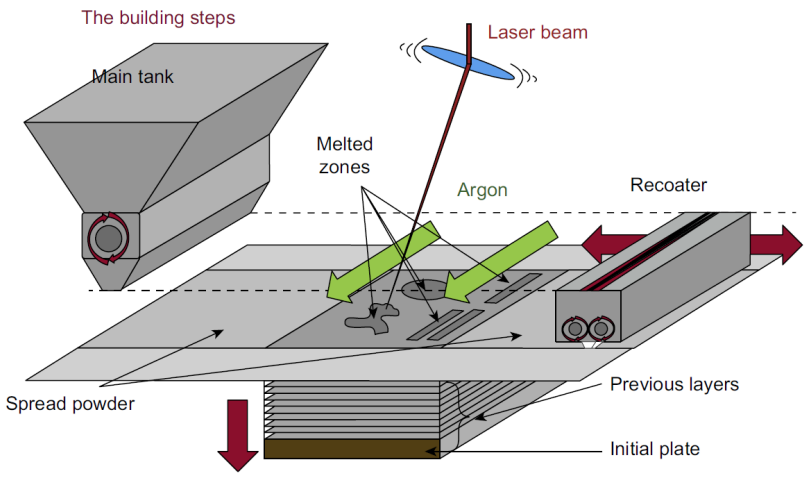


Figure 2.16: Schematic representation of the *Laser-Powder Bed System* process. Reproduced from [31].

The process described above takes place in a closed chamber, which is either under vacuum conditions or filled with an inert gas (usually Nitrogen or Argon) [33] [34]. This is to ensure that the metallic powder is safe from oxidative degradation. Another key point is that the powder is maintained at an elevated temperature, either by means of resistive heaters attached to the powder bed or infrared heaters above the build platform. Preheating of the powder prior to the laser scanning and maintaining it at an elevated

temperature throughout manufacturing achieves to minimise the energy consumption of the laser beam, as less thermal energy is required in order for the powder to reach its melting point, as well as prevents warping of the printed part during building, a result of non-uniform thermal expansion and contraction [33]. Finally, it is also of importance to allow the newly printed parts to cool down before removing them from the printing chamber and exposing them to ambient conditions. Premature exposure of L-PBF-produced parts can result in powder degrading due to the atmospheric Oxygen and to the part warping due to uneven thermal contraction and expansion rates [33].

Lasers are chosen as the heat source as they provide a high-intensity, highly collimated energy beam which allows for quick and precise motion in a controlled manner achieved with the aid of directional mirrors [33]. The type of processing that the laser beam provides for L-PBF systems revolves around heating [33], meaning that the power source provides sufficient thermal energy to melt the metallic powder. The goal is for the metallic powder to be melted in a controlled manner, avoiding the development of excessive heat across the powder bulk [33], so that when the laser has scanned a specific point of the powder bed and the energy it provides is removed, the molten metal will be able to rapidly solidify. In the majority of systems either solid-state or fibre lasers are being fitted, as they provide high efficiency, improved lifetime and greater reliability [33].

Any metal which is deemed suitable for welding is thought to also be suitable for manufacturing by L-PBF methods, in contrast to alloys which are prone to cracking under high solidification rates [33]. Up to this day, various stainless and tool steels, Ti and its alloys, Ni-based alloys, CoCr alloys, as well as precious metals have been employed for manufacturing by L-PBF [33].

Since the early days of *Powder Bed Fusion* methods several machines have been developed which utilise one of the four Powder Fusion mechanisms; solid-state sintering, chemically-induced binding, liquid phase sintering and full melting. The most common method employed for L-PBF of metallic alloys is the fourth mechanism. This requires that the entire region of the powder material affected by the heat of the energy source is melted to a depth exceeding that of the layer thickness, and, in addition to that, the energy of the subsequent scans is enough for remelting a previously solidified portion of the newly formed solid structure [33]. The result of this powder fusion mechanism is well-bonded, high density parts produced from engineering metals which possess a set of unique properties, oftentimes more desirable than those obtained by traditional manufacturing [33].

Amongst the greatest advantages of this type of systems is their ability to produce parts with high dimensional stability, to incorporate internal passages in the bulk of the structures, a feature characteristic for all AM processes, as well as the ability to build features with very high resolution [32]. Additionally, in many cases the end-product material properties are comparable to many engineering-grade polymers, metals and ceramics manufactured by conventional methods [33].

2.2.1 Process Parameters

In principle, most metallic materials can be processed by the L-PBF method, however, the difficulty associated with their processing actually varies significantly from one metal to the other [31]. Aspects such as chemical composition, laser absorption, surface tension, thermal conductivity and melt viscosity determine the so-called process windows of every material to be fabricated by L-PBF [31]. The common way of dealing with the complexities of the nature of every metal and these of the processing method is through the implementation of *process parameters*.

For the case of L-PBF fabrication, these parameters can be divided into four main categories, as can be seen in the diagram of Figure 2.17. These four main categories distinguish parameters into those related to the laser power source, the scanning procedure, the powder material and the temperature. As one can easily observe from the full diagram of Figure 2.17, the list contains a rather large number of parameters, making it hard to exercise exact control over all of them during manufacturing. For this reason, the most prominent parameters include the laser power, P, the layer thickness, t, the laser scanning speed, v, the hatch distance, h, the laser spot size, d, and the laser beam scanning strategy. The first four of these can be visualised with the aid of Figure 2.18, where an illustration of a section of a material fabricated by L-PBF is shown with the process parameters marked upon it. The scanning strategy will be analysed in depth in Section 2.2.2.

The manufacturing process can be characterised in a more accessible manner by means of a few key

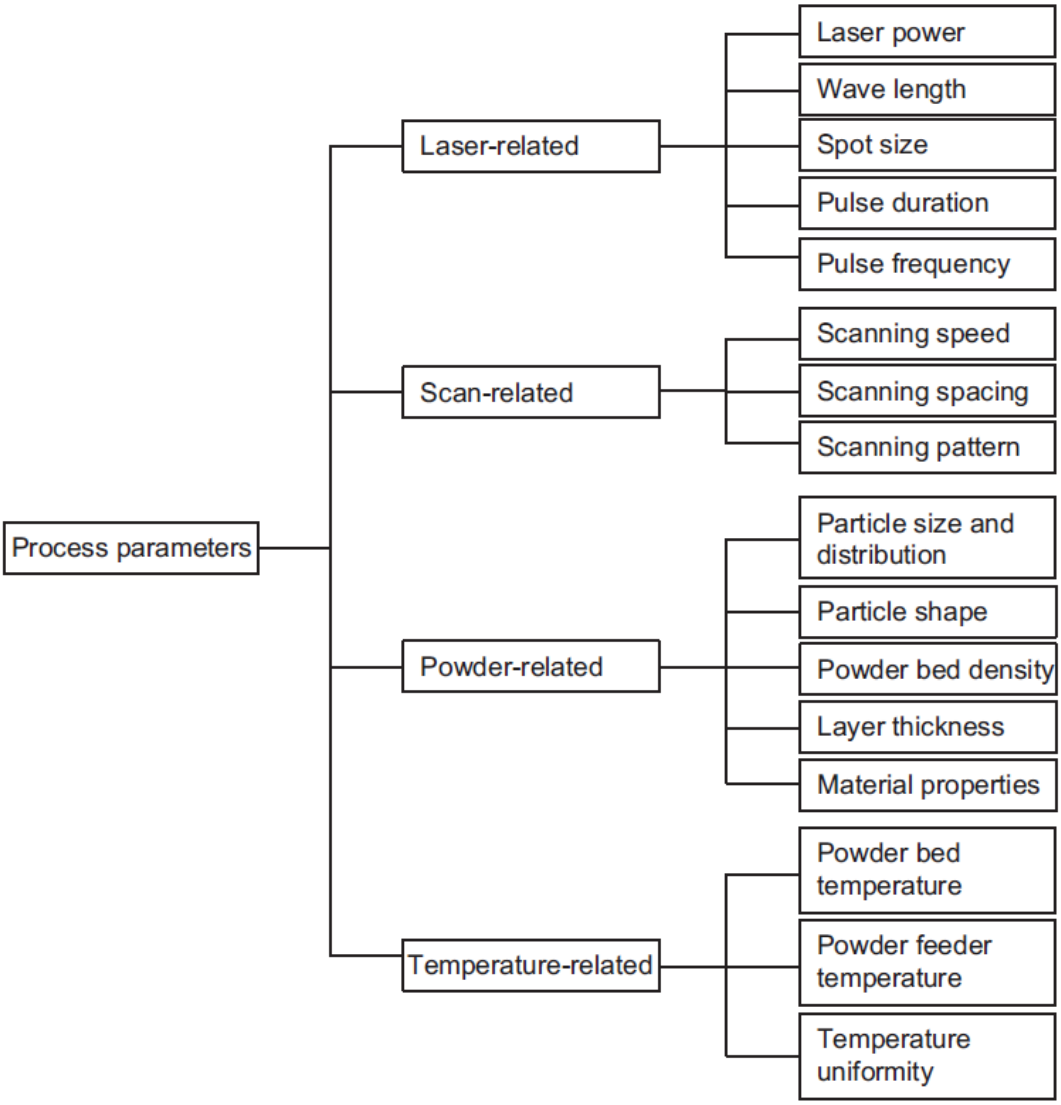


Figure 2.17: Process parameters involved in the L-PBF process. Reproduced from [31].

variables which can be derived by combining various of the process parameters detailed above.

- ***Volumetric Energy Density, (VED)***, $[J/mm^3]$ [31]

$$E_V = \frac{P}{v \cdot h \cdot t} \tag{2.1}$$

- ***Linear Energy Density, (LED),*** $[J/mm]$ - the power input per unit speed of the laser beam [31].

$$E_L = \frac{P}{v} \tag{2.2}$$

- ***Linear Input Energy***, $[J/mm^3]$ [31]

$$E_I = \frac{4P}{\pi \cdot v \cdot d^2} \tag{2.3}$$

- ***Surface Energy Density,*** $[J/mm^2]$ - the energy density applied to the surface of the powder bed [31].

$$E_S = \frac{P}{v \cdot d} \tag{2.4}$$

- ***Optimal hatch spacing*** [31]

$$h = 0.7 \times \text{laser beam diameter} \tag{2.5}$$

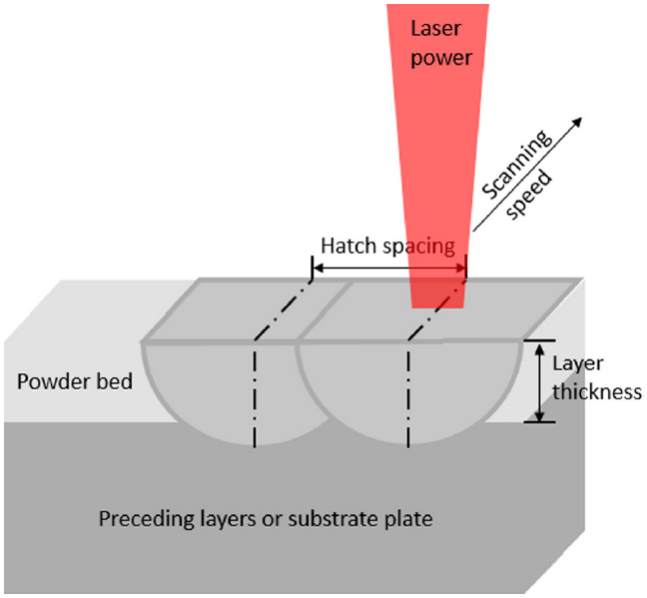


Figure 2.18: Schematic illustration of layer thickness, laser power, scanning speed and hatch distance process parameters. Reproduced from [34].

A careful look at the nature of the process parameters given above makes obvious the fact that the majority of them are strongly interdependent and interrelated [33]. For instance, the laser power required for fabrication is increased as the melting point of the powder processed increases, whereas it decreases as the temperature of the powder bed increases [33]. At the same time, laser power varies with the ability of the powder to absorb it, a property influenced by the material that constitutes said powder, the shape of the powder particles, their size and the powder's packing density [33].

Additionally, aspects related to the finished products are also heavily dependent on the process parameters, as well as various combinations of them. For example, residual stresses, which tend to accumulate in the L-PBF-fabricated parts due to the thermal nature of the process, are influenced by a combination of melt pool characteristics, scanning strategy and the scan pattern followed during fabrication [33]. Fine-tuning of the powder bed temperature, the scanning speed, the laser power and the scanning spacing (or hatch distance) has been found to achieve optimal melt pool size which leads to good dimensional accuracy, surface finish and build rates, as well as good mechanical properties of the final part [33].

Various combinations of laser power and powder bed temperature have been proven to affect the quality of the L-PBF-processed parts differently. High laser power and high bed temperatures usually lead to the production of very dense parts, a feature desired in L-PBF manufacturing, combined, however, with poor recyclability and difficulties in cleaning the part of the remaining powder after fabrication [33].

On the other hand, low laser power and low powder bed temperatures provide better dimensional accuracy but with detrimental effects in the density and greater tendencies for delamination [33]. Another combination of the two parameters, i.e. high laser power with low bed temperatures, leads to non-uniform shrinkage of the finished parts and also enhances the accumulation of residual stresses, a combination of which leads to part curling [33].

Another point of interest is the synergy between parameters such as laser power, scanning speed and layer thickness. These three parameters essentially determine the energy input to the process. Insufficient energy input, or, in other words, low laser power combined with high scanning speeds and large layer thickness leads to a phenomenon termed as *balling* [34]. It consists of the molten metal forming spheroidal beads due to insufficient wetting of the preceding layer combined with the existing surface tension forces [34]. Macroscopically, on the finished part, these beads give the appearance of a rough surface [34]. On the contrary to this, a combination of high laser power and low scanning speeds leads to excessive evaporation of the powder material and to the so-called *keyhole effect*. This effect is manifested as keyhole-shaped pores inside the metal resulting from the collapse of unstable melt pools which entrap gas bubbles from the vapour depression [35]. Finally, insufficient hatch distance during L-PBF results in adjacent melt lines being unable to completely fuse together, leading to increased porosity inside the bulk of the fabricated parts [34].

2.2.2 Effect of the scanning strategy on parts produced by Laser-Powder Bed Fusion

As briefly mentioned in Section 2.2.1, the scanning strategy is one of the process parameters affecting the fabrication of metallic parts via L-PBF. The scanning strategy is defined as the spatial geometric pattern followed by the laser beam during the deposition process [36]. For the scanning of a single layer of powder by the laser beam, the scanning strategy can be fully defined by using a variety of parameters including the scanning direction, the scanning sequence, the scanning vector rotation, the scanning vector length, the scanning time and, finally, the hatch spacing [36]. Figure 2.19 presents in a graphical format a variety of scanning strategies, employed in PBF fabrication processes, which is, by no means, exhaustive. Additionally, a variety of various other interlayer rotation angles of the scanning vector have been employed, most notably 30°, ±45°, 67°. In practice, scanning strategies oftentimes are combinations of the basic strategies shown in Figure 2.19; for example a hybrid strategy of bi-directional scan in island patterns and 90° interlayer rotation combined with point scanning of each layer at random locations for avoiding overheating during fabrication [37].

The major difference between each possible scanning strategy concerns the thermal profile and history of each point of the powder, or, equivalently, each individual laser bead and melt pool that it creates. This thermal profile is manifested by quantities such as the thermal gradient, G, the direction of the heat flux and the associated cooling rate. All these quantities play an important role in the solidification of the crystals, described by the growth rate, R, relating to both their size and morphology, see Figure 2.20. It is clear that the scanning strategy, due to the fact that it is described by all the individual parameters mentioned in the paragraph immediately above, has an enormous effect on the thermal profile of the molten metal. Hence, selecting an optimal scanning strategy, which is essentially the result of a combination of the various aspects comprising the scanning strategy (e.g. vector direction, rotation, length, scanning time, sequence and hatch spacing), can place the solidification profile within the different areas marked on the plot of Figure 2.20 [38].

A basic description of the solidification process which takes place during L-PBF is as follows. In general, crystals grow during solidification in a direction parallel to the maximum thermal gradient that exists in a certain volume of material and always in a direction perpendicular to the solid-liquid interface that has formed, usually referred to as the melt pool [26]. Hence, it becomes apparent that the scanning strategy creates this solid-liquid interface in the first place, affecting its geometry by means of the hatch spacing and through that, affecting the crystal growth in terms of size, morphology and orientation via the way it directs the thermal gradient in space by means of the scanning vector and, finally, how this gradient dissipates its energy to the environment [39]. Changes in the manner in which each layer is scanned are, therefore, bound to result in changes the melt pool that arises. Of particular significance is the angle of rotation between two successive layers (also called the *interlayer rotation angle*), which inevitably leads to changes in the new melt pool that arises by the superposition and merging of two

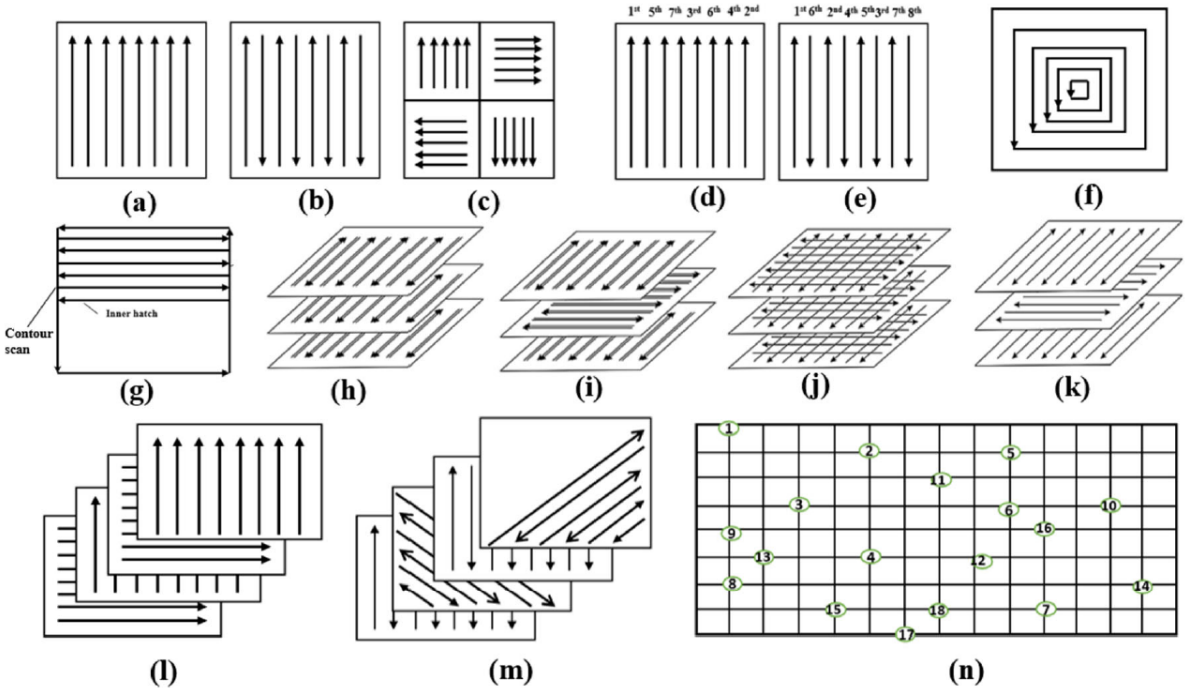


Figure 2.19: Schematic representation of different scanning strategies. ***a)*** Unidirectional scan, ***b)*** bi-directional scan (or zigzag), ***c)*** island scan, ***d)*** unidirectional scan with varied scanning sequences, ***e)*** bi-directional scan with varied scanning sequences, ***f)*** helix scan with square cross-section, ***g)*** contour scan, ***h)*** laser double-pass bi-directional scan, ***i)*** laser double-pass bi-directional scan with 90° interlayer rotation of the scan vector, ***j)*** cross scan, ***k)*** bi-directional scan with 90° interlayer rotation of the scanning vector, ***l)*** unidirectional scan with 90° interlayer rotation of the scanning vector, ***m)*** bi-directional scan with 45° interlayer rotation of the scanning vector, and, ***n)*** point melting scan. Reproduced from [36].

successive melt pools, see Figure 2.21 c).

The scanning strategy also affects the thermal history of the metal being processed by L-PBF methods due to the fact that each passing of the laser causes re-melting of previously deposited layers. Re-melting is a crucial aspect of L-PBF fabrication as it eliminates the nucleation barrier for solidification and creates a planar solidification front, thus causing the (partially) remelted grains (also referred to as the *parent grains*), as well as the ones arising in the newly deposited material to solidify epitaxially and grow across multiple layers [40]. Additionally, it has been reported to mitigate surface roughness, macroscopic fabrication-related defects and to achieve high density parts [36].

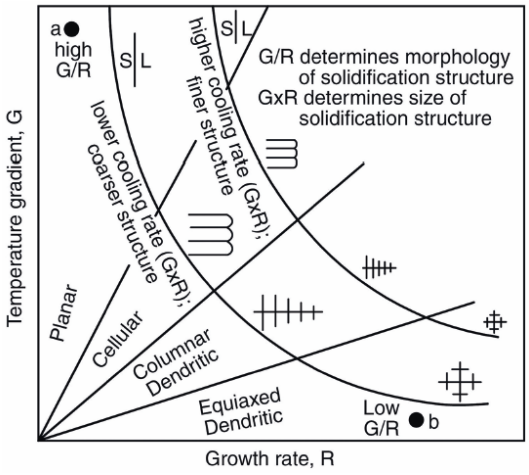


Figure 2.20: ***a)*** Growth rate, R, versus temperature gradient, G, plot depicting their effect on the size and morphology of the crystals during solidification processes. Reproduced from [4].

Moreover, it is known that crystalline materials have a specific *"easy-growth direction"*, which is related to the crystal orientation they naturally adopt during their solidification process [41]. Solidification during L-PBF fabrication is no exception, as grains growing out of a newly deposited layer will adopt the crystallographic orientation of the parent grain since due to the epitaxial solidification process they essentially grow "out" of it. The consequence of this is that, in general, grains solidifying during the L-PBF fabrication process have a natural tendency to exhibit specific spatial orientations, which potentially, under the right scanning conditions could be enhanced.

Probably the most powerful of those scanning conditions is the angle of rotation between two successively deposited layers. The effect of the absence of such interlayer rotation to the microstructure created can be visualised with the help of the study conducted by L. Xue et al. on Ni-rich NiTi SMA [42]. The material, as a cubic metal, has its $\langle 001 \rangle$ orientation as its easy-growth direction. When fabricated using a bi-directional scanning strategy with 0° interlayer rotation, such as the one in Figure 2.19 k), both $\langle 011 \rangle$ and $\langle 001 \rangle$ orientations along the BD of the sample are possible. The hatch distance, which can influence the overlap between adjacent melt pools, and the shape of the melt pool, controlled by the energy density and the scanning speed, would be the deciding factors for which orientation would eventually arise, see Figure 2.21 b), whereby the orientation of each cube, representing the orientation adopted by the crystals is a result of the Linear Energy Density [42]. Yet another aspect of the absence of rotation between consecutive layers is that it leads to more anisotropic temperature gradients which do not promote fusion of the particles scanned during different laser passes [36].

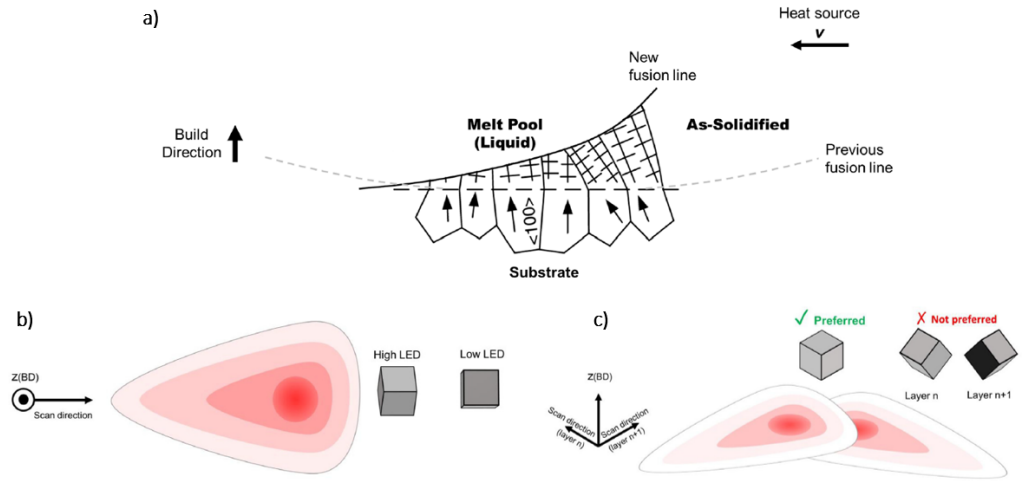


Figure 2.21: ***a)*** Schematic representation of the mechanism of competitive epitaxial grain growth in one melt pool during solidification process of L-PBF as the laser source moves away from the scanned area. The arrows in the crystals solidified indicate the easy-growth direction. Reproduced from [41]. ***b) and c)*** Schematic representation of the effect of the interlayer rotation of the scanning strategy. In b), there is no rotation between successive layers (0° interlayer scanning), the melt pools are superimposed on one another and the grains can attain any of the two orientations shown by the cubes on the side (namely, the $\langle 011 \rangle$ and the $\langle 001 \rangle$). In c), there is a 90° rotation between layers, and although the same orientations are possible, only the $\langle 001 \rangle$ is preferred and expressed as it minimises the misalignment with the previously deposited layer. Reproduced from [42].

Incorporation of a 90° interlayer rotation in the scanning strategy, creates a situation whereby the $\langle 001 \rangle$ orientation is preferred in comparison to the other, as it is promoted through the condition of the epitaxial solidification. That is because it offers the least misalignment with respect to the previously sintered layers [42]. The situation that arises can be viewed as a competition between the crystals of the two orientations, whereby the orientation whose direction deviates significantly from the direction of the solidification as this is dictated by the maximum thermal gradient, is "crowded out" by the grains that are more conveniently oriented [41]. This phenomenon is called *competitive epitaxial grain growth* and is essentially responsible for the creation of anisotropy in the orientation of the grains in the metals which are manufactured by means of L-PBF [40]. Figure 2.21 a) shows a schematic representation of it. Rotation of the scan vector by different angles leads to various degrees of misalignment between the easy-growth direction of the crystals and the direction for the solidification, leading to the effect of the *competitive epitaxial grain growth* to become more or less pronounced and hence resulting in the emergence of crystallographic textures of various intensities and types in the metal being processed

[40] [42] [41] [36]. It has been hypothesised that this mechanism can allow for the manipulation of the crystallographic texture for various alloys, including NiTi SMAs fabricated by AM methods, such as L-PBF [42]. Additionally, the presence of the rotation enhances the fusion between the scanning tracks, due to the melt pools alternating in direction between the layers, see Figure 2.21 c) [36].

The following example aims at thoroughly presenting the aforementioned topics. The claims of the possibility of controlling the crystallographic texture through the AM scanning strategy were verified in the case of the L-PBF fabrication of Ni-25 at.% Mo alloy [43]. The authors of the publication concluded that varying the scanning strategy can effectively control the texture obtained in the particular alloy, and furthered their remarks by stating that such a conclusion can be safely reached for other alloys of the cubic crystal nature.

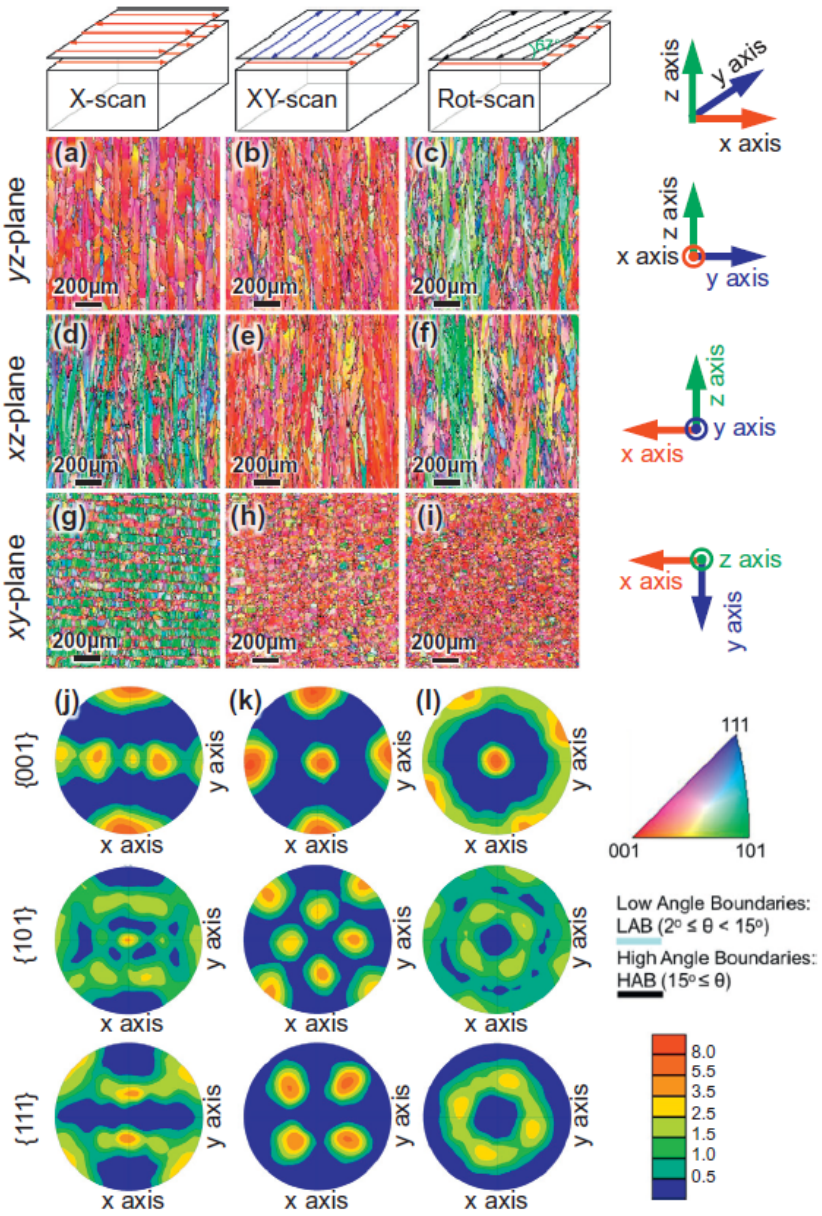


Figure 2.22: ***a) - i)*** Crystal orientation maps depicting the crystallographic texture resulted from different scanning strategies. Three different planes are shown for each scanning pattern followed. The corresponding scanning strategy is schematically shown at the top of the image and, for each strategy, the associated images are shown along a vertical line below the sketch (X-scan: *a), d), g) & j)*, XY-scan: *b), e), h) & k)*, Rot-scan: *c), f), i) & l)*). ***j) - l)*** At the bottom half of the image, the inverse pole figures for three families of planes are shown, illustrating the concentration intensity of the orientations observed directly above. Reproduced from [43].

In this study, three different laser scanning strategies were examined, see top of Figure 2.22, which were then evaluated in terms of the crystallographic textures in which they resulted. The differences in texture in all three planes of the manufactured samples can be readily seen in Figure 2.22. More specifically, both the X-scan (0° rotation) and the XY-scan (90° rotation) resulted in a "single-crystalline-like texture" with a short range ordering of the Mo atoms in the alloy. In the XY-scan strategy, the $\langle 001 \rangle$ alignment observed was found to be along all three directions of the samples, whereas, in the X-scan the same alignment was observed along the x-direction and it shifted to a $\langle 101 \rangle$ in the other two directions. As the researchers stated, the two textures are similar; the X-scan simply rotates it by 45° about the x-axis [43]. The Rot-scan (67° rotation) on the other hand, exhibits a strong alignment of the grains in the $\langle 001 \rangle$ direction only along the building direction. This, combined with the inverse pole figures included in Figure 2.22, gives evidence for the development of a $\langle 001 \rangle$ fibre texture, as in the $\{001\}$ pole figure the $\langle 001 \rangle$ intensity shows a ring-shaped distribution regarding the z-axis in addition to the strong intensity along the same axis [43].

The different scanning strategies resulted in different shapes of the melt pools identified in the samples, as can one see in Figure 2.23 (a, c and e) and Figure 2.24 (a, c and e). These figures show two different faces of the cubic samples manufactured in the study, both of which lie parallel to the building direction. For instance, the X-scan resulted in periodically arranged melt pools with the shape of half an ellipse in the yz-plane and parallel flat bands in the xz-plane; the Rot-scan gave flatter and more irregularly placed melt pools in both the yz-plane and the xz-plane, whereas in the XY-scan, melt pools arose in two shapes, same in both viewing planes as well; half ellipses and band-like structures which are the result of the scan along the y-direction [43].

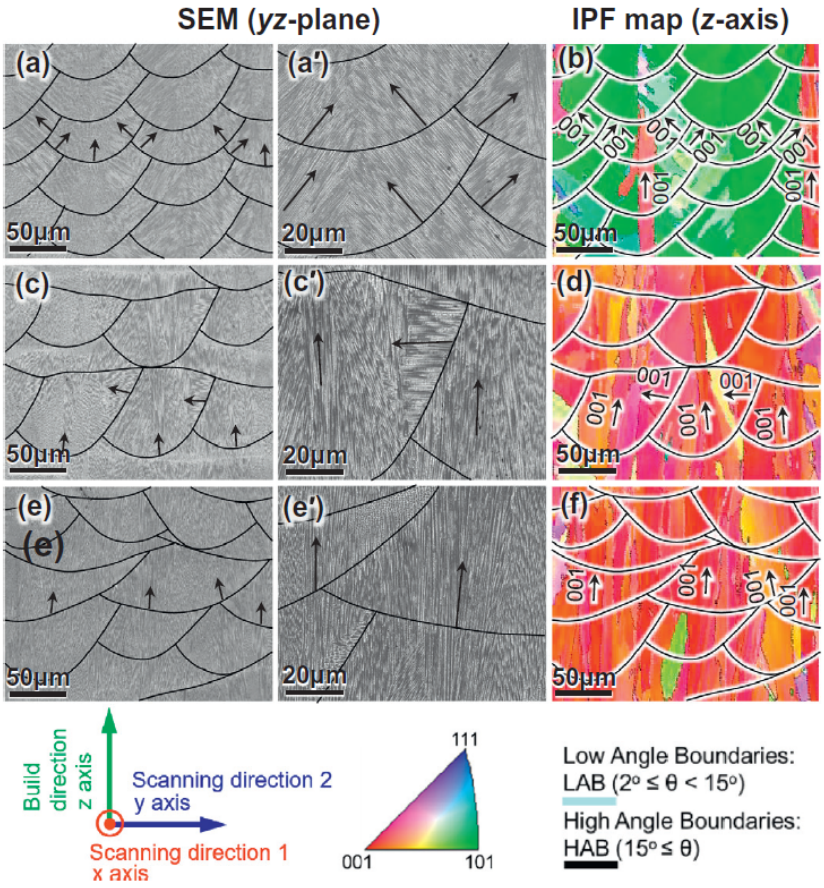


Figure 2.23: ***a), c) & e)*** SEM images with overlaid melt pool boundaries for the different scanning strategies. ***a'), c') & e')*** are higher magnification images of the SEM images shown in (a, c & e). ***b), d) & f)*** inverse pole figure maps of the corresponding areas analysed by SEM-EBSD. ***a), a') & b)*** correspond to the X-scan strategy, ***c), c') & d)*** are the samples fabricated using the XY-scanning and ***e), e') & f)*** show the Rot-scan samples. Black arrows noted in the SEM images denote the direction into which the columnar grains observed in the samples tend to grow. The samples are viewed along the building direction, on the yz-plane. Reproduced from [43].

But the differences are not limited in the shape of the melt pools, rather, they extend to the directions into which the crystals grow. In the XY-scan and the Rot-scan strategies, the majority of the columnar cells which form tend to grow parallel to the building direction, merging with grains that form in layers deposited above them, hence elongating and developing beyond the boundaries of a single melt pool. The orientation of the crystals comprising said grains is found to be the $\langle 001 \rangle$ (refer also to Figure 2.22), thus leading to the development of a strong $\langle 001 \rangle$ texture along this sample direction [43]. Additionally, the XY-scan results in a number of grains growing towards the horizontal direction, or, as noted in Figure 2.23, the y-axis. These grains are located in the areas where melt pool tracks overlap, and this is believed to be the reason causing these grains to grow towards this direction [43]. As far as the X-scan is considered, the situation appears to be slightly more complex. Indeed, grains located at the centre of the melt pools grow along the building direction of the part, whereas the rest of the grains that form within the melt pool grow at directions inclined 45° to the building direction, as can be seen in the corresponding micrographs in Figure 2.23 a) and a'). Combining these SEM images with the corresponding information of Figure 2.22, it can be seen that the grains extend to directions parallel to the $\langle 001 \rangle$, which results in the central columnar grains giving a weak $\langle 001 \rangle$ texture parallel to the building direction and the inclined crystals giving a strong $\langle 101 \rangle$ texture along the building direction [43].

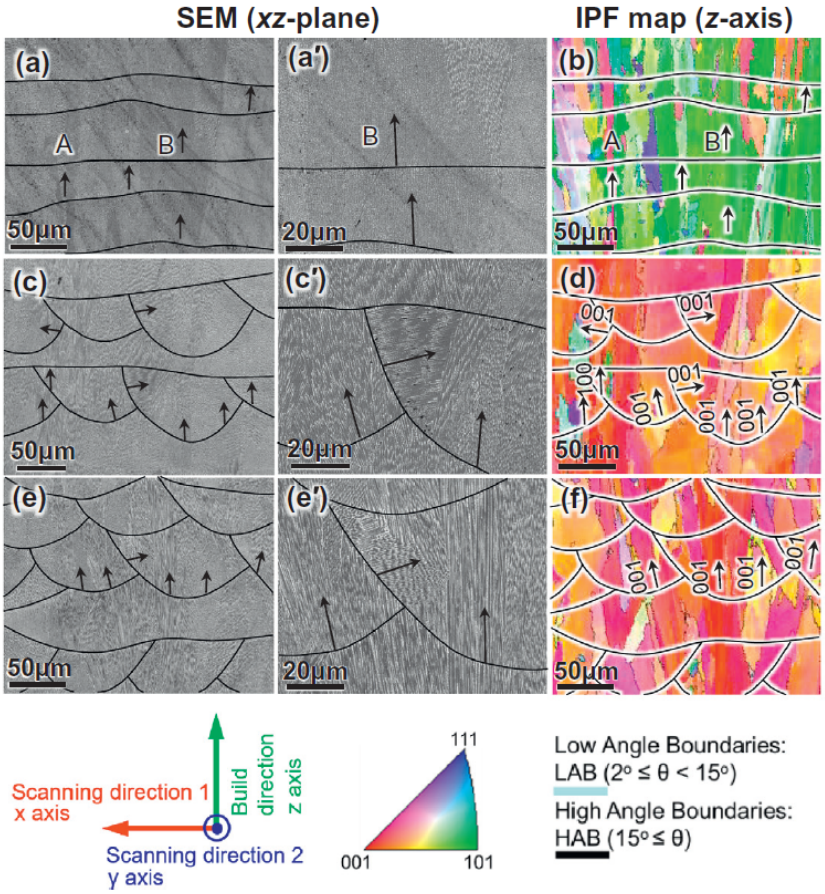


Figure 2.24: ***a), c) & e)*** SEM images with overlaid melt pool boundaries for the different scanning strategies. ***a'), c') & e')*** are higher magnification images of the SEM images shown in (a), c) & e)). ***b), d) & f)*** are inverse pole figure maps of the corresponding areas analysed by SEM-EBSD. ***a), a') & b)*** correspond to the X-scan strategy, ***c), c') & d)*** are the samples fabricated using the XY-scanning and ***e), e') & f)*** show the Rot-scan samples. Black arrows noted in the SEM images denote the direction into which the columnar grains observed in the samples tend to grow. The samples are viewed along the building direction, on the xz-plane. Reproduced from [43].

Evidently, one of the most important conclusions of the study is that implementation of the scanning strategy is a powerful means by which strong textures can be developed in both FCC and BCC alloys, as they manage to successfully manipulate the melt pools and dictate the crystal growth directions and alignments.

Finally, the topic of residual stresses must be included in the discussion of the scanning strategy. Fabrication of metallic parts by means of selective laser melting processes, such as L-PBF, are known to introduce very large residual stresses to the final objects [44]. According to P. Mercelis and J-P. Kruth, the most crucial parameters which influence and determine the magnitude and shape of the profile of the residual stresses are the material properties, the height of the printed part and that of the substrate, the scanning strategy and the heating conditions [44]. Residual stresses, as the form of stress that remains inside a material after it has reached an equilibrium state with its environment, usually after the completion of its manufacturing, can be due to thermal processing conditions, different phases coexisting inside a material as well as due to dislocations affecting the metal at the atomic scale [44]. The first type are usually treated in literature with relation to L-PBF.

This type of residual stresses are caused by the large thermal gradients imposed by the laser beam and tend to vary over large distances, typically equal to the part dimensions [44]. Two mechanisms have been identified for creating residual stresses during L-PBF. The first one, called Temperature Gradient Mechanism (TGM), unfolds during the motion of the laser, which causes regions to almost instantaneously heat to the point of melting and then cool down, giving rise to very steep temperature gradients. The heated layer expands, however, it is simultaneously restricted by the previously deposited material, which is in a solid phase at lower temperature. As a result, this solid volume of material is elastically compressed, and in the case of very large expansions it is possible that the yield strength of the metal is exceeded, creating a plastically compressed top layer. Upon completion of the printing, the compression remains within the part, leading to the shrinking and warping of the upper layers, resulting in compromising the final part quality [44] [45]. The second mechanism concerns the cooling down of the molten top layers during L-PBF, which forces them to shrink due to the thermal contraction they experience. This contraction is now constrained by the solid layers below, creating tensile stresses at the top of the part and compressive stresses below [44].

The discussion which preceded showed that the scanning strategy has a tremendous effect on the thermal profile and history of the metals during L-PBF. Therefore, it is obvious that it shall have a strong connection with the residual stresses which develop during the fabrication. In general, scanning strategies which manage to disperse the heat evenly throughout the part during the printing tend to limit the residual stresses introduced to the parts, as the thermal gradients are less steep and therefore create smaller differences between the expanded molten material and the solid volumes beneath it [36]. Unfortunately, opinions are divided over the directions at which the maximum stress values are developed, with publications arguing that the stresses developed parallel to the scanning direction are considerably larger than those that arise along the height of the parts [46], and others supporting the opposite [44]. It has been stated, however, that the peak values are always located at the onset of the scanning tracks [46].

The general take-outs regarding the topic of residual stresses developing during L-PBF are centred around the necessity of implementing scanning strategies which use varying sequencing of the scanning tracks, see Figure 2.19 d) and e), as these can reduce the deformation exhibited by the finished parts due to the more even heat distribution along each layer [45]. Moreover, reducing the length of the scanning vectors has also been widely reported as a very successful method of controlling residual stresses [45] [47] [46] [48]. Hence, strategies which divide the deposition layer into smaller units, for example island strategies, tend to perform better in terms of reducing the residual stresses of the finished parts [36]. It shall be noted here, that the size of the island is also critical, as too large island, or equivalently scanning vector lengths, tend to produce denser parts with reduced cracking but relatively large residual stresses, whereas too small islands result in decreased residual stresses but more pronounced cracking [36].

2.3 Laser-Powder Bed Fusion of NiTi Shape Memory Alloys

2.3.1 Microstructural evolution & defects

The complex thermal processing to which laser-based AM techniques subject metallic materials during fabrication is the main governing factor of the microstructure that forms in the final part. Naturally, NiTi parts manufactured by L-PBF are no exception to this. As the laser beam scans the powder bed and melts one layer of material, it also remelts the layers which have been sintered during earlier laser

passes. This phenomenon termed as *remelting* leads to what is known as *epitaxial solidification* and results in strengthening the bonding between the metallic layers and enhancing the continuity between them, ultimately making the fabricated structures stronger [16]. In the case where the optimal laser parameters have been selected for the fabrication of a given NiTi part, epitaxial solidification leads to microstructures characterised by grains with increased length and width, as opposed to equiaxed crystals [16]. When the microstructure of a NiTi part produced by L-PBF in which epitaxial solidification has taken place is seen in a view parallel to the building direction, the metallic grains appear to have an elongated platelet shape parallel to the direction of the laser path, as can be seen in Figure 2.25 a) [16]. This microstructure's topview, Figure 2.25 b), gives the impression of grains shaped into the letter *"S"* forming a grid, a result of the motion of the laser beam, as the crystals tend to re-orient themselves towards the direction of the highest thermal gradient during fabrication which, by definition, is parallel to the direction that the laser travels [16].

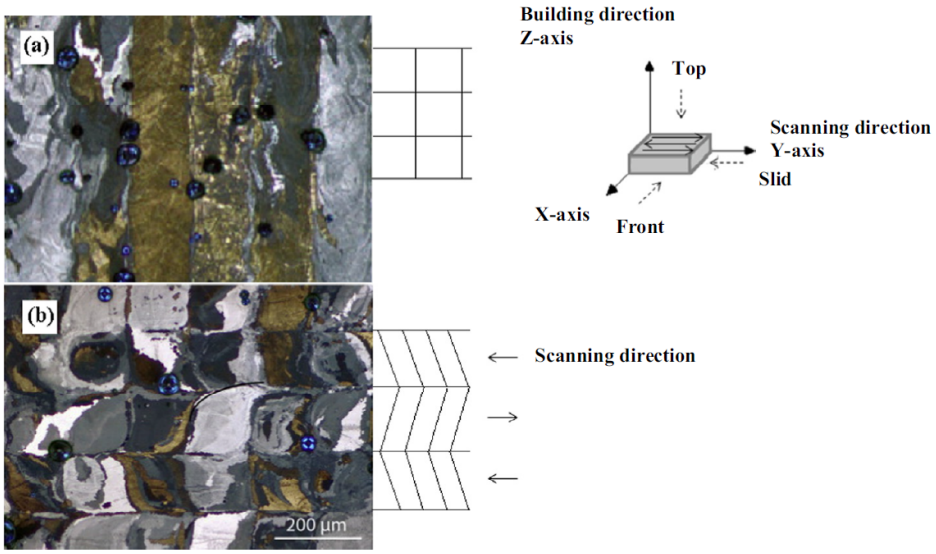


Figure 2.25: Optical microscopy images of L-PBF fabricated NiTi alloy. The schematic on the right gives orientation information for the AM process. The top image is the side view, showing elongated columnar grains along the building direction. The bottom image is a top view of the associated x-y plane, showcasing the S-shaped grain morphology. Schematics on the side of the micrographs show the scanning direction. Reproduced from [16].

It has been found that in order for the microstructure to grow epitaxially, a minimum, critical level of energy input has to be provided to the NiTi powder during fabrication [16]. In the cases where the laser energy input is either higher or lower than this critical value the resulting microstructure exhibits coarser grains [16] without any epitaxial solidification occurring. In the case of higher than the critical laser energy input this happens because the energy provided by the laser creates a superheated melt pool which extends to a large volume of the material, meaning that the solidification of the melted NiTi will require more time and, thus, the crystal grains will have the time to grow in size [16]. When the energy input is lower than the critical value, the melt pool that forms is small and unable to penetrate to the layers underneath it. Simultaneously, low laser energy densities are known to result in pore formation in the interlayer area. The combined effect leads to a decrease in the solidification rate of the deposited material due to the poor heat conduction, resulting in the formation of coarser grains in the microstructure [16].

Another characteristic of L-PBF fabrication of NiTi is the variation in the microstructure within one part [16]. Usually, crystal grains tend to get finer as one moves away from the print bed because the heat fluxes conducted through the already solidified NiTi layers are higher the more the height of the object being printed increases [16]. This is partly because there exist a temperature difference between the print bed and the NiTi powder which is being processed by the laser beam, and partly because the lowest region of a part contains the supporting structure, which, in the majority of cases, contains large hollow sections so the heat conduction is not as effective in this area as in the bulk NiTi metal areas. The high heat fluxes give rise to high solidification rates which result in finer grains in the

microstructures, see Figure 2.26 a). On the other hand, the weaker heat fluxes near the base of the parts expose the NiTi in the melt pool to higher temperatures for longer times as the solidification rates are lower, leading to the formation of larger crystal grains. Additionally, in these areas the variation in the observed microstructures is also qualitative, as the high temperatures enhance Ni evaporation from the NiTi matrix, leading to the formation of grains of Ti-rich phases, such as Ti_2Ni, which have also an effect on the transformation temperature of the final parts, see Figure 2.26 b) [16].

It is commonly encountered that various types of defects appear during L-PBF fabrication due to the processing environment, and, L-PBF of NiTi alloys is no exception to this. The two main types of defects most commonly arising in NiTi parts manufactured by L-PBF are pores and cracks [16].

Porosity in L-PBF NiTi SMAs can be either irregular or spherical in shape. Irregularly shaped pores arise because of the balling effect discussed in Section 2.2.1, whereas spherical pores arise due to the mixing of the ambient air and the NiTi powder prior to or during AM, when the trapped air cannot escape the melt pool and creates pores in the solidified metal. Therefore, porosity can be avoided via the selection of optimal process parameters which ensure epitaxial solidification, as was also indicated and discussed in Section 2.2.1. Additionally, it can be achieved by decreasing Oxygen levels inside the fabrication chamber, as this gas tends to get trapped between the layers sintered and the ones immediately above them causing cavities which expand and then collapse to pores as the laser beam scans them [16].

Cracks, on the other hand, appear due to the high thermal gradients which, in turn, cause residual stresses to develop within the part volume and initiate cracks in the NiTi parts [16]. Balling is yet another contributor to crack initiation in NiTi parts fabricated by L-PBF, together with vapourisation which leads to pores forming in the NiTi structure at an excessive rate [16]. Nevertheless, although cracks do form during L-PBF of NiTi, they can still be alleviated by choosing the optimal process parameters, especially laser energy input and laser power, however, due to the rapid cooling to which the material is subjected during the process, these cracks do not propagate after they have formed [16].

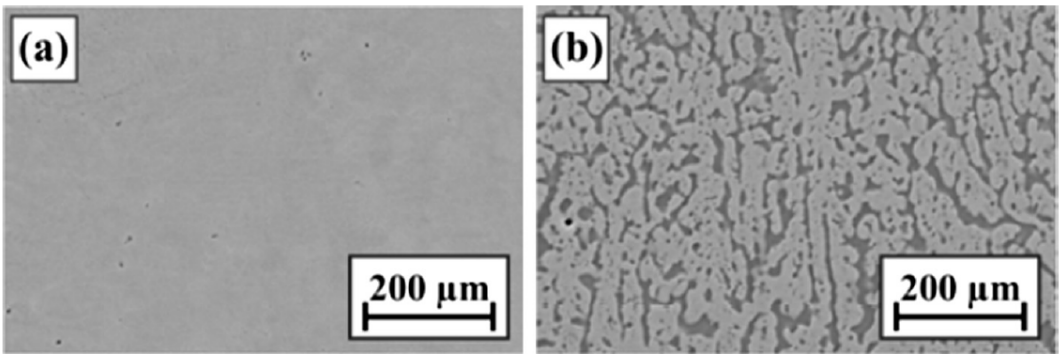


Figure 2.26: ***a)*** Microstructure of NiTi alloy produced by L-PBF as found at the centre of the sample. Fine grain structure results in a homogeneous microstructure at this level of magnification. ***b)*** Microstructure of L-PBF-produced NiTi as found near the bottom region of the sample. The dark grey areas on the right-hand side micrograph are Ti_2Ni precipitates, combined with large NiTi grains arising due to the lower heat fluxes. Both micrographs together exhibit the variation found in the microstructure of NiTi parts produced by L-PBF. Reproduced from [16].

Processing maps linking various kinds of defects with processing parameters which have been found to play a role in their formation have been synthesised, indicating sets of process parameters' values for successfully mitigating defect formation in NiTi parts fabricated by L-PBF [35].

2.3.2 Crystallographic texture

Yet another characteristic of the microstructures frequently observed in metallic parts is crystallographic texture, whereby the crystals of the alloy tend to adjust their spatial positions along preferred orientations. It is well established that metallic alloys with cubic structures, like NiTi's austenite phase, have a tendency to solidify obtaining a $\langle 001 \rangle$ orientation [49]. In addition to that, as shown by Dadbakhsh et al. [50], L-PBF fabrication orients the austenitic crystal grains in NiTi SMAs along the building direction of the part and this is the source of the anisotropic mechanical and functional behaviour of the

alloy. Consequently, the question arises of whether the crystallographic texture can be yet another microstructural feature of NiTi SMAs that can be controlled via the choice of suitable L-PBF process parameters.

Over the years, a number of publications has treated the relation between the process parameters of the L-PBF method and the resulting crystallographic texture specifically in NiTi alloys. The process parameters which have monopolised the focus of various research groups are mainly the scanning strategy including the hatch distance, the build orientation employed during printing processes as well as the laser beam focus and diameter. The reason is, as also explained in Section 2.2.2, that changes in these parameters can have a significant effect on the melt pool characteristics, and consequently affect the solidification process of the material. In a nutshell, process parameters which affect the thermal conditions during fabrication are those who are going to grant control over the crystallographic texture characteristics of the final part. Since the effect of the scanning strategy on the crystallographic texture has already been treated in Section 2.2.2, where it was concluded that the same principles should apply to NiTi SMAs, the rest of the process parameters will be discussed in the following lines.

Varying the build orientation of Ni-rich NiTi parts when fabricated by the L-PBF method was found to be another effective way of controlling the crystallographic texture of parts with direct consequences to the mechanical behaviour observed. Optimum process parameters ensured epitaxial solidification resulting in columnar grains along the build direction (BD) of the samples, whereas by changing the building orientation of the parts inside the L-PBF printer bed it was attempted to align the preferred $\langle 001 \rangle$ crystal orientation of the grains to the loading direction (LD) of the samples manufactured [51]. As a result, samples fabricated using a build orientation of 90° exhibited a strong $\langle 001 \rangle$ texture in all three directions (Figure 2.27 b)), when at the same time, samples processed with a 45° build orientation showed a strong $\langle 001 \rangle$ texture along the scanning direction and a strong $\langle 011 \rangle$ texture in the other two directions, see Figure 2.27 a) [49].

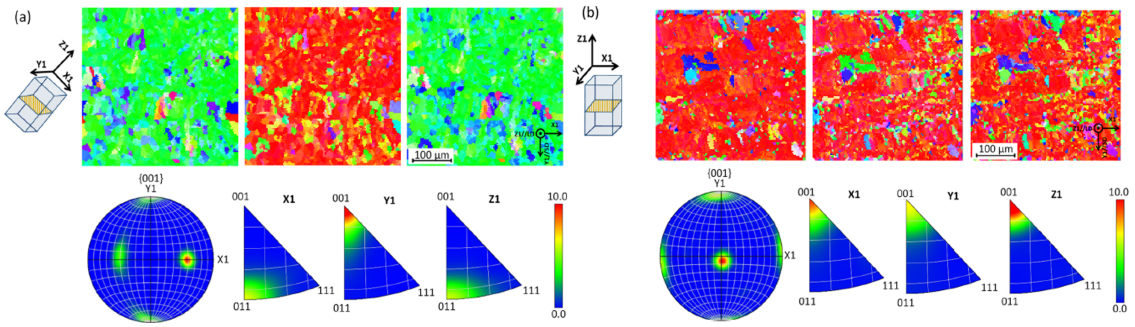


Figure 2.27: Electron Backscatter Diffraction (EBSD) maps, inverse pole figure maps and pole figures of samples fabricated via L-PBF utilising ***a)*** a 45° build orientation , and ***b)*** a 90° build orientation, as obtained from the plane normal to the building direction. At the left of the maps a schematic insert shows the build orientation of the samples inside the L-PBF print bed, as well as the associated coordinate system. The plane normal to the building direction is also shown and is the plane normal to the loading direction of each sample. Reproduced from [49].

The difference arising in the observed texture resides in the fact that the build orientation essentially causes different morphologies of the melt pool on the plane normal to the loading direction of the samples, see inserts in Figure 2.27. The process parameters used together with the scanning strategy employed, which was bidirectional scanning of the powder with a 90° rotation from layer to layer, resulted in aligning the strong $\langle 001 \rangle$ texture with all three directions of the parts, marked as X1, Y1 and Z1 in the insert in Figure 2.27 b). In the sample with the 90° build orientation, these directions coincide with the coordinate system of the printer, thus giving the expected strong $\langle 001 \rangle$ texture in all three part directions. However, when the build orientation changed in the 45° sample, it caused the crystallographic orientation with respect to the local LD//Z1 direction to rotate by 45° with respect to the building direction, resulting in a $\langle 011 \rangle$ orientation of the crystals in the X1 and Z1 coordinates [49]. These are the first and third Electron Backscatter Diffraction (EBSD) maps in Figure 2.27 a).

Another method by which texture was promoted in Ti-rich NiTi alloys during their fabrication by L-PBF was proposed by J.-N. Zhu et al [26]. In this study the depth and shape of the melt pool were manipulated by means of the focus of the laser beam. In more detail, by employing a divergent laser beam

with positive defocus, which resulted in a beam diameter of $500\ \mu$m, a shallow and wide elliptical melt pool was created. In this melt pool thermal gradients tend to have a consistent direction parallel to the building direction, which eventually enhances the formation of a strong $\langle 001 \rangle$ texture along this direction of the sample [26]. Figure 2.28 shows the melt pool shape obtained by the divergent laser beam in combination with a schematic representation of the expected grain growth, which, when combined with the preferred orientation of NiTi crystals along the $\langle 001 \rangle$ direction, results in the desired strong $\langle 001 \rangle$ crystallographic texture along the BD of the sample.

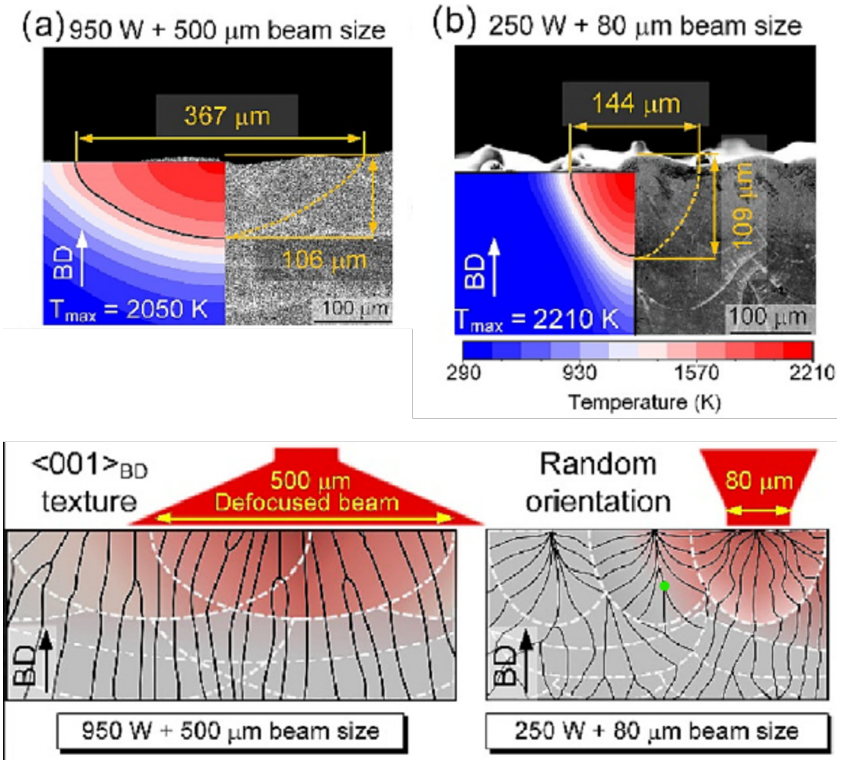


Figure 2.28: ***a)*** Cross sectional view of the melt pool formed in Ti-rich NiTi fabricated by L-PBF using 950 W laser power and 500 μm laser beam diameter and corresponding schematic representation of the grain growth over several deposited layers. ***b)*** Cross sectional view of the melt pool formed in Ti-rich NiTi fabricated via L-PBF using 250 W laser power and 80 μm laser beam diameter with the corresponding schematic representation of the grain growth over several deposited layers. Reproduced from [26].

In summary, the overarching goal in order to obtain textured components by L-PBF fabrication is to depart from the normally obtained equiaxed grains to the columnar ones and, then, to suitably orient those in space. Specifically for a strong superelastic response, grains shall adopt the *ideal texture* of a $\langle 001 \rangle$ along the BD.

2.3.3 Phase Transformations

The trend observed regarding the transformation temperatures of NiTi SMAs when the composition of the alloy is varied remains unaffected by the L-PBF process [16]. Hence, Ti-rich NiTi alloys fabricated by L-PBF show higher transformation temperatures than equiatomic NiTi which, in turn, also exhibit higher transformation temperatures compared to Ni-rich NiTi.

One of the effects studied is the one concerning the laser energy density and the transformation temperatures, showing a direct influence of the fabrication process to the resulting material. It was found that, as the laser energy density increases, the transformation temperatures also increase for all three distinct Ni/Ti ratios possible (i.e. Ti-rich, near equiatomic and Ni-rich) [16] [52]. The effect is clearly visible on the three DSC curves shown on the top of Figure 2.29 a), b) and c), as for all three Ni/Ti ratios chosen, the peaks signifying the phase transformations during both heating and cooling shift to the right as the laser power input is increased. This effect is explained by the fact that as the energy input is increased, the rate of the Ni evaporation off the NiTi powder is enhanced, as Ni evaporates at

lower temperatures compared to Ti. This causes the NiTi matrix to be depleted of its Ni content and, consequently, reach a Ti-rich state, associated with higher transformation temperatures as explained in Section 2.1.2. Simultaneously, the higher energy inputs during L-PBF lead to increased levels of impurity pick-up which, as was described in Section 2.1.2, lead to the formation of Ti-rich phases within the NiTi matrix (e.g. $Ti_4Ni_2O_x$), which eventually shifts the compositions towards higher Ni contents. As can one understand, these two mechanisms counteract one another, however, it was found that the first compensates and even overcomes the effects of the second, which explains why the higher the energy input during L-PBF, the higher the phase transformation temperatures of the finished parts will be [52].

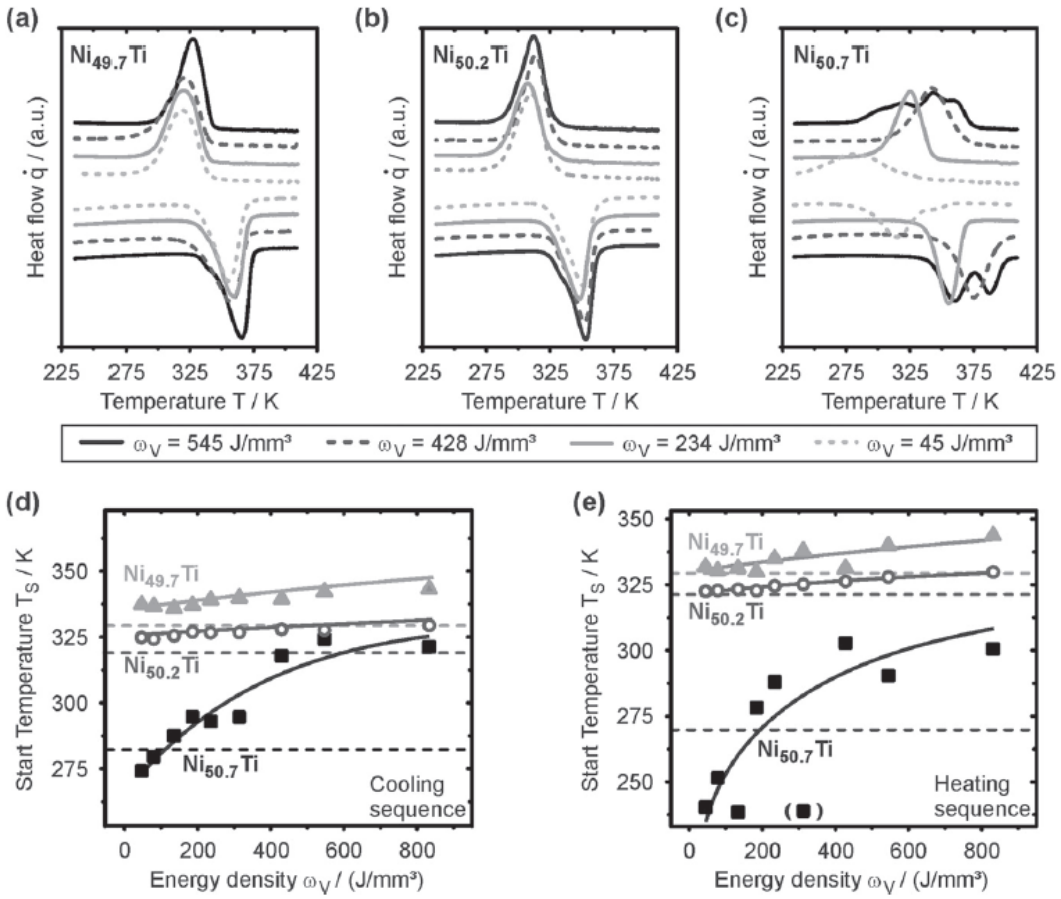


Figure 2.29: Effect of the laser energy density, $[J/mm^3]$, on the transformation temperatures of three NiTi samples with ***a)*** Ti-rich (Ni49.7Ti), ***b)*** near equiatomic (Ni50.2Ti) and ***c)*** Ni-rich (Ni50.7Ti) compositions. ***a), b) & c)*** are the DSC graphs for various energy densities, see legend box below them. ***d) & e)*** Comparison between the phase transformation temperatures of the raw NiTi material (dashed lines) and the L-PBF final parts (solid lines) for each composition. Reproduced from [52].

Ni-rich NiTi powders suffer from this effect of the increased laser energy density more severely compared to the Ti-rich and equiatomic compositions [16] [52], a trend verified by the corresponding DSC plot of Figure 2.29 c). One possible explanation for this is that the Ni-rich metastable phases, such Ni_4Ti_3, Ni_3Ti_2, Ni_3Ti, which form in Ni-rich NiTi alloys due to the system's limited solubility for excess Ni (see Section 2.1.2) do not participate in the martensitic transformation, but do deplete the matrix of its Ni and so, they only affect the temperature at which these transformations occur [52]. These metastable phases grow in volume as the energy input increases during fabrication and, combined with the increased rates of Ni evaporation, the DSC curves exhibit untypical behaviours. The two peaks which can be now identified at higher energy inputs could be attributed to either the emergence of an intermediate phase transformation (the rhombohedral R-phase), or the increased chemical inhomogeneity induced by these phases which results in the transformation to martensite occurring over a temperature range rather than at a specific temperature (multi-step transformation) [52].

The effect of the L-PBF process itself on the transformation temperatures of the material can be more readily seen at Figure 2.29 d) and e). Figure 2.29 d) corresponds to the cooling sequence during a DSC measurement, whereas Figure 2.29 e) corresponds to the heating part of the experiment. The horizontal dashed lines represent the transformation start temperatures for the powder material used for the fabrication, i.e. the raw material. The solid lines show how the energy density of the laser beam affects the transformation temperature of the final NiTi samples produced by L-PBF. It is clear, therefore, that the fabrication process has a strong effect on the temperature at which the solid phase transformations occur in NiTi parts, an effect which is also influenced by the compositions of the material.

2.3.4 Mechanical Properties

Hardness, compressive strength and damping properties of NiTi parts are also of interest in relation to the way in which they are affected by L-PBF. In the case of hardness, it is found that for perfect NiTi parts manufactured by L-PBF (i.e. parts which are pore- and crack-free), the microhardness levels are approximately 1.5 - 2 times higher than the microhardness of conventionally manufactured NiTi parts [16]. Ti-rich NiTi manufactured by L-PBF performs better in terms of microhardness, due to the formation of $NiTi_2$ precipitates in its microstructure [16]. However, it shall be noted here, that as one might expect, the increased microhardness is accompanied by lower levels of ductility [16].

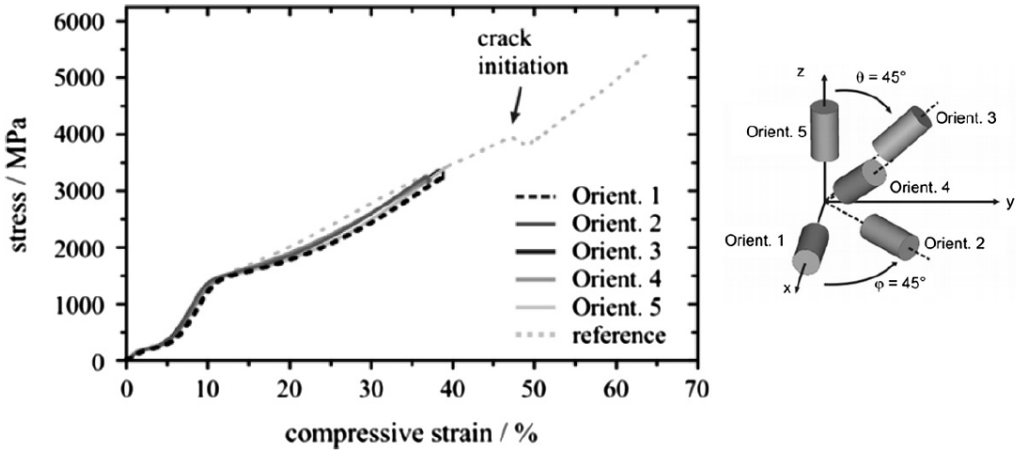


Figure 2.30: Stress, σ, [MPa] versus strain, ε, [%] curves until failure for Ti-rich NiTi alloy manufactured both conventionally and by L-PBF. The AM samples were also manufactured taken into account various orientations as shown on the graphic on the right. L-PBF NiTi parts fail earlier than their conventionally produced counterparts. Reproduced from [16].

As far as the compressive strength goes, Ti-rich NiTi samples fabricated by L-PBF exhibit similar behaviour to conventionally manufactured NiTi alloys when subjected to compression tests [16]. Nevertheless, failure occurs at lower stress levels for the L-PBF NiTi parts when compared to their conventionally manufactured counterparts, as can be seen in Figure 2.30. A similar trend can also be observed in the compression behaviour of Ni-rich NiTi parts produced by L-PBF, as seen in Figure 2.31 [16].

The effect of the process parameter of build orientation has also been studied for both Ni-rich and Ti-rich L-PBF-manufactured parts, as can be seen in the plots of Figures 2.30 and 2.31. In general, the effect of the fabrication orientation seems to be insignificant with respect to the behaviour of the parts under compressive loading [16]. However, in the same review it was reported that horizontally fabricated NiTi parts seemed to exhibit better tensile performance and greater resistance to compression when compared to parts fabricated vertically [16]. The superposition of the lines on the plots on both Figure 2.31 and Figure 2.30 offer support to such conclusion. Lastly, the behaviour exhibited under torsional loading seems to be far less influenced by the orientation dependency of the NiTi parts during fabrication [49].

Furthermore, L-PBF has been reported as producing NiTi parts which have stronger structures and

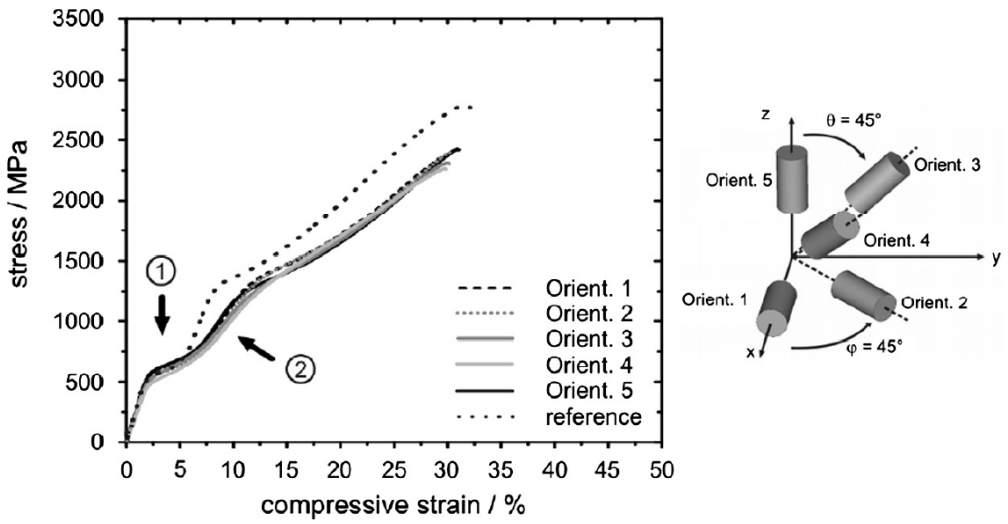


Figure 2.31: Stress, σ, [MPa] versus strain, ε, [%] curves until failure for Ni-rich NiTi alloy manufactured both conventionally and by L-PBF. The AM samples were also manufactured taken into account various orientations as shown on the graphic on the right. The parts fabricated by L-PBF all show similar behaviour, irrespective of fabrication orientation, but different to the behaviour of the conventionally manufactured sample. Reproduced from [16].

exhibit higher values of fracture stress, as the increasing laser power and scan speed affect the melting process of the material and lead to its rapid solidification [16].

2.3.5 Functional Properties

As has been explained in earlier parts of this report, NiTi alloys are able of exhibiting functional properties in addition to the standard load-bearing capabilities that all materials possess. The functionalities that NiTi SMAs are able to exhibit are the Shape Memory Effect (SME) and the Superelastic behaviour (SE). As it has been already discussed in Section 2.1.2, neither of these functionalities remain unchanged during the service lifetime of a NiTi part, rather, they degrade during use. The degradation of both of these effects is defined as the accumulation of irreversible strains inside the NiTi lattice during each cycle of transformation they undergo during service [16]. Irreversible strains arise due to the nucleation of dislocations within the lattice of the alloy during service [52]. Dislocations can contribute to the increase of irreversible strains either by directly resulting to plastic deformation, or by enabling the stabilisation of certain martensitic variants, rendering them unable to participate in the transformation process and consequently limiting the material's ability to support the functional behaviour.

- ***Shape Memory Effect***

As a manufacturing method, L-PBF seems to not have a significant effect on the manifestation of the SME behaviour of NiTi parts, meaning that both conventionally manufactured NiTi components, as well as the parts manufactured by AM are able of showcasing the SME [16]. For the compression loading test procedure outlined in Figure 2.32 a), NiTi samples of near-equiatomic composition (50.2 at.% Ni) manufactured by the L-PBF technique (Figure 2.32 b)), and by conventional methods (Figure 2.32 c)), both exhibit the SME behaviour. However, when Figure 2.32 d) is also taken into account, the differences in the quality of the functional behaviour imposed by the manufacturing methods become clear. In detail, L-PBF equips the NiTi parts with more stable recovery for the first five cycles of their lifetime, an effect which diminishes after the sixth cycle of reversible compression loading. As suggested by the researchers who conducted this study, this may be attributed to the lower critical stress levels observed for the AM-NiTi samples. According to their rationale, lower stress values for the start of the transformation plateau during the loading portion of the test suggest that a lower dislocation density might evolve during the cyclic loading of these samples, compared to the samples manufactured via conventional methods [52]. As one can see from Figure 2.32 b), these stress values decrease as the cycles progress, leading to believe that the irreversibilities reduce as the tests advance and the shape recovery behaviour between the two groups of samples tends to homogenise [52].

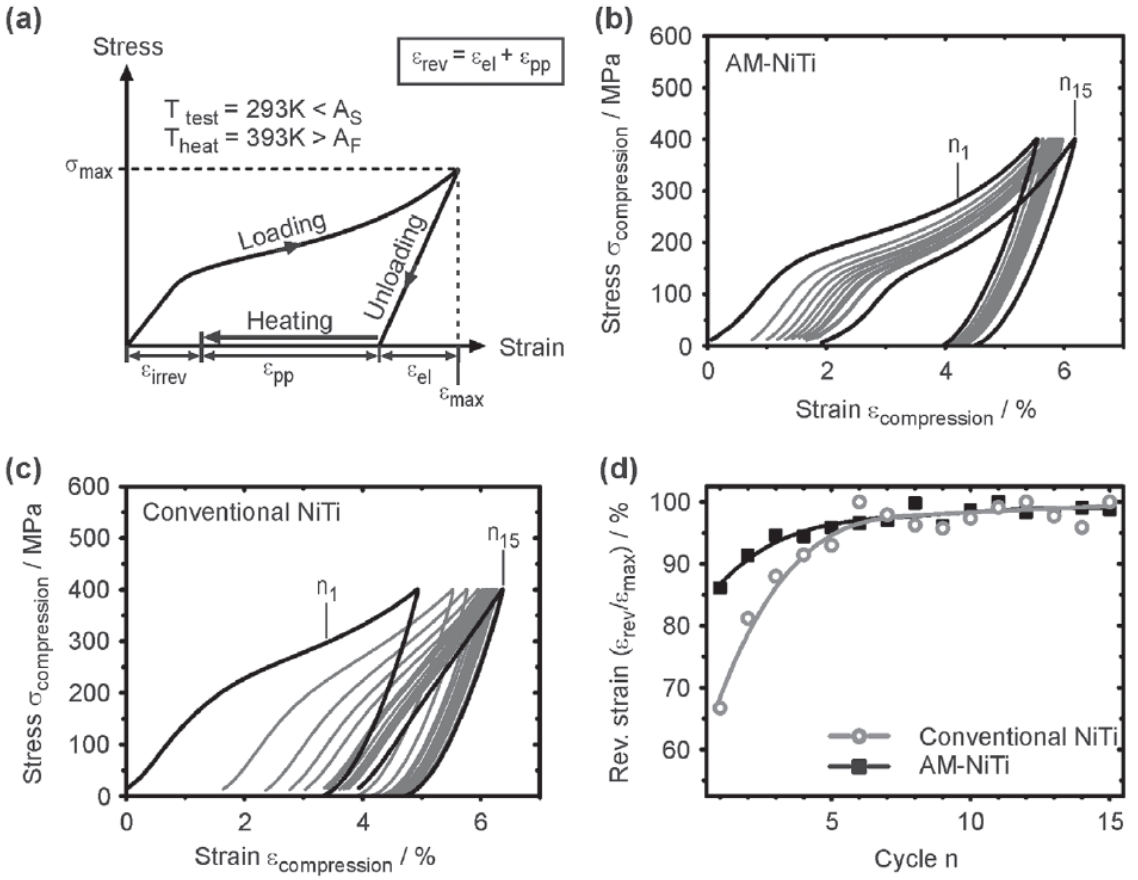


Figure 2.32: ***a)*** Schematic representation of a single cycle of the testing procedure followed to evaluate the SME of NiTi samples. Values of importance concerning temperature, T, stress, σ, and strain, ε, are also noted on the graph for reference. ***b) &c)*** Stress, σ, [MPa] versus strain, ε, [%] curves showing the SME for NiTi alloys manufactured by ***a)*** AM and conventional methods respectively. ***d)*** The ratio between reversible and maximum strains plotted against the number of loading cycles for the two manufacturing methods. Reproduced from [52].

Special reference deserves the fact that the irrecoverable strain of the material after 15 loading cycles is 2.5%, when for the conventionally manufactured alloy this value reaches 3.9% [16]. Even for loading conditions which reach stress levels where the detwinned martensite is almost fully elastically loaded, i.e. above the 400 MPa stress level shown in the tests performed in Figure 2.32, the irreversible strains are also reported higher for parts manufactured by conventional methods, bolstering the beneficial nature of L-PBF fabrication [16].

A potential explanation for this difference may lie in the differences observed in the microstructures of the samples. As discussed in Section 2.3.1, L-PBF can result in large epitaxial crystal grains of several μm in size, whereas conventional manufacturing techniques usually produce microstructures of smaller crystals increasing the density of grain boundaries within the microstructure, which are known to impede the motion of dislocations during deformation [52]. For this reason, L-PBF-produced NiTi may be able to showcase better ability for deformation than the conventionally produced alloy, along with the fact that microscopic pores present in the AM material may also enhance its deformability [52]. Hence, the maximum strain at maximum load values which are observed for the L-PBF samples are different to those values seen for the conventionally fabricated parts.

The influence of the microstructural characteristics of the alloy to the Shape Memory functional response can also be reinforced by the following example. Microstructural design methods via manipulation of the laser beam focus resulted in epitaxially grown columnar grains in a Ni-lean alloy. Samples with strong $\langle 001 \rangle$ texture along their building direction and others where texture was absent were tested for evaluation of the SME and Two-Way SME capabilities, see Figure 2.33. In the first SME cycle, the textured alloy showed almost 100% recoverable strain for a 4% compressive engineering strain, good

cyclic stability and, after the course of 50 SME cycles, it showcases approximately 1.6% recoverable strain, see Figure 2.33 a), c) and d) [26]. The Two-Way SME, see Section 2.1.1, has also been confirmed for this particular material in the same study [26]. For comparison, the non-textured samples showed approximately 18% residual deformation in the first compression cycle (Figure 2.33 b)), about 33% lower recoverable strains overall after the 50 loading cycles (Figure 2.33 c)) and comparable TWSME behaviour (Figure 2.33 d)) [26].

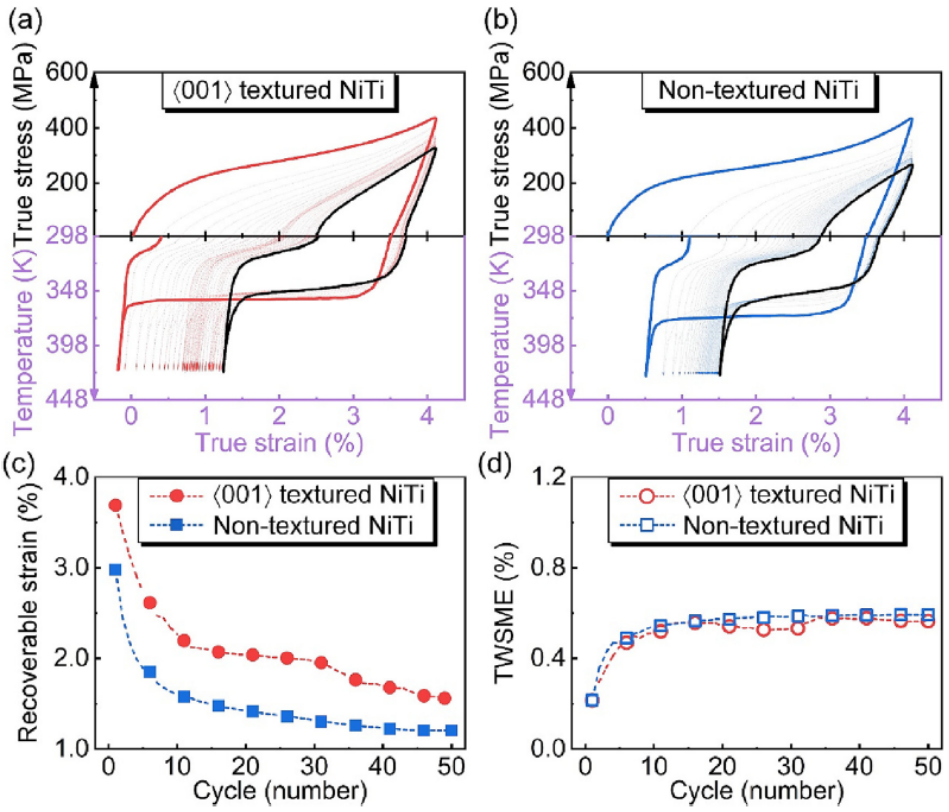


Figure 2.33: ***a)*** True stress, σ_{true}, [MPa] versus true strain, ε_{true}, [%] versus temperature, T, [K] curves for the Ti-rich superelastic alloy developed by Zhu et al. in [26]. First cycle is marked in red, final cycle is shown in black. ***b)*** The same type of curve is given for the same composition alloy which has not been crystallographically designed as means of comparison. Blue line shows the first cycle and black line gives the last. For both cases, the mechanical portion of the loading occurred at room temperature. ***c)*** The recoverable strain measured for each material as a function of the loading cycles, and, ***d)*** the Two-Way SME as a function of the cycles. Reproduced from [26].

- ***Superelasticity***

Superelastic behaviour is mostly related to Ni-rich NiTi alloys because of their higher intrinsic strength when compared to either their Ti-rich or their equiatomic counterparts, which makes them more suitable for showcasing high superelasticity under the correct conditions [16].

It was initially believed that, in order for NiTi parts to exhibit superelastic behaviour, additional heat treatments must be performed following the fabrication process in order for the behaviour to reach an acceptable level, as well as to be tuned to the desired temperature conditions and application characteristics. In general, it is often the case that martensite is nucleated in austenitic regions within the material, inhibiting the alloys' ability to fully recover its strength [16], hence downgrading the material's superelastic response. According to the relevant literature, solution annealing and subsequent aging treatments are necessary in order for the Ni-rich alloy to realise its superelastic capabilities. Solution annealing is exploited in order to provide a new equilibrium state for the alloy by means of reducing both the residual stresses left after the L-PBF fabrication, as well as the microstructural defects, such as precipitates, that are created during the process [16]. If the annealing procedure is also followed by aging treatments, then Ni-rich precipitates (such as Ni_4Ti_3, Ni_3Ti_2 and Ni_3Ti) are allowed to form in the NiTi matrix in certain desirable sizes and distributions [52]. These precipitates increase the yield strength, as they contribute to hardening, while also acting as dislocation barriers [52]. The result is

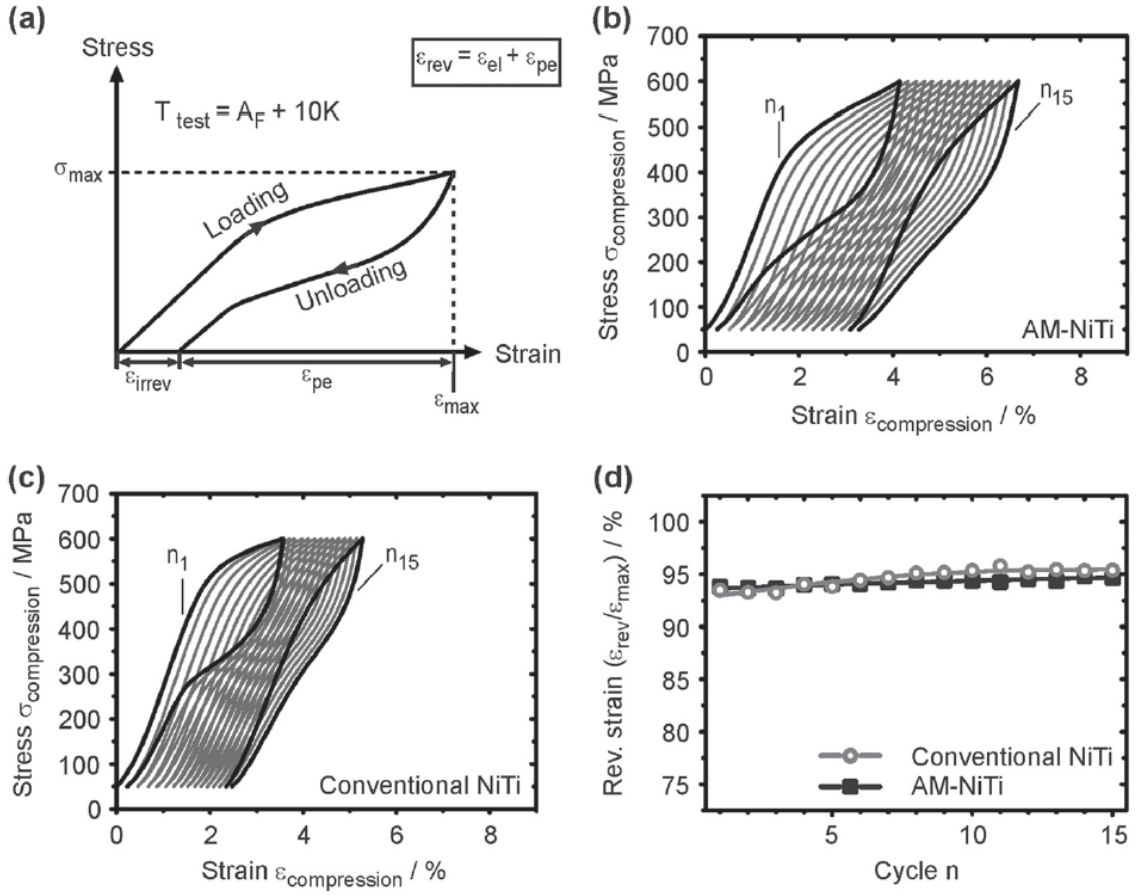


Figure 2.34: ***a)*** Schematic representation of one cycle of the testing procedure followed to evaluate the SE behaviour of NiTi samples. Values of importance concerning temperature, T, stress, σ, and strain, ε are also noted on the graph for reference. ***b) & c)*** Stress, σ, [MPa] versus strain, ε, [%] curves showing the superelastic response for Ni-rich NiTi alloys manufactured by AM followed by heat treatments and conventional methods respectively. ***c)*** The ratio between reversible and maximum strains plotted against the number of loading cycles for the two manufacturing methods. Reproduced from [52].

that, at this point, the material is able to fully recover its initial strength since the level of irreversible deformation during loading is reduced [16].

Nevertheless, the final superelastic behaviour exhibited by Ni-rich NiTi parts manufactured by L-PBF and subsequently heat treated and aged is marginally different to this of the conventionally manufactured alloy, as can be seen in Figure 2.34 d). In this particular study, a NiTi alloy containing 50.7 at.% Ni was subjected to solution annealing for 5.5 hours at 950°C, followed by aging for 24 hours at a temperature of 350°C. The typical hysteretic superelastic behaviour can be observed in both the cases of the post-processed and the conventionally manufactured samples, as well as the corresponding plateau regions which are associated to the phase transformation. As generally expected, the width of the hysteresis is decreasing as the loading cycles advance, showing the anticipated functional degradation for both the L-PBF and the conventionally manufactured NiTi samples. The most striking difference between the two materials, and the one that can be directly attributed to the manufacturing method, is that the L-PBF NiTi shows higher maximum strains together with a higher recoverable deformation compared to the conventional NiTi, Figure 2.34 b) and c) [52]. Finally, for both materials the reported recovery ratios are of the order of 95% after 15 cycles of compressive loading up to 600 MPa [16]. It shall be noted here, that the explanations given in the previous paragraphs, concerning the larger cyclic stability and the higher maximum strains at maximum load values observed between the AM-NiTi and the conventional samples, hold also for the superelastic behaviour discussed here (for more details, the reader is referred to [52]). Table 2.1 gives a selection of post-processing heat treatments employed by various research groups for inducing the superelastic response in Ni-rich NiTi alloys.

It becomes immediately apparent from the contents of Table 2.1 that the post-processing methods em-

Table 2.1: A selection of post-process heat treatments used for achieving SE in Ni-rich NiTi SMAs together with the stabilised values of recoverable strain achieved

Material	AM method	Solution annealing	Aging	ε_{rec}	Recovery Ratio
$Ni_{55}Ti_{45}$, [53]	LENS *	775°C, 10 hr	500°C, 1 hr	3%	NA
$Ni_{50.8}Ti_{49.2}$, [54]	SLM	950°C, 5.5 hr	350°C, 18 hr	4.2%	95%
$Ni_{50.8}Ti_{49.2}$, [55]	SLM	-	600°C, 1.5 hr	5.5%	NA

* *LENS, i.e. Laser-Engineered Net Shaping is an AM technology utilising nozzle injection of powdered metallic materials deposited in a layer-by-layer fashion by means of a laser beam [56].*

ployed for enhancing the superelastic response of NiTi alloys increase the time required for fabrication, and, inevitably, also increase the production costs. Additionally, not all NiTi alloys are suitable for being subjected to heat treatments; several studies report that although Ni-rich NiTi alloys, with Ni contents above 50.6 at.%, respond well to post-processing heat treatments, Ni contents below that threshold as well as the Ti-rich and the equiatomic alloys do not lend themselves to such processing [57]. Therefore, the need for establishing superelasticity in the alloys in their as-fabricated condition straight after AM production via some different route becomes imperative.

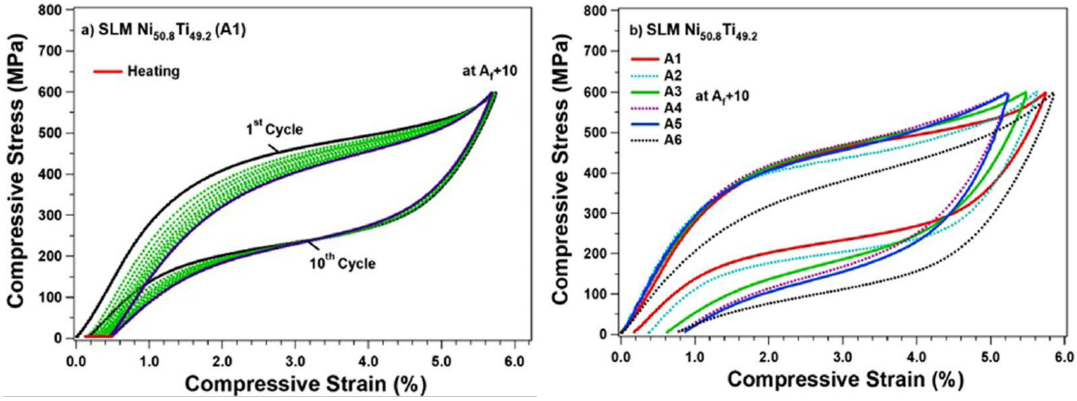


Figure 2.35: ***a)*** Cyclic compressive strain [%] versus stress [MPa] at temperature A_f + 10°C plot for sample manufactured by L-PBF with hatch distance 80 μm. ***b)*** Compressive strain [%] versus stress [MPa] at temperature A_f + 10°C for samples fabricated using different hatch distance values. These are as follows: A1 - 80 μm, A2 - 100 μm, A3 - 120 μm, A4 - 140 μm, A5 - 160 μm and A6 - 180 μm. Adapted from [57].

Luckily, attempts for enhancing the superelastic behaviour of Ni-rich NiTi alloys through tuning the processing parameters associated with L-PBF have borne successful results. In a study published in 2019, and one of the first in this direction, researchers managed to enhance the superelastic response of a marginally Ni-rich NiTi alloy (50.8 at.% Ni) by varying the hatch distance during L-PBF [57]. As can be seen in Figure 2.35 b), for compression tests performed at 10°C above the A_f temperature of the alloy, in a single loading cycle up to 600 MPa, the specimens fabricated using the smallest hatch distance, i.e. h = 80 μm depicted by the red curve on the graph, exhibited the best superelastic response. When the cyclic stability of the superelastic behaviour of this sample was tested, it was found that the response was remarkable. Strain recovery in the first cycle reached 5.62% with a recovery ratio equal to 98%, whereas the stabilised behaviour reached a strain recovery of 5.2% after 10 cycles, as can be seen in Figure 2.35 a).

The observed superelasticity is attributed to the presence of a strong texture along the $\langle 001 \rangle$ direction, which can be verified in Figure 2.36, where the inverse pole figure map and the pole figure texture plot is given for the sample with hatch distance of 80 μm [57]. Transmission Electron Microscopy (TEM)

analysis of the samples verified the absence of Ni_4Ti_3 precipitates from the alloy's lattice which have been exclusively linked to strong superelastic responses in Ni-rich NiTi alloys, leading to the conclusion that the superelastic behaviour observed was mainly attributed to the presence of the crystallographic texture [57].

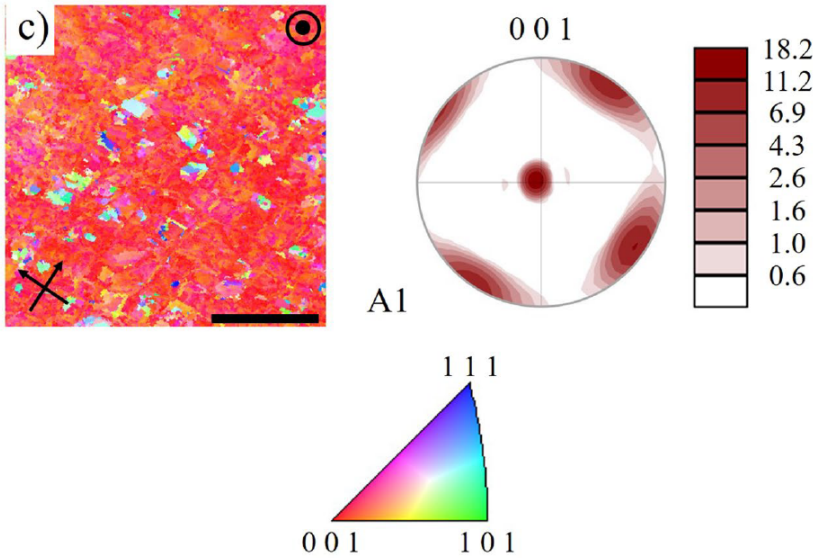


Figure 2.36: Inverse pole figure map of a section of the sample fabricated using hatch distance of $80\ \mu m$ perpendicular to the building direction. The two black arrows indicate the scanning directions and the scale bar is equal to $300\ \mu m$. On the right, the pole figure texture plot of the sample is given, verifying the strong texture observed in the sample. Adapted from [57].

Finally, one of the most recent advancements in the field of L-PBF fabrication of NiTi SMAs has come to completely disrupt the above categorisation of the functional behaviour with respect to the composition of the alloy. In a study published this year, crystallographic design enabled the fabrication of Ti-rich NiTi alloy with superior superelasticity, extended to even higher temperatures than usually achieved by traditional methods. The research group employed L-PBF for fabrication of a 49.4 at.% Ni NiTi alloy, which showed remarkable superelastic response with 4% recoverable strain from 353 K to 413 K, an operating temperature range for the functional response equal to approximately 110 K and the maximum temperature at which superelasticity is observed reaching 453 K, see Figure 2.37 [26].

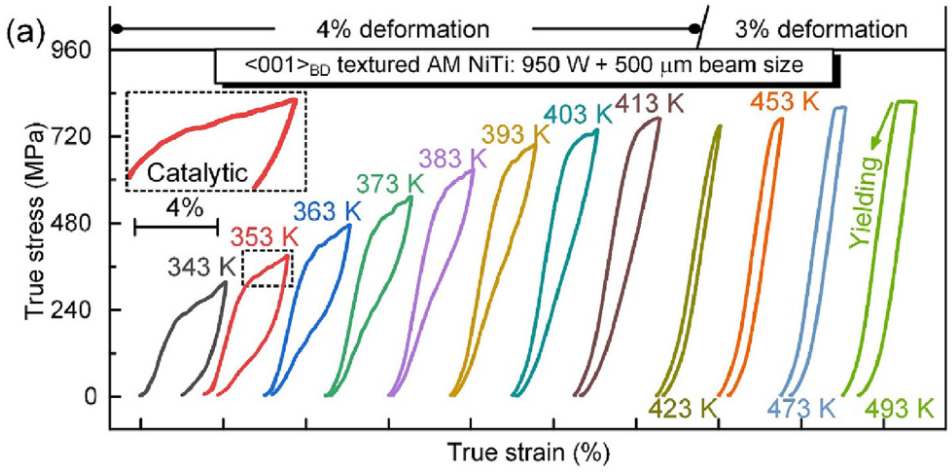


Figure 2.37: True stress, σ_{true}, [MPa] versus true strain, ε_{true}, [%] curves as a function of the testing temperature for the Ti-rich NiTi alloy exhibiting high-temperature SE. Superelastic response is obtained for all temperatures shown, starting at 343 K up until 453 K. In the last two curves, the alloy shows yielding. Reproduced from [26].

The significance of the result is twofold. Firstly, it is the first time that superelastic capability is reported for the Ti-rich alloy [26]. And secondly, this high-temperature superelasticity is unique as it can only be achieved with ternary HTSMAs (discussed in Section 2.1.2), and specifically those alloyed with Hf [26]. The impact is, therefore, significant on both the cost reduction and the increasing availability of the material, as Hf, a rare Earth element is no longer required. Additionally, the ease of fabrication has improved considerably, as intricate alloying, thermal and mechanical post-processing methods are no longer required for the alloy to exhibit the desired functional response.

Note that Figure 2.33 is testimony to the potency of crystallographic design as a method to manipulate and tune the thermomechanical behaviour of NiTi alloys, especially in terms of the crystallographic texture of the metal.

2.4 Conclusions & Research Objectives

In summary, NiTi SMAs are a class of metallic alloys with tremendous potential as they combine a number of highly sought-after properties with two unique functionalities; the Shape Memory Effect and superelasticity. This report aimed at presenting in a concise manner a short story of the physical background of these alloys together with a more in-depth overview of their fabrication by Laser-Powder Bed Fusion and its effect on their functional behaviour. The specific conclusions which can be drawn from the entirety of the report are as follows:

1. The heavy dependency that NiTi-based SMAs show on their composition and concentration allows for precise control of the thermomechanical behaviour of the material.
2. Laser-Powder Bed Fusion is a manufacturing method controlled by a large number of process parameters. These parameters have a distinct effect on various features of the material being processed, as the density, the impurity level, the microstructure, the mechanical properties and the overall performance. NiTi-based SMAs lend themselves to being fabricated by the AM technique and are simultaneously being benefited from the unique processing that they undergo during this type of manufacturing.
3. Laser-Powder Bed Fusion allows for in-situ microstructural control of materials, realising crystallographic design of parts via the optimisation of the process parameters. The precision of this microstructural design process is also considerably greater than what can be achieved with traditional manufacturing techniques. Moreover, aspects such as production time and costs can be also considerably affected and improved.
4. Extensive research undertaken throughout the last 30 years has managed to map the effect of various process parameters of the L-PBF method to their effect on the microstructure and the thermomechanical behaviour of NiTi SMAs. However, there still exist process parameters which have not been fully studied in terms of their ability to affect and control the mechanical and functional response of NiTi SMAs.
5. Scanning strategy emerges as a process parameter with substantial potential for controlling various features of NiTi SMAs. However, its full potential has not been revealed yet, as its influence on the material and the fabrication process is multifaceted. Nevertheless, as can be seen throughout this report, the scanning strategy can become a key process parameter when fabricating NiTi SMAs by L-PBF, as it can ultimately affect the properties of the metal, both the conventional and the functional. Its nature will also allow it to be employed when functional grading of NiTi parts is required.
6. Finally, crystallographic texture emerges as one of the components of the microstructure of the NiTi SMAs with the power to tailor the functional response. As was described in the text, texture can have such an effect on both Shape Memory Effect and the superelasticity so that the dependence on expensive alloying processes, complicated heat post-processing treatments and intricate post-manufacturing deformation methods is significantly reduced.

The conclusions listed above inevitably give rise to a series of questions which can be used to guide experimental research on the topic of NiTi SMAs fabricated by L-PBF. Initially, is there an effect of the scanning strategy implemented during L-PBF on the microstructure of the material? Does a unique

crystallographic texture arise in each microstructure manufactured by a different scanning strategy? Are there differences in the mechanical and the functional behaviour exhibited by each of those microstructures? An finally, can there be established a relationship between the scanning strategy, the microstructure and the mechanical and functional behaviour of the resulting NiTi parts?

Finally, before concluding this Chapter the research objectives which shall be achieved by the end of this thesis are as follows:

- ***Research Objective 1*** - What is the effect of L-PBF scanning strategies on the microstructure of Ni-rich NiTi SMAs?

- ***Research Objective 2*** - What is the effect of L-PBF scanning strategies on the superelastic response of Ni-rich NiTi SMAs?

- ***Research Objective 3*** - What is the effect of loading direction and crystal orientation on superelastic response of Ni-rich NiTi SMAs?

- ***Research Objective 4*** - What is the nature of the residual strain measured after the superelastic response has stabilised?

3

Materials & Methods

This Chapter aims at presenting an overview of the material studied, the manufacturing process as well as a detailed description of the various characterisation methods employed throughout this research project.

3.1 Material & Fabrication

Laser-Powder Bed Fusion (L-PBF) of commercial NiTi powder (51.4 at.% Ni and 48.6 at.% Ti) produced by gas atomisation was used for manufacturing samples under a protective argon atmosphere. Fabrication was performed by an Aconity3D Midi printer equipped with a laser beam of Gaussian distribution. The powder utilised, seen in Figure 3.1, consisted of particles with spherical shape and D-values of 23 μm (D10), 40 μm (D50) and 67 μm (D90).

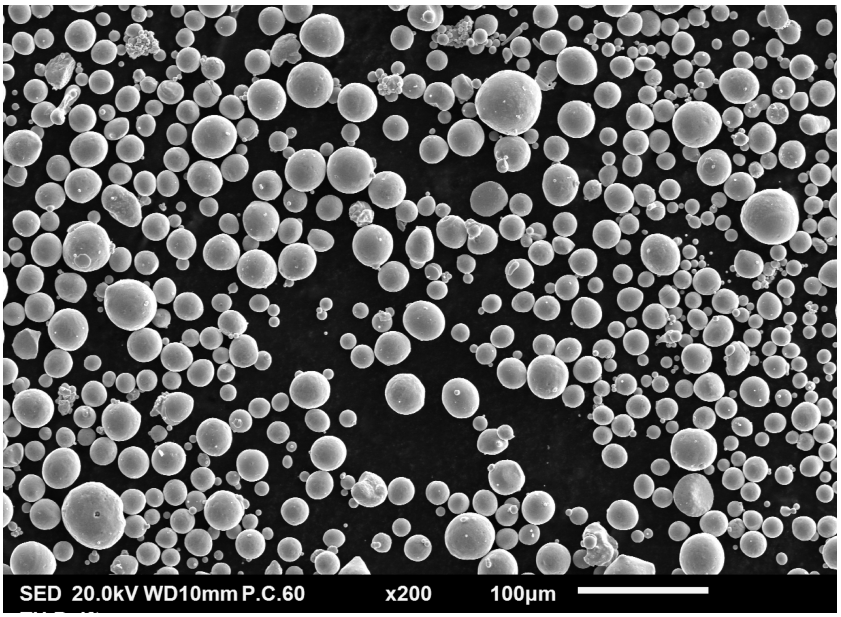


Figure 3.1: Scanning Electron Microscopy micrograph of the NiTi powder used for Laser-Powder Bed Fusion fabrication of the samples.

Two sets of samples were investigated during the experimental part of this project in order to thoroughly examine the effect of the scanning strategy on the crystallographic texture of the material and

its associated thermomechanical and functional behaviour. The first set of samples included specimens fabricated using the same process parameters and varying only the scanning strategy. They are named after the rotation used in their respective printing process, see Table 3.1 for a full list. The second set of samples was manufactured utilising another set of processing parameters and aimed at elucidating the effect of a higher laser power on the resulting crystallographic texture and related properties in synergy with the scanning strategy. These specimens were manufactured using only one scanning strategy and their name combines the high laser power condition of their manufacturing and the scanning strategy employed and they are also presented in Table 3.1. The process parameters implemented for the fabrication of both sample sets can be found in Table 3.2. Additionally, a visual representation of all scanning strategies investigated in this project can be found in Figures 3.2 and 3.3.

Table 3.1: Scanning strategies and sample labels

Scanning Strategy [Rotation in *degrees*]	Sample Name	Number of Layers in One Period
0° bidirectional, single layer	0	1
90° bidirectional, single layer	90	2
30° bidirectional, single layer	30	6
67° bidirectional, single layer	67	~ 5
67° bidirectional, with 1×1 mm island patterns	island_67	~ 5
67° bidirectional, single layer	HLP_67	~ 5

The scanning strategies studied in this project were chosen considering their applicability for fabricating samples with square cross-sectional areas, hence spiral or circular strategies were not included. One reason for selecting these specific scanning vector rotations is the fact that they have been extensively used in research in the past decades, hence their implementation here would guarantee that this study and its results would be comparable with other similar studies carried out by various research groups. Additionally, the most important aspect in selecting the scanning strategies to be studied was the number of layers required before the scanning pattern begins to repeat again, referred to as the period. This feature can be seen in the last column of Table 3.1, where the period for each sample is listed. Specifically, samples 0, 90 and 30 were fabricated by implementing interlayer rotation angles which resulted in the scanning strategy being repeated after 1, 2 and 6 layers respectively. The 67° interlayer rotation angle strategies, with which samples 67, island_67 and HLP_67 were fabricated, did not in fact repeat after any amount of layers, as the prime number of rotation used cannot perfectly divide one full rotation of the scanning vector. Nevertheless, after approximately five layers the strategy results in the scanning vector being directed close-by to the “initial” layer, and that is the reason why a five layer period is considered here, albeit in an excessive manner.

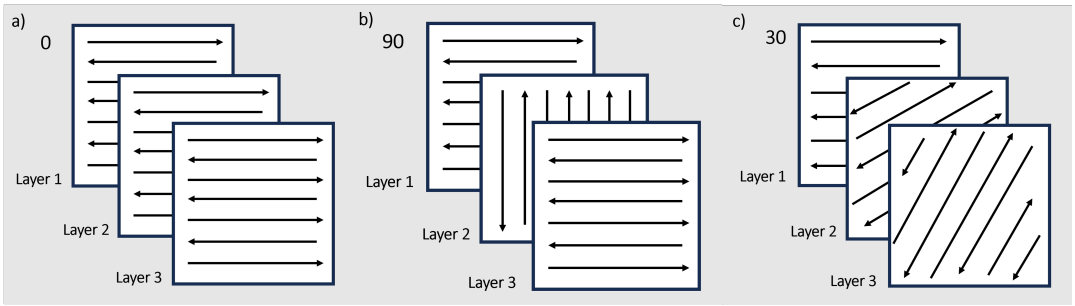


Figure 3.2: Schematic representations of the ***a)*** 0° rotation, ***b)*** 90° rotation and ***c)*** 30° rotation scanning strategies implemented for sample fabrication.

The fabrication process defined above was used for manufacturing several cubic samples of 10 × 10 × 10 mm size. Electrical Discharge Machining (EDM) was utilised for cutting the cubes, removing a layer of thickness equal to 1 mm from each side and forming four cuboids of dimensions 8 × 4 × 4 mm per cube. Prior to any further actions the cuboids were ground to remove surface damage caused by the cutting process.

Table 3.2: Process parameters employed for the fabrication

Process Parameter	0, 90, 30, 67 & island_67 samples	HLP_67 sample
Laser power, P, [W]	400	950
Scan velocity, v, [mm/s]	1200	650
Layer thickness, t, [mm]	0.03	0.04
Hatch distance, h, [mm]	0.12	0.18
Laser beam diameter, d, [μm]	80	700
Laser beam type	Gaussian	Flat top
Volumetric Energy density, VED, [J/mm^3]	93	203
Modified Volumetric Energy Density [J/mm^3] from [52]	216	88

Another important aspect of the fabrication of the samples studied is the oxygen content. A Bruker G8 Galileo + IR analyser was used for measuring the oxygen levels of the samples. Prior to the measurement, the samples were ground for removing excess oxidation caused by the environment or cutting techniques. The oxygen content measured are presented and discussed in detail in Chapter 4.

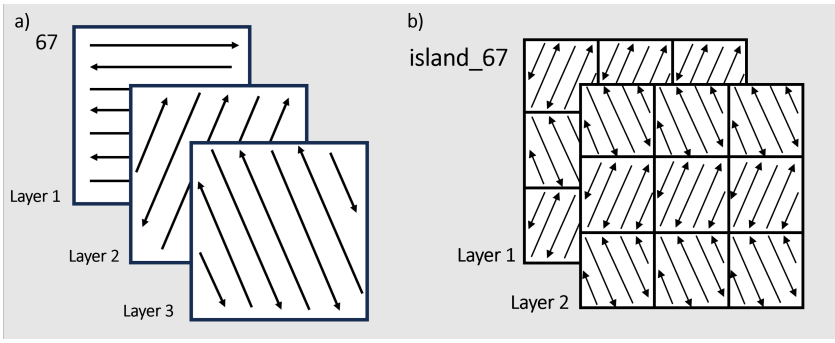


Figure 3.3: Schematic representations of the ***a)*** 67° rotation and ***b)*** the 67° rotation in island patterns scanning strategies implemented for sample fabrication.

3.2 Characterisation Methods & Procedures

3.2.1 Microstructure

Microstructural characterisation of the material was performed by means of Optical Microscopy, Scanning Electron Microscopy (SEM) - Energy Dispersive X-ray Spectroscopy (EDS) and Electron Back-Scatter Diffraction microscopy (EBSD). For all three techniques the cuboid samples were initially cut using the Struers Accutom-100 cutting equipment into two pieces allowing for the investigation of both their top side (4 × 4 mm face corresponding to the top or xy plane of the as-fabricated cubes) and their

side parallel to the build direction (BD) (8 × 4 mm face corresponding to the xz plane of the as-fabricated cubes), see Figure 3.4.

The samples were subsequently mounted into electrically conductive resin, using hot mounting for the samples investigated in their as-fabricated condition and cold mounting for the samples examined after the thermomechanical testing. Mechanical grinding using SiC abrasive papers with grit size values 800, 1200 and 2000 and water cooling was performed, followed by polishing until mirror surface quality, using cloths and suitable polishing diamond suspensions with particle sizes 9 μm, 3 μm, 1 μm and 0.25 μm. Thorough cleaning with isopropanol in ultrasonic bath conditions was frequently performed during the preparation process. In the cases where further preparation steps, specific to a characterisation technique were taken, these will be discussed separately in their corresponding sections.

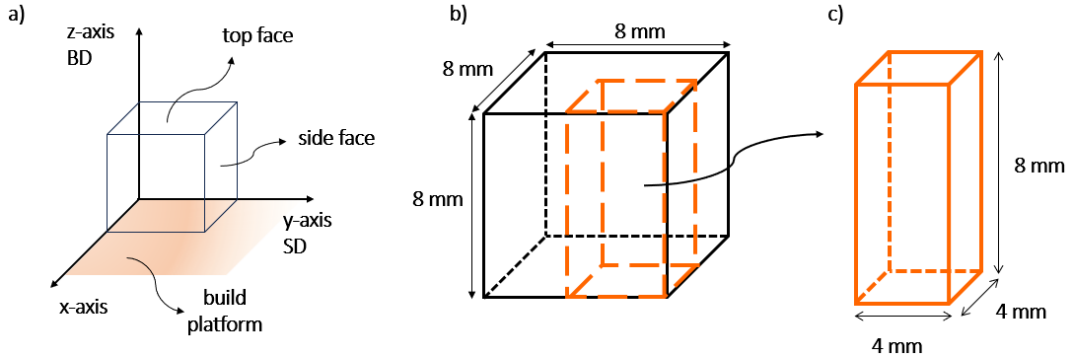


Figure 3.4: ***a)*** Coordinate system defining the three dimensions associated with the L-PBF fabrication of the samples. It is customary to refer to the z-axis as the build direction (BD) and the y-axis as the scan direction (SD). The top, or xy, and side, or xz, faces of the cubic samples are also denoted. ***b)*** Schematic of the cubic sample fabricated by L-PBF for this thesis showing the dimensions after the EDM machining step. The intermittent lines outline one of the four cuboids into which each 10 × 10 × 10 mm is cut for further characterisation and testing. ***c)*** Schematic representation of the 8 × 4 × 4 mm cuboid sample used for the mechanical and TMA testing. A cut along the plane parallel to the xy plane of this cuboid produces the necessary sectioning to the sample for microstructural and phase characterisation.

Optical Microscopy (OM)

Optical Microscopy images were obtained using Keyence VHX Digital Microscope for visible light measurements, as well as Leica DMLM Optical Microscope under conditions of polarised and visible light.

The preparation of the samples included an additional step of chemical etching using etching solution prepared by 120 ml distilled water, 15 ml HCl, 15 g $Na_2S_2O_5$,10 g $K_2S_2O_5$ and 2 g NH_4-HF in order for various features of the metallic microstructure to become visible.

Electron Back-scatter Diffraction (EBSD)

Crystallographic texture measurements were primarily performed by the Helios G4 SEM microscope equipped with EDAX EBSD detector. Measurements were performed using 25 kV accelerating voltage and 13 nA beam current.

The preparation of the samples for the EBSD measurements included an additional final chemical polishing step using a solution of Struers OP-S silica suspension with grain size 0.25 μm diluted with 30% H_2O_2. Before as well as after the chemical polishing step, the samples which were measured in their as-fabricated condition, were immersed in a boiling water bath for approximately five minutes, which allowed them to transformed to their austenitic phase for better measurement quality. For the samples which were measured by EBSD after they had undergone mechanical testing, the boiling water immersion step was omitted.

Data analysis of the EBSD measurements was performed using EDAX OIM Analysis 8 software. Appropriate cleanup parameters were implemented for producing the final texture maps presented throughout this report.

Scanning Electron Microscopy - Energy Dispersive X-ray Spectroscopy (SEM-EDS)

The SEM-EDS technique was employed for obtaining information on the Ni and Ti content of the as-fabricated samples, as it was important to specify the exact concentration of the alloy after the possible changes it underwent during L-PBF fabrication, such as Ni evaporation. Measurements were performed using the JEOL 6500F Field Emission Scanning Electron Microscope equipped with the UltraDry EDS detector by Thermo Fisher Scientific, USA. Measurements were taken using accelerating voltage of 20 kV and 500x magnification. Three areas were measured per sample and the final result was the average of the three measurements. Appendix B provides the full details of the measurements completed for each sample.

Sample preparation included the steps described in the section dedicated to the EBSD technique, i.e. chemical polishing with OP-S silica suspension and hot water baths. The samples used for the measurements had previously undergone mechanical testing.

Data were analysed statistically in order for the mean atomic percentage (at.%) concentration, μ, and standard deviation, σ of the three measurements for each sample to be determined according to the equations:

$$\mu = \frac{\mathrm{Area}_1 + \mathrm{Area}_2 + \mathrm{Area}_3}{3} \tag{3.1}$$

$$\sigma = \sqrt{\frac{\sum \left(\mathrm{Area}_i - \mu\right)^2}{3}} \tag{3.2}$$

3.2.2 Transformation & Phases

X-Ray Diffraction (XRD)

X-Ray Diffraction was implemented for phase identification and preliminary texture investigation in as-fabricated samples as well as the NiTi powder used for the L-PBF fabrication. The measurements were carried out by a Bruker D8 Discover diffractometer fitted with an Incoatec Microfocus Source (IμS). The measurements were performed with 50 kV and 1000 μA current using Cu Kα radiation. Montel Optics ELM32 with parallel beam, UBC collimator 1 mm were employed together with a UMC 1516 sample stage, an Eiger 2 500k detector and LL=7200. Laser video was used for adjusting the sample positions and heights. A $\theta - 2\theta$ scan in the range $25^\circ - 85^\circ$ with stepsize equal to 0.05° and time per step equal to 1 second was used. Both 1D and 2D XRD patterns were obtained with the measurements. The data were evaluated using the software Bruker DiffracSuite.EVA vs 6.1.

The as-fabricated samples were measured along their build direction as this would allow for a larger area to be exposed to the beam and hence provide better statistics for the measurement.

The polishing of the solid samples was identical to the one described for the EBSD technique.

Differential Scanning Calorimetry (DSC)

In order for the phase transformation between the austenite and the martensite phases of the alloy to be examined so that crucial information regarding the functional behaviour of the material to be obtained Differential Scanning Calorimetry (DSC) measurements were carried out using a TA Instruments mDSC250 calorimeter. The measurements were conducted in a cyclic manner, whereby as-fabricated samples were subjected to 16 heating and cooling cycles between -70.0 °C and +150.0 °C. Figure 3.6 presents the temperature versus time profile of the measurements. The number of cycles was chosen so that the behaviour of the alloy would be stabilised by the time the last heating and cooling cycle would be completed and safe conclusions about the functional behaviour could therefore be drawn.

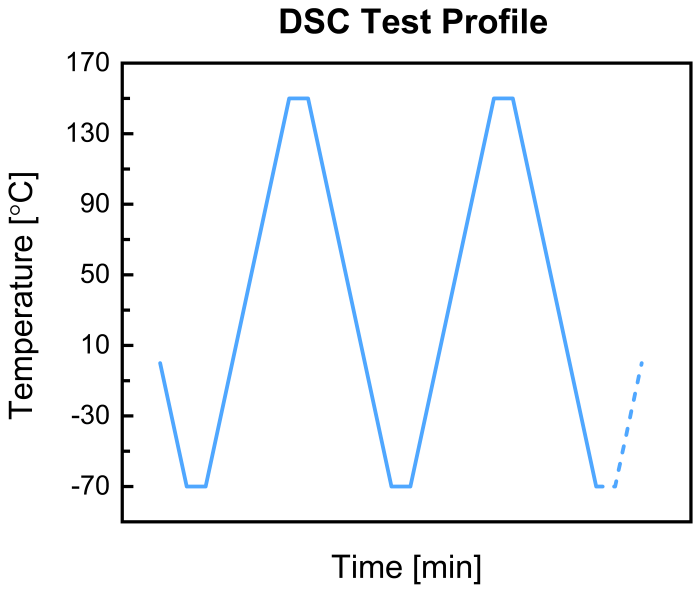


Figure 3.5: Time [min] - Temperature [°C] profile for the DSC measurements. For simplicity, only the first two cycles are shown.

Samples for this type of measurements were obtained by cutting a thin slice (1 -2 mm) as close as possible to the middle of the length of the cuboid, as described in Figure 3.4 c). The slice was ground using up to 1200 grit size SiC abrasive paper in order to remove any potential residue from the surface which could affect the measurement. The specimens were then weighed and sealed inside TA Instruments hermetic cups and lids suitable for use with the measuring equipment.

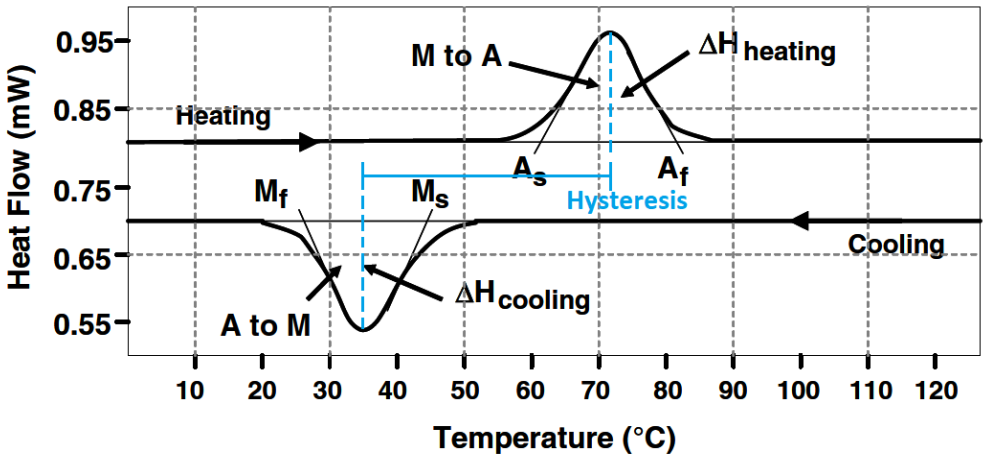


Figure 3.6: Typical DSC curve, Heat Flow [mW] versus temperature [°C] for a generic SMA. The four transformation temperatures are noted on the diagram together with the latent heat of transformation during both cooling and heating. The thermal hysteresis is also shown in blue, here taken as the difference between the peaks of the heat fluxes occurring during the two phase transformations. Adapted from [1].

Data analysis was performed on Origin 2022 graphing and data analysis software by OriginLab using the method of intersecting lines attached to the part of the baseline before and after the peak and the points at the maximum rate of change of the transformation peaks. Figure 3.6 depicts a typical DSC

curve for a generic SMA, where the various characteristic quantities obtained by the measurement can be visualised, such as the thermal hysteresis and the latent heat of the transformations. The intersecting lines for temperature measurements are also shown.

For ensuring the highest quality of the measurement, the first cycle was excluded for all samples, and instead, the transformation temperatures were measured by the method described above for the second and the 16^{th} cycles, of course wherever that was possible. A note of importance here is that in various samples the transformation seemed to include more that one peaks, in which case, for measurement of the onset and completion temperatures the curvature of the dominant peak was used.

3.2.3 Functional Properties

Mechanical Testing - Cyclic Axial Compression Tests

The mechanical and functional behaviour of the NiTi samples fabricated for this project was investigated by means of cyclic mechanical tests where compressive loading was applied along the build direction of the $8 \times 4 \times 4$ mm cuboid samples. Two different temperature conditions were chosen, both above the A_f temperature established by the DSC measurements, in order to allow for the superelastic response of the material to be evaluated. The first group of samples was tested at the so-called Low Temperature condition, labelled thereafter as the LT group, with test temperatures ranging from room temperature (RT) to 52°C. The other group was tested at conditions of temperature equal to 64°C, well above the A_f of all samples, and was termed as the High Temperature group, mentioned thereafter as the HT group. Table 3.3 contains a detailed list of the temperature conditions for all samples tested. At least two specimens per sample were tested for each group to ensure reproducibility and reliability of the results. One specimen from each sample was chosen for detailed presentation of the results in Chapter 4, whereas the results of the other specimens tested are given in Appendix C.

Table 3.3: Temperature conditions for the cyclic compression mechanical tests along the build direction

Sample	LT group, [°C]	HT group, [°C]
0	50	64
90	43	64
30	45	64
67	45	64
island_67	45	64
HLP_67	RT	no test

The testing procedure included 16 cycles of axial compression loading until 6% nominal engineering strain, with strain rate 1×10^{-3} s^{-1} and unloading until zero force levels, performed in the 25 kN load cell MTS 858 Table Top System using hydraulic grips. A strain-time profile of the test procedure can be found in Figure 3.7. Heating was achieved by an induction coil paired with three air nozzles for optimal temperature conditions and control. The temperature was controlled by the Hüttinger Elektronik TruHeat HF 3005 using a type K thermocouple attached to the sample in at least sixteen points (four points per wire per sample face), whereas the air supply was uninterrupted. A ceramic rod extensometer with gauge length equal to 10 mm was employed for accurate strain measurements, attached either directly onto the samples or to specially designed sample holders manufactured by 3D printing using PEEK. The set-up can be viewed in Figure 3.9.

In addition, for the purpose of investigating the possible effect that the direction of the compressive load application may have on the superelastic response of the material, a third group of samples was subjected to the same test procedure as the one described above, this time applying the compressive loads at a angle 90° to the build direction of the sample. This third group of tests, thereafter referred

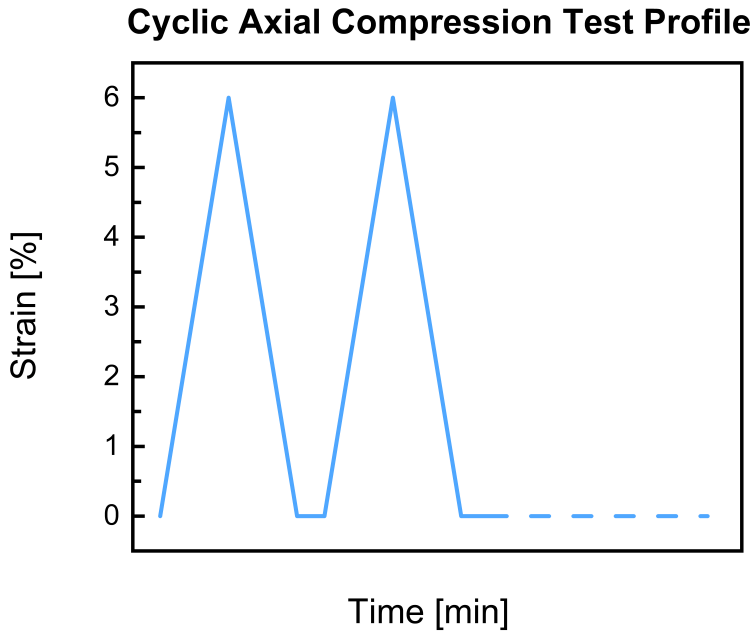


Figure 3.7: Time [min] versus strain [%] profile of the axial compression tests. For simplicity, only the first two cycles are shown.

to as Rot group and using the suffix “R” to the sample name, was performed at room temperature conditions, see Table 3.4. For this type of tests, the cuboid samples were cut in half their lengths, creating cubic samples with side size approximately equal to 4 mm. For ensuring the good attachment of the thermocouple wires on these samples, arc welding attachments were inserted on three side faces.

Table 3.4: Rotated (Rot) group samples for the cyclic mechanical tests

Sample	Rot group, [°C]
0-R	RT
90-R	RT
30-R	no test
67-R	RT
island_67-R	RT
HLP_67-R	RT

Data were acquired using the MTS Station Manager software and processed using Origin 2022 graphing and data analysis software as well as Excel. The method of parallel lines was employed for obtaining the required values for determination of the various segments of the loading and unloading portions of the stress-strain curves.

The test procedure itself as well as the material’s response to the compressive deformation it is subjected to can be understood with the aid of Figure 3.10. When NiTi alloys are axially loaded in compression while being at temperatures above their A_s temperature, three stages of deformation can be identified in the resulting stress versus strain plots. Stage I involves the elastic response of the austenite phase to the compression loading, with elastic modulus equal to E_A, until a critical stress value ($\sigma_{cr}^{A \rightarrow M}$) is reached and the phase transformation is initiated, entering Stage II.



Figure 3.8: The cuboid sample prepared for the mechanical test. The K type thermocouple is attached on two consecutive sample sides using arc welding in several spots along the wire lengths.

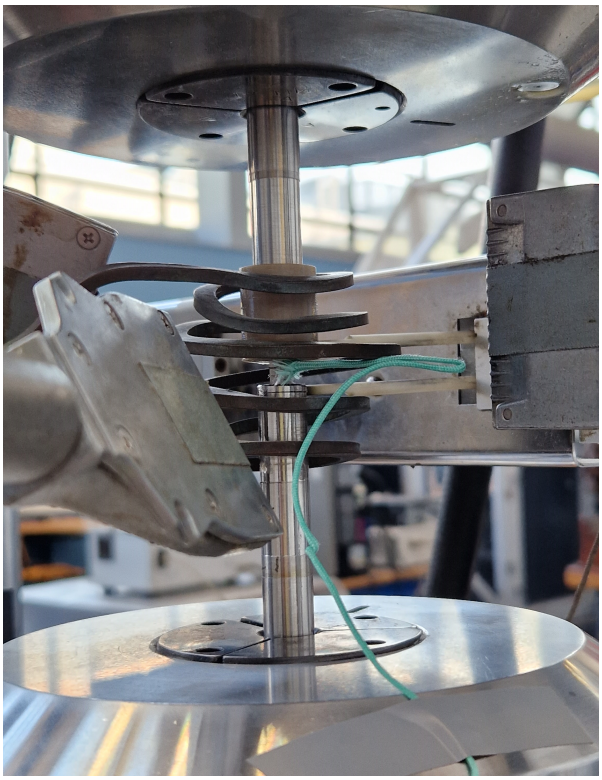


Figure 3.9: Close-up of the mechanical test set-up showing the induction coil, the air nozzles, the sample holder, the extensometer and the sample.

At the initial part of Stage II, where strain values are relatively small, the phase transformation takes place, indicated by a plateau. This near-zero slope of the curve depends on the crystallographic texture of the metal in the case of polycrystalline samples [25]. As the compression proceeds, the martensite that forms is being elastically deformed while the austenite experiences slip if stress levels reach the critical value, σ_{cr}^{A} which depends once again on the crystal orientation as well as potential aging treatments [25]. In the case of crystal orientations unfavourable for slip, the austenite strength levels are higher. When the end of the ability of the martensite phase to be elastically deformed is reached (i.e. the critical stress for martensite yield has been reached, σ_{cr}^{M}), the deformation has entered Stage III. At

this stage, a downward curvature can be spotted on the plot, and in terms of the material deformation, the martensite continues in slip deformation until either fracture or heavy deformation occurs.

Provided that the sample has not been deformed to the point of failure, unloading begins with the elastic deformation of the martensite, characterised by the elastic modulus E_m. A change of the slope indicates the initiation of the reverse phase transformation, highlighting the superelastic behaviour of the material. The residual strain left in the crystals after the stress levels have reached zero can be recovered upon heating to a temperature above the A_f temperature. However, usually a certain amount of strain will remain in the material, even after the heating, and cannot be recovered, accumulating as plastic strain in the lattice. The amount of that plastic strain depends on the value of the maximum strain the material experienced during the loading part of the cycle. A note of special significance for the compression tests performed in this project is the fact that cycling the NiTi samples during Stage II of their deformation, gives rise to hardening which is considered to be an indication of dislocation-related activity within the material [25].

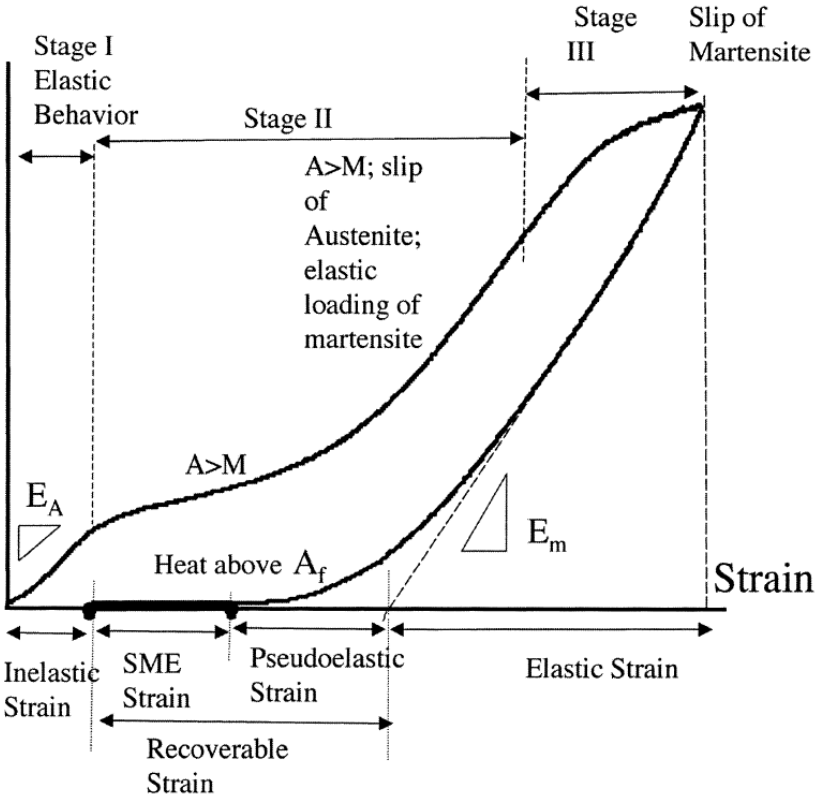


Figure 3.10: Stress versus strain diagram showing the deformation behaviour of single crystal NiTi subjected to compression at temperatures above the A_f. Strain definitions are also provided. Reproduced by [25].

Thermo-Mechanical Analysis (TMA)

Thermo-Mechanical Analysis (TMA) was implemented in order to achieve the maximum possible strain recovery after the cyclic mechanical compression. This way, the nature of the residual strain remaining in the metal after the stabilisation of its superelastic response would be possible to be investigated, together with the alloy's ability for showcasing the TWSME.

The tests were performed using a Perkin Elmer TMA 4000 thermomechanical analyser equipped with an expansion probe. The strain was measured along the build direction of the samples after the mechanical test was completed to ensure compatibility between the two methods and their results. For comparison, a set of as-fabricated samples was also measured in the same conditions. Figure 3.11 presents the temperature versus time profile of the tests performed. As can be inferred by the profile, a

total of two full heating and cooling cycles were imposed to each sample during the measurement. The as-fabricated samples tested with the TMA equipment were ground using SiC sanding papers (grit sizes 800, 1000, 1200) and then ultrasonically cleaned in isopropanol. The samples after the mechanical test were prepared by ultrasonic bathing in isopropanol.

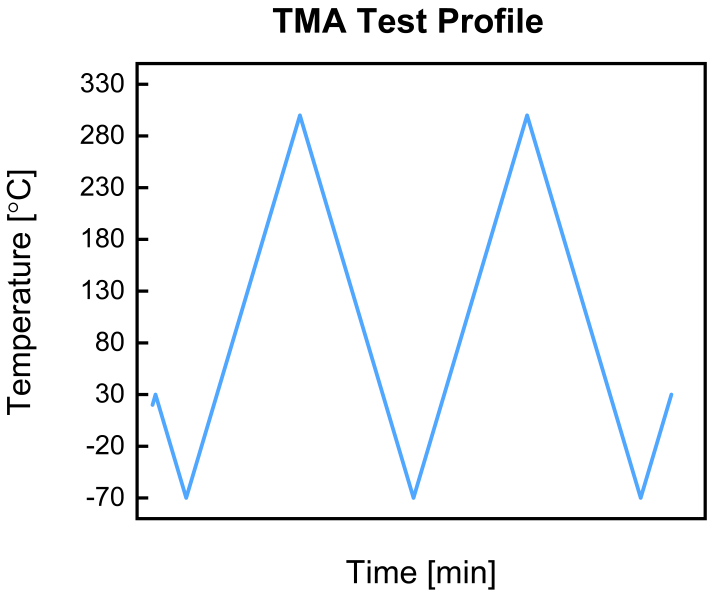


Figure 3.11: Time [min] versus temperature [°C] profile of the TMA test procedure.

Data analysis was performed on Origin 2022 graphing and data analysis software by OriginLab. Data manipulation tools included in the software were utilised for the removal of the contributions of thermal expansion effects to the strain measured during the tests. Thermal expansion was removed prior to performing any calculations concerning the strains given in Chapter 4, Section 4.4. However, it must be stressed that the $\sigma - \varepsilon - T$ graphs included in the same Section do include the thermal expansion effects, for the sake of completeness.

4

Results & Discussion

This Chapter presents the results of the experimental research conducted during this thesis. In-depth discussion of the findings and critical assessment of the outcomes of the research are also included.

4.1 Effect of Scanning Strategy on Crystallographic Texture & Functional Behaviour

4.1.1 Microstructure & Phase Transformation Features

The initial stages of analysis of the L-PBF fabricated samples included analysis of their chemical composition by means of the SEM-EDS technique. The results are presented in Figure 4.1 a) in graphical format and in Table 4.1 the exact values of the Ni and Ti contents per sample can be viewed. The influence of the scanning strategy on the alloy composition can be observed, as samples 90, 67 and island_67 are the three samples showing compositions closest to the powder composition used for the AM production of the specimens (51.0 at.% Ni (90), 50.8 at.% Ni (67) and 50.8 at.% Ni (island_67) versus 51.4 at.% Ni for the powder). Complete discussion of the EDS results is given at the end of this Section, where the results can be evaluated together with the phase transformation information provided by the DSC measurements.

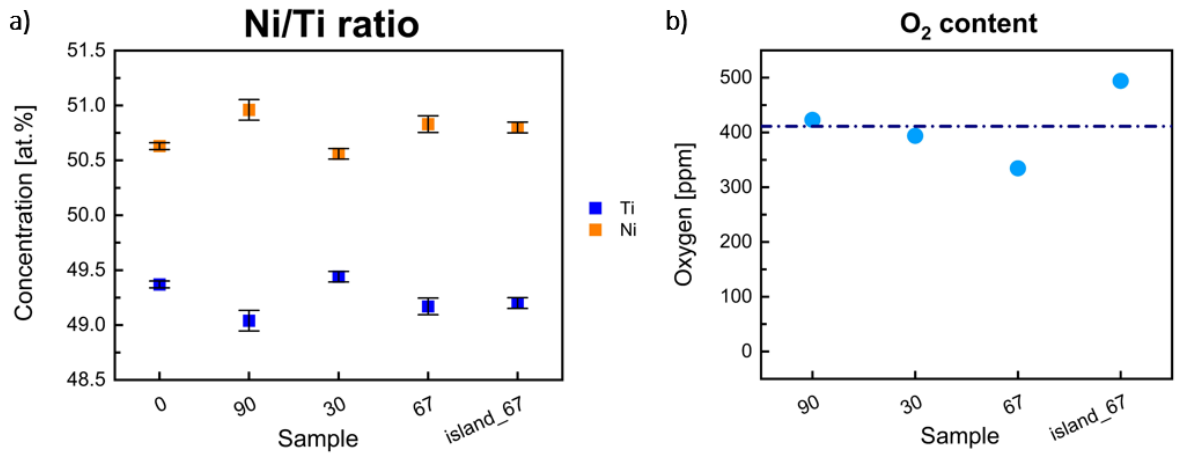


Figure 4.1: ***a)*** Chemical composition of the 0, 90, 30, 67 and island_67 samples after the L-PBF fabrication measured by EDS. ***b)*** Oxygen content of the 0, 90, 30, 67 and island_67 samples measured after the L-PBF fabrication.

Oxygen levels were measured for select samples, namely the 90, 30, 67 and island_67. The results can be seen in Figure 4.1b), where the individual measurements are plotted together with the average Oxygen content value, shown as a blue intermittent line. As expected, the scanning strategy's influence

to the Oxygen contamination of the alloy during L-PBF is marginal. The island_67 sample shows the largest deviation from the rest, which can be explained by taking into consideration the fact that the scanning of the powder in island patterns, characterised by short scanning vectors, has the potential to leave the entire layer at a higher overall temperature before the next layer is spread over it and scanned [47] [36]. Allowing the metal to stay at high temperatures for longer can lead to an increase in its absorption of contaminants, in this case Oxygen, resulting in this slightly increased Oxygen content of the island_67 sample.

Table 4.1: Chemical composition of the fabricated 0, 90, 30, 67 and island_67 samples

Sample	Average Ti content, [at.%]	Standard deviation of Ti content	Average Ni content, [at.%]	Standard deviation of Ni content
0	49.4	0.0	50.6	0.0
90	49.0	0.1	51.0	0.1
30	49.4	0.0	50.6	0.0
67	49.2	0.1	50.8	0.1
island_67	49.2	0.0	50.8	0.0

The microstructure of the fabricated samples was initially inspected by means of OM under conditions of both visible and polarised light, whereby micrographs of selected areas of specific samples were obtained. Micrographs obtained under visible light conditions can be seen in Figure 4.2 for the 0, 30 and 67 samples. It can be readily seen on those micrographs that overall the L-PBF fabrication method was successful in that it produced parts without any major defects, such as areas affected by lack of fusion or balling effects. Porosity however does occur, with the 0 sample showing pores of considerable size and the 67 sample showing fewer and smaller pores, a result supported by literature, whereby it is stated that rotation between layers during the AM fabrication ensures remelting of the metal, characterised by heat flow towards different directions which can be beneficial for reducing the amount of pores arising and producing an overall more uniform and well-bonded structure [58] [36].

Aside from observations regarding the possible defects and the overall result of the fabrication method, areas corresponding to the two different phases of the NiTi alloy can also be distinguished in the micrographs of Figure 4.2. Areas which appear to have a needle-like structure are comprised of martensite crystals. A note shall be added here, as an early disclaimer for the XRD results discussed next, that the OM images of the samples were obtained after their mechanical training, therefore the presence of martensite in the microstructure is fully justified and, in some degree, expected (see also the discussion in Section 4.4)

The effect of the scanning strategy can be assessed by polarised light OM images as under these conditions the scanning tracks can be revealed, see for example Figure 4.3 where the XZ and XY views of the 0 sample are shown. The scanning tracks are clearly defined along with the resulting crystal grains, allowing for a first inspection of the grain morphology obtained by the fabrication method. The image obtained is characteristic of the 0° rotation scanning strategy employed for the fabrication of this particular sample. The scanning tracks appear parallel to one another at both the XZ and the XY faces of the sample, with grains elongated and extending beyond one powder layer, however such elongation is not constant on neither of the two faces. Notably, for the case of the XY view, the effect of the various components comprising the scanning strategy on the grain morphology becomes even clearer, as grains at the end of the tracks (i.e. at the edges of the sample) are smaller in size, indicating that were created by more rapidly proceeding solidification processes compared to the longer grains seen at the middle area of the XY face. This effect is a result of the inertial effects of the laser beam head, which, as it moves along the surface of the print bed, its acceleration changes as it reaches the ends of the scanning tracks, leaving a "*mark*" on the microstructure in the form of smaller grains arising from the uneven energy distribution caused by the motion [36]

XRD measurements confirmed the presence of only Ni and Ti peaks in all five samples manufactured.

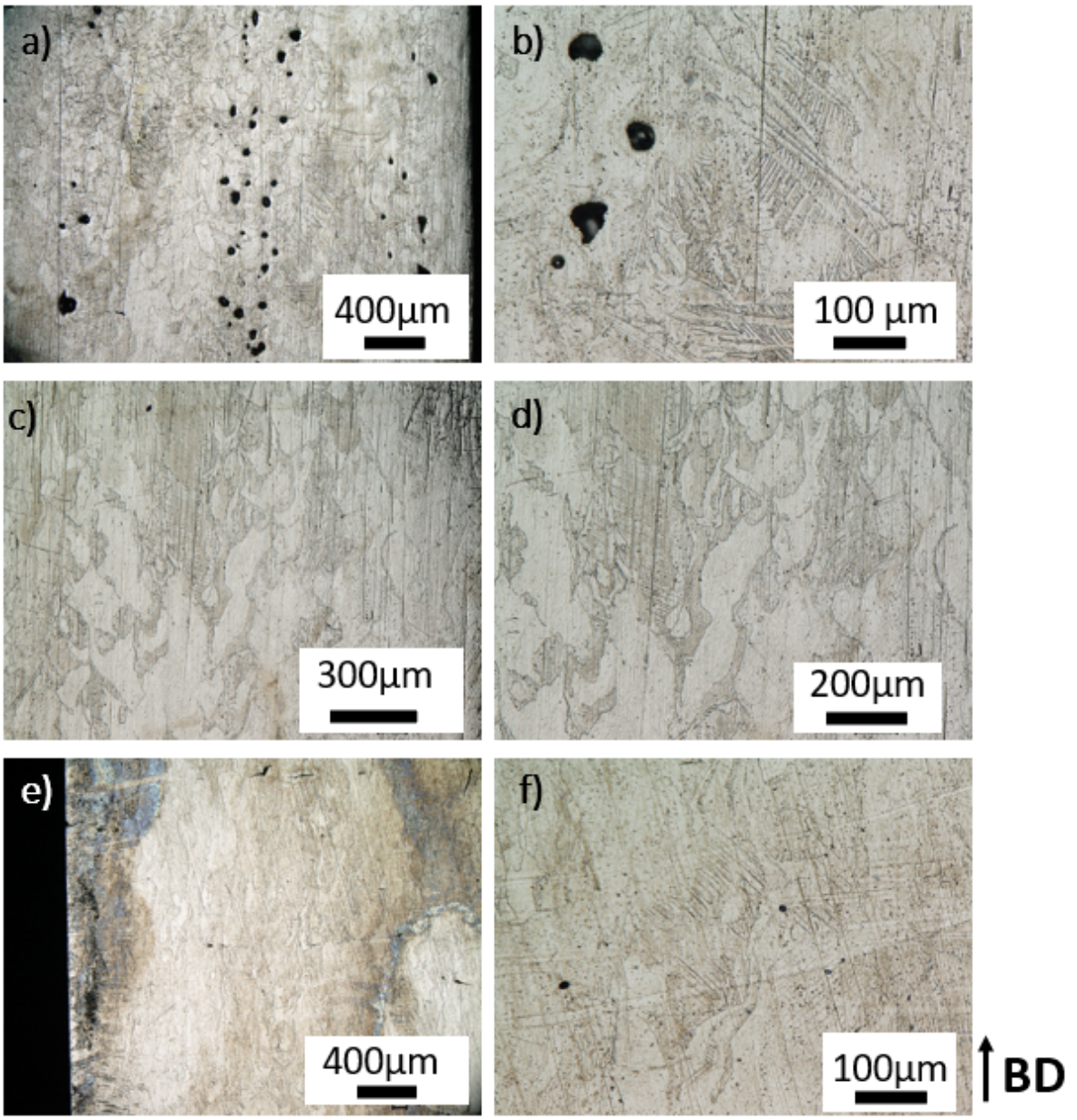


Figure 4.2: Optical micrographs obtained under visible light conditions of the samples 0 (***a***), 30 (***b***) and 67 (***c***). All images were taken along the BD of the samples.

Moreover, no additional or undesired phases were detected, such as secondary phases or precipitates. This is particularly important for the island_67 sample which showed the highest levels of Oxygen contents, as it means that even though the sample would theoretically be in a compositional state which favours the formation of precipitates, such an event did not actually happen. The dominant phase detected in all samples was austenite with the expected cubic lattice (BCC_B2), whereas significantly smaller fractions of the monoclinic martensite $B19'$ phase were found to be present, indicating the strong presence of the austenite phase in the Ni-rich NiTi alloy used for the fabrication of the samples. This also confirms the anticipated result, whereby Ni-rich NiTi alloys tend to comprise of the austenite phase at ambient temperature conditions, a result which can be confirmed by the DSC plots which will be discussed at the following parts of this Section. The diffraction peaks corresponding to the martensite phase may arise due to residual stresses introduced in the lattice by the L-PBF manufacturing. As argued by Dadbakhsh et al., stresses of 350-400 MPa are able to force austenite regions of the metal to transform into *Stress-Induced Martensite*, (SIM) and this level of stresses is below the typical residual

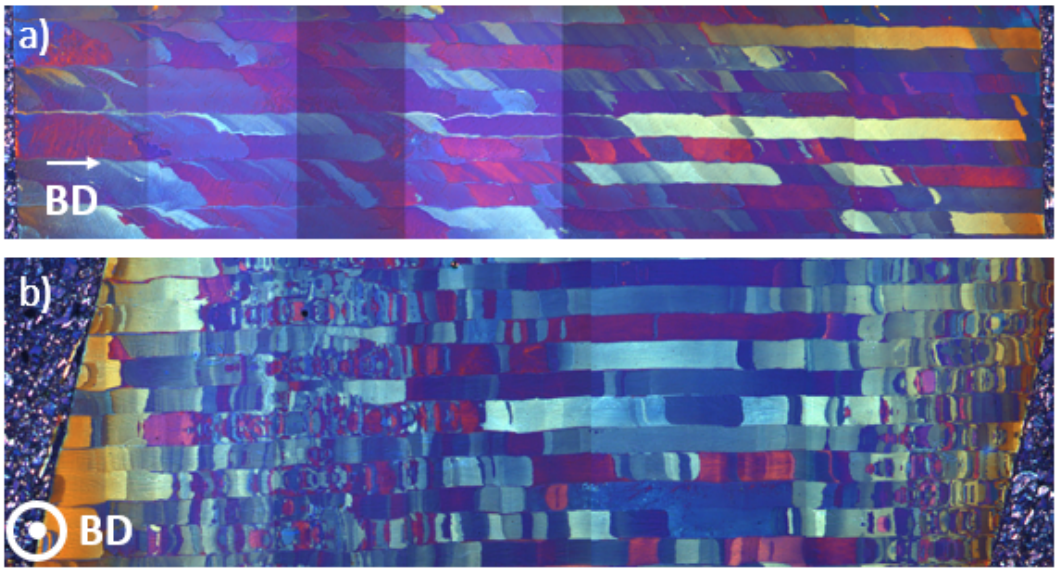


Figure 4.3: OM images of the 0 sample obtained under polarised light conditions. ***a)*** Micrograph shows the xz plane of the sample (i.e. along the BD), ***b)*** xy view (i.e. perpendicular to the BD).

stress levels considered to arise during L-PBF fabrication [50]. Therefore, although the NiTi samples should be completely in an austenitic phase, peaks belonging to the martensitic phase is also possible to be recorded by XRD measurements. Figure 4.4 gathers the one dimensional (1D) XRD spectra obtained from the measurements of all samples.

All printed samples showcase a deviation of the measured intensities from the expected values as these can be determined by comparison to the one dimensional (1D) XRD spectrum belonging to the NiTi powder, see Figure 4.4. It is notable that all five sample show an increase in the intensity of the peaks corresponding to the (110) diffraction planes, whereas samples 30 and 67 also exhibit more intense peaks for the (200) diffraction planes always compared to the powder spectrum. This deviation is an indication of the existence of crystallographic texture in the printed samples, which can also be better visualised with the aid of the two dimensional (2D) spectra by means of the intensity variation along the diffraction rings, see Figure 4.5. In the case of the powder, no crystallographic texture can be detected as, by definition, cannot exist in such sample. The diffraction rings do not appear continuous, but rather consist of a number of bright points, a signature mark of powder diffraction spectra. The large size of those bright spots indicates the large size of the crystallites comprising the NiTi powder used in the L-PBF fabrication.

In order for the crystallographic texture to be further examined and analysed, SEM-EBSD measurements were performed on all samples immediately after their fabrication. This technique allowed for detailed observations of both the texture as well as the microstructure morphology to be made.

Samples fabricated using the 0° rotation scanning strategy, as also observed by the polarised light OM technique, Figure 4.3, consist of grains strictly contained within the boundaries of each scanning track. Due to the lack of rotation of the scanning between consecutive layers of the NiTi powder during the L-PBF fabrication, the highest thermal gradient present in the volume of material being scanned by the laser beam follows an upward direction along the BD and parallel to the build platform is directed in the positive and negative SD. Hence, strongly uneven temperature gradient, G, develops in both the z and the y axes, and since the grains tend to grow along the largest local thermal gradient, a microstructure which appears like the one in Figure 4.3 and 4.6 a) and b) will develop by the 0° rotation scanning strategy [27]. High degree of anisotropy is evident in the microstructure of the 0 sample in both the xy and the xz planes, see Figure 4.6 a) and b).

A closer look at the xz Inverse Pole Figure (IPF) map given in Figure 4.6 a), reveals that the crystals do grow through multiple layers of powder, attaining a columnar shape, however, they are far from the desired situation, whereby they can occupy the entire or at least very large portions of the sample

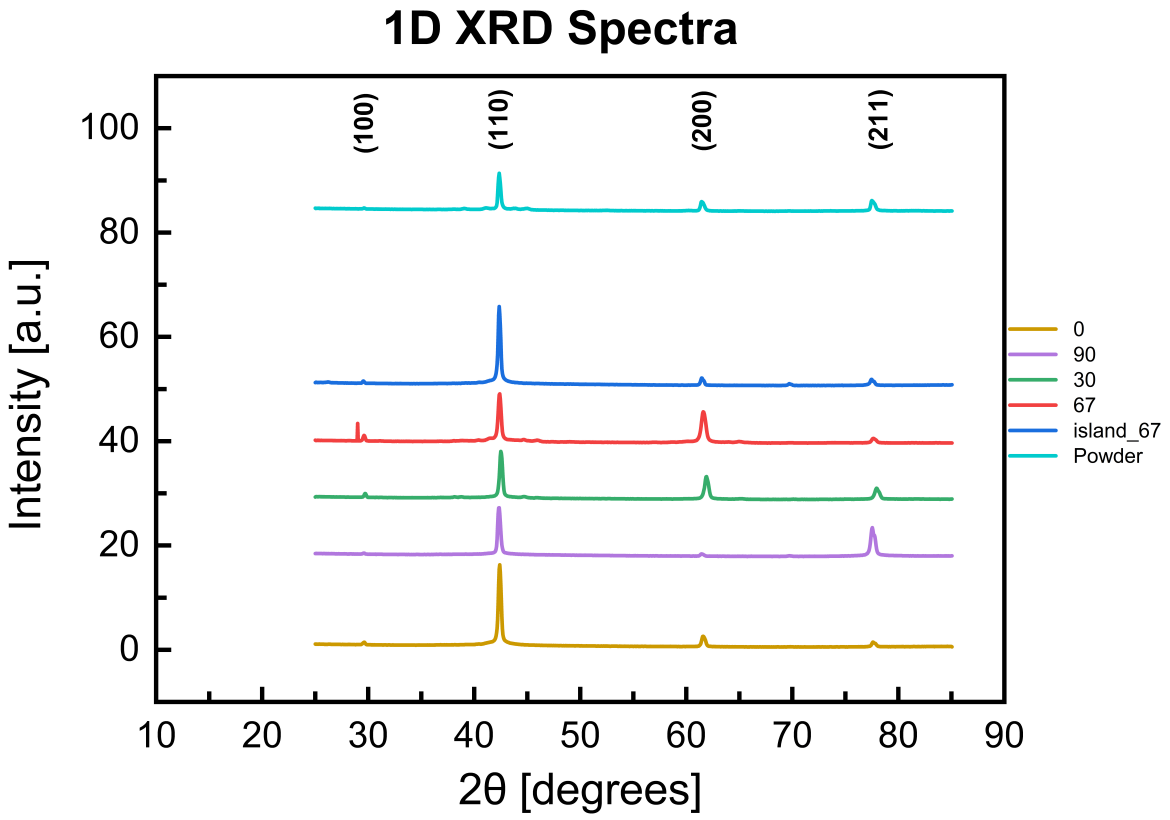


Figure 4.4: 1D XRD spectra for the 0, 90, 30, 67 and island_67 samples. Additionally, the spectrum of the NiTi powder used for the L-PBF fabrication of the samples is also included for reference. The diffraction planes at 2θ values equal to 29.9°, 42.8°, 62.1° and 78.4° are also marked.

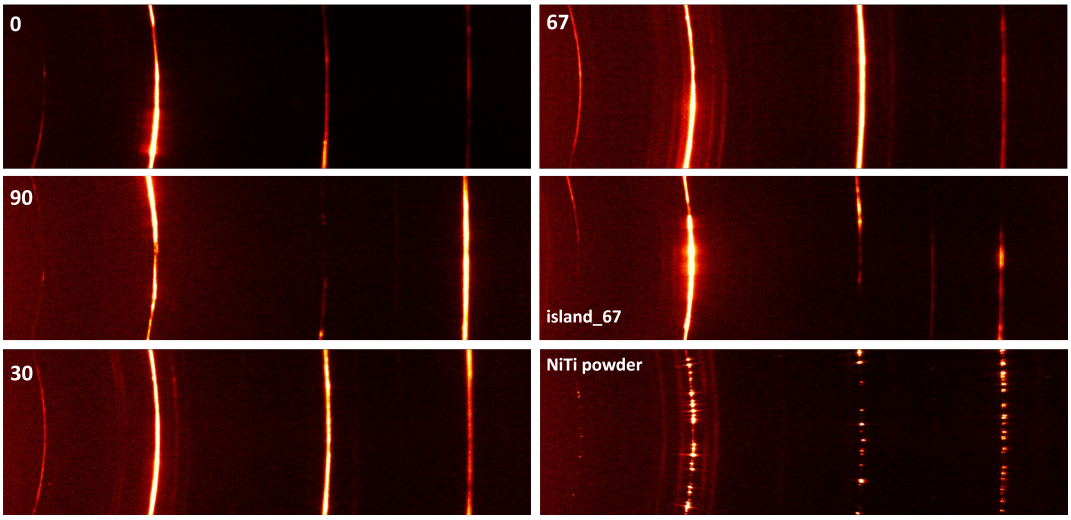


Figure 4.5: 2D XRD spectra for the 0, 90, 30, 67 and island_67 samples showing the diffraction rings. The rings correspond to the diffraction angles in which peaks are measured in the 1D spectra. The spectrum of the NiTi powder utilised for the L-PBF fabrication of the samples is also included. In this case, rings appear in a discontinuous fashion, due to the fact that the powder consists of numerous crystallites.

height. As far as the morphology of the grains seen on the xy plane of the 0 sample, see Figure 4.6 b), the anticipated grain appearance is again found with grains following the direction of the scanning tracks, staying within the boundaries, as they solidify following the highest thermal gradient which travels together with the laser beam on the scanning tracks.

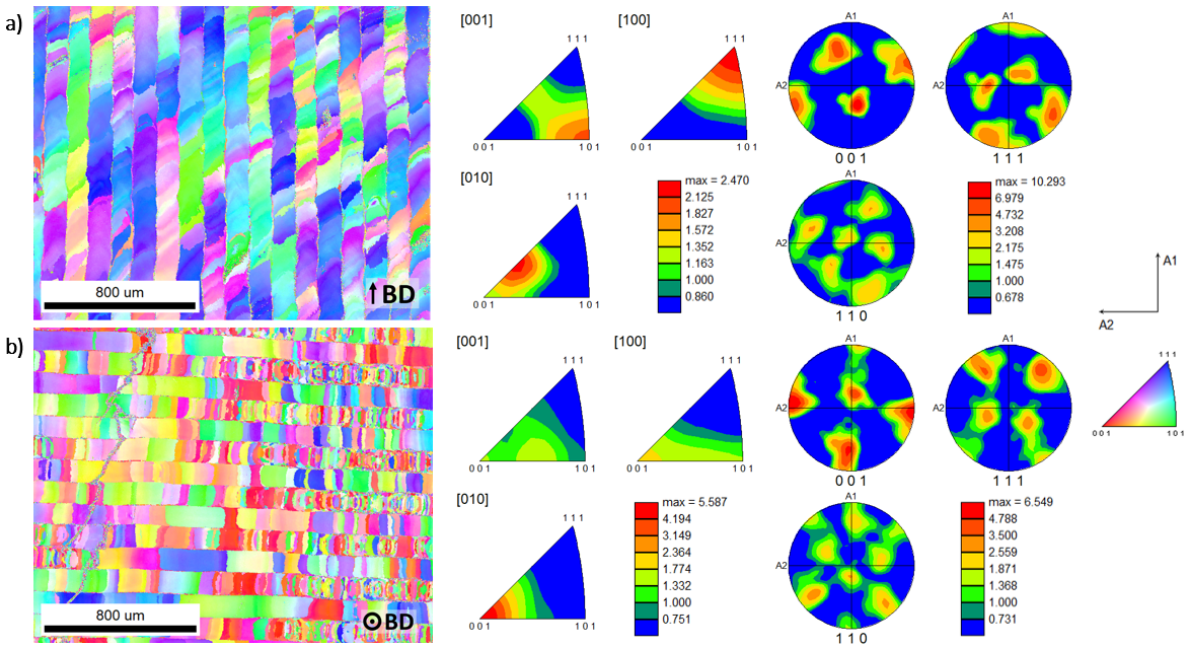


Figure 4.6: EBSD map of the xz plane, ***a)***, and the xy plane, ***b)***, for sample 0. The associated Inverse Pole figures and the pole figures are also included.

With regards to the crystallographic texture seen in this particular sample, a few notes can be made. Firstly, the texture along the BD is focused on the $\langle 111 \rangle$ orientation, hence, is different from the desired $\langle 001 \rangle$ orientation along the BD for optimal superelastic response. Additionally, the weakness of the texture measured is also of importance, as it indicates that the scanning strategy results in a weak (111) texture along the BD of the samples fabricated. The crystallographic texture developed by this particular scanning strategy appears to be different to the texture obtained by Sun et al. for the same scanning strategy in Ni-25 at.% Mo alloy produced by L-PBF, indicating the significant role that the type of the material plays in the final microstructure obtained by the AM fabrication [43].

The impact of interlayer rotation in the scanning strategy becomes immediately apparent when considering the first of the scanning strategies studied on this project which involves an angular rotation. Most notably the appearance of the microstructure which results from a rotating scanning strategy is drastically different, see Figures 4.7 a) and b) where the EBSD results of the 90 sample are presented. IPF maps along the BD of the sample reveal the tendency of the grains to intertwine and mix, spreading outside of the boundaries of the scanning tracks, as they follow and re-orient themselves along the highest thermal gradient in their neighbourhood dictated by the laser beam motion. Simultaneously, the desired columnar structure is also observed; the crystals tend to grow perpendicularly to the build platform for a considerably larger number of layers compared to the 0 sample, extending in size and approaching closer to the desired morphology.

The overall impression is also improved regarding the xy plane view when comparing the 90 sample to the 0° scanning strategy. Grains are now visibly attaining a shape closer to the ideal “letter S shape”, as the microstructure begins to vaguely resemble a grid. Nevertheless, they do appear to be constrained within the boundaries of a scanning track, yet another characteristic feature of the microstructure obtained by L-PBF with rotational scanning strategies, see also discussion in Chapter 2.

Texture-wise discussion concerning the 90 sample includes the observation that a collective crystal orientation of the $\langle 001 \rangle$ direction arises in both along the BD and the xy plane, a cube texture starts appearing which is closer to the $\langle 001 \rangle$ texture sought after. When compared to the intensity of the 0 sample, in this case the texture is more intense, however, not to the point where it could be considered strong enough to have a significant effect on the thermomechanical response of the material.

The 30 sample is the one produced using the smallest rotation angle between each powder layer and the one with the most number of layers being scanned before the scan pattern repeats again (6

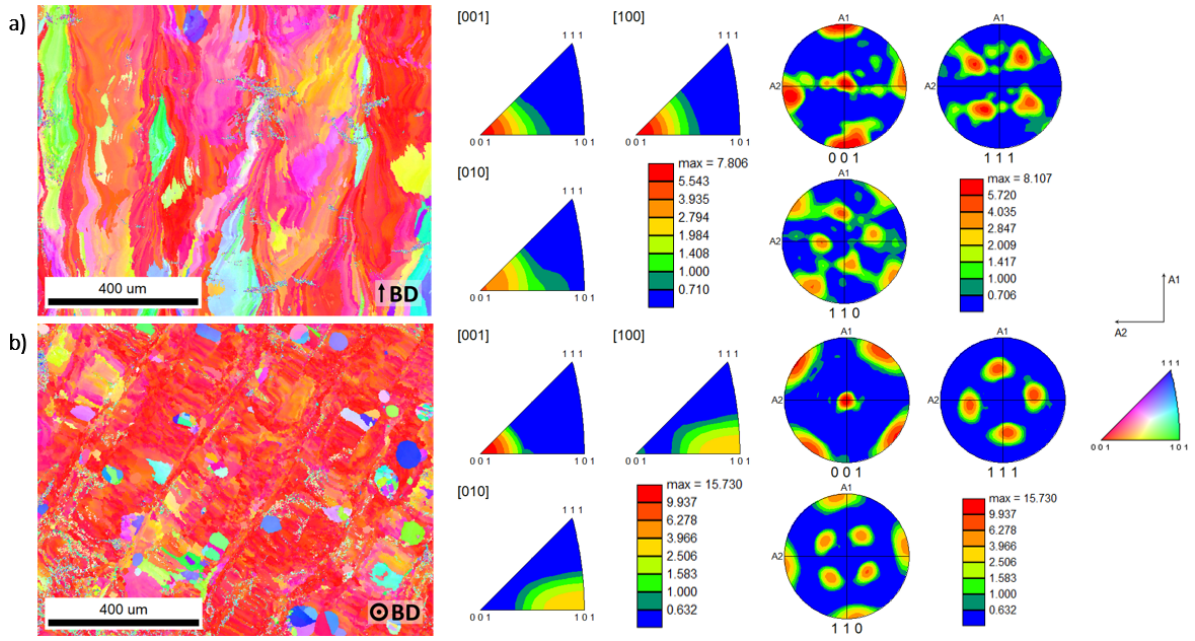


Figure 4.7: EBSD map of the xz plane, ***a)***, and the xy plane, ***b)***, for sample 90. The associated Inverse Pole figures and the pole figures are also included.

layers). Inevitably, the scanning strategy has a clear effect on both the morphology of the resulting microstructure as well as the crystallographic texture arising, refer to Figures 4.8 a) and b). As was the case with the 90 sample, the epitaxial growth of the grains can also be confirmed for this sample. Simultaneously, the grains seem to once again spread outside the borders of the scanning tracks; a feature attributed to the existence of a rotation in the scanning strategy. The major difference in the case of the 30 sample is that this time more grains seem to achieve to obtain a columnar structure which extends for a large number of layers. When the 30 sample grain morphology is compared to this of the 90 sample, it can be seen that almost all grains depicted in the IPF map grow along the BD for the entire height of the image (IPF map in Figure 4.8 a)), a feature which is not so pronounced in the IPF map of the 90 sample (IPF map in Figure 4.7 a)).

It is also a possibility that this exact morphology, namely grains which grow for longer distances along the BD, is connected to and affected by the existence of residual stresses which arise within the build volume during fabrication. In general, the less uniform the distribution of the heat flow throughout the object, the more likely that high residual stresses will develop [36] [45]. In fact, the 30° rotation scanning strategy leads to a more even heat flux distribution during fabrication when compared to the 90° interlayer rotation strategy, due to the smaller angle of rotation. Hence, it is expected that lower residual stresses will arise in the 30 sample compared to the 90, which could potentially have an effect on how grains orient themselves during their solidification. Grains located at the lower parts of the printed cubes will have solidify in a certain way and may exert forces to the newly deposited layers which cause them to adopt other orientations and inclinations along the BD of the sample or to grow for a smaller number of layers. Please note here, that both maps were obtained with the same magnification as stated by the scale bars shown at their bottom left part, so such comparison is feasible. Regarding the morphology of the microstructure on the xy plane of the sample, the expected *S-shaped* grains forming a grid can be now be undeniably observed.

However, even though in terms of grain morphology the 30° scanning strategy appears to be producing a microstructure even closer to the *ideal* one, with regards to the crystallographic texture the situation seems to deteriorate. Along the BD of the sample, the texture is a mixture of $\langle 001 \rangle$ and $\langle 101 \rangle$ orientations, with a particularly large crystal found on the left half of the texture map of Figure 4.8 a) aligning along the $\langle 101 \rangle$ orientation. This situation infers that a rather weak texture is formed along the BD of the 30 sample during the L-PBF manufacturing. In the xy plane of the 30 sample, the crystal orientations seem to be more focused around the $\langle 001 \rangle$ orientation, however, a large scatter can be found in

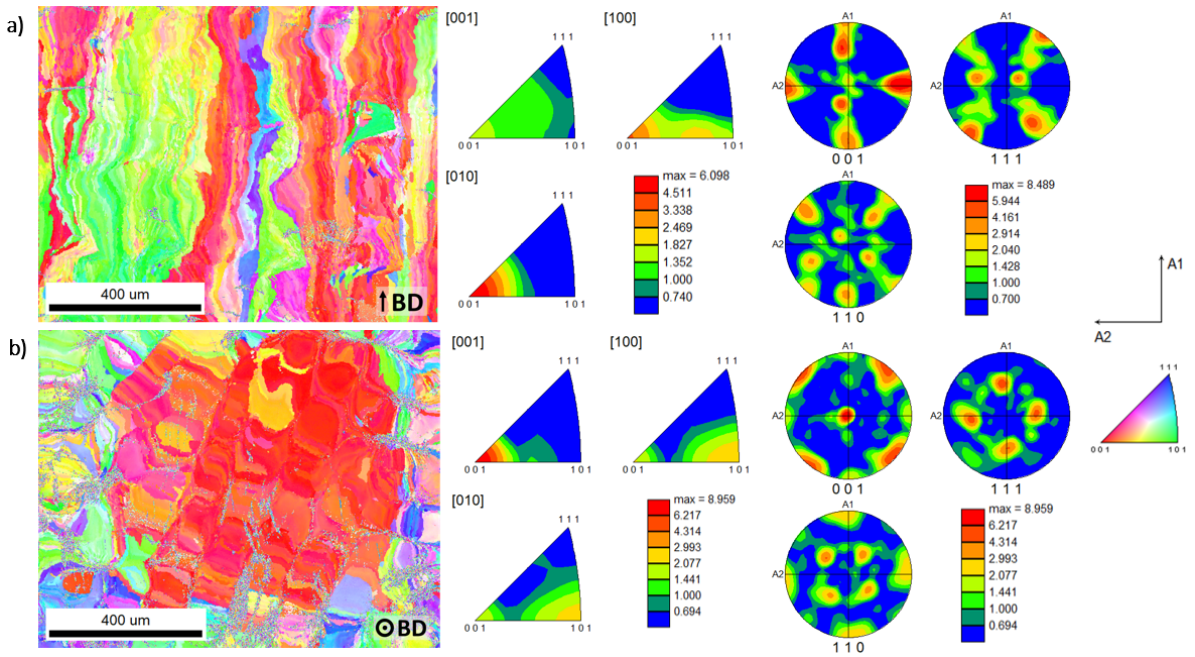


Figure 4.8: EBSD map of the ***a)*** xz view and ***b)*** the xy view of sample 30. The Inverse Pole Figures and the Pole Figures are also included.

the orientations measured. Nevertheless, the cube type of the texture remains unchanged for the 30 sample.

Progress towards the goal in terms of both microstructural morphology as well as crystallographic texture appears to be made in the case of the 67° rotation scanning strategy. Epitaxial grain growth has definitely been achieved during the L-PBF fabrication in the 67 sample, as the IPF map of Figure 4.8 a) confirms. Grains appear to grow almost in parallel to the BD of the sample, forming columnar structures which extend for very large number of layers. At the same time, the xy view IPF map (Figure 4.9 b)) also presents the grain morphology of a successful L-PBF fabrication.

Texture considerations are also more positive for the 67 sample. It can be said that this is the first scanning strategy to produce a really textured material, as the intensity is exceeding 10% for the first time, refer to pole figures and inverse pole figure in Figure 4.9 a). Along the BD of the sample, the sought-after $\langle 001 \rangle$ orientation has been achieved, with only small grains oriented to other directions. Strong texture arises also on the xy plane, Figure 4.9 b), where the texture along the BD does appear slightly disturbed in its alignment, most likely due to misalignment during the cutting steps of sample preparation. Nevertheless, the 67 sample can be safely stated that is the first scanning strategy which shows all the desired characteristics is likely to result in good thermomechanical response. Moreover, a shift in the type of the texture is observed for this scanning strategy, whereby the cube texture seen in the 90 and 30 samples, now shifts to a fibre texture.

Finally, the last scanning strategy considered in this thesis, brings yet another point into the discussion and that is the possible effect that patterns in the scan can create. As can be seen in Figures 4.10 a) and b), indeed combining the 67° rotation with island patterns in the scanning strategy has an effect on both the morphology of the microstructure as well as its spatial orientation. Epitaxial growth of the crystals is again achieved in the island_67 sample, as was the case in the simple 67 specimen, however, it shall be noted that this time the grains do not appear to be aligned as parallel to the BD as in the 67 sample. XY plane IPF map (Figure 4.10 b)) reveals the *S-shaped* structure of the crystals forming a grid of fine grains, although the island patterns cannot be distinguished in this particular micrograph, as the magnification is too high.

Crystallographic texture, on the other hand, is where the island_67 sample surpasses the 67 sample. In both the direction along the BD and perpendicular to it, the texture obtained in even stronger than the texture measured for the 67 sample, again focused on the $\langle 001 \rangle$ crystal orientation, refer to the inverse

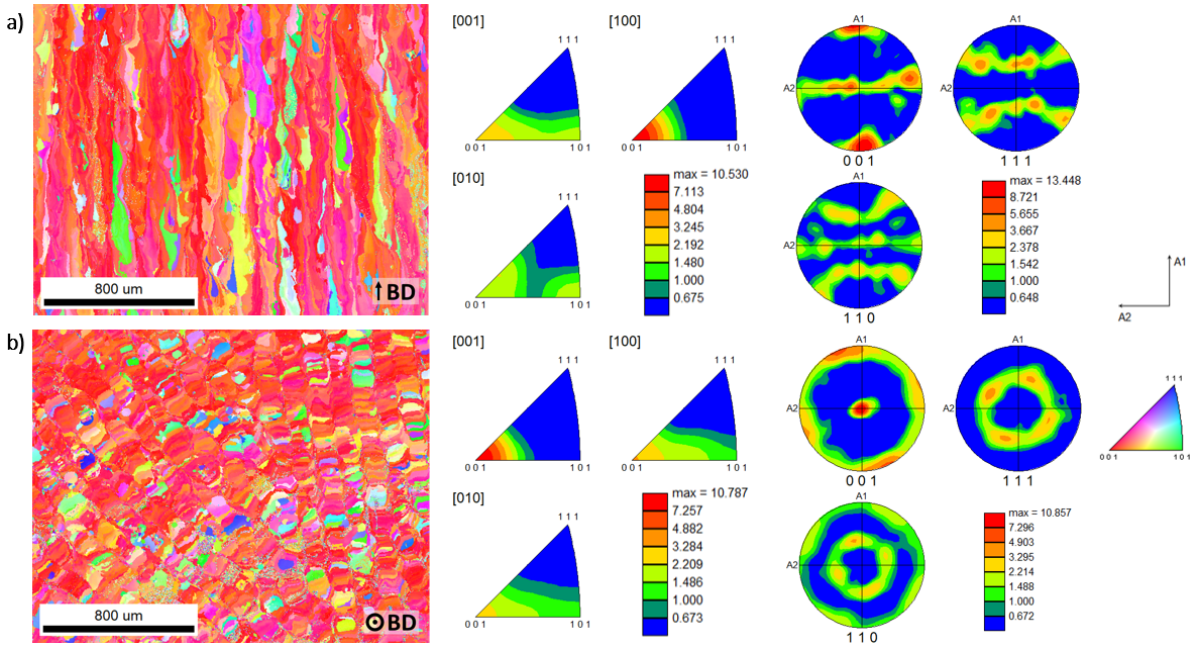


Figure 4.9: EBSD map of the ***a)*** xz view and ***b)*** the xy view of sample 67. The Inverse Pole Figures and the Pole Figures are also included.

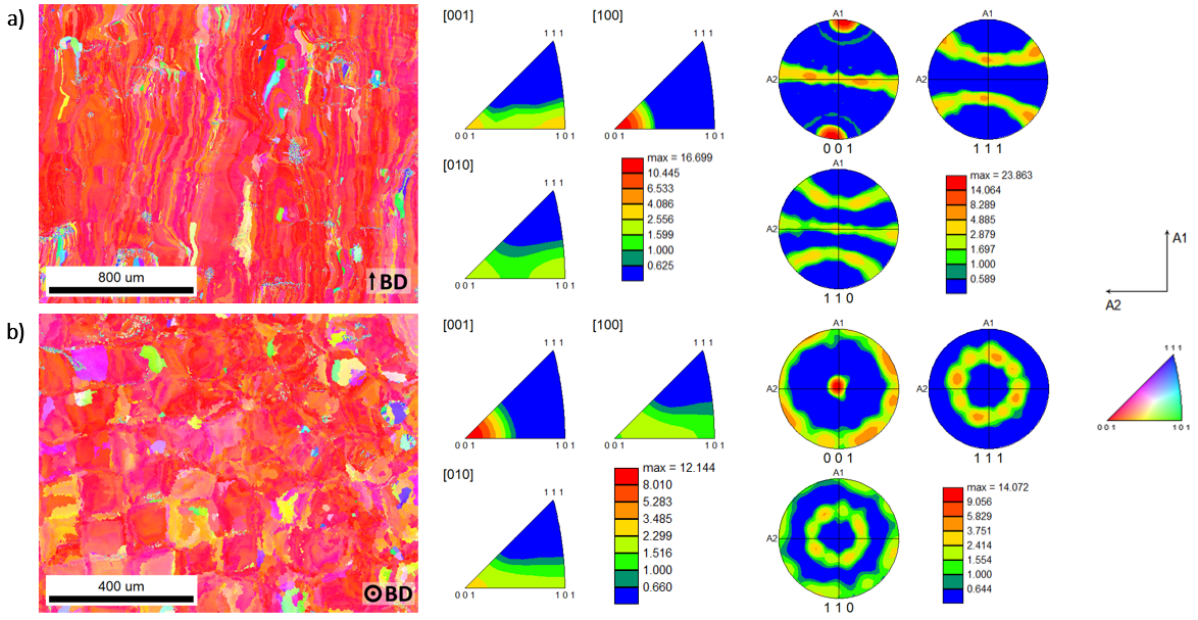


Figure 4.10: EBSD map of the ***a)*** xz view and ***b)*** the xy view of sample island_67. The Inverse Pole Figures and the Pole Figures are also included.

pole figure and the pole figures included in Figures 4.10 a) and b), which show a clear banding of the grains in the three pole figures, more even than the one observed in the corresponding pole figures of the 67 sample. Additionally, grains attaining other orientations, are considerably smaller in size when compared to the 67 sample, which contributes further to the high intensity of the crystallographic texture measured for the island_67 specimens. The fibre character of the texture is preserved in this sample, allowing to conclude that a 67° interlayer rotation of the scanning strategy leads to fibre textures to develop in NiTi alloys fabricated by L-PBF.

Therefore, the effect of the scanning strategy employed during L-PBF fabrication of the NiTi samples

considered has been shown to have an immediate effect on the metallic microstructure observed, both in terms of the grain morphology and the crystallographic texture. As explained in Chapter 2, introducing an interlayer rotation in the scanning strategy results in a constant changing of the directionality of the heat flow as one moves through the height of the sample along the BD. The fact that the crystallographic textures obtained in the samples examined progressively get closer to the "desired" $\langle 001 \rangle$ texture shows that as the rotation angle changes the spatial relations between the direction of the maximum local thermal gradient and the preferred easy growth crystal orientation also change. It is possible that for the case of the 90° and the 67° rotation scanning strategies the direction of the heat flow and the preferred easy growth orientation are very compatible and their effect results in developing a crystallographic texture of the desired type, namely $\langle 001 \rangle$ parallel to the BD. The difference in the intensity between the 90 and the two 67° rotation samples could be attributed to the fact that possibly the mismatch between the thermal gradient direction and the $\langle 001 \rangle$ direction is larger for the 90° scanning strategy, so there are grains which do not adopt this orientation but rather another one. On the contrary, for the 67° rotation scanning strategy, the mismatch could be lower and so more grains succeed in the competitive epitaxial growth process that takes place, therefore resulting in a stronger texture in the 67 and the island_67 samples.

The same explanation could be provided for the situation encountered in sample 30, whereby the texture observed along the BD seems to be focused on two orientations, the $\langle 001 \rangle$ and the $\langle 101 \rangle$, see Figure 4.8 a). Of course, such statements cannot be verified by means of the EBSD measurements provided in this Section. Thermal modelling techniques as well as in-situ measurements during the fabrication could prove the above suppositions. As explained in [59], both the interlayer rotation of the scanning strategy as well as the rest of the process parameters have an exceptional effect on the crystallographic texture that eventually develops in a part fabricated by L-PBF methods. What is however, clear from the above measurements and results is that the 0° rotation scanning strategy seems to be the one which provides the least possibility for tailoring the microstructure in terms of both the texture and the grain morphology.

Focusing finally on the differences seen between the two samples employing a 67° interlayer rotation in their scanning strategy, the effect of the patterns which can be incorporated into the strategy becomes clearer. The parameter that mainly differentiates the two strategies is the length of the scanning vector; for the island_67 sample that is significantly shorter than for the 67 sample (1 mm versus 10 mm). That difference in the length has a considerable effect on the thermal gradient that develops across the surface of a scanned layer. In the case of the 67 sample the heat flux is once again directed towards the positive and the negative sides of the SD, whereas for the island_67 sample the flow is diffused in nearly all directions. This even distribution has a tremendous effect in lowering the thermal gradient that develops along the xy plane, as heat does not accumulate so severely and creates a more even condition in terms of the surface temperature across the entire layer, allowing for the next scan to take place at much higher temperature than in a single layer scanning strategy [36]. Consequently, it is possible that the solidification rate reduces in the island strategy, providing more time for the grains to orient themselves along the preferred easy growth orientation direction, and eventually obtain a strong $\langle 001 \rangle$ texture along the BD of the sample.

As a comparison between the crystallographic textures obtained by each of the scanning strategies employed for the fabrication of the samples for this thesis and various publications, there are instances where the textures reported here are significantly different to what has been reported in literature. For example, L. Thijs et al. report in their 2013 publication on SLM fabrication of Ti6Al4V alloy that a strong texture with fourfold symmetry arises for scanning strategies with 90° interlayer rotation angle, which progressively weakens as the rotation angle is varied between 30° and 60°, attaining a fibre character in the process [59]. In the samples discussed in this Section, the intensity of the texture follows the opposite road; it starts at its weakest in the 90 sample, and intensifies for the 30 and finally is the strongest at the two 67° rotation samples. As far as the type of the crystallographic texture, the 90 sample does show the fourfold symmetry of a cube texture but so does the 30 sample, whereas the character changes for the 67° rotation to the fibre texture. On the other hand, F. Geiger et al. reported a picture equivalent to the one presented in this report for the textures their research group managed to obtain for the IN738LC alloy manufactured by SLM [60]. Publications specific to NiTi alloys confirming the texture described in this report also include the following references which mostly concern the scanning strategy with 90° interlayer rotation [61] [57]

Finally, the transformation behaviour of the NiTi samples fabricated for the purposes of this project was investigated using Differential Scanning Calorimetry. Figure 4.11 a) to e) shows the DSC curves obtained for all five scanning strategies studied. As can be seen on the figure, differences arise between the samples which, given the fact that the only varying process parameter in their fabrication was the scanning strategy, they can be attributed to it.

The first, most striking difference is the incomplete reverse transformation (from the austenite to the martensite phase) during the cooling segment of the cycles concerning the 0, 30, 67 and island_67 samples. In fact, it seems that the only sample which is able of completing the reverse transformation within the specified temperature window of the test is the 90 sample. Especially when the 30 and 67 samples are regarded, the reverse transformation appears to show a deviating behaviour; a non-smooth increase is detected in the heat flow of both specimens which, however, fails to show the characteristic smooth peak expected and actually seen in the other three samples. The 0 and island_67 samples, do show the expected shape of the transformation peak, nevertheless this peak is abruptly stopped at the minimum temperature specified for the DSC measurement which is before the transformation is completed for both specimens. Unfortunately, it was not possible to repeat the tests with even lower minimum temperature. It is believed however, that all samples would show reverse transformation peaks if the DSC measurements were repeated and the lower temperature value was decreased even further than -85°C. For the reasons stated in this paragraph and from the specifics of the thermomechanical behaviour of the material of interest for this project, the transformation of importance is the forward transformation (from the martensite phase to the austenite phase) which is well captured by the DSC measurement for all samples.

Another notable feature of the DSC curves is the varying height, width and positioning with respect to the temperature axis of the transformation peaks measured for the forward phase transformation, see a close-up image of this part of the curves in Figure 4.11 f). Concerning the position of the peaks with respect to the temperature axis of the plots, or, equivalently the temperatures characteristic of the forward transformation for each sample, it can be said that they provide an indications of the degree of nickel evaporation which occurred during the L-PBF fabrication of the samples. As was explained in Chapter 2, the Nickel content is inextricable to the temperature at which the phase transformations in the material take place and is also affected by evaporation due to the high processing temperature conditions. Hence, a link could be established at this point between the scanning strategy and the amount of nickel evaporation during L-PBF of the metal through the variation in the temperatures at which the transformation occurs for each sample. Taking into consideration at this point the results of the chemical composition measurements obtained by the SEM-EDS method and analysed in the beginning of this Section, one can spot a different trend between the data. The DSC curves suggest that the 90 and 0 samples should be the two samples with the lowest Ni content, as the A_{peak} and the area under the peak of the transformation curve are the largest compared to the rest of the samples. Interestingly, this is not confirmed by the SEM-EDS data, where the 90 sample has the highest Ni content and the 0 sample has the lowest. As is generally perceived, however, DSC measurements provide greater confidence in terms of their accuracy, the trends showcased by the DSC measurements will be adopted as the most reliable results regarding the composition and the phase transformation-related information. The same trend appears for the island_67 and the 67 samples as well, where the SEM-EDS and the DSC show conflicting results, however, the Ni contents measured by the SEM-EDS method for these two samples are the same, so it is reasonable to assume that in this case the two methods agree to a satisfactory degree. Figure 4.11 f) contains a plot of the three temperatures defining the forward phase transformation of the samples and Table 4.2 lists those temperatures for reference. Moreover, in Appendix A the full list of the transformation temperatures measured for each sample can be found, together with calculations of the thermal hysteresis.

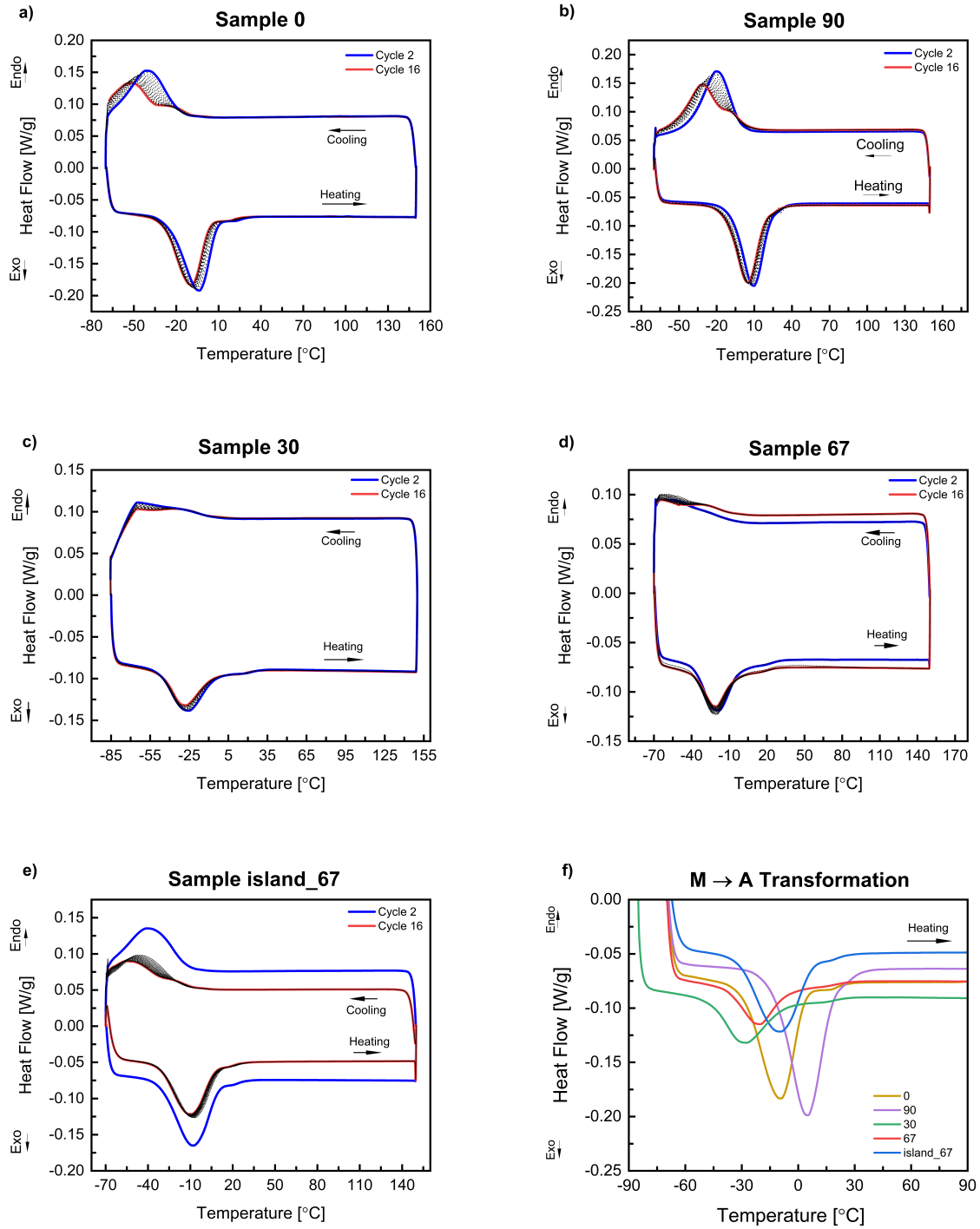


Figure 4.11: ***a) - e)*** DSC curves (cycles 2 to 16) for the 0, 90, 30, 67 and island_67 samples respectively. For all specimens, the second cycle is depicted in blue, the 16th cycle in red and the cycles in-between are given by black dotted lines. ***f)*** Detail of DSC heating segments, where the martensite to austenite phase transformation can be seen during heating.

The height (associated to the latent heat of the transformation, ΔH) and the width of the transformation peaks (showing the thermal hysteresis, ΔT_H) are also presenting differences between the different scanning strategies. DSC and SEM-EDS results agree well together when these two values are concerned for the 67 and island_67 samples. According to T. Kakeshita et al., the DSC peak must start vanishing, meaning that its height should decrease, which is seen for these two samples and the reverse transformation peak should also not appear whole, fading towards very low temperatures, also observed in the DSC curves [62]. Finally, the broadening of the peaks is yet another feature of the DSC

curves obtained for the samples and it can be related to compositional inhomogeneities in the material as well as the presence of different sizes of crystals in the microstructure. According to Figure 4.11 f), the 90 sample is the one with the most narrow transformation peak, followed by the 0 sample. The 30, 67 and island_67 samples present peaks which become progressively more broad. Indeed, for these three samples differences in the grain sizes can be detected even in the EBSD maps presented earlier in this section, possibly explaining, at least in part, this broadening observed.

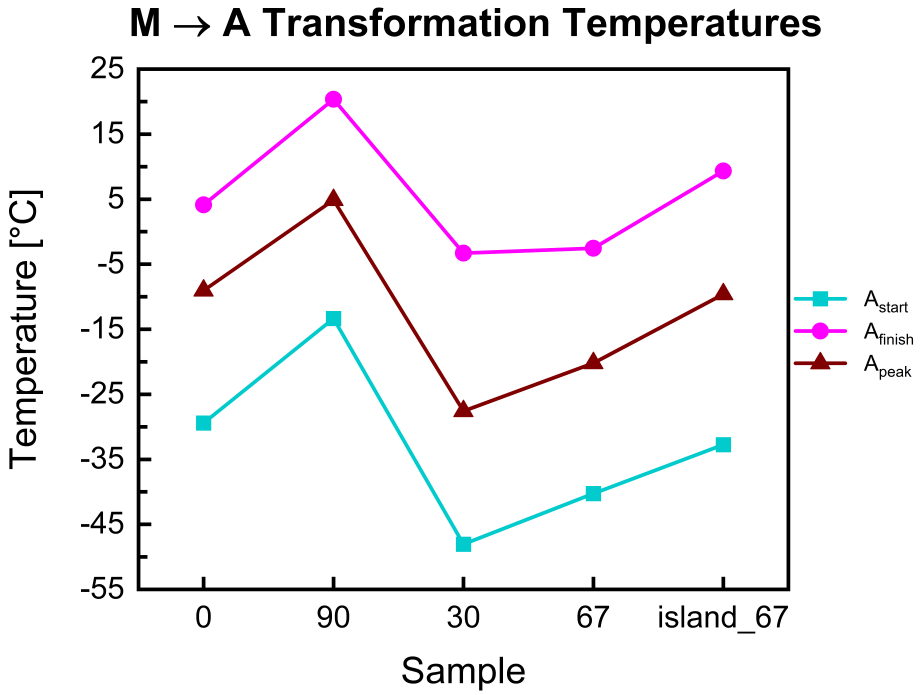


Figure 4.12: Plot of the temperatures related to the forward phase transformation for each sample. The A_s is given in cyan, the A_f is given in magenta and the A_{peak} is given in wine red. The specific temperature values can be found in Table 4.2.

Table 4.2: Forward transformation temperatures

Sample	A_s, [°C]	A_f, [°C]	A_{peak}, [°C]
0	-25.7	9.4	-3.8
90	-8.5	24.5	9.5
30	-49.1	-1.0	-25.5
67	-39.4	0.8	-18.3
island_67	-32.2	11.7	-7.9

4.1.2 Functional Behaviour

- ***High Temperature test group***

Figures 4.13 a), 4.14 a), 4.15 a), 4.16 a) and 4.17 a) present the response of the 0, 90, 30, 67 and island_67 samples when subjected to the axial compression tests at the HT condition. Figure 4.18 a) provides an overview of the first cycle of the compression tests for the HT group for all five samples and allows for direct comparisons between the measured superelastic responses to be made. The discussion of the results include the following points: the loading and unloading portions of the compression cycles, the plateau regions and the associated phase transformations, the hardening rate for the forward transformation, the recovery ratio and the residual strain as well as the maximum stress

levels and the stress hysteresis observed. The focus will be on the first and, on some cases, the last compression cycle. Repeatability and reproducibility of the results was ensured by the fact that two specimens were tested for each temperature condition for each sample. The full results, including the full mechanical test plots of the specimens not discussed in this Chapter can be found in Appendix C.

Inspection of Figure 4.18 a) with respect to Figure 3.10 reveals that all samples follow the expected behaviour when it comes to the loading part of their superelastic response, a fact proven by the shape of the loading portion of the first compression cycle curves. Differences in the compression responses and therefore in the superelastic response begin to appear only during the unloading segments of the compression. It shall be noted here, that as it becomes apparent from the compression curves, all samples underwent Stage I and part of Stage II deformation as these were defined in Figure 3.10. Samples 0, 90 and 30 show rather similar superelastic responses, see Figure 4.18 a), whereby the loading portion of their curves corresponding to the first compression cycle begins with the elastic loading region of the austenite phase. In all three samples the forward transformation appears to be triggered at approximately the same stress levels, and from that point onwards, the plateau region of their curves, corresponding to the phase transformation proceeds in a comparable manner. All three samples reach comparable levels of maximum stress, as the data listed in Table 4.3 confirm. Minor differences can be spotted in the unloading portions of the 0, 90 and 30 samples' curves, however, overall, the reverse transformation appears to proceed in a similar way for all three samples, showcasing rather poor superelastic response. The initial elastic unloading segment is barely detectable in all three curves (see also the plots for each individual sample, Figures 4.13 a), 4.14 a) and 4.15 a)) and the plateau region corresponding to the reverse phase transformation can also hardly be traced.

The average hardening rates calculated for these three samples are comparable, with a mean value equal to 30.7 MPa. Of the three samples, the 90 sample shows a more improved response in terms of the recoverable strain, where it reaches 4.8% in the first cycle and stabilises at 4.0% at cycle 16, as well in terms of the recovery ratio, with 79.3% in the first cycle and 66.4% in the last cycle. Sample 0 follows with 3.7% at the first cycle and 2.7% at cycle 16. Sample 30 shows the poorest performance of the three in terms of both the recoverable strain and the recovery ratio, 2.9% and 47.9% at the first cycle respectively. It shall be noted here, that due to technical issues, this sample did not run the entirety of the 16 compression cycles, therefore data for the first cycle are only available and taken into account here.

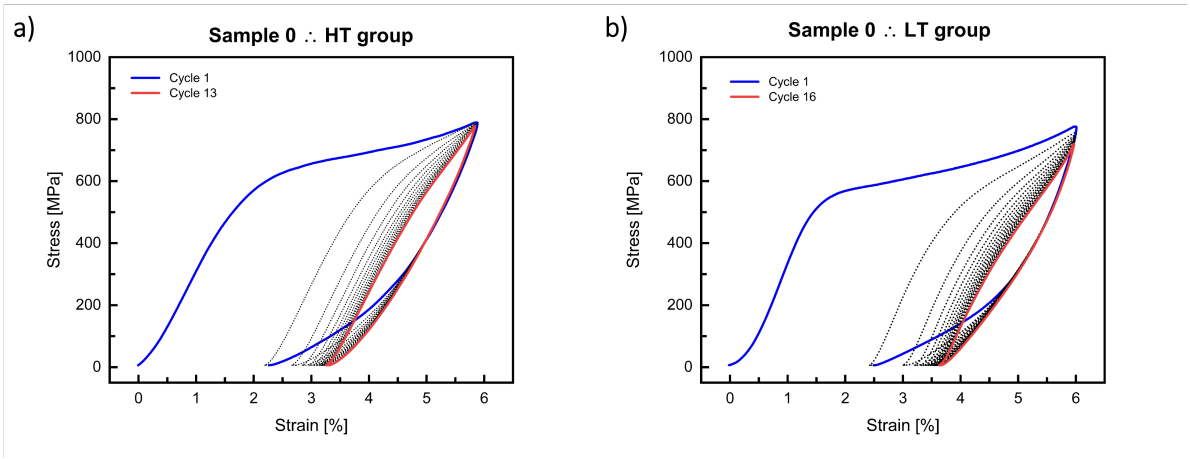


Figure 4.13: Mechanical response of the 0 sample for the HT, ***(a)***, and the LT, ***(b)***, groups.

The situation changes considerably when the next two samples are taken into account as both the 67 and the island_67 samples show an overall improved superelastic response. A look at Figure 4.18 a) confirms the improved performance of the 67 sample. The loading portion of the first compression cycle does not exhibit any significant difference when compared to the 0, 90 and 30 samples, however, the situation is clearly improved when the unloading section of the compression cycle is considered. Firstly, both the linear elastic unloading of the martensite phase and the transformation plateau region can be clearly marked on the curve. Secondly, the recoverable strain is also improved, reaching values equal to 5.4% for the first cycle and stabilising at 4.5% at the end of the compression test. The recovery ratio

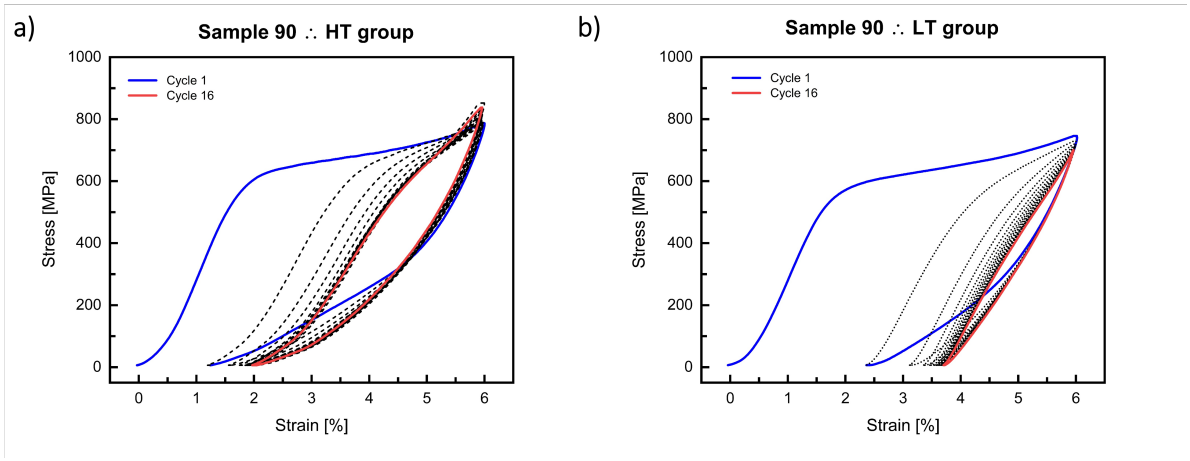


Figure 4.14: Mechanical response of 90 sample for the HT, ***(a)***, and the LT, ***(b)***, groups.

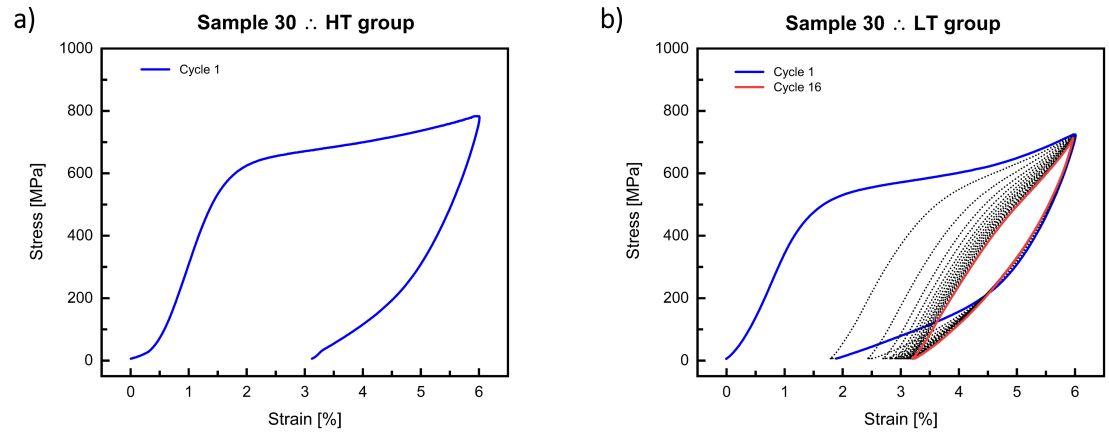


Figure 4.15: Mechanical response of 30 sample for the HT, ***(a)***, and the LT, ***(b)***, groups.

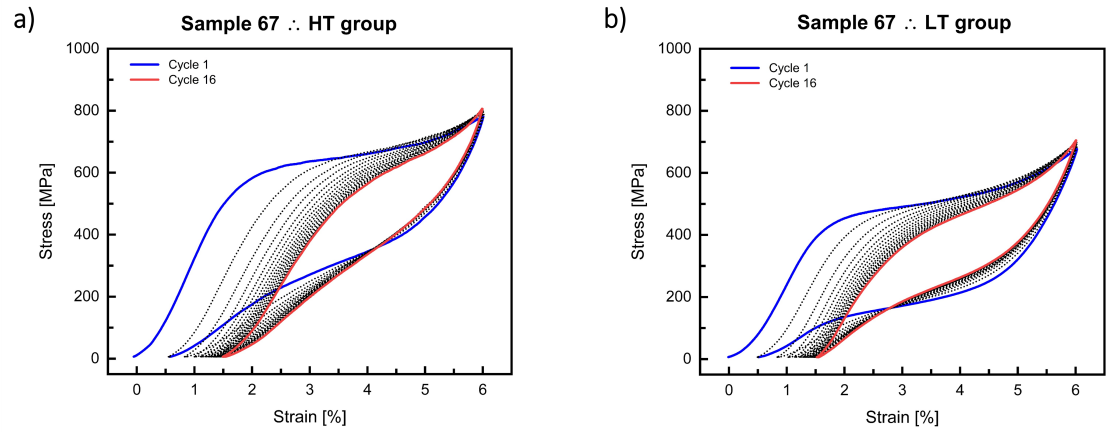


Figure 4.16: Mechanical response of 67 sample for the HT, ***(a)***, and the LT, ***(b)***, groups.

has consequently increased, starting at 90.5% in the first compression cycle before finally stabilising at 74.4% in the last cycle. The stress hysteresis measured has also decreased for the first time in all samples considered so far.

Undoubtedly, the best performance is given by the island_67 sample, confirmed by Figure 4.18 a) as

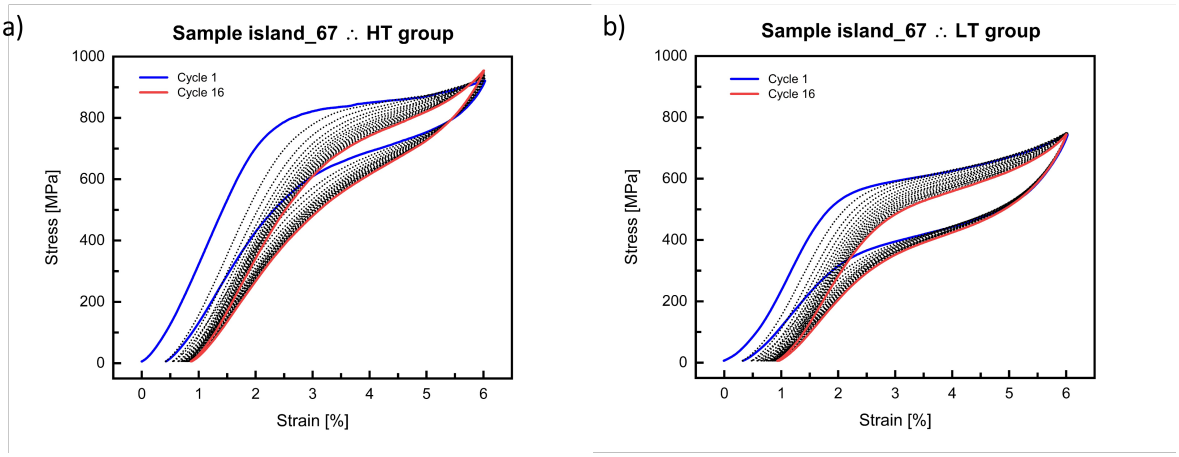


Figure 4.17: Mechanical response of island_67 sample for the HT, ***(a)***, and the LT, ***(b)***, groups.

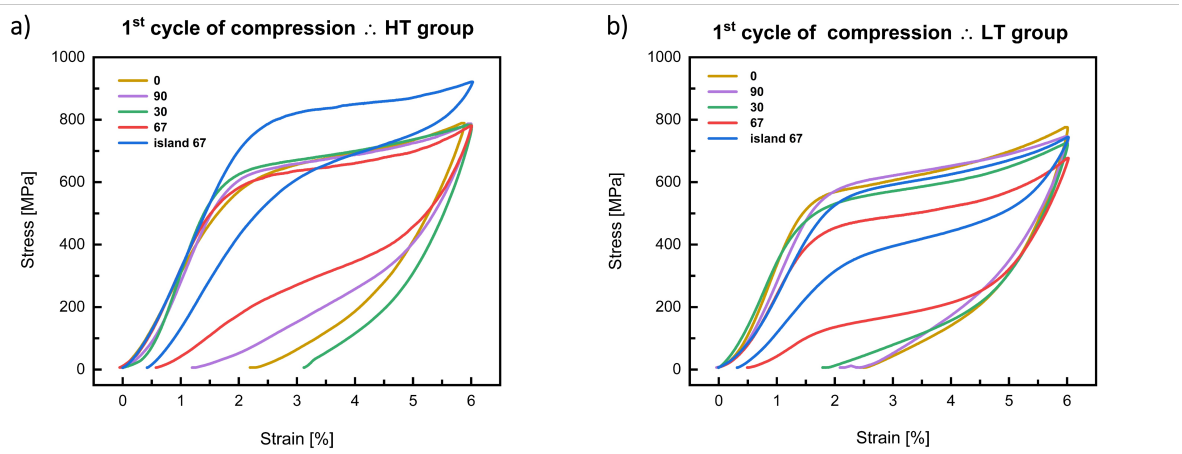


Figure 4.18: First cycle of compression for all samples for the HT group, ***(a)***, and the LT, ***(b)***, groups.

well as the data of Table 4.3. Apart from the salient improvement in the unloading portion of the curve, which signifies the improved superelastic performance, the most notable difference of the behaviour of this sample is the stress levels it reaches, with maximum stress of 922 MPa in the first cycle and 955 MPa in the last cycle. Moreover, the stress level at which the transformation to martensite is triggered is also the highest observed amongst all samples tested (814 MPa at the first cycle). Such behaviour could be attributed to the low residual stresses left in the island_67 sample after the L-PBF fabrication [36] [58], as well as to the development of high internal stresses in the lattice due to the thermomechanical processing of the fabrication and the creation of such strong texture [20]. Regarding the low residual stress accumulated in the island_67 sample after its fabrication, it is possible that they could allow it to trigger the transformation to martensite at higher stress levels compared to the rest of the samples, which due to the accumulation of residual stresses may experience that the transformation of their austenitic grains to the B19' crystals is aided by those residual stresses and hence is triggered at lower σ_{SIM} levels. The rationale behind the explanation of such behaviour by the internal stresses of the matrix lies in the fact that internal stresses, which can develop due to the presence of precipitates (which, however, have not been found in the samples examined in this study), can increase the yield strength of the austenite and hence cause this phase to transform at higher stresses [20]. It is also possible that these internal stresses could arise by the interaction of the favourably oriented $\langle 001 \rangle$ grains and the few other grains which have obtained different orientations. Such interactions could delay the transformation and cause it to occur at higher stress levels, resulting in this behaviour of the island_67 sample for this temperature group. It is evident that further research shall be undertaken for this behaviour to be clarified and explained to a satisfactory degree. Apart from this, the recovery

ratio stabilises above 85% and the recoverable strain starts at 5.6% in the first cycle and stabilises at 5.1% at cycle 16. The sample exhibits the smaller stress hysteresis, lending itself for applications with requirements for low energy absorption and dissipation levels.

In short, the performance of all the five samples considered for the HT group testing in terms of the hardening rate, the recoverability and the stress hysteresis can be viewed in Figures 4.19 a), 4.20 a) and 4.21 a). Sample island_67 shows the lowest hardening rates for both the first and the last cycle, followed by sample 67. In terms of the recovery ratio, island_67 exhibits the largest recoverability, closely followed by sample 67. Finally, regarding the stress hysteresis response, island_67 exhibits the lowest values in cycle one of the compression test, again followed by the 67 sample.

The final discussion points for the HT group samples concern the cyclic stability of the superelastic response measured by the axial compression tests. This regards the progression of both the recoverable strain values and the recovery ratio through the cycles. The cyclic stability of the superelasticity for the HT group can be seen in Figure 4.22 a). According to the plot, sample 30 showcases the poorest superelastic response, followed by the 0 sample. The island_67 sample exhibits the best performance, which also includes the least sharp decrease in the recoverable strain values, indicating that the metal is able to recover the largest part of the 6% strain to which is subjected to at an almost constant rate. Sample 67 follows close by, although in this case the decrease through the cycles is considerably larger.

Sample 90 lies in-between the two best performing samples and the two poorest performances, showing however a rather interesting response. As can be concluded by examination of Figure 4.14 a), the specimen exhibits an increase of its stress values at maximum strain as the cycles progress,suggesting a cyclic hardening process to take place during its mechanical compression tests. Such behaviour is not unprecedented for NiTi SMAs; it has been reported as a usual occurrence which is related and influences their fatigue performance [63] [64] [65]. In Figures 4.22 a) and 4.23 a), the behaviour is manifested by the increase in both the recoverable strain values measured per cycle as well as the recovery ratio per cycle. The behaviour appears to be starting at cycle six and to last through cycle 14, where the strain and recovery ratio values decrease again and then stabilise for the last two cycles. This increase observed in Figures 4.22 a) and 4.23 a) arises as the material is able to recover slightly larger amounts of strain when its peak stress values are increasing for the cycles seven to 14. In general, NiTi SMAs are able of showcasing both stress hardening and softening behaviours when cycled [64], with the effects arising more prominently when the loading is compressive rather than tensile [64]. The hardening process usually appears during the first 10 cycles (approximately), after which the stress tends to increase less rapidly, before eventually stabilising [63]. Here, sample 90 exhibits the hardening effect after the sixth cycle, giving signals of a stabilisation at the last two cycles; meaning that is following the expected trend of the behaviour within reason. The stress hardening effect of NiTi SMAs has been connected to the increase of the density of dislocations in the austenite phase which generate by the cycling process and usually tend to reduce the amount of the material which is available for deforming via phase transformations [65] [63] [66]. Moreover, according to P. Sedmák al., the instabilities observed in the superelastic response of NiTi wires are caused by the redistribution of internal stresses which arise within the polycrystalline matrix due to the combined action of dislocation motion and martensitic transformations [67].

The stability of the recovery ratio for the HT group samples can be found in Figure 4.20 a). The situation here does not present significant differences than in the case of the cyclic stability of the recoverable strain, due to the fact that both plots are a result of strain-related calculations. Samples 30 and 0 showcase the poorest performance, with low values at the first cycle which decrease rapidly throughout the course of the compression test (this point can only be made for the case of the 0 sample). Island_67 and 67 samples are the first and second best performances, with the major difference being the rate at which the recovery ratio decreases through the cycle progression. Finally, the 90 sample lies again in-between the two extremes.

Table 4.3: Details of the superelastic response of the HT group

Sample	Cycle	Recoverable strain, ε_{rec}, [%]	Recovery Ratio, [%]	Maximum stress, σ_{max}, [MPa]	Stress Hysteresis, [MPa]	Hardening Rate, [MPa]
0	1	3.7	62.3	789	321	37
0	13	2.7	44.7	777	37	246
90	1	4.8	79.3	787	223	28
90	16	4.0	66.4	838	112	174
30	1	2.9	47.9	784	336	27
67	1	5.4	90.5	781	141	25
67	16	4.5	74.4	806	13	97
island_67	1	5.6	93.0	922	25	20
island_67	16	5.1	85.5	955	113	76

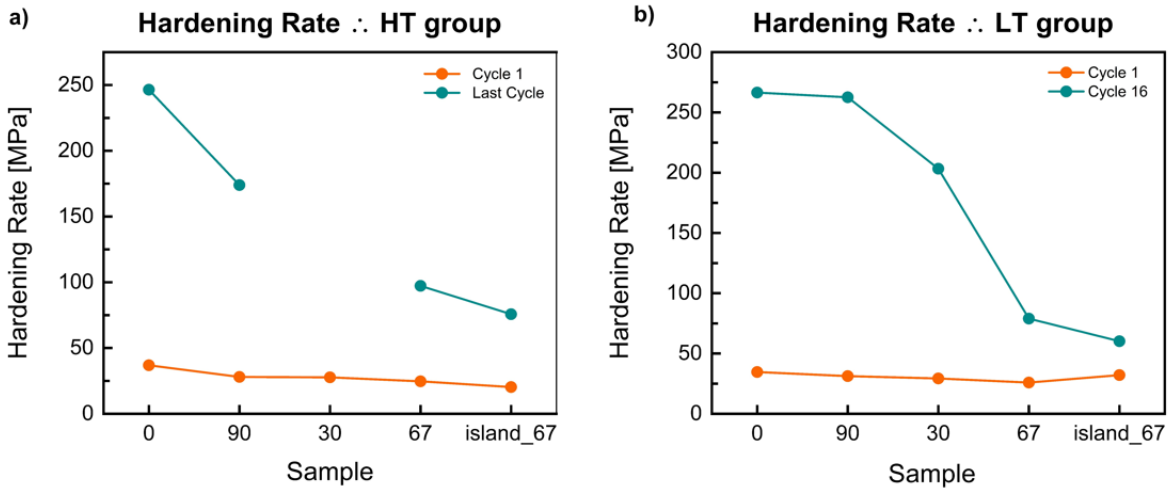


Figure 4.19: Hardening rate for HT, ***a)***, and LT, ***b)***, groups. Sample 30 test produced only one compression cycle.

- ***Low Temperature test group***

Inspection of the mechanical response of the samples tested under the LT condition, as this can be done by examining Figures 4.13 - 4.18, reveals that the overall superelastic behaviour of the samples is not drastically different between the two testing temperature conditions. One of the most evident remarks that can be made is that the expected dependency of the stress of the NiTi on temperature holds true for these tests. In general, the maximum stress levels which all the samples reach during the course of the compression test are relatively lower to those observed in the HT group. The most notable decrease is seen for the island_67 sample, which was the one which reached the highest stress levels amongst the other samples of the HT, which notably were all tested at the same temperature. In contrast, the LT group includes tests performed at various temperatures, which, although they are not vastly different, they are expected to showcase the dependency of the material behaviour on the temperature according to the Clausius-Clapeyron relation.

In general, the superelastic response of the samples of the LT group is not extremely different than this obtained for the HT group. In fact comparing Figures 4.18a) and b), one can immediately note that the same trend in the behaviour is repeated. Samples 0, 90 and 30 have an overall poorer superelastic response, as the unloading portions of their respective cycle one curves fails to show the characterist-

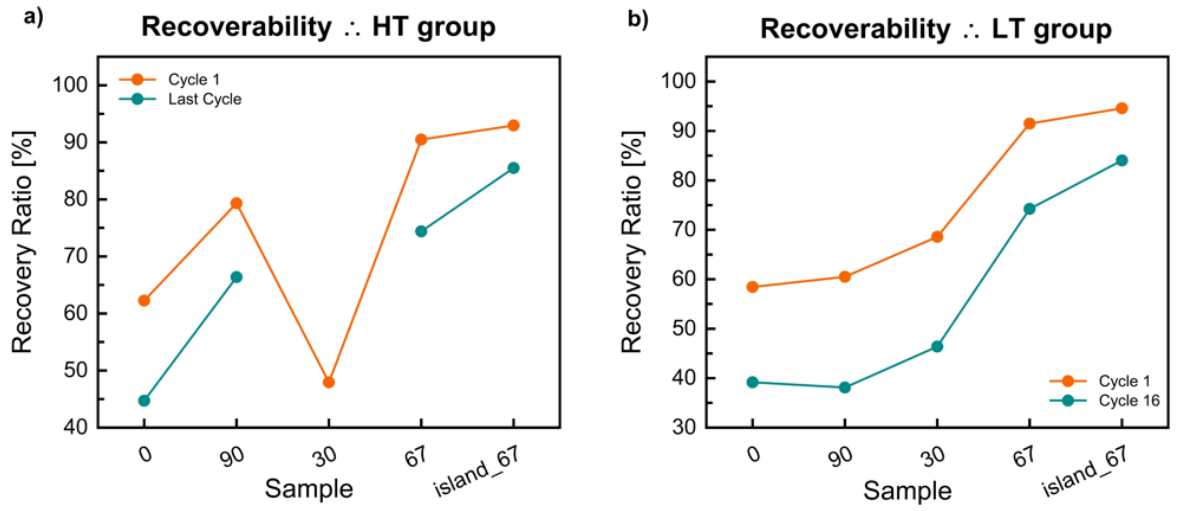


Figure 4.20: Recovery ratio for HT, ***a)***, and LT, ***b)***, groups. Sample 30 test produced only one compression cycle.

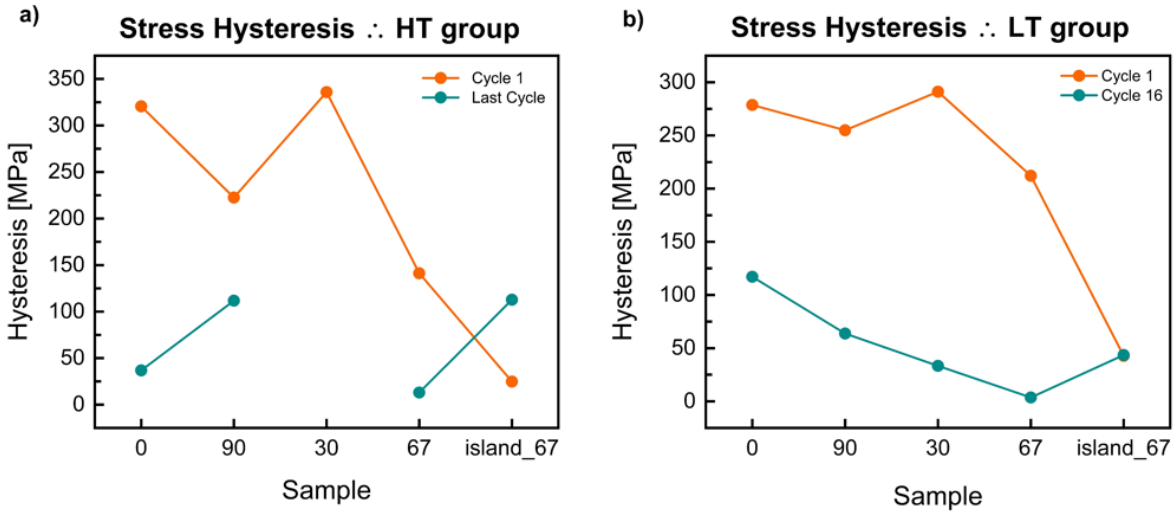


Figure 4.21: Stress hysteresis for HT, ***a)***, and LT, ***b)***, groups. Sample 30 test produced only one compression cycle.

ics indicative of a good phase transformation recovery. Similarly to the HT group, the reverse transformation characteristics for both the 67 and the island_67 samples are considerably improved when compared to the other three samples.

The indicated better superelastic response can be verified by the plots presented in Figures 4.19 b), 4.20 b) and 4.21 b) as well as the data listed in Table 4.4. It is worth to mention here that the island_67 sample achieves recoverable strain value equal to 5.7% in the first compression cycle, which stabilises at 5.0% at the last compression cycle. The 67 sample follows close by, with recoverable strain value equal to 5.5% in the first cycle and stabilised value at 4.5%. The stabilised recovery ratios for these two samples are 84% and 74.2% respectively.

The cyclic stability of this group of specimens aids in further distinguishing the two best superelastic performances from the poorer ones. Figures 4.22 b) and 4.23 b) showcase a clear gap between the island_67 and 67 samples and the 0, 90 and 30 samples, indicating a clear difference in their functional behaviour both in terms of the cyclic progression of the recoverable strain and in terms of the recovery ratio through the cycles. However, the main difference with the HT group is that the 90 samples show a marginally poorer performance when compared to the 0 sample, and the 30 sample exhibits a vastly better superelastic response to the one it showcases in the HT condition. That could be attributed to

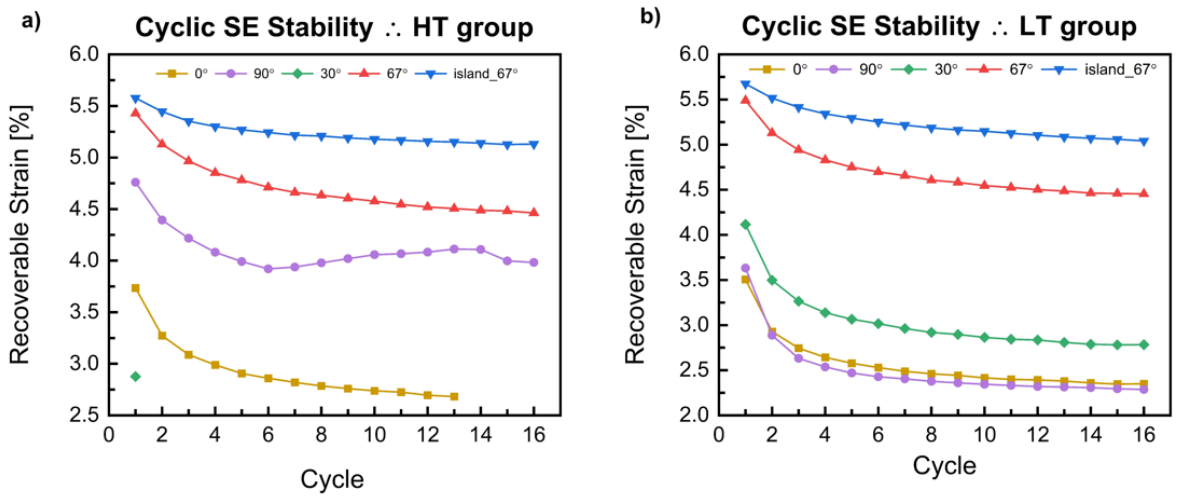


Figure 4.22: Recoverable strain versus compression cycles for the samples of the HT group, ***a)***, and the LT group, ***b)***.

the testing temperature of the HT group being very high for this particular sample, for which the A_f is equal to -1°C, and the sample approaching a deformation behaviour closer to plasticity. However, due to the fact that the full 16 cycles of compression was not possible to be completed for this sample at this temperature condition, it is impossible to draw a definite conclusion on its superelastic behaviour. As a final point, the hardening behaviour observed in the 90 sample of the HT group seems to not occur in this temperature condition. As discussed in [63], the fatigue behaviour exhibited by NiTi SMAs is dependent upon their transformation temperatures as well as the temperatures at which they are loaded, hence, the fact that the stress hardening effect is absent for this test group is completely justified.

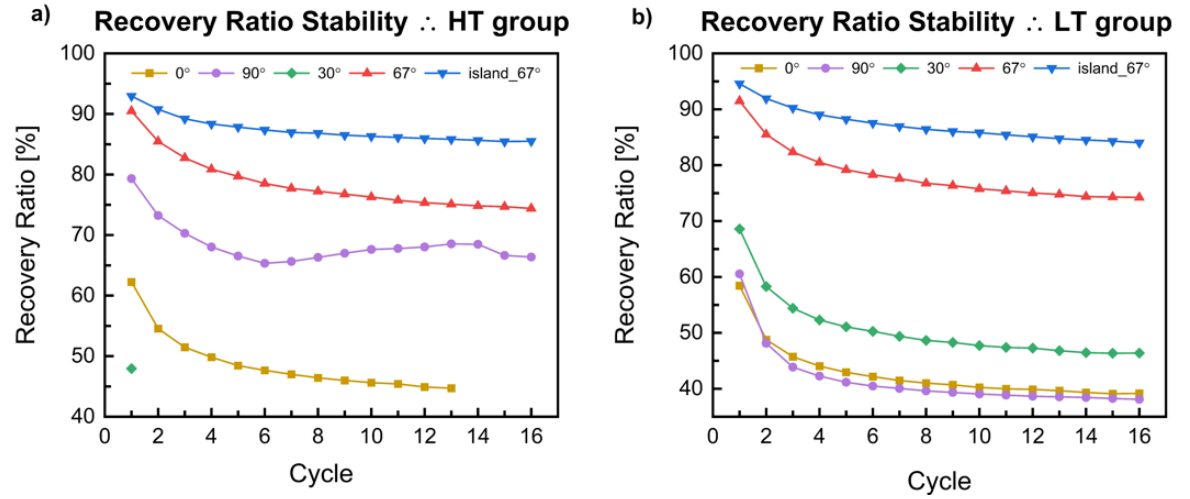


Figure 4.23: Recovery ratio versus compression cycles for the samples of the HT group, ***a)***, and the LT group, ***b)***.

In concluding remarks to the discussion on the mechanical performance the following can be stated. Firstly, the differences between the functional responses obtained from each sample are palpable. Despite minor discrepancies between the behaviours of specific samples between the two temperature groups, the general image emerging is the following. The island_67 sample exhibits the best superelastic response when compared to all the rest. Sample 67 follows close by, leaving the other three samples with varying but overall rather poor superelastic responses. Considering the fact that the scanning strategy is the sole varying process parameter between the samples, the fact that, as shown in Section 4.2.1, it has a clear effect on the microstructure obtained by L-PBF and finally the fact that, as explained in Chapter 2, a relation has been established between microstructural features and the superelastic functional response of NiTi alloys, it can be safely stated that indeed the island_67

Table 4.4: Details of the superelastic response of the LT group

Sample	Cycle	Recoverable strain, ε_{rec}, [%]	Recovery Ratio, [%]	Maximum stress, σ_{max}, [MPa]	Stress Hysteresis, [MPa]	Hardening Rate, [MPa]
0	1	3.5	58.4	776	279	35
0	16	2.4	39.2	720	117	267
90	1	3.6	60.5	746	255	31
90	16	2.3	38.1	701	64	263
30	1	4.1	68.6	725	291	29
30	16	2.8	46.4	713	33	203
67	1	5.5	91.5	677	212	26
67	16	4.5	74.2	705	4	79
island_67	1	5.7	94.6	744	43	32
island_67	16	5.0	84.0	745	44	60

scanning strategy succeeds in producing the best superelastic response compared to the other four scanning strategies examined. Furthermore, scanning each powder layer in one passing while maintaining a 67° rotation between successive layers is the second most successful strategy for fabricating parts with superior superelastic functional response.

As a final remark, Table 4.5 presents a list of various values obtained for the recoverable strain and the recovery ratio from a variety of publications, mainly concerning Ni-rich NiTi fabricated by L-PBF and tested for its superelastic response under a variety of conditions. The results listed contain both cases where the superelasticity was obtained after post-processing heat treatments, as well as one case of a Ti-rich alloy which was crystallographically designed to exhibit superelastic response. When juxtaposing the 67 and island_67 samples discussed in this Section, both the HT and the LT group, it can readily be seen that these two samples exhibit performance at the top tier of those included in Table 4.5. Especially the island_67 sample showcased recoverable strains equal to at least 5.0% and recovery ratio above 84% at the stabilised condition, being only inferior to the 5.2% recoverable strain mentioned at the top of the second column. This comes to bolster the arguments presented in the preceding paragraphs concerning the supreme performance of the samples fabricated for this thesis, especially since even the samples which were considered as showing poor superelastic response can be compared to those listed in Table 4.5. It shall also be considered the fact that all five samples discussed in this Section showcase their superelastic responses without any post-processing heat treatments; rather, they draw their functional behaviour straight from their fabrication conditions, a substantial benefit especially when manufacturing costs are considered.

4.2 Effect of Laser Power, Beam Size & Shape on the Crystallographic Texture & Functional Behaviour

4.2.1 Microstructure & Phase Transformation Features

The microstructural and functional behaviour investigation presented in detail in Section 4.1 illustrated the effect of the scanning strategy as a process parameter on the superelastic response of NiTi samples through successful manipulation of their crystallographic texture. The result of this study indicated that scanning strategies which involve a 67° rotation between successive layers during L-PBF fabrication are those that produce microstructures with both the desired grain morphology and spatial orientation. In fact, implementing an island pattern during the scanning, further enhances the performance achieved,

Table 4.5: Recoverable strain and recovery ratio values from various publications. All values correspond to the stabilised behaviour unless stated otherwise.

Superelastic Ni-rich NiTi		Superelastic Ti-rich NiTi
With post-processing	No post-processing	
ε_{rec} = 3.4% & recovery ratio 95% at cycle 1 [52]	ε_{rec} = 5.2% [57]	ε_{rec} = 4% [26]
ε_{rec} = 4.2% & ε_{rec} = 3.8% [54]	ε_{rec} = 3.4% [57]	
ε_{rec} = 3% [53]		
ε_{rec} = 5.5% [55]		

All values correspond to the stabilised behaviour unless stated otherwise.

leading to the conclusion that the 67 and island_67 samples are the two best performing samples of all those studied.

As explained in Chapter 2, one of the ways by which is possible to tailor the NiTi microstructure during L-PBF is by controlling the laser energy density. Various publications have shown that successful implementation of suitable laser power can lead to parts with grain morphologies and textures close to the *ideal* situation for supreme superelastic behaviour, i.e. columnar grains with $\langle 001 \rangle_{\parallel BD}$ orientation. Naturally, the next stage of this project aims at investigating whether a combination of the two process parameters which have been proven to be able to manipulate the microstructure and, through that, the functionality of NiTi parts would result in further improving their performance. Therefore, in this Section the results of the experimental testing of the HLP_67 sample, which was fabricated using volumetric energy density equal to 203 J/mm^3, are going to be discussed and viewed in conjunction to the 67 and island_67 samples of the LT group, which were producing using a volumetric energy density equal to 92.6 J/mm^3.

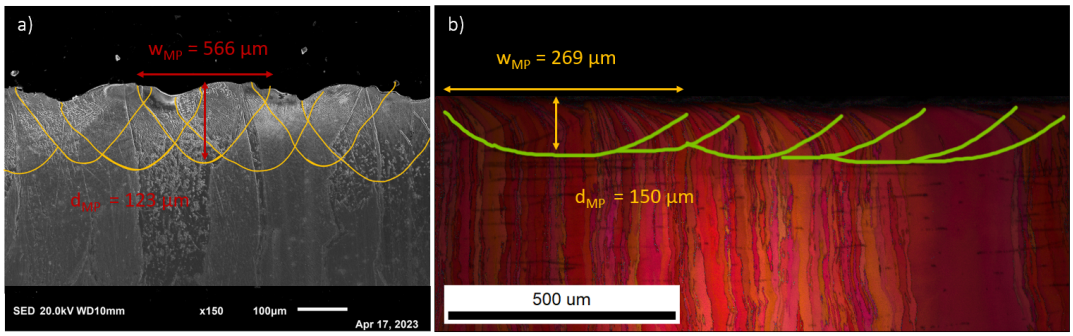


Figure 4.24: SEM micrographs of the melt pools created by ***a)*** the low laser condition, i.e. samples of Section 4.1 and ***b)*** the high laser condition, i.e. the HLP_67 sample. The melt pool boundaries have been annotated for multiple melt pools as well as the dimensions of width, w_{MP} and depth, d_{MP}.

In addition to the potent effect of the volumetric energy density of the laser beam on the particular conditions of the L-PBF fabrication of the samples, the implementation of a larger beam spot size in combination with the energy density, changes the conditions of the printing process even more as the laser/powder absorptivity is affected by the other process parameters. This is quantified in the modified volumetric energy density value calculated for the two laser conditions and given in Table 3.2. The tangible effect of those changes on the process is manifested in the melt pool created during the scanning process as this is depicted in Figure 4.24 for both the high laser condition as well as the low laser condition, i.e. the samples presented in Section4.1. As can be verified by Figure 4.24 b), the new set of process parameters implemented for the fabrication of the HLP_67 sample results in the creation of a wider and more shallow melt pool, with width equal to 566 μm and depth equal to 123 μm. In contrast, the samples treated in Section 4.1 had an average melt pool size of 269 μm for the

width and 150 μm for the depth, see Figure 4.24 a). These wide and shallow shaped melt pools which are overlaid so close together is extremely helpful for promoting grain growth exactly parallel to the z-direction, as shown by J.N. Zhu et al. for a Ti-rich NiTi alloy [26], see Section 2.3.2. It is therefore believed, that in the case of the Ni-rich NiTi samples fabricated and studied in this thesis, the same grain structure will emerge from printing under a set of conditions which promote this shape of conduction mode melt pool.

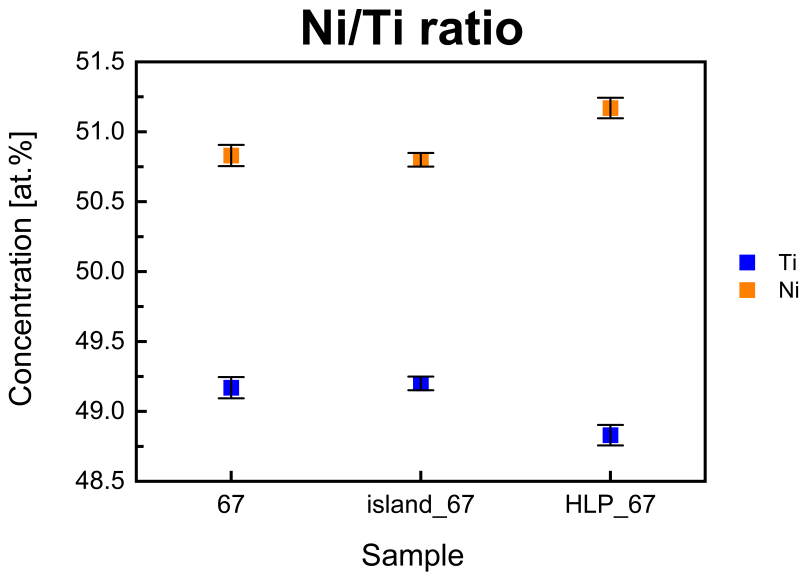


Figure 4.25: Chemical composition [at.%] of the 67, island_67 and HLP_67 samples after the L-PBF fabrication as measured by EDS.

SEM-EDS measurements were performed in order to define the chemical composition of the HLP_67 sample. The results are shown with comparison to the 67 and island_67 samples in Figure 4.25 and in Table 4.6. As can be seen the HLP_67 sample suffered the least Ni evaporation during its fabrication, as its composition emerges as the overall closest to the composition of the powder (51.4 at.% Ni). Its Oxygen contents are considered to be comparable to those presented in Section 4.1.

Table 4.6: Chemical composition for the fabricated HLP_67, island_67 and 67 samples

Sample	Average Ti content, [at.%]	Standard deviation of Ti content	Average Ni content, [at.%]	Standard deviation of Ni content
HLP_67	48.8	0.1	51.2	0.1
island_67	49.2	0.0	50.8	0.0
67	49.2	0.1	50.8	0.1

XRD measurements were implemented once more to provide insight into various features of the microstructure of the HLP_67 sample. Initially, it was confirmed that the L-PBF fabrication of this sample was also according to the standards and expectations, without any secondary or undesired phases present in the metal. Furthermore, the only phase detected was austenite with the BCC_B2 lattice. Once more, the measurements detected indications of presence of preferred orientation of the crystals, illustrated by both the differences of the measured peak intensities when compared to the spectrum of the powder, see Figure 4.26, as well as by the variation in the brightness measured in the 2-dimensional diffraction rings, given in Figure 4.27.

The primary conclusions of the existence of a preferred spatial orientation of the crystals comprising the HLP_67 sample provided by the XRD technique were further investigated by means of SEM-EBSD

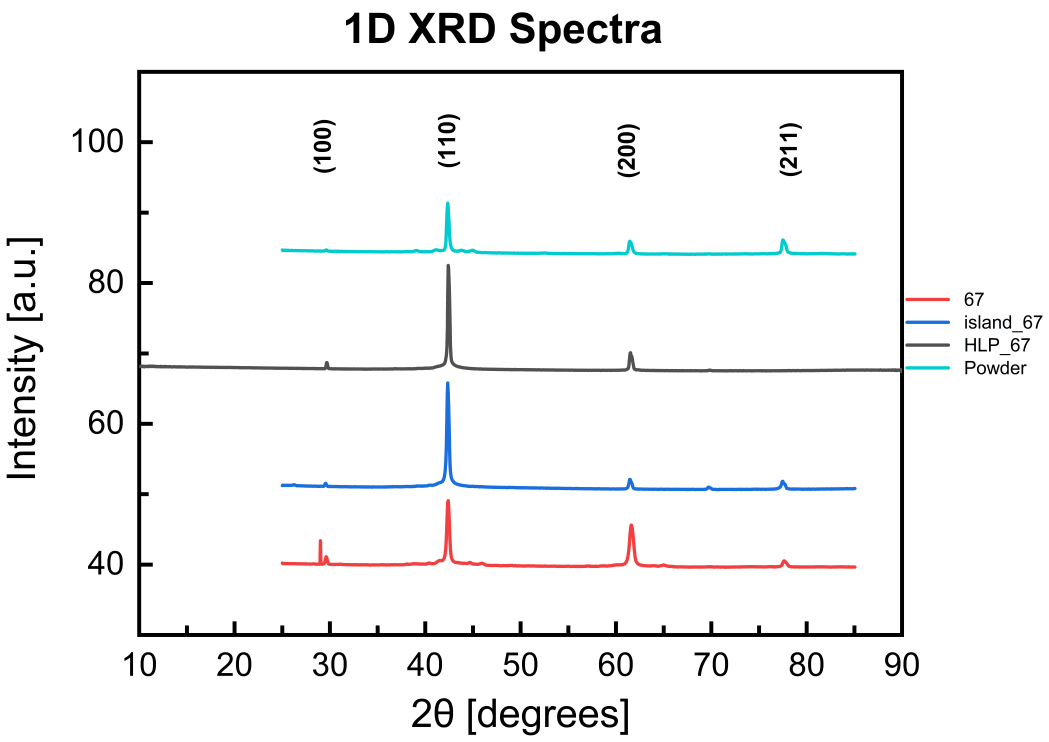


Figure 4.26: 1D XRD spectrum for HLP_67. Samples 67 and island_67 are shown for reference, as is also the spectrum of the NiTi powder.

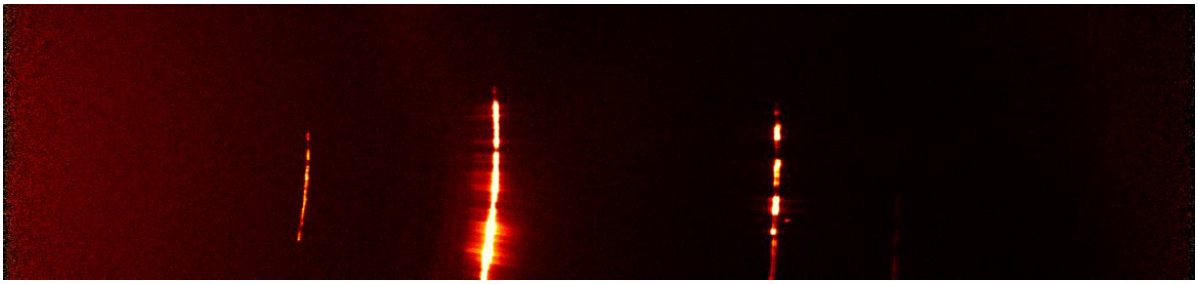


Figure 4.27: 2D XRD spectrum for HLP_67, diffraction rings.

measurements. The results along the BD of the sample can be found in Figure 4.28. As can be seen in the IPF map, the grain morphology of the sample approaches the *ideal* case. Grains indeed grow epitaxially, forming long columnar structures which extend for almost the entirety of the height of the micrograph. They also appear to be parallel to the BD of the sample, in an overall image which shows considerable improvements compared to the respective IPF maps of samples 67 and island_67 (see Figures 4.9 a) and 4.10 a)). Therefore, the changes implemented in the process parameters concerning the laser beam for the fabrication of this sample proved to be successful in obtaining a grain morphology almost identical to the one discussed in [26].

Considering the crystallographic texture of the HLP_67 sample, shown in Figure 4.28, the following remarks can be stated. The grains have solidified attaining a $\langle 001 \rangle$ orientation along the BD, with angle misorientations between the different grains being so small that the sample effectively approaches the state of the single crystal, see zoomed-in areas provided in Figure 4.29 where the lattice models overlaid show the spatial orientation of various grains along a line. The misorientations between the cubic lattice models are exceptionally small, as nearly all cubes appear to similarly oriented in space. Yet another argument in favour of this statement is provided by the pole figures included in Figure 4.28, whereby a single crystal-like texture with four-fold symmetry can be seen for this specific sample. In quantitative terms, this sample shows very strong $\langle 001 \rangle$ texture along the BD, which approaches percentages of

30%, signifying the stronger crystallographic texture obtained between all samples examined during this thesis project.

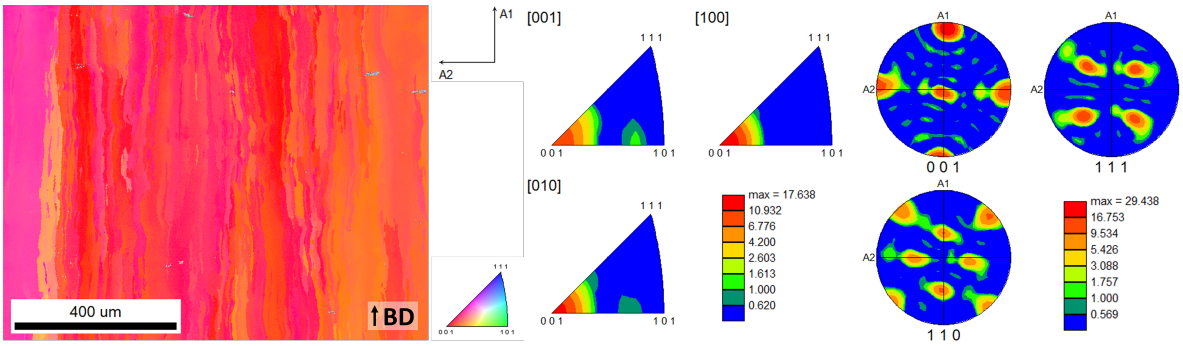


Figure 4.28: EBSD map of the xz plane for samples HLP_67. The associated Inverse Pole figures and the pole figures are also included.

It follows that the combination of a higher volumetric energy density and a interlayer rotation in the scanning strategy which orients the crystal grains along the easy-growth direction is possible to create a very strong crystallographic texture in NiTi alloys. Considering the fact that, as argued by H. Sehitoglu et al. [25] and K. Gall et al. [68], single crystals of NiTi with orientations $\langle 001 \rangle$ along the loading direction showcase supreme superelastic response under compression loading with the maximum theoretical recoverable strain values of 5.3%, the achievement of manufacturing a sample with such almost single crystalline microstructure so strongly textured predisposes for superior superelastic response.

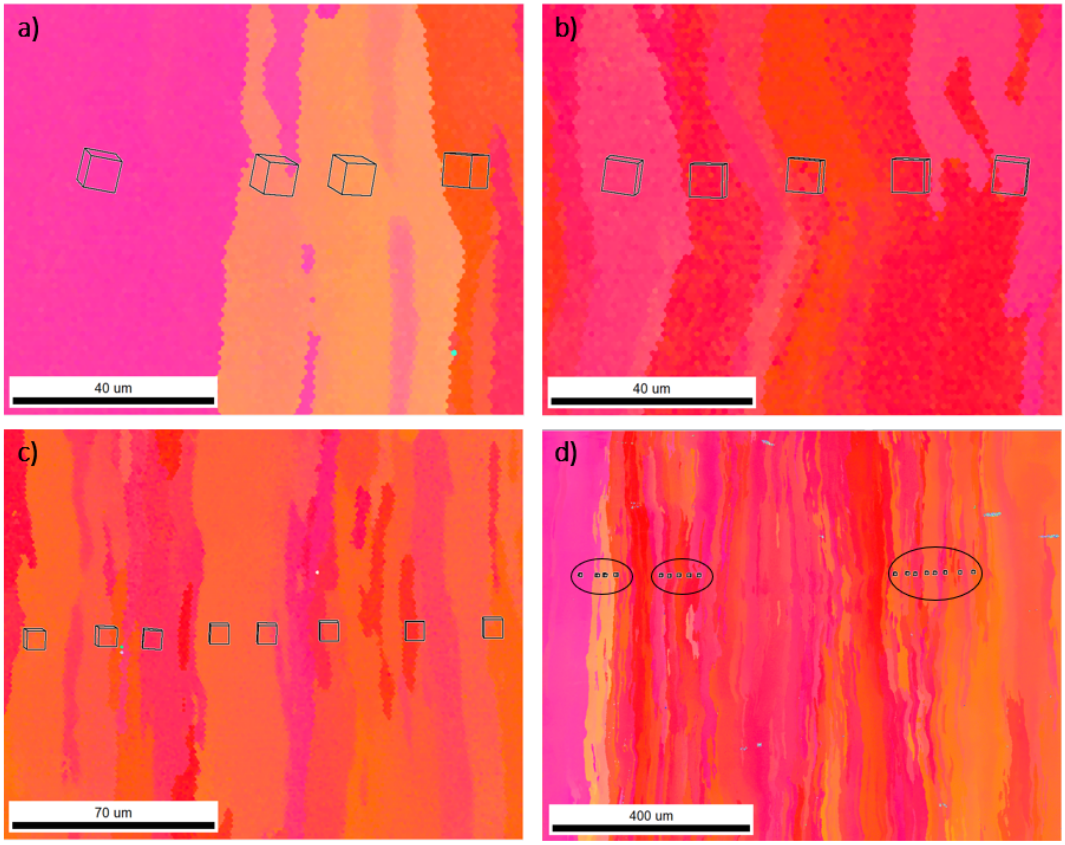


Figure 4.29: ***a), b) & c)*** Zoomed-in areas along a line of the EBSD map of the HLP_67 sample with a cubic lattice unit cell model showing the spatial orientation of the various grains. ***d)*** The positions of those zoomed-in areas with respect to the entire map.

As far as the phase transformations integral to the functional behaviour of the NiTi HLP_67 sample

are concerned, DSC measurements were performed on the sample in order to study them. The result can be seen in Figure 4.30 a). Significantly different behaviour is observed for this sample, as the peaks corresponding to both the forward and the reverse phase transformation are extremely shallow, a feature not encountered in any other sample, as can be verified in Figure 4.30 b) for the cases of the 67 and the island_67 samples. This result is however expected and also supported by the SEM-EDS findings regarding the chemical composition. According to the contents of Ni and Ti measured by the SEM-EDS, the HLP_67 sample shows the highest Ni content of the three samples, meaning that is closer to the excess 1.4 at.% Ni of the powder, which as explained in [62] is the reason which causes the reverse transformation peak to vanish and the forward transformation peak to appear extremely shallow. Figure 4.31 and Table 4.7 present the temperatures associated with the forward phase transformation, confirming that the HLP_67 sample shows the largest difference between its A_{peak} and A_f temperatures between the three 67° rotation-based samples. It is evident that due to the absence of a fully formed peak for the $A \rightarrow M$ phase transformation, aspects such as thermal hysteresis and latent heat of transformation cannot be discussed.

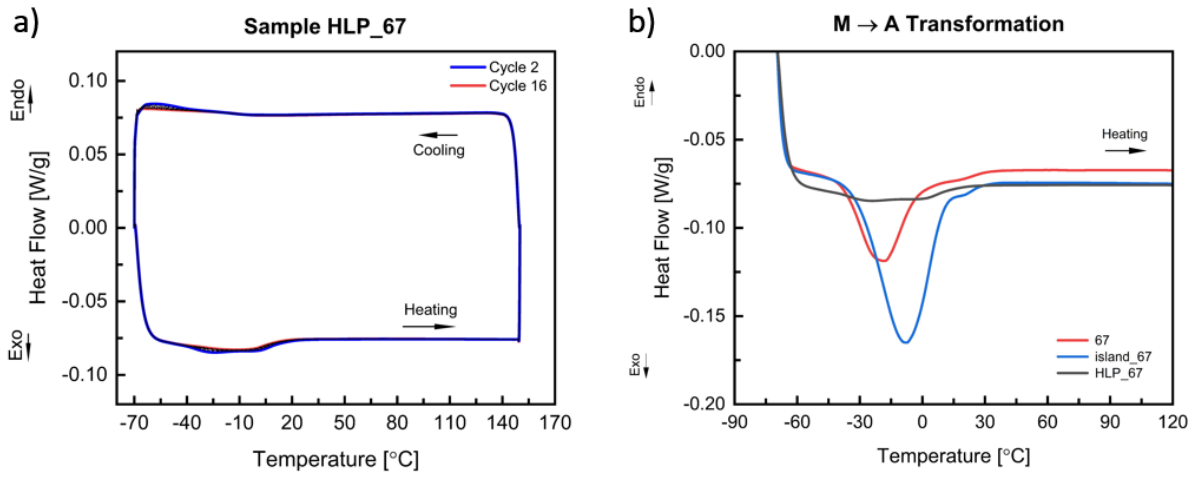


Figure 4.30: ***a)*** DSC curves for HLP_67 sample, and ***b)*** close-up of the forward phase transformation as captured in the DSC measurements for samples 67, island_67 and HLP_67 b).

Table 4.7: Forward transformation temperatures for the 67, island_67 and HLP_67 samples

Sample	A_s, [°C]	A_f, [°C]	A_{peak}, [°C]
HLP_67	cannot be determined	17.2	-12.0
island_67	-32.8	9.3	-9.6
67	-40.3	-2.5	-20.2

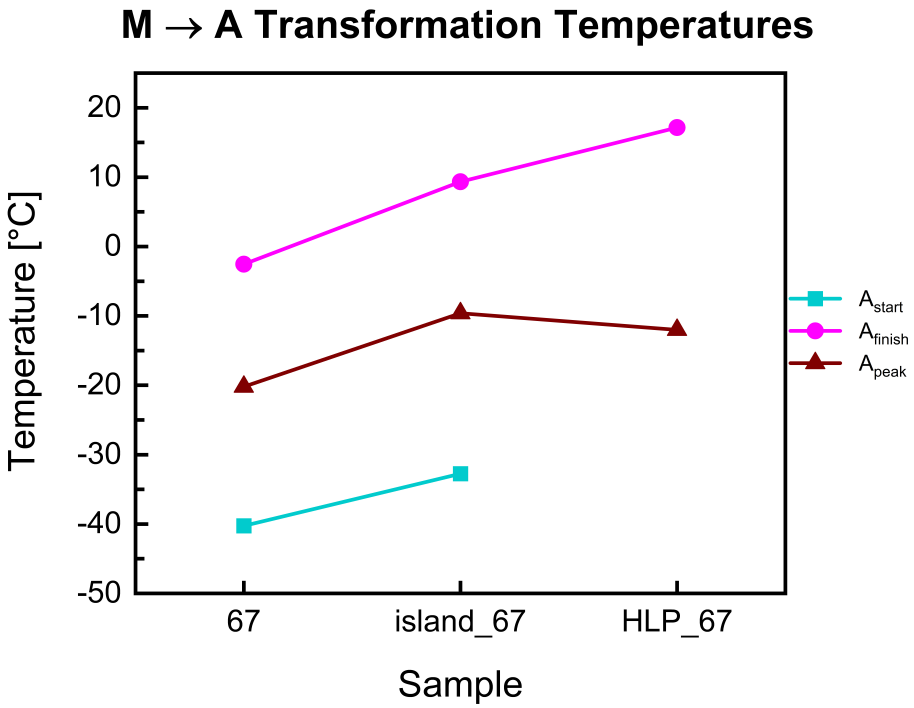


Figure 4.31: Plot of the temperatures associated with the forward phase transformation for the 67, island_67 and HLP_67 samples. The A_s is given in cyan, the A_f in magenta and the A_{peak} in wine red.

4.2.2 Functional Behaviour

The next step of this part of the research revolved around the examination of the superelastic response of the HLP_67 sample and how this compares to the responses exhibited by the 67 and the island_67 samples. It shall be noted at this point, that both the 67 and the island_67 samples to which the HLP_67 sample is compared to throughout this Section are the ones belonging to the LT group discussed in Section 2.2.2. The reason for this is that the temperature conditions of the mechanical tests were comparable between these three samples, so the responses measured can also be compared.

The results of the cyclic axial compression test for the HLP_67 sample can be found in Figure 4.32, whereas in Figure 4.33 the first compression cycle of the HLP_67 sample is plotted together with the corresponding compression cycles of the 67 and the island_67 samples for comparison purposes. As can be observed in Figure 4.33, the superelastic response obtained by the HLP_67 sample is different to this of both the 67 and the island_67 samples in numerous ways. Initially, although the maximum stress levels reached by all three specimens are relatively similar, refer to Table 4.8 for specific values for all variables discussed here, the critical stress value for triggering the forward phase transformation is considerably higher for the HLP_67 sample. Hence, the material is able to accommodate elastically larger amounts of deformation in its austenite phase before this starts to distort and transforms into the martensite phase. Additionally, the hardening rate experienced by the HLP_67 sample is lower than the island_67 sample and the 67 sample, indicated by the slope of the plateau region in the curves of Figure 4.33 and by the plot in Figure 4.34 a). Both of these behaviours could be attributed to the microstructure and its strong crystallographic texture. Since all of the crystals are oriented in an almost identical way, they shall all be deforming at the exact same manner and at the same stress levels, leading to the small hardening rate. The fact that these stress levels are so high could potentially be attributed to the fact that a higher volumetric energy density is able to produce parts which show enhanced mechanical properties.

Regarding stress hysteresis considerations, the HLP_67 curve appears to be as wide as the island_67 during the first cycle of compression and considerably narrower compared to the 67 sample, see Figure 4.33 and Figure 4.35. Notable is the fact that the HLP_67 and the island_67 samples show very small variations in the stress hysteresis between the first cycle and the last, refer also to Table 4.8. In

terms of the recovery ratio and the recoverable strain measured for the HLP_67 sample, both show improvement compared to the two other samples. HLP_67 achieves recovery ratio equal to 97.6% at the first compression cycle with recoverable strain value of 5.9%, and the stabilised behaviour shows recovery ratio equal to 91.5% and recoverable strain at 5.5%. The improvement is considerable especially as far as the stabilised response is concerned, indicating that the HLP_67 is more resistant to the degradation of its functional property, at least during the initial stage of its stabilisation.

This last remark can be further supported by the cyclic stability plots concerning the recoverable strain and the recovery ratio, Figure 4.36. The rate of decrease of both the recoverable strain and the recovery ratio for sample HLP_67 is lower than the rates observed for the island_67, whose performance comes second, and the 67 sample, which achieves the third best performance. Even though the differences in the cyclic stability between the three samples seem large, it should be noted here that all three samples exhibit stabilised recovery ratios above 74%, indicating very good superelastic performance.

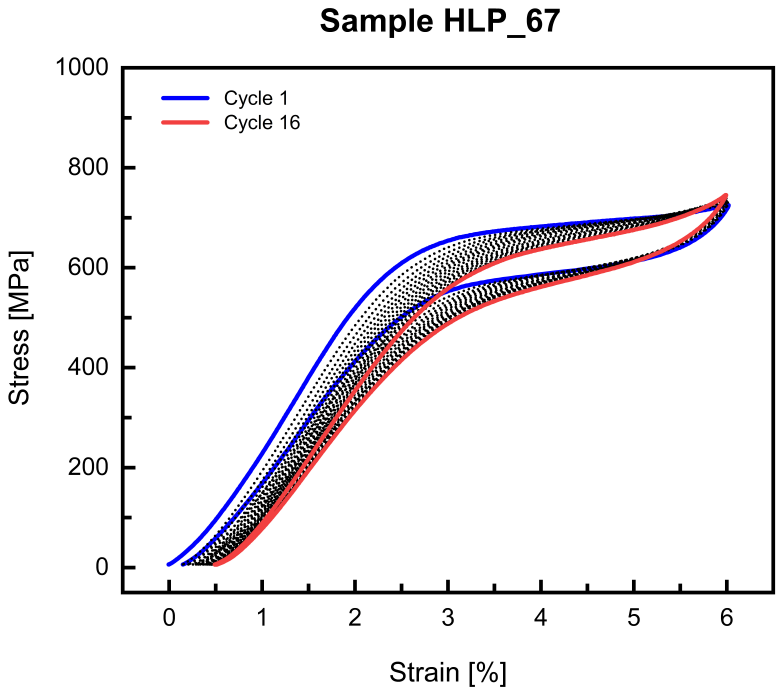


Figure 4.32: Cyclic axial compression test for HLP_67, showing the full superelastic response of the sample.

Table 4.8: Details of the superelastic response of the HLP_67 sample

Sample	Cycle	Recoverable strain, ε_{rec}, [%]	Recovery Ratio, [%]	Maximum stress, σ_{max}, [MPa]	Stress Hysteresis, [MPa]	Hardening Rate, [MPa]
HLP_67	1	5.9	97.6	725.2	33.1	16.9
HLP_67	16	5.5	91.5	745.4	37.6	37.0
island_67	1	5.7	94.6	744.2	42.7	32.1
island_67	16	5.0	84.0	745.0	43.5	60.2
67	1	5.5	91.5	677.4	212.1	25.9
67	16	4.5	74.2	704.8	3.6	78.9

Concluding this Section, the beneficial influence of an increased laser power setting on producing parts

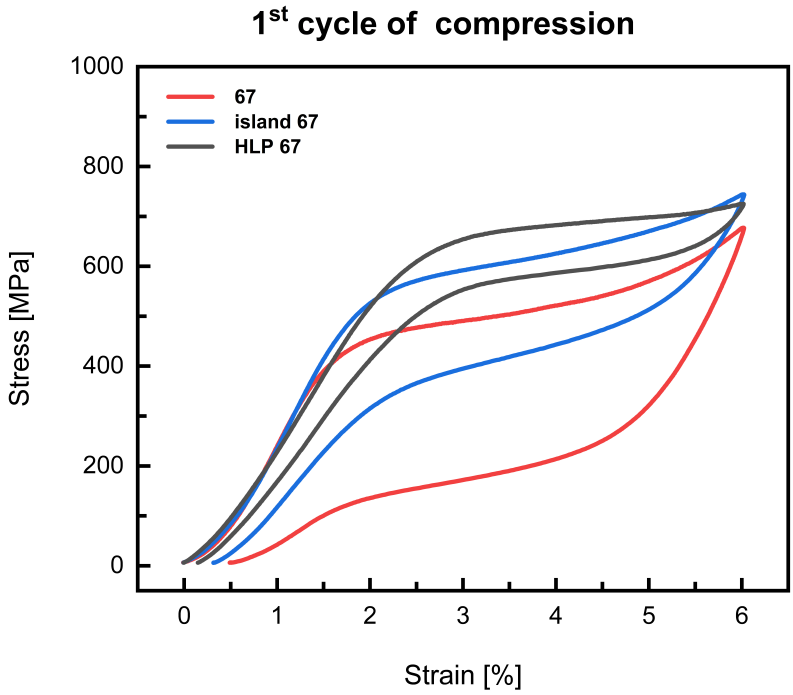


Figure 4.33: 1st compression cycle for HLP_67, island_67 and 67 samples.

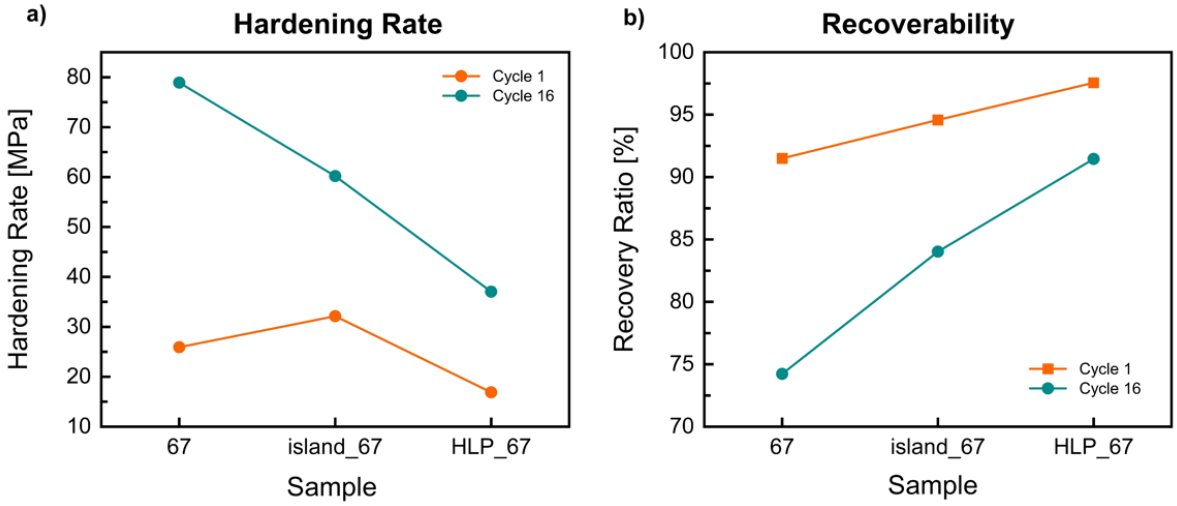


Figure 4.34: ***a)*** Hardening rate and ***b)*** recovery rate plots for samples HLP_67, island_67 and 67.

by the L-PBF method which showcase supreme superelastic response has been illustrated. The effect of the laser power on the microstructure morphology and texture is once again proven by means of various characterisation techniques, and, in addition to that, the superb functional response that such a process parameter can produce when paired with a suitable scanning strategy is shown here for the first time. It is evident from the results of the mechanical test that various features of the superelastic behaviour can be influenced by implementing a higher laser power condition together with a scanning strategy which was proven to be beneficial for the superelastic response, opening up new possibilities for increased control of the resulting microstructure and functional behaviour of NiTi parts fabricated by L-PBF. Referring back to Table 4.5 these statements are further supported, as comparisons drawn between several NiTi alloy parts manufactured via L-PBF methods show that the HLP_67 sample presented here has managed to exhibit one of the best superelastic responses.

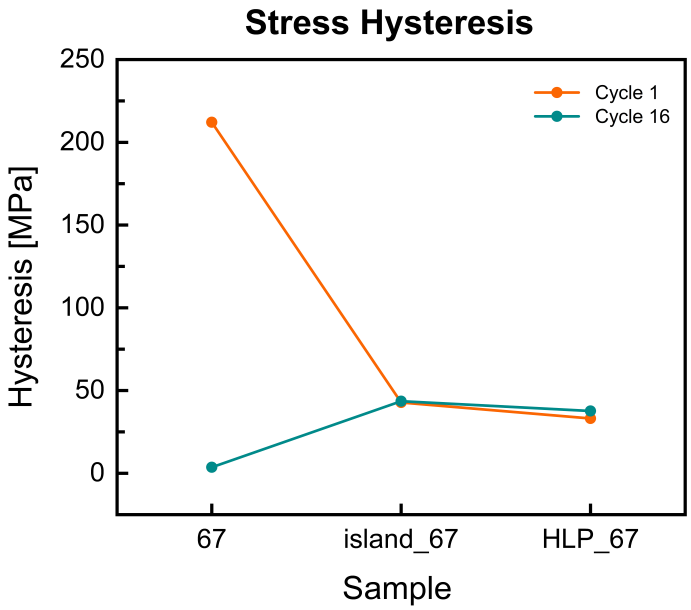


Figure 4.35: Stress hysteresis plot for sample HLP_67. Samples 67 and island_67 are also included for reference.

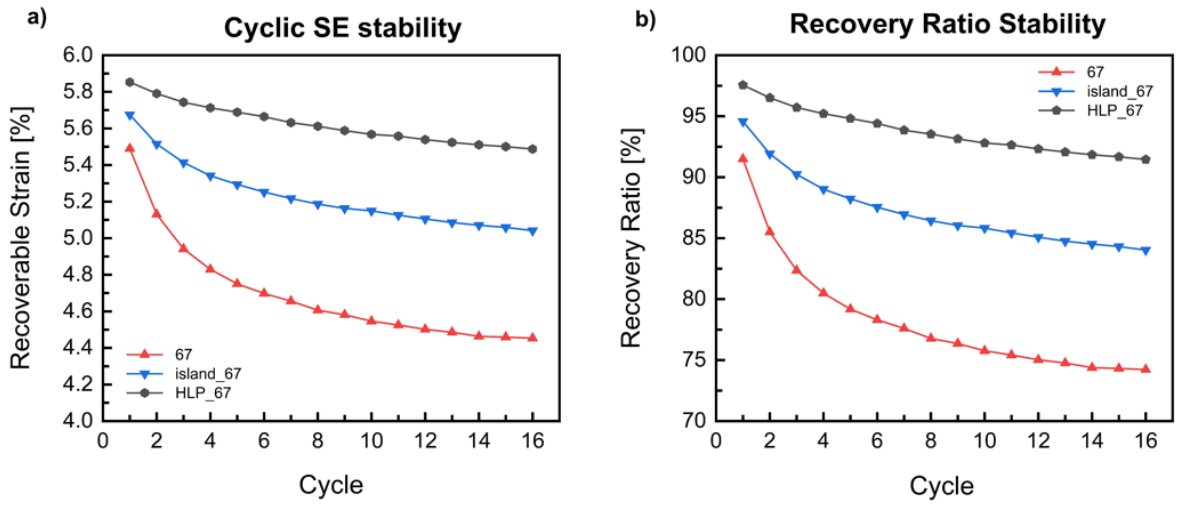


Figure 4.36: Cyclic stability plots for sample HLP_67. ***a)*** Recoverable strain versus cycles, and, ***b)*** Recovery ratio versus cycles. Samples 67 and island_67 are also included for reference.

4.3 Effect of the Loading Direction on the Functional Behaviour

4.3.1 Microstructure & Phase Transformation Features

As explained in Chapter 3, one batch of samples was axially compressed at a 90° angle to their BD, labelled as the Rot group. The purpose behind these tests was to investigate the functional response of the material at a loading scenario different to the one they were specifically designed to serve. This way, the effect of the loading direction on the thermomechanical behaviour of the samples would be studied.

As this test group essentially consisted of the samples fabricated using the 0°, 90°, 67° and 67° in island patterns scanning strategies, as well as the sample fabricated under the high laser power condition, several characterisation results remain unchanged. These include the SEM-EDS and Oxygen content measurements, all the OM results, the XRD analyses, as well as the DSC measurements. The reader is referred to Section 4.1.1, where these results are being discussed in detail.

Nevertheless, the situation is different for the EBSD measurements. For this characterisation method, the grain morphology results are obviously the ones discussed in Section 4.1.1 so they will not be repeated here. What does change for the Rot group however, is the orientation of the crystals with respect to the new loading direction for this set of compression tests. Therefore, the crystallographic texture characteristics of the Rot group samples are going to be separately discussed in this Section. It shall be noted that for this test group, the relevant Inverse Pole Figures are the [010] for the xz plane view maps (i.e. parallel to the BD) and the [100] for the maps corresponding to the xy plane of the samples.

Starting with the first sample, the 0-R sample, the immediate observation is the presence of a very weak texture in both the xz and the xy EBSD maps. Specifically, in the xz plane view, see Figure 4.37 a), a slightly tilted off-axis $\langle 001 \rangle$ is measured, whereas for the xy side of the sample it changes to a mixture of $\langle 001 \rangle$ and $\langle 101 \rangle$ orientations, with a slight dominance of the $\langle 001 \rangle$ crystal orientation, see Figure 4.37 b).

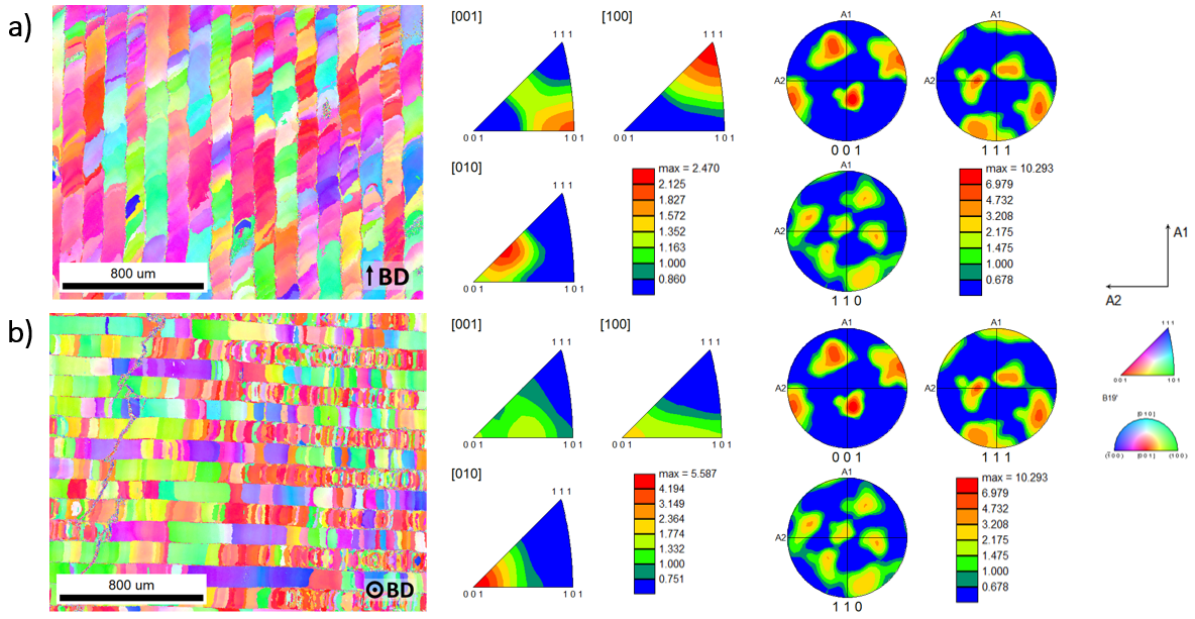


Figure 4.37: EBSD map of the xz plane, ***a)***, and the xy plane, ***b)***, for sample 0-R. The associated Inverse Pole figures and the pole figures are also included.

Sample 90-R does not show any significant difference, especially when considering the intensity of the texture observed. Figure 4.38 a) contains the information about the texture viewed along the sample's BD, where a mixture of $\langle 001 \rangle$ with a hint of $\langle 101 \rangle$ cube texture is measured, again in a very weak intensity. The view of the xz plane offers a marginally stronger texture, with the main crystal orientation measured as being the $\langle 101 \rangle$, see Figure 4.38 b).

Sample 67-R is the first of the five samples examined in the Rot group where texture starts becoming more pronounced. The spatial orientation of the NiTi crystals along the BD creates a mixture of $\langle 001 \rangle$ and $\langle 101 \rangle$ orientations, see Figure 4.39 a), with clear banding of the grains, see the pole figures of the same figure. Viewing the sample along its xy plane, there is a fibre texture observed, mainly comprised of orientations starting at the $\langle 001 \rangle$ orientation and covering all orientation between this and the $\langle 101 \rangle$ orientation, see Figure 4.39 b) the mosaic of red, yellow and green grains.

The island_67-R sample is the sample where texture becomes adequately pronounced. Along the BD, Figure 4.40 a), crystals solidified obtaining a mixture of $\langle 001 \rangle$ and $\langle 101 \rangle$ orientations. The fibre texture seen on the xy plane offers the same mixture of orientations, see Figure 4.40 b).

Finally,the HLP_67-R sample, as expected shows the strongest texture along its BD, with crystals attaining the $\langle 001 \rangle$ almost exclusively. There is one or possibly more crystals seen at the left side of the EBSD map of Figure 4.41 with the $\langle 101 \rangle$ orientation, but generally the pole figures suggest the existence of a strong cube texture mainly revolving around the $\langle 001 \rangle$ orientation.

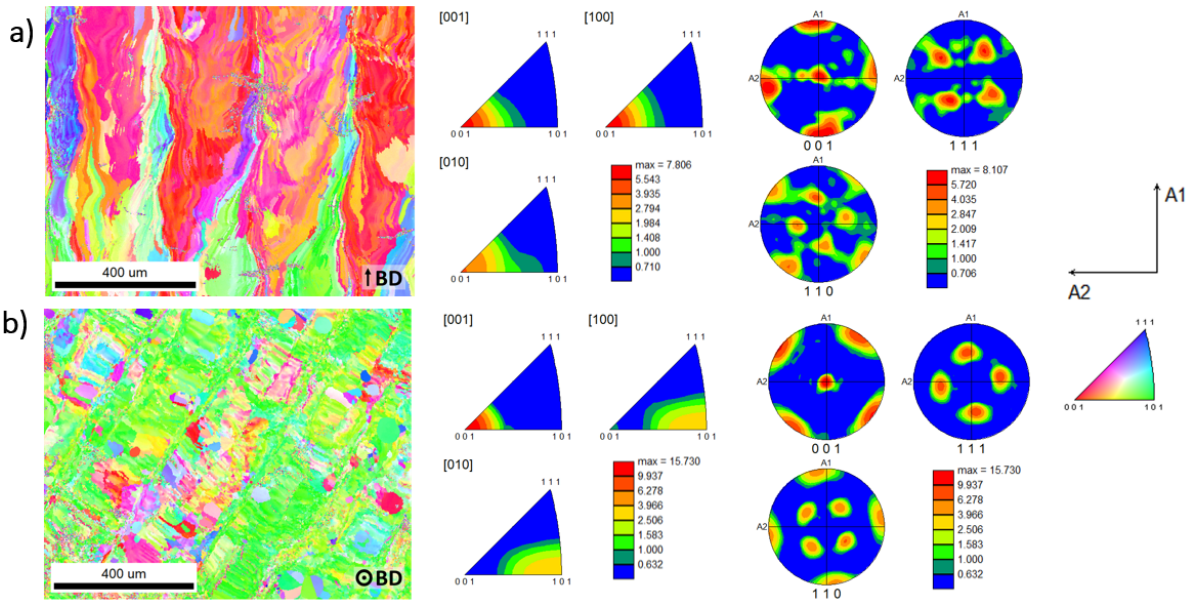


Figure 4.38: EBSD map of the xz plane, ***a)***, and the xy plane, ***b)***, for sample 90-R. The associated Inverse Pole figures and the pole figures are also included.

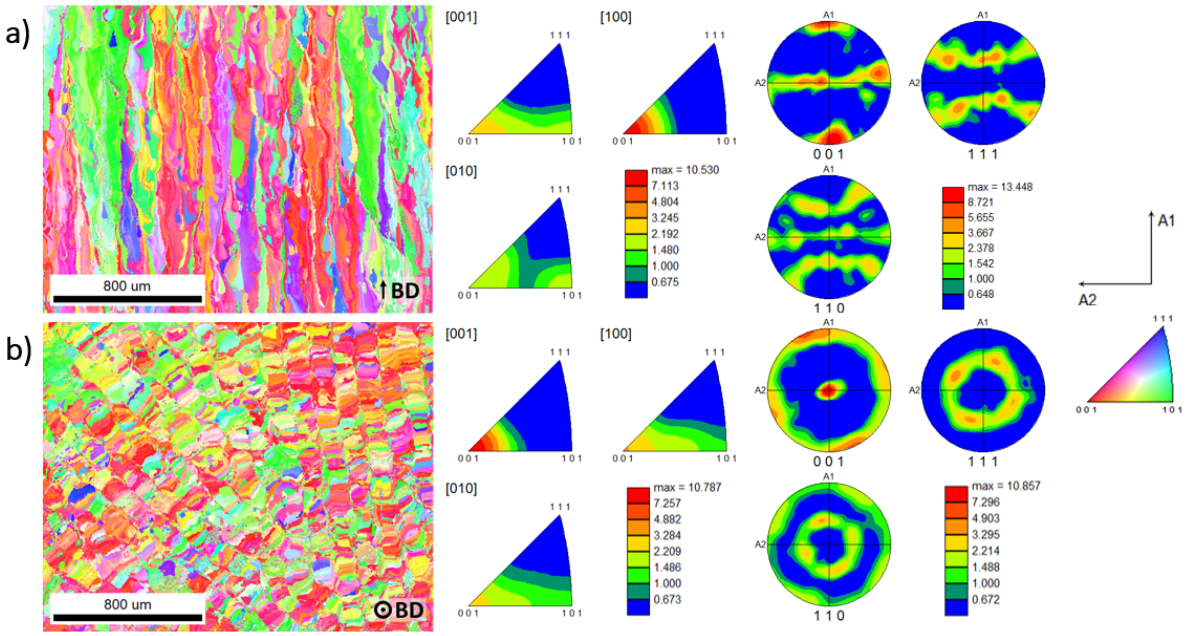


Figure 4.39: EBSD map of the xz plane, ***a)***, and the xy plane, ***b)***, for sample 67-R. The associated Inverse Pole figures and the pole figures are also included.

Overall, the crystallographic textures observed for this group of samples do not provide any particular new aspect to the situation analysed so far. As expected, orientations of the crystals do indeed differ, as they are “seen” from a different vantage point relative to the crystal lattices. Certainly though differences in the functional behaviour are expected to stem from those microstructures, as superelasticity is a behaviour heavily dependent on the crystal orientation and morphology.

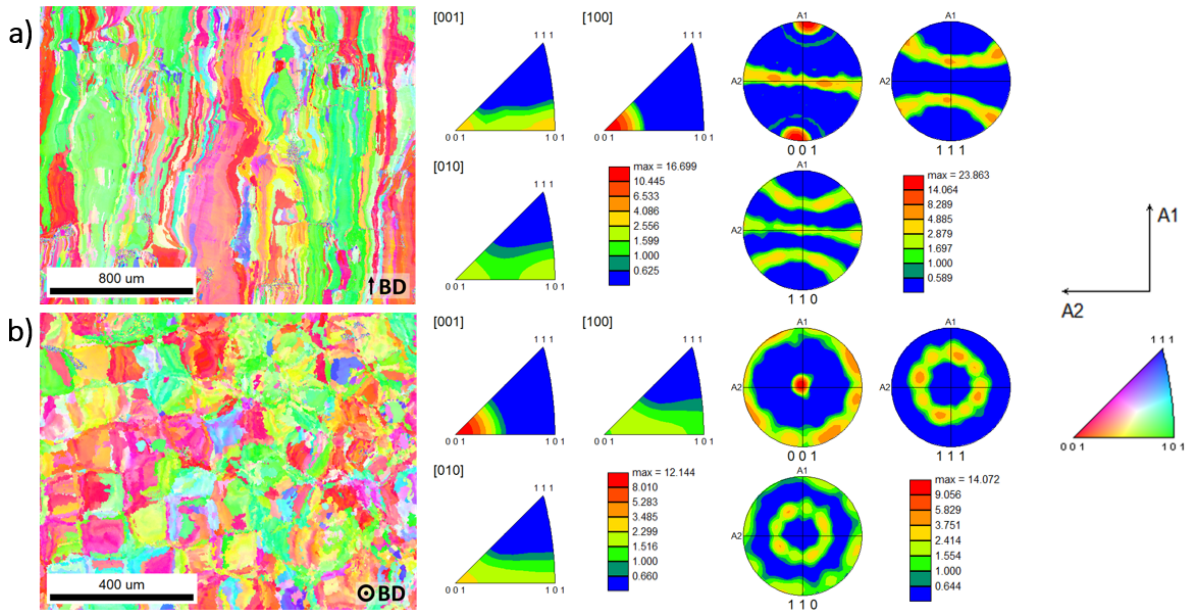


Figure 4.40: EBSD map of the xz plane, ***a)***, and the xy plane, ***b)***, for sample island_67-R. The associated Inverse Pole figures and the pole figures are also included.

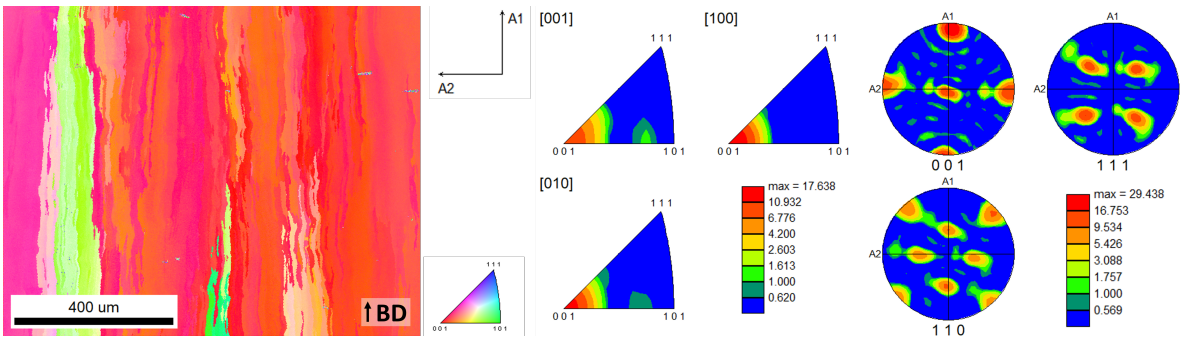


Figure 4.41: EBSD map for the xz plane view of the HLP_67 sample. The associated Inverse Pole figures and the pole figures are also included.

4.3.2 Functional Behaviour

Figure 4.42 a) - e) presents the full compression test results for the five samples of the Rot group. Figure 4.42 f) gathers the first compression cycle for all the samples and allows for comparisons between the superelastic responses produced by each of the samples.

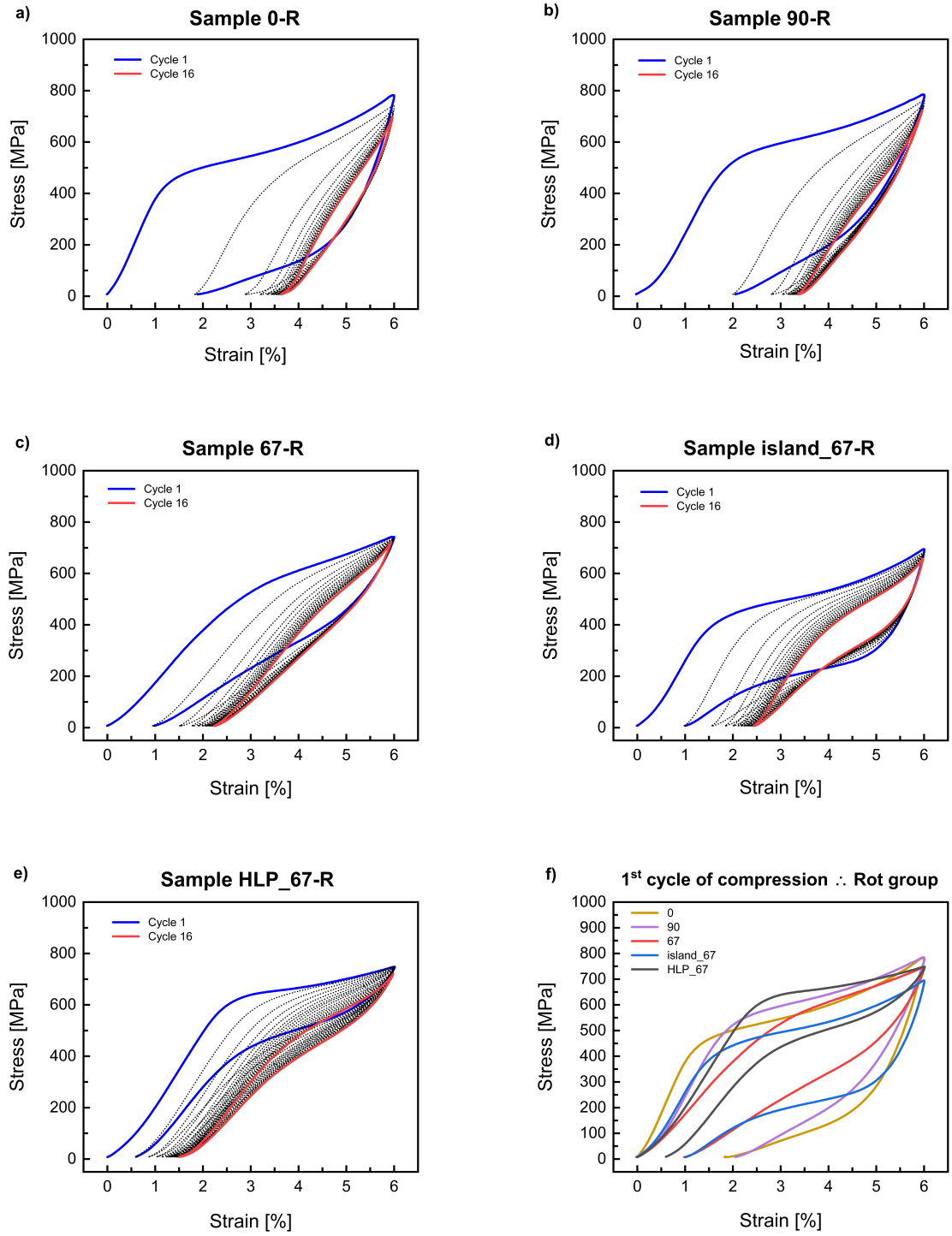


Figure 4.42: ***a) - e)*** Cyclic axial compression test for the 0-R, 90-R, 67-R, island_67-R and HLP_67-R samples respectively. For all specimens, the first compression cycle is depicted in blue, the 16th cycle in red and the cycles in-between are given by black dotted lines. ***f)*** First cycle of the compression test for all samples of the Rot group.

Starting the discussion from the least textured samples, the 0-R and the 90-R samples, the first observation is the relatively improved superelastic response both of them showcase under this loading condition with respect to their counterparts analysed in Section 4.1.2. This is stated mainly because of the improved behaviour during the unloading portion of the compression curves, which for both the 0-R and the 90-R samples resembles the theoretical behaviour more closely. In both samples the linear elastic unloading part of the curve can be seen, similarly the transformation plateaus for both the

forward and the reverse transformations can be detected, see Figure 4.42 f). Such behaviour can be attributed to the fact that the grains of both samples are now oriented along the $\langle 001 \rangle$ direction along their BD, something which was not the case for the 0 sample when the loading was parallel to the z axis. Therefore, for this loading scenario, the grains are more favourable oriented for a accommodating the loading through the phase transformation. Nevertheless, the superelastic response is not very strong, as both samples stabilise to recoverable strain value around 2.5% and recovery ratios below 50%, see Table 4.9. Additionally, both samples exhibit large hardening rates and stress hysteresis, see Figures 4.43 a) and 4.44.

The superelastic response of sample 67-R as seen in Figure 4.42 c) at first glance seems rather disappointing, however, close inspection of the data presented in Table 4.9, the actual situation is much different. Although the phase transformation regions on the compression curves of the sample are not very pronounced, the sample showcases improved recovery ratio and recoverable strain values when compared to the 0-R and 90-R samples. Recoverable strain after 16 cycles reaches values of 3.7% with recovery ratio of the order of 62.4%. The differences in the behaviour can once more be attributed to the crystallographic texture. For this loading condition, the 67 sample has its grains oriented in both the $\langle 001 \rangle$ and the $\langle 101 \rangle$ directions, in contrast to the pure $\langle 001 \rangle$ shown by the 67 sample examined in Section 4.1. This means that the superelastic response is bound to be less potent as the deformation is accommodated by grains favourably oriented as well as less favourably oriented to the applied stress.

The island_67-R sample shows very good superelastic response as did the island_67 sample discussed in Section 4.1.2, apparently because there are no substantial changes between the crystallographic orientations adopted by the grains between the two samples. The plateau regions associated with the phase transformations responsible for the superelasticity are clear in this sample, see Figure 4.42 d) and f). It shall be noted that this sample exhibits the lowest maximum stress levels than any other sample of the Rot group, see Table 4.9. Nevertheless, its recoverability, both in terms of recoverable strain and recovery ratio resides in the neighbourhood of the values measured for the 67-R sample, i.e. 3.5% and 60% respectively after 16 cycles of compression loading.

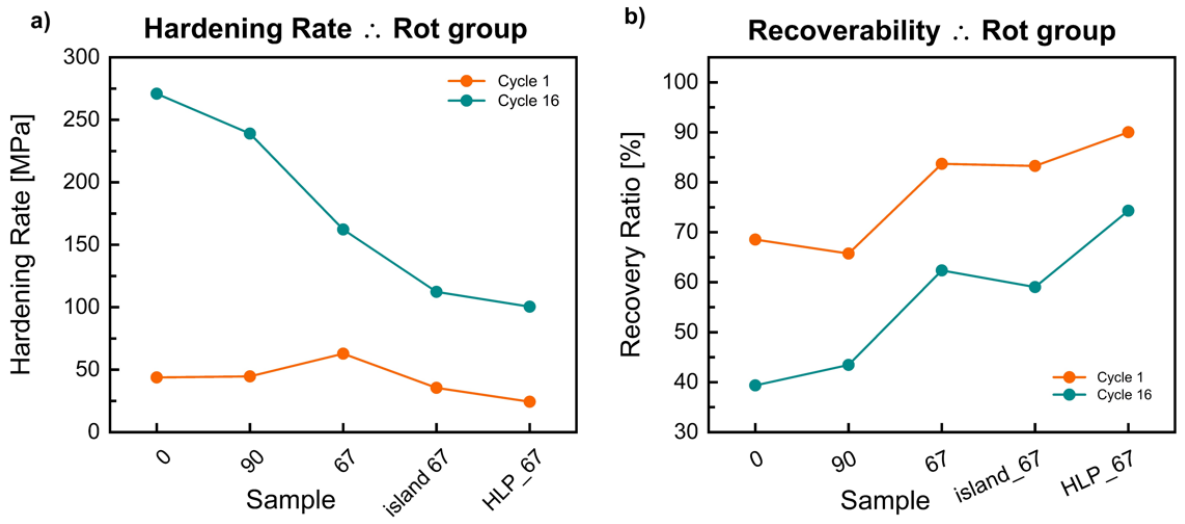


Figure 4.43: Plots of the hardening rate, ***a)***, and the recoverability, ***b)*** for the samples of the Rot group.

Finally, the HLP_67-R sample shows the best superelastic response of all, Figure 4.42 e). This is the sample with the highest value of the critical stress for the triggering of the forward phase transformation, see Figure 4.42 f), as well as the best recoverability. The measured recoverable strain after 16 cycles of loading reaches 4.5% with corresponding recovery ratio equal to 74.3%, see Table 4.9. Notable is the fact that in the first compression cycle the recovery rate of the HLP_67-R sample equals 90%. The result is not surprising, as in terms of its microstructure this sample showed both morphology and texture very close to the “ideal” situation.

HLP_67-R as well as island_67-R are the two samples whose stress hysteresis increases as the cycles progress, see Figure 4.44, corresponding to an increase in the amount of energy associated with the

phase transformation. The other three samples, namely 0-R, 90-R and 67-R, all show decreasing stress hysteresis through the course of their compression.

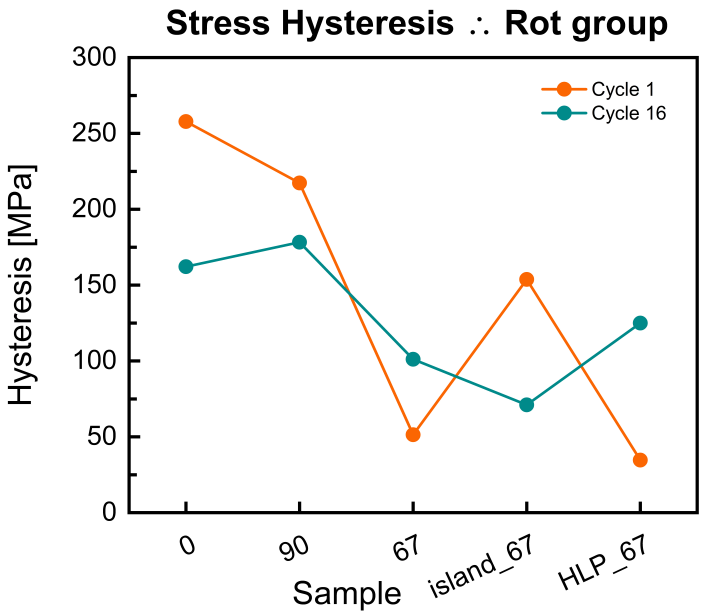


Figure 4.44: Plot of the stress hysteresis measured for the samples of the Rot group.

As far as the cyclic stability of the superelasticity of the Rot group samples a few remarks are due. Firstly, there is a clear differentiation between the five samples and their behaviours. As one can see in Figure 4.45 a) and b), samples 0-R and 90-R appear to group together as do samples 67-R and island_67-R. The HLP_67-R sample is the one showing superior superelasticity in terms of recovery ratio and recoverable strains as function of the compression cycles, a behaviour which also appears to be less susceptible to degradation during the cycling, (comparison of the drops in the curves between cycle 1 and cycle 16).

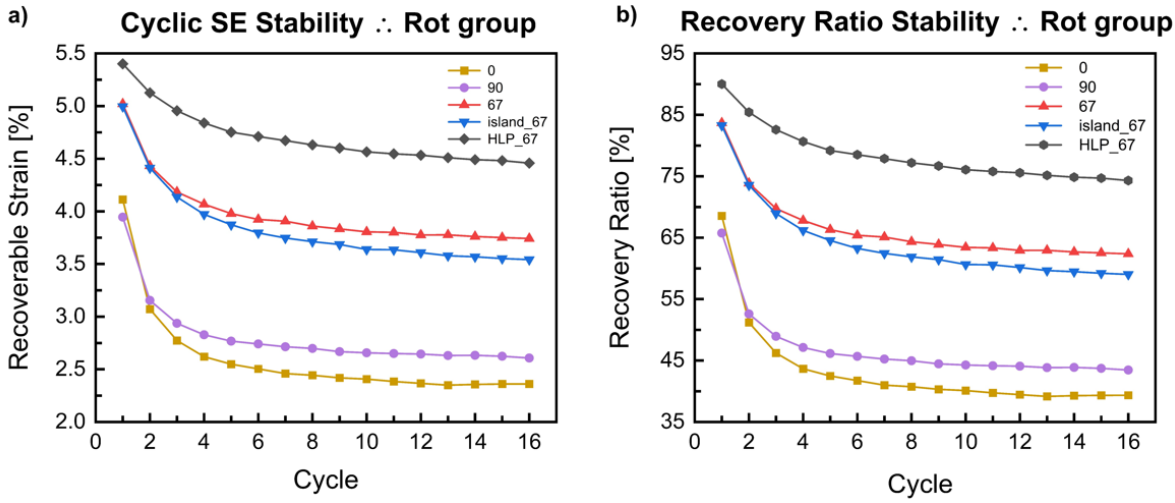


Figure 4.45: Cyclic stability plots for the samples of the Rot group. ***a)*** shows the recoverable strain as function of the cycles and ***b)*** depicts the recovery ratio versus the cycles.

Table 4.9: Details of the superelastic response of the samples of the Rot group

Sample	Cycle	Recoverable strain, ε_{rec}, [%]	Recovery Ratio, [%]	Maximum stress, σ_{max}, [MPa]	Stress Hysteresis, [MPa]	Hardening Rate, [MPa]
0-R	1	4.1	68.5	782.4	257.8	43.8
0-R	16	2.4	39.3	697.1	162.1	270.9
90-R	1	3.9	65.7	785.2	217.3	44.6
90-R	16	2.6	43.5	724.3	178.3	239.0
67-R	1	5.0	83.7	742.4	51.3	62.8
67-R	16	3.7	62.4	723.1	101.0	162.2
island_67-R	1	5.0	83.3	694.8	153.7	35.5
island_67-R	16	3.5	59.0	657.4	71.1	112.3
HLP_67-R	1	5.4	90.0	748.4	34.7	24.4
HLP_67-R	16	4.5	74.3	721.0	125.0	100.5

Concluding this Section, it can be said that the loading direction does not appear to have an extremely large effect on the superelastic response of the samples tested in the Rot group, in the sense that the behaviour, although admittedly inferior to the one measured for the LT and HT groups, is not heavily imbalanced. The scanning strategy effect on the thermomechanical response of the NiTi samples is clear; it renders the response directional in nature as the orientation of the crystals, which is inextricably tied to the functionality, is determined by the scanning strategy as explained in previous points of this report [36]. In general, the samples' performances are found to be following the same trend observed when the compression was applied along the BD, namely the HLP_67 shows the best performance, followed by the island_67 and the 67 samples, with the 0 and 90 samples showing poorer superelasticity. The result is expected, as all samples showed varying degrees of $\langle 001 \rangle$ orientations in their crystalline structures usually mixed with grains showcasing $\langle 101 \rangle$ orientations. Therefore, superelasticity was expected to arise as a functionality, to a lesser extend nonetheless. This result can provide useful insight into the functional response of NiTi SMAs fabricated by L-PBF in situations more closely resembling real-life scenarios, where purely uniaxial loading is rarely encountered.

4.4 Investigation of the Nature of Residual Strain

As seen in the graphs depicting the compression tests from the first to the last cycle, refer to Sections 4.1.2 and 4.2.2, at the end of the compression cycling a certain amount of strain has accumulated in the material and is common for it to be perceived as residual strain. In publications this residual strain is clearly reported, however, its nature is usually not investigated. According to the theoretical descriptions of the NiTi SMAs and superelasticity, the property is bound to degrade throughout the lifetime of the metallic part. This functional degradation is manifested by the accumulation of strain within the lattice, together with the increase of microstructural defects and dislocations, which over time inhibit the ability of the material to elastically transform between the two crystal structures associated with the austenite and the martensite phases. The reader is referred to Chapter 2 for an in-depth treatment of this concept.

However, not all of the residual strain which is measured at the end of every cycle of a mechanical test is strain which is truly unrecoverable, or, in other words plastic. There is a possibility that this residual strain, or some part of it, is actually associated with grains which were not able to transform back to the austenite phase during the reverse phase transformation that takes place during the mechanical unloading. These untransformed martensite grains are usually constrained by their surrounding crystals, which causes their inability to participate in the transformation process. Consequently, they require higher levels of stress in order for the transformation to be triggered for them and if these stress levels are not reached during the unloading, then these grains shall remain in their martensite phase, adding up to the general amount of residual strain found in the lattice.

On the other hand, as cycling of the NiTi alloy progresses, dislocations and other sources of plasticity arise within the lattice and gradually become stabilised and devoid the crystals from their ability to undergo transformations between the two solid phases. As a consequence, they create residual strains within the material, which due to their origin is impossible to be recovered, accumulate over time and lead to functional degradation and eventual loss of the property.

The idea behind the experimental approach described in this section was the need to be able to differentiate between the two possible components of the residual strain monitored at the end of the compression cycling of the NiTi samples. As explained in Chapter 3, specimens were heated to a high temperature, equal to 300°C in order for them to be fully able to recover all of their residual strain which could be recoverable, leaving behind the true plastic strain accumulated in the lattice due to the mechanical cycling. Meanwhile, this entire procedure enabled a glimpse into the ability of the samples to exhibit the TWSME, as this was discussed in Section 2.1.1. Essentially, it was investigated whether the samples, after undergoing isothermal mechanical training, they would be able to repeatedly reach a high temperature and a low temperature shape under a cyclic thermal loading condition.

EBSD measurements were taken for the samples after the end of the compression cycling described in Section 4.1.2 and Section 4.2.2. These can be seen in Figures 4.46, 4.47, 4.48, 4.49 and 4.50, where EBSD maps, IPF and pole figures are shown for the xz plane view of samples 90, 30, 67, island_67 and HLP_67 respectively. The purpose of the EBSD measurements was to identify possible areas of the martensite phase structure, as well as to detect any changes on the crystallographic texture which would be attributed to the cyclic compression loading during the mechanical tests. Due to the specifications of the SEM microscope which was used for the EBSD measurements, the martensite phase was not possible to be directly identified and measured by the equipment; instead, it emerges as points which were not indexed by the software, appearing as a mixture of grey-blue dots in the Figures. Obviously, appropriate cleanup procedures were applied to the data acquired by the measurements, which it is believed that have adequately separated, isolated and, in this way, correctly identified the non-indexed points which correspond to grains of the martensite phase.

Starting the discussion with the results of the high temperature strain recovery via TMA for sample 0, for which no EBSD map is available, it is seen in Table 4.10 that residual strain equal to 3.65% was measured at the end of the compression cycling. Figure **??** a) presents the combined graph of the compression test (cycles one and 16) and the strain recovery at high temperature via TMA, where the strain recovery can be clearly visualised. In fact the material undergoes a phase transformation during its heating to 300°C, indicated by the four changes in the slope of the curve corresponding to the heating. During this phase transformation the 0 sample manages to recover 66% of its residual strain, leaving behind 1.25% strain as plastic. Detailed presentation of the strain values and calculations can

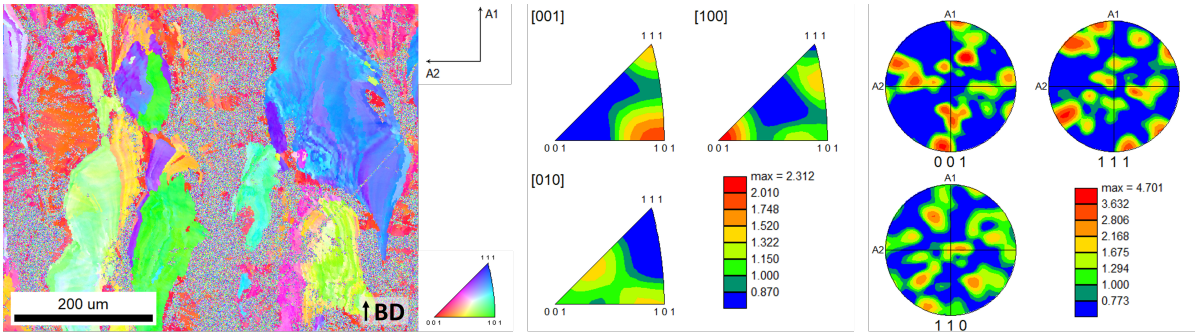


Figure 4.46: EBSD map for the xz plane view of sample 90 after the end of the cyclic compression. The associated Inverse Pole figures and the pole figures are also included.

be found for all samples in Table 4.10. Figure 4.55 shows in a graphical form the percentage of strain recovery achieved by TMA for each sample.

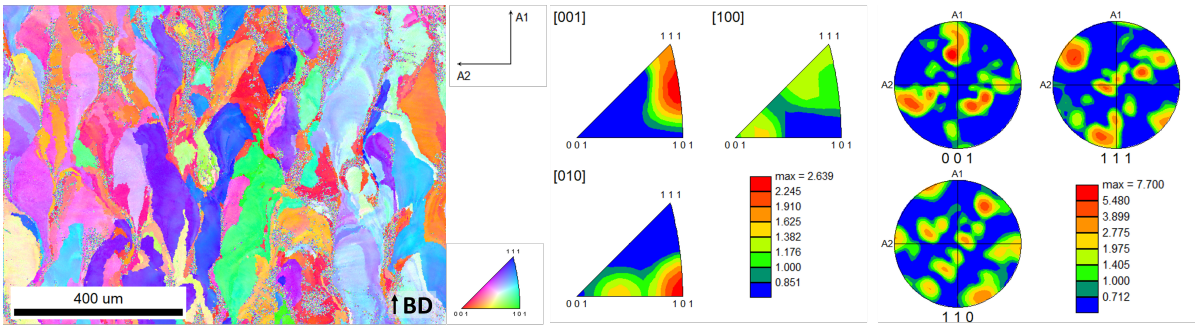


Figure 4.47: EBSD map for the xz plane view of sample 30 after the end of the cyclic compression. The associated Inverse Pole figures and the pole figures are also included.

Sample 90 shows large areas identified as martensite in its EBSD map shown in Figure 4.46 and a total of 2.02% of residual strain was measured for the sample after its 16 cycles of compression. Heating to 300°C led to a 92% recovery of that residual strain, amounting to nearly 2% of strain recovered via TMA and leaving 0.16% plastic strain in the lattice. This sample indeed exhibited the best performance in terms of the recovery of its residual strain via high temperature heating. This can lead to hypothesising that the poor superelastic response which it exhibited, see Figure 4.14 and Figure 4.18, was mainly due to its inability to transform the martensite created during the forward phase transformation back to the austenite phase during the unloading. Comparison of the first cycle of the 90 sample to the corresponding cycles of the 0 and the 30 samples, the three samples which show the poorest superelastic responses, indicates that the unloading portion of the 90 sample is marginally closer to the "*ideal*" shape of the unloading curve, as this is depicted in Figure 3.10.

The inability of sample 90 to show a successful superelastic response during its unloading is possible to be partly related to its weak crystallographic texture and partly to the presence of high residual stresses in the lattice which were introduced during the L-PBF fabrication. In general, in a bi-directional scanning strategy the direction of the heat dissipation is also bi-directional as it follows along the scanning vector [69]. Applying a 90° interlayer rotation in the scanning strategy forces the heat flux to rotate as well, closely following that rotation angle. Since the largest stress develops along the direction of the scanning vector [48], it becomes apparent that the stresses that develop internally in the lattice during the L-PBF process are very directional and they inevitably affect the microstructure. One way of doing so may be by constraining grains during the deformation process, thereby not allowing them to transform to the other crystal structure. Heating at high temperature would lead to these stresses being relieved, eventually allowing the associated grains to experience the phase transformation, which would explain this enormous strain recovery observed for sample 90.

For sample 30 it was impossible to complete the entire 16 cycles of compression during its mechanical

test, hence the recovery via TMA only concerns the residual strain accumulated in the lattice during the first cycle of compression. For this reason the results of this sample should be handled with care when comparisons are being drawn between this and the rest of the samples studied in this Section, as its superelastic behaviour cannot be in any way considered stabilised. Nevertheless, the EBSD measurements, Figure 4.47, revealed signs of untransformed martensite grains within its microstructure, by no means as extended as in the case of the 90 sample, which is expected since the sample's functional response is not developed or fully stabilised at this point. Strain recovery via TMA achieved a 65% recovery of the residual strain observed after the one cycle of mechanical compression, recovering 2.03% strain out of the 3.12% measured after the compression cycle. Table 4.10 summarises the results, where it can be seen that for sample 30, approximately 1.1% of plastic strain is calculated to have accumulated in the NiTi lattice after the high temperature recovery step.

The 30° interlayer rotation angle of the scanning strategy used for fabricating this particular sample ensures that a very uniform spatial distribution of the heat flow will occur. Therefore, the residual stresses which will inevitably arise during the L-PBF manufacturing shall be lower in magnitude and shall also be more evenly distributed causing more uniform deformation of the sample after fabrication, e.g. warping [45]. Hence, even though the thermomechanical behaviour of this particular sample is rather unidentified, it is likely that the unrecoverable strains encountered at the end of the compression cycles are related more to plasticity-inducing defects, such as dislocations, than to internal stresses developed during manufacturing.

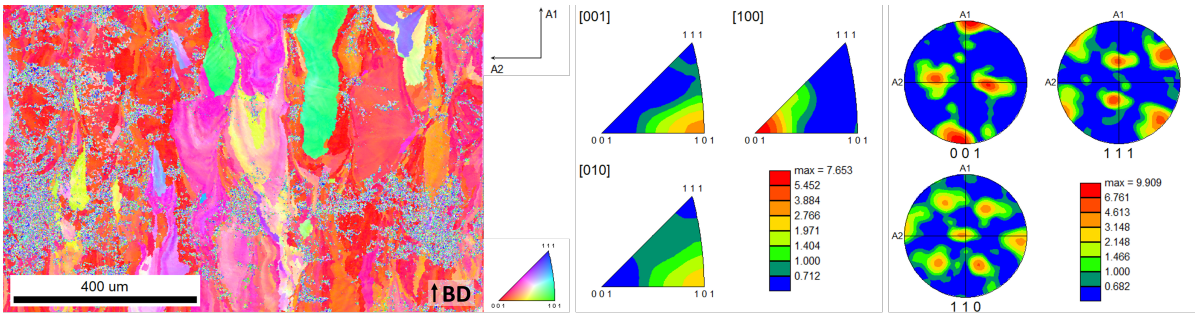


Figure 4.48: EBSD map for the xz plane view of sample 67 after the end of the cyclic compression. The associated Inverse Pole figures and the pole figures are also included.

As can be seen in Table 4.10, sample 67 recovered approximately half of the residual strain it was accumulated at the end of the 16 compression cycles, or 0.85% strain was recovered upon the high temperature heating step. Although the sample does not seem to be ridden by untransformed martensitic grains at the end of its mechanical testing, see Figure 4.48, it does show considerable amount of areas associated with the B19' phase. Additionally, another look at the EBSD map of Figure **??** reveals that a considerable amount of grains have solidified adopting a $\langle 101 \rangle$ orientation. These grains is highly likely that did not participate successfully in the superelastic response of the sample, contributing to the residual strain. High temperature heating would allow these grains to recover their strain, leading to strain recovery above 50% by TMA for sample 67.

As the data of Table 4.10 reveal, island_67 sample was the specimen for which the second smallest amount of residual strain was measured after the 16 cycles of compression loading were completed (0.87% residual strain), an effect expected as the sample showcased a strong $\langle 001 \rangle$ crystallographic texture along its BD, leading to its superior superelastic behaviour. EBSD measurements did not indicate extensive areas of the martensite phase left after the stabilisation of the superelasticity, in fact, a rather limited number of grains seem to be in a state of martensite phase, see Figure 4.49. The most notable difference between the microstructure of the as-fabricated condition and the superelasticity stabilised condition (see Figure 4.10 a)) is the reorientation of a number of grains, as the texture measured appears to have become stronger after the cyclic compression loading. High temperature strain recovery via TMA achieves the recovery of 72% of the residual strain, leaving an estimated 0.24% of plastic strain in the lattice, the second smallest amount calculated after sample 90.

Another interesting fact about this particular sample is that according to studies concerning the effect of the scanning strategy on the residual stresses developing during L-PBF fabrication, the island scanning

of the powder layers leads to reduction of the residual stresses much greater than those observed by strategies which scan the entire layer at once [36] [69] [58]. This is because the length of the scanning vector is drastically reduced in scanning strategies which incorporate island patterns which results in maintaining the scanned layer surface at a higher temperature at the moment when the next layer is scanned, decreasing the temperature gradient that arises along the solidification front and effectively leading to reduced levels of residual stresses in the metallic part. Therefore, for the case of the island_67 sample the conjecture can be made that the internal stresses developed during L-PBF contribute little to the residual strain measured at the end of the compression test. In this case, the very high percentage of strain recovery via TMA measured comes again from the grains which had solidified at orientations different than the $\langle 001 \rangle$, mostly the $\langle 111 \rangle$, which, during the high temperature heating become unconstrained of their surroundings and recover their deformations.

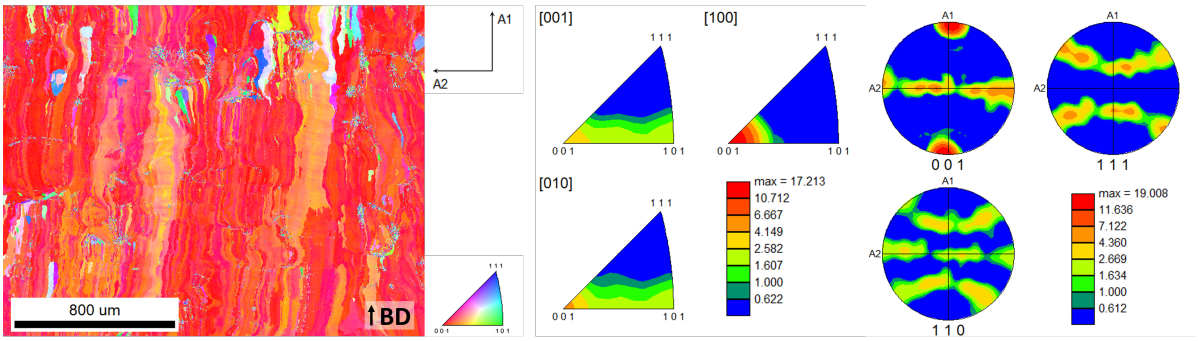


Figure 4.49: EBSD map for the xz plane view of sample island_67 after the end of the cyclic compression. The associated Inverse Pole figures and the pole figures are also included.

Sample HLP_67 exhibited the highest recovery ratio associated with its superelastic response, see Figure 4.34 b) and Table 4.8, with 0.51% strain left as residual in the lattice after the 16 cycles of mechanical compression loading. The EBSD map, shown in Figure 4.50, depicts almost no signs of martensite left in the matrix untransformed after the superelastic response has stabilised, but comparison between the {001} pole figure of Figure 4.50 and Figure 4.28 indicates a slight decrease in the intensity of the measured texture. Moreover, as the [100] inverse pole figures of those figures suggest, there has been some reorientation of some of the grains, as orientations other than the $\langle 001 \rangle$ appear as well after the compression. High temperature strain recovery via TMA, seen in Figure **??** f), achieved a recovery of only 2.0% of the residual strain (equal to 0.01% strain being recovered), leaving a total of 0.5% plastic strain, see Table 4.10.

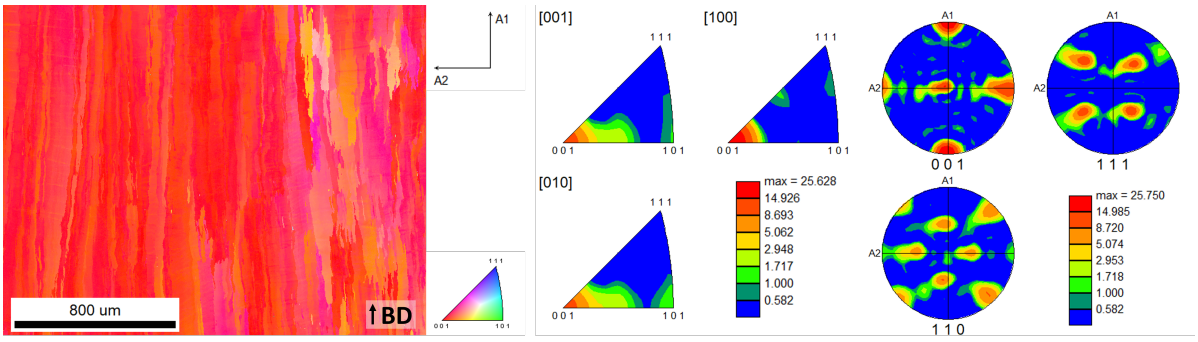


Figure 4.50: EBSD map for the xz plane view of sample HLP_67 after the end of the cyclic compression. The associated Inverse Pole figures and the pole figures are also included.

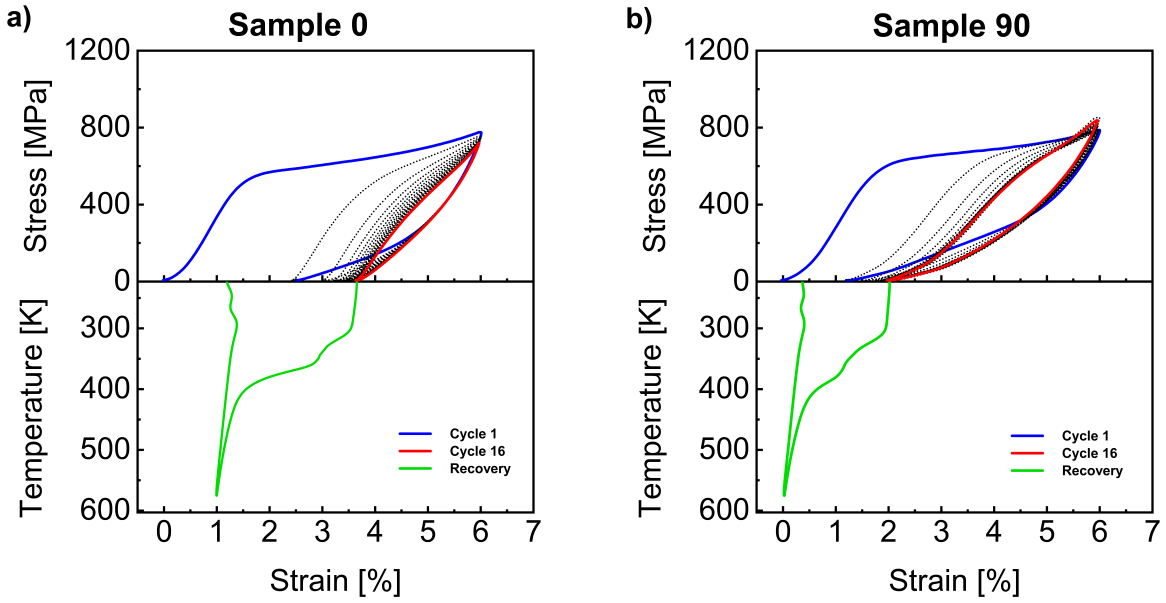


Figure 4.51: ***a)*** Plot depicting the superelastic response of sample 0, and, ***b*** sample 90. The plots include the amount of strain recovered during the high temperature heating during the TMA test.

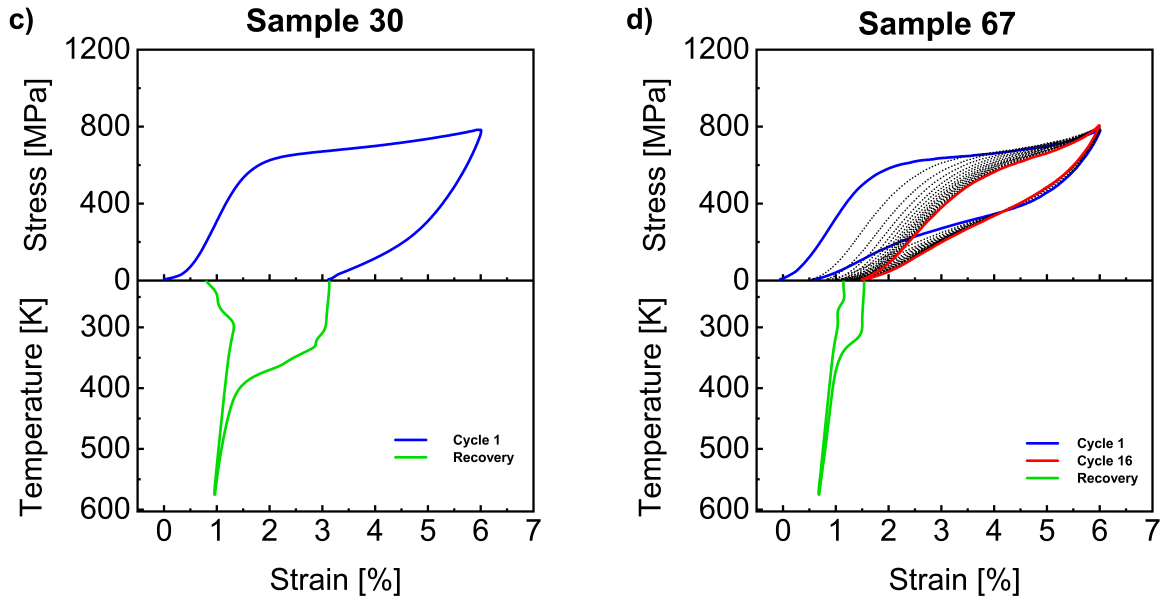


Figure 4.52: ***c)*** Plot depicting the superelastic response of sample 30, and, ***d*** sample 67. The plots include the amount of strain recovered during the high temperature heating during the TMA test.

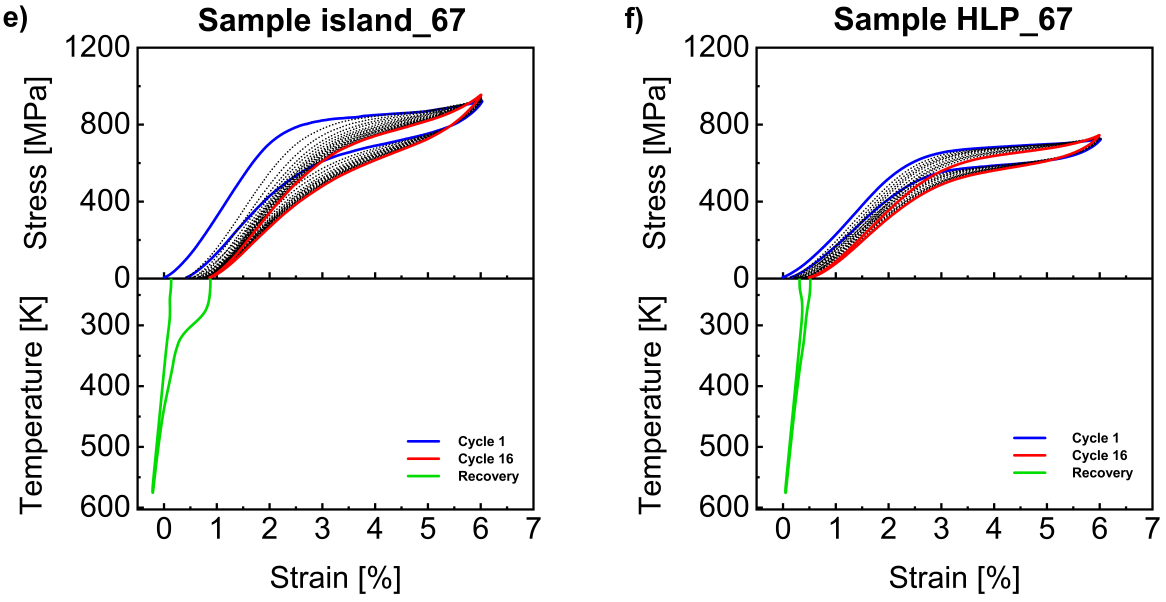


Figure 4.53: ***e)*** Plot depicting the superelastic response of sample island_67, and, ***f*** sample HLP_67. The plots include the amount of strain recovered during the high temperature heating during the TMA test.

Overall, the high temperature strain recovery attempt discussed in this section was successful in determining the nature of the residual strain left in the samples after the stabilisation of their superelastic behaviour has been achieved. All samples showed that a percentage of what was reported as residual strain was in fact associated with grains still in their martensite phase after the lattice had supposedly undergone its reverse transformation. In the cases of the samples which were found in the previous sections of this Chapter to perform rather poorly in terms of their superelasticity, large percentages of the residual strain were recovered during the high temperature heating via TMA presented in this Section, a confirmation that their poor superelastic response was due to the very weak reverse transformation they managed to exhibit during their mechanical compression test. This could be traced back to the weak and overall *non-ideal* crystallographic texture of these three samples, which was a direct consequence of their respective scanning strategies, as explained in Section 4.1. The effect of internal stresses developing during the L-PBF fabrication of the samples on their ability to recover strains was also discussed, and attempts were made to link this aspect to the behaviour exhibited by the samples during this type of tests.

Table 4.10: Details of strain values associated with the high temperature recovery

Sample	Residual strain after SE, ε_{res}^{SE}, [%]	Residual strain recovered during TMA, ε_{rec}^{TMA}, [%]	Plastic strain, $\varepsilon_{plastic}$, [%]	Percentage of strain recovered by TMA, [%]
0	3.65	2.4	1.25	65.8
90	2.02	1.86	0.16	92.1
30	3.12	2.03	1.09	65.1
67	1.54	0.85	0.68	55.2
island_67	0.87	0.63	0.24	72.3
HLP_67	0.51	0.01	0.5	2.9

Focusing on the two best performing samples, namely the HLP_67 and the island_67, a clear difference can be seen in their responses to the high temperature strain recovery. The island_67 sample shows an impressive strain recovery via TMA, which reaches almost 73% of its residual strain, with nearly

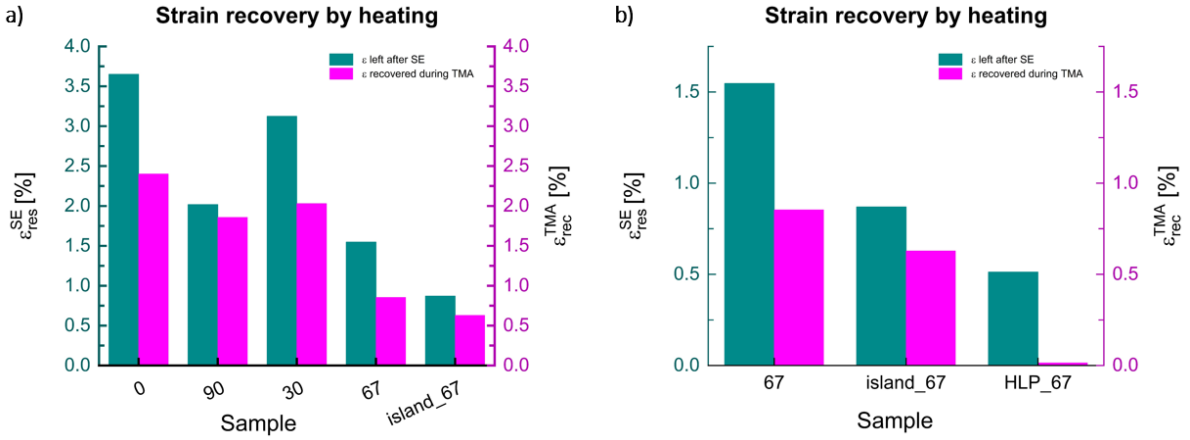


Figure 4.54: Comparison between the residual strain left after the stabilisation of the superelastic behaviour, ε_{res}^{SE}, and the strain recovered by the high temperature heating during TMA, ε_{rec}^{TMA}. Samples discussed in Section 4.1 are shown in ***a)*** and samples 67, island_67 and HLP_67 are shown in ***b)***.

half the amount of plastic strain accumulating in the lattice compared to the HLP_67 sample. On the other hand, the HLP_67 sample, although it recovers only 2% of its residual strain, and it accumulates double the plastic strain calculated for the island_67 sample, it overall seems that, due to its superior superelastic response, is able to recover the majority of its recoverable strain purely by the mechanical loading. This fact is of great significance, as by definition the superelastic behaviour is strictly induced by means of pure mechanical loading. Hence, this frivolously perceived poor aspect of the HLP_67 sample performance, truly is yet another testament to its superior superelastic response, as it achieves excellent levels of strain recovery solely by mechanical loading.

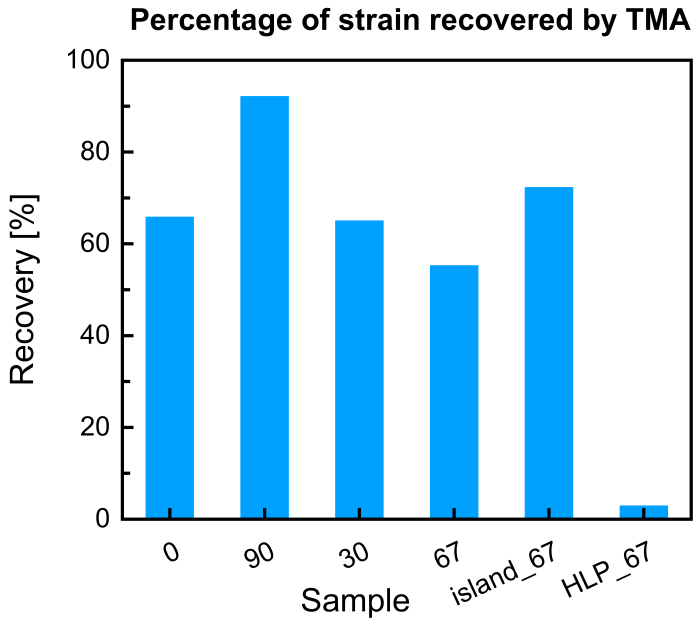


Figure 4.55: Percentage of strain recovery achieved by the TMA test procedure for all samples. Values are given in the last column of Table 4.10

5

Conclusions

In summary, this thesis aimed at presenting the investigation of five different scanning strategies implemented during L-PBF fabrication of Ni-rich NiTi SMA with respect to their influence on the microstructure and the functional response of the material. Based on the Research Objectives stated in Section 2.4, the following conclusions can be drawn from this study:

Research objective 1 - What is the effect of L-PBF scanning strategies on the microstructure of Ni-rich NiTi SMAs?

The scanning strategy employed during AM fabrication has a clear effect on the microstructure of Ni-rich NiTi parts manufactured by L-PBF. Incorporating an interlayer rotation of the scanning vector in the scanning strategy promotes the fusion of neighbouring melt pools, increasing their width and decreasing their depth, consequently leading the solidification process to proceed epitaxially and in a direction parallel to the BD.

Simultaneously, rotation angles which enhance the alignment of the *easy-growth direction* of the NiTi B2 lattice to the direction of the maximum heat flow, induce crystallographic textures of varying intensities focused on the $\langle 001 \rangle$ orientation. A 67° rotation angle between successive layers was found to be the one which results in both columnar grains solidifying epitaxially along the BD of the samples and in strong $\langle 001 \rangle$ fibre crystallographic texture along the direction of the z-axis.

Implementation of process parameters, other than the scanning strategy, which result in increasing the volumetric energy density, such as a flat top laser beam with larger beam size which affects the absorption of the laser energy by the NiTi powder, is known to result in melt pools of increased width and decreased depth. Such geometry of the conduction-mode melt pool favours grain solidification to occur almost exactly parallel to the BD. This research has successfully demonstrated that combining this condition with the successful 67° rotation scanning strategy can yield NiTi samples which are nearly single-crystalline in nature, with a strong $\langle 001 \rangle$ along the BD texture, with intensity reaching 30%.

Research objective 2 - What is the effect of L-PBF scanning strategies on the superelastic response of Ni-rich NiTi SMAs?

Superelastic behaviour can be successfully manipulated by the crystallographic texture and the grain morphology, which are in turn affected by the scanning strategies. Each scanning strategy studied in this project produced a unique superelastic response, with varying levels of recovery ratio, recoverable strain, stress hysteresis and cyclic stability effects. It was found that the scanning strategies which resulted in large columnar grains oriented in the $\langle 001 \rangle$ direction along the BD, also showcased supreme superelasticity. The single crystal structure of the HLP_67 sample exhibited recoverable strain stabilised at 5.5% with corresponding recovery ratio equal to 91.5%, whereas the less intensely textured island_67 measured 5.0% stabilised recoverable strain with 84% recovery ratio and the third best performing sample, sample 67, exhibited 4.5% recoverable strain with 74.2% recovery ratio. All three samples

compare exceptionally well with the theoretical maximum recoverable strain for [001] oriented NiTi single crystals of 5.3%, reported by K. Gall et al. [68].

Research objective 3 - What is the effect of loading direction and crystal orientation on superelastic response of Ni-rich NiTi SMAs?

The orientation-dependence of the functional behaviour of the NiTi alloys is also taken into consideration in this study. In general, loading perpendicularly to the sample's BD did yield the superelastic functionality, however this was found to be degrading more rapidly through the compression cycles, finally stabilising at significantly lower values for both the recoverable strain and the recovery ratio. Once again, samples manufactured using an interlayer rotation of 67° exhibited the best functional responses, concluding that these scanning strategies, i.e. both the single layer scanning and the one implementing island patterns, are likely to produce parts which can be used in real-life loading scenarios, where loading is multi-directional.

Research objective 4 - What is the nature of the residual strain measured after the superelastic response has stabilised?

An additional novelty of this thesis involves the investigation of the nature of the residual strain measured at the end of the cyclic compression tests. Varying levels of strain associated to martensite grains, which were not transformed during the mechanical loading alone, were found in the samples. These strains are thought to have been caused by the particular microstructure obtained by each scanning strategy (i.e. grain morphology and orientations) during L-PBF fabrication. Additionally, it is also possible that the internal stresses left in the lattice by the manufacturing have not been relieved during the cyclic compression tests, and consequently have accumulated as residual strain. The HLP_67 sample showed the least recovery by high temperature heating, indicating its tremendous superelastic capability, whereas the island_67 sample recovered 72% of its stabilised residual strain, illustrating the enormous effect that the few spatially "misoriented" grains have on the superelastic functionality. Most notably, sample 90 showed a recovery of 92% of its residual strain, indicating the significant role that internal stresses induced during the fabrication can have on both the microstructure and the functional property.

Finally, the following concluding remarks can be stated for the entirety of the research presented in the preceding Chapters:

1. One of the most interesting takeaways of this research is that although not all scanning strategies proved to be successful in producing parts with exceptional superelastic capabilities, it is likely that they hold the potential to induce certain microstructural features which can tailor said functionality to show specific characteristics. One example of such characteristics could be the width of the stress hysteresis.
2. In all respects, it was once again shown that the scanning strategy can be a vital tool in tailoring the crystallographic texture and the microstructural morphology of NiTi alloys, allowing for desired functional responses to be yielded from the additively manufactured alloy.

6

Recommendations for Future Research

The following recommendations are proposed for the continuation of the study presented in this thesis:

1. Additional rounds of axial compression tests are required in order to further increase confidence in the results obtained and presented in this study. This way aspects such as the stress hardening effect observed for sample 90 and the significantly high σ_{SIM}^{M} of the island_67 samples can be further investigated. Moreover, additional tests shall allow for better investigation of the behaviour of sample 30, which for technical reasons was not possible to be fully studied.
2. Reproducibility and repeatability of the Thermo-Mechanical Analysis (TMA) experiments presented in Section 4.4 is necessary to be established by performing more measurements. In parallel, these shall be conducted in tandem with recommendation points 3 and 5 to fully understand and explain the nature of the residual strain left in each specimen after the stabilisation of its superelastic response.
3. Transmission Electron Microscopy (TEM) measurements of the microstructure of the samples before and after the stabilisation of their superelastic response would yield meaningful results concerning various aspects of the crystalline structure. These could pertain to the presence internal stresses developed by the scanning strategy employed during fabrication, possible defects and secondary phases not detectable by XRD measurements as well as the dislocations which shall arise during the cycling of the material.
4. With respect to furthering the research into the scanning strategies and their effect on the microstructure of the alloy and the functional response, it would be recommended to explore the combination of a 67° rotation scanning with island patterns and the high volumetric energy density condition to establish whether it obtains crystallographic textures and superelastic responses even stronger than than the ones exhibited by the HLP_67 sample studied in this thesis.
5. Another scanning strategy worth exploring would be a bidirectional single-layer scanning, with 67° interlayer rotation angle and variable scanning sequence in the low Volumetric Energy Density condition. According to the information presented in Chapter 2, varying the scanning sequence in single-layer scanning can have beneficial effects on the heat dissipation during L-PBF, lowering the residual stresses that arise during manufacturing, while also possibly creating the desired $\langle 001 \rangle_{\parallel BD}$. Along the same rationale, a single-layer bidirectional scanning strategy with 67° interlayer rotation and a helix pattern could theoretically also have the potential to fabricate NiTi parts with the desired crystallographic texture while successfully managing to keep the residual stresses low within the lattice during L-PBF.
6. It is crucial to obtain a sound and complete image of the reasons which explain the different crystallographic textures and functional responses obtained by each scanning strategy, or, in other words, increase confidence on why each scanning strategy produces the results presented throughout Chapter 4 of this report. In-situ thermal monitoring studies during the L-PBF fabrication of the Ni-rich NiTi samples would reveal the exact mechanisms behind the effect of the interlayer rotation angle and the grain growth direction. Additionally, computer modelling as well as phys-

ical tests could be implemented for defining the existence of residual stresses arising during the fabrication and caused by the scanning strategy. This information together with the recommendations in point 3 could provide valuable insights into the interplay between internal and residual stresses, the interlayer rotation angles of the scanning vectors and the crystallographic texture which arises during manufacturing and how these affect the superelastic functional behaviour.

7. Finally, it is of particular interest to expand the study to integrate axial tensile loading conditions. As it is well-known, NiTi SMAs exhibit a large tension-compression anisotropy which arises by the fact that different martensite variants are created under tensile stresses to those created when the stress state is compressive [63]. These difference in the variants of the martensite phase cause differences in the plateau stresses, the shape memory recovery strains and the critical resolved shear stresses measured between the two loading conditions [63]. Additionally, different transformation paths are activated for the stress induced martensite transformation in the superelastic austenite phase between the tensile and the compressive loading conditions [63]. Hence, it becomes apparent that it will bear tremendous benefits to test samples manufactured by the conditions outlined in this report under axial tension loading to investigate their functional behaviour and further explore the possibilities of tailoring the microstructure, the texture and the superelasticity of the material for this type of loading conditions.

References

[1] Dimitris C. Lagoudas. *Shape memory alloys: modeling and engineering applications*. Chapter 1. Springer, 2008. DOI: 10.1007/978-0-387-47685-8.

[2] George B. Kauffman and Isaac Mayo. "The story of nitinol: the serendipitous discovery of the memory metal and its applications". In: *The chemical educator* 2.2 (1997), pp. 1–21. DOI: https://doi-org.tudelft.idm.oclc.org/10.1007/s00897970111a.

[3] Ganesh Shimoga, Tae-Hoon Kim and Sang-Youn Kim. "An Intermetallic NiTi-Based Shape Memory Coil Spring for Actuator Technologies". In: *Metals* 11.8 (2021), p. 1212. DOI: https://doi.org/10.3390/met11081212.

[4] Jia-Ning Zhu. "Development of Nickel-Titanium Shape Memory Alloys via Laser Power Bed Fusion". PhD thesis. Delft University of Technology, 2023. DOI: https://doi.org/10.4233/uuid:62a12e6d-d7d2-4244-8df9-89413ec133da.

[5] Vladimir Buljak and Gianluca Ranzi. "Chapter 9 - Shape memory alloys". In: *Constitutive Modeling of Engineering Materials*. Ed. by Vladimir Buljak and Gianluca Ranzi. Academic Press, 2021, pp. 293–313. ISBN: 978-0-12-814696-5. DOI: https://doi.org/10.1016/B978-0-12-814696-5.00014-9. URL: https://www.sciencedirect.com/science/article/pii/B9780128146965000149.

[6] Christian Lexcellent, Sylvain Leclercq, Bertrand Gabry and Gilles Bourbon. "The two way shape memory effect of shape memory alloys: an experimental study and a phenomenological model". In: *International Journal of Plasticity* 16.10-11 (2000), pp. 1155–1168. DOI: https://doi.org/10.1016/S0749-6419(00)00005-X.

[7] Thomas Waitz, Thomas Antretter, Franz Dieter Fischer and Hans-Peter Karnthaler. "Size effects on martensitic phase transformations in nanocrystalline NiTi shape memory alloys". In: *Materials Science and Technology* 24.8 (2008), pp. 934–940. DOI: https://doi.org/10.1179/174328408X302620.

[8] Bo Xu, Chao Yu and Guozheng Kang. "Phase field study on the microscopic mechanism of grain size dependent cyclic degradation of super-elasticity and shape memory effect in nano-polycrystalline NiTi alloys". In: *International Journal of Plasticity* 145 (2021), p. 103075. DOI: https://doi.org/10.1016/j.ijplas.2021.103075.

[9] Jia-Ning Zhu, Evgenii Borisov, Xiaohui Liang, Richard Huizenga, Anatoly Popovich, Vitaliy Bliznuk, Roumen Petrov, Marcel Hermans and Vera Popovich. "Controlling microstructure evolution and phase transformation behavior in additive manufacturing of nitinol shape memory alloys by tuning hatch distance". In: *Journal of Materials Science* 57.10 (2022), pp. 6066–6084. DOI: https://doi.org/10.1007/s10853-022-07007-z.

[10] Jaronie Mohd Jani, Martin Leary, Aleksandar Subic and Mark A. Gibson. "A review of shape memory alloy research, applications and opportunities". In: *Materials & Design (1980-2015)* 56 (2014), pp. 1078–1113. DOI: https://doi.org/10.1016/j.matdes.2013.11.084.

[11] Eduard Farber, Jia-Ning Zhu, Anatoliy Popovich and Vera Popovich. "A review of NiTi shape memory alloy as a smart material produced by additive manufacturing". In: *Materials Today: Proceedings* 30 (2020), pp. 761–767. DOI: https://doi.org/10.1016/j.matpr.2020.01.563.

[12] J. Frenzel, A. Wieczorek, I. Opahle, B. Maaß, R. Drautz and G. Eggeler. "On the effect of alloy composition on martensite start temperatures and latent heats in Ni–Ti-based shape memory alloys". In: *Acta Materialia* 90 (2015), pp. 213–231. DOI: https://doi.org/10.1016/j.actamat.2015.02.029.

[13] Kazuhiro Otsuka and Xiabing Ren. "Physical metallurgy of Ti–Ni-based shape memory alloys". In: *Progress in materials science* 50.5 (2005), pp. 511–678. DOI: https://doi.org/10.1016/j.pmatsci.2004.10.001.

[14] D. Piorunek, O. Oluwabi, J. Frenzel, A. Kostka, H.J. Maier, C. Somsen and G. Eggeler. “Effect of off-stoichiometric compositions on microstructures and phase transformation behavior in Ni-Cu-Pd-Ti-Zr-Hf high entropy shape memory alloys”. In: *Journal of Alloys and Compounds* 857 (2021), p. 157467. DOI: https://doi.org/10.1016/j.jallcom.2020.157467.

[15] J. Frenzel, Easo P. George, A. Dlouhy, Ch. Somsen, M.F.-X. Wagner and G. Eggeler. “Influence of Ni on martensitic phase transformations in NiTi shape memory alloys”. In: *Acta Materialia* 58.9 (2010), pp. 3444–3458. DOI: https://doi.org/10.1016/j.actamat.2010.02.019.

[16] Mohammad Elahinia, Narges Sh. Moghaddam, Mohsen Taheri Andani, Amirhesam Amerinatanzi, Beth A. Bimber and Reginald F. Hamilton. “Fabrication of NiTi through additive manufacturing: A review”. In: *Progress in Materials Science* 83 (2016), pp. 630–663. DOI: https://doi.org/10.1016/j.pmatsci.2016.08.001.

[17] Kerri M. Horvay and Christopher T. Schade. “Development of nitinol alloys for additive manufacturing”. In: *Mater. Sci. Technol* 1-P (2018), pp. 63–70. DOI: 10.7449/2018mst/2018/mst_2018_63_70.

[18] Josiah Cherian Chekotu, Robert Groarke, Kevin O’Toole and Dermot Brabazon. “Advances in selective laser melting of nitinol shape memory alloy part production”. In: *Materials* 12.5 (2019), p. 809. DOI: https://doi.org/10.3390/ma12050809.

[19] T. Simon, A. Kröger, C. Somsen, A. Dlouhy and G. Eggeler. “On the multiplication of dislocations during martensitic transformations in NiTi shape memory alloys”. In: *Acta Materialia* 58.5 (2010), pp. 1850–1860. DOI: https://doi.org/10.1016/j.actamat.2009.11.028.

[20] M. Karimzadeh, M.R. Aboutalebi, M.T. Salehi, S.M. Abbasi and M. Morakabati. “Adjustment of aging temperature for reaching superelasticity in highly Ni-rich Ti-51.5 Ni NiTi shape memory alloy”. In: *Materials and Manufacturing Processes* 31.8 (2016), pp. 1014–1021. DOI: https://doi.org/10.1080/10426914.2015.1048468.

[21] Wei-Neng Hsu, Efthymios Polatidis, Miroslav Šmíd, Steven Van Petegem, Nicola Casati and Helena Van Swygenhoven. “Deformation and degradation of superelastic NiTi under multiaxial loading”. In: *Acta Materialia* 167 (2019), pp. 149–158. DOI: https://doi.org/10.1016/j.actamat.2019.01.047.

[22] Tian-xing Zhao, Guo-zheng Kang, Chao Yu and Qian-hua Kan. “Experimental investigation of the cyclic degradation of the one-way shape memory effect of NiTi alloys”. In: *International Journal of Minerals, Metallurgy and Materials* 26 (2019), pp. 1539–1550. DOI: https://doi.org/10.1007/s12613-019-1884-8.

[23] Yong Liu, Zeliang L Xie, Jan Van Humbeeck and Luc Delaey. “Effect of texture orientation on the martensite deformation of NiTi shape memory alloy sheet”. In: *Acta materialia* 47.2 (1999), pp. 645–660. DOI: https://doi.org/10.1016/S1359-6454(98)00376-0.

[24] G. Laplanche, T. Birk, S. Schneider, J. Frenzel and G. Eggeler. “Effect of temperature and texture on the reorientation of martensite variants in NiTi shape memory alloys”. In: *Acta Materialia* 127 (2017), pp. 143–152. DOI: https://doi.org/10.1016/j.actamat.2017.01.023.

[25] H. Sehitoglu, I. Karaman, R. Anderson, X. Zhang, K. Gall, H.J. Maier and Y.J.A.M. Chumlyakov. “Compressive response of NiTi single crystals”. In: *Acta Materialia* 48.13 (2000), pp. 3311–3326. DOI: https://doi.org/10.1016/S1359-6454(00)00153-1.

[26] Jia-Ning Zhu, Kai Liu, Ton Riemslag, Frans D. Tichelaar, Evgenii Borisov, Xiyu Yao, Anatoly Popovich, Richard Huizenga, Marcel Hermans and Vera Popovich. “Achieving superelasticity in additively manufactured Ni-lean NiTi by crystallographic design”. In: *Materials & Design* 230 (2023), p. 111949. DOI: https://doi.org/10.1016/j.matdes.2023.111949.

[27] Ali S. Turabi. “Effects of magnetic field on the shape memory behavior of single and polycrystalline magnetic shape memory alloys”. PhD thesis. University of Kentucky, 2015. DOI: https://uknowledge.uky.edu/me_etds/58.

[28] Dana M. Elzey, Aarash Yusefzadeh Nagh Sofla and Haydn N.G. Wadley. “A bio-inspired high-authority actuator for shape morphing structures”. In: *Smart structures and materials 2003: Active Materials: Behavior and Mechanics*. Vol. 5053. SPIE. 2003, pp. 92–100. DOI: https://doi-org.tudelft.idm.oclc.org/10.1117/12.484745.

[29] D. Wever, J. Elstrodt, A. Veldhuizen et al. “Scoliosis correction with shape-memory metal: results of an experimental study”. In: *European Spine Journal* 11.2 (2002), pp. 100–106. DOI: https://doi.org/10.1007/s005860100347.

[30] Paulo Silva Lobo, João Almeida and Lúıs Guerreiro. “Shape memory alloys behaviour: a review”. In: *Procedia Engineering* 114 (2015), pp. 776–783. DOI: https://doi.org/10.1016/j.proeng.2015.08.025.

[31] Shoujin Sun, Milan Brandt and M.J.L.A.M. Easton. “Powder bed fusion processes: An overview”. In: *Laser additive manufacturing* (2017), pp. 55–77. DOI: https://doi.org/10.1016/B978-0-08-100433-3.00002-6.

[32] William E. Frazier. “Metal additive manufacturing: a review”. In: *Journal of Materials Engineering and performance* 23.6 (2014), pp. 1917–1928. DOI: https://doi.org/10.1007/s11665-014-0958-z.

[33] Ian Gibson, David W. Rosen, Brent Stucker, Mahyar Khorasani, David Rosen, Brent Stucker and Mahyar Khorasani. *Additive manufacturing technologies*. Vol. 17. Springer, 2021. DOI: https://doi.org/10.1007/978-3-030-56127-7.

[34] Chor Yen Yap, Chee Kai Chua, Zhi Li Dong, Zhong Hong Liu, Dan Qing Zhang, Loong Ee Loh and Swee Leong Sing. “Review of selective laser melting: Materials and applications”. In: *Applied physics reviews* 2.4 (2015), p. 041101. DOI: https://doi.org/10.1063/1.4935926.

[35] Jia-Ning Zhu, Evgenii Borisov, Xiaohui Liang, Eduard Farber, M.J.M. Hermans and V.A. Popovich. “Predictive analytical modelling and experimental validation of processing maps in additive manufacturing of nitinol alloys”. In: *Additive Manufacturing* 38 (2021), p. 101802. DOI: https://doi.org/10.1016/j.addma.2020.101802.

[36] Haolin Jia, Hua Sun, Hongze Wang, Yi Wu and Haowei Wang. “Scanning strategy in selective laser melting (SLM): a review”. In: *The International Journal of Advanced Manufacturing Technology* 113 (2021), pp. 2413–2435. DOI: https://doi.org/10.1007/s00170-021-06810-3.

[37] Łukasz Żrodowski, Bartłomiej Wysocki, Rafał Wróblewski, Agnieszka Krawczyńska, Bogusława Adamczyk-Cieślak, Joanna Zdunek, Piotr Błyskun, Jarosław Ferenc, Marcin Leonowicz and Wojciech Święszkowski. “New approach to amorphization of alloys with low glass forming ability via selective laser melting”. In: *Journal of Alloys and Compounds* 771 (2019), pp. 769–776. DOI: https://doi.org/10.1016/j.jallcom.2018.08.075.

[38] Naresh Nadammal, Tatiana Mishurova, Tobias Fritsch, Itziar Serrano-Munoz, Arne Kromm, Christoph Haberland, Pedro Dolabella Portella and Giovanni Bruno. “Critical role of scan strategies on the development of microstructure, texture, and residual stresses during laser powder bed fusion additive manufacturing”. In: *Additive Manufacturing* 38 (2021), p. 101792. DOI: https://doi.org/10.1016/j.addma.2020.101792.

[39] Benedikt Diepold, Mathias Sebastian Palm, Andreas Wimmer, Torsten Sebald, Heinz Werner Höppel, Steffen Neumeier and Mathias Göken. “Rotating scan strategy induced anisotropic microstructural and mechanical behavior of selective laser melted materials and their reduction by heat treatments”. In: *Advanced Engineering Materials* 23.12 (2021), p. 2100622. DOI: https://doi-org.tudelft.idm.oclc.org/10.1002/adem.202100622.

[40] Lore Thijs, Maria Luz Montero Sistiaga, Ruben Wauthle, Qingge Xie, Jean-Pierre Kruth and Jan Van Humbeeck. “Strong morphological and crystallographic texture and resulting yield strength anisotropy in selective laser melted tantalum”. In: *Acta Materialia* 61.12 (2013), pp. 4657–4668. DOI: https://doi.org/10.1016/j.actamat.2013.04.036.

[41] Fuyao Yan, Wei Xiong and Eric J Faierson. “Grain structure control of additively manufactured metallic materials”. In: *Materials* 10.11 (2017), p. 1260. DOI: https://doi.org/10.3390/ma10111260.

[42] L. Xue, K.C. Atli, C. Zhang, N. Hite, A. Srivastava, A.C. Leff, A.A. Wilson, D.J. Sharar, A. Elwany, R. Arroyave et al. “Laser powder bed fusion of defect-free NiTi shape memory alloy parts with superior tensile superelasticity”. In: *Acta Materialia* 229 (2022), p. 117781. DOI: https://doi.org/10.1016/j.actamat.2022.117781.

[43] Shi-Hai Sun, Koji Hagihara and Takayoshi Nakano. “Effect of scanning strategy on texture formation in Ni-25 at.% Mo alloys fabricated by selective laser melting”. In: *Materials & Design* 140 (2018), pp. 307–316. DOI: https://doi.org/10.1016/j.matdes.2017.11.060.

[44] Peter Mercelis and Jean-Pierre Kruth. “Residual stresses in selective laser sintering and selective laser melting”. In: *Rapid prototyping journal* 12.5 (2006), pp. 254–265. DOI: https://doi-org.tudelft.idm.oclc.org/10.1108/13552540610707013.

[45] Davi Ramos, Fawzi Belblidia and Johann Sienz. “New scanning strategy to reduce warpage in additive manufacturing”. In: *Additive Manufacturing* 28 (2019), pp. 554–564. DOI: https://doi.org/10.1016/j.addma.2019.05.016.

[46] Yang Liu, Yongqiang Yang and Di Wang. “A study on the residual stress during selective laser melting (SLM) of metallic powder”. In: *The International Journal of Advanced Manufacturing Technology* 87 (2016), pp. 647–656. DOI: https://doi-org.tudelft.idm.oclc.org/10.1007/s00170-016-8466-y.

[47] Patcharapit Promoppatum and Shi-Chune Yao. “Influence of scanning length and energy input on residual stress reduction in metal additive manufacturing: Numerical and experimental studies”. In: *Journal of Manufacturing Processes* 49 (2020), pp. 247–259. DOI: https://doi.org/10.1016/j.jmapro.2019.11.020.

[48] L. Parry, I.A. Ashcroft and Ricky D. Wildman. “Understanding the effect of laser scan strategy on residual stress in selective laser melting through thermo-mechanical simulation”. In: *Additive Manufacturing* 12 (2016), pp. 1–15. DOI: https://doi.org/10.1016/j.addma.2016.05.014.

[49] Keyvan Safaei, Nasrin Taheri Andani, Mohammadreza Nematollahi, Othmane Benafan, Behrang Poorganji and Mohammad Elahinia. “The Build Orientation Dependency of NiTi Shape Memory Alloy Processed by Laser Powder Bed Fusion”. In: *Shape Memory and Superelasticity* 8.4 (2022), pp. 265–276. DOI: https://doi.org/10.1007/s40830-022-00389-8.

[50] Sasan Dadbakhsh, Bey Vrancken, J.-P. Kruth, Jan Luyten and Jan Van Humbeeck. “Texture and anisotropy in selective laser melting of NiTi alloy”. In: *Materials Science and Engineering: A* 650 (2016), pp. 225–232. DOI: https://doi.org/10.1016/j.msea.2015.10.032.

[51] Keyvan Safaei, Mohammadreza Nematollahi, Parisa Bayati, Fatemeh Kordizadeh, Mohsen Taheri Andani, Hossein Abedi, Behrang Poorganji and Mohammad Elahinia. “On the crystallographic texture and torsional behavior of NiTi shape memory alloy processed by laser powder bed fusion: Effect of build orientation”. In: *Additive Manufacturing* 59 (2022), p. 103184. DOI: https://doi.org/10.1016/j.addma.2022.103184.

[52] Christoph Haberland, Mohammad Elahinia, Jason M. Walker, Horst Meier and Jan Frenzel. “On the development of high quality NiTi shape memory and pseudoelastic parts by additive manufacturing”. In: *Smart materials and structures* 23.10 (2014), p. 104002. DOI: 10.1088/0964-1726/23/10/104002.

[53] Pratik R. Halani, Irfan Kaya, Yung C. Shin and Haluk E. Karaca. “Phase transformation characteristics and mechanical characterization of nitinol synthesized by laser direct deposition”. In: *Materials Science and Engineering: A* 559 (2013), pp. 836–843. DOI: https://doi.org/10.1016/j.msea.2012.09.031.

[54] Soheil Saedi, Ali Sadi Turabi, Mohsen Taheri Andani, Christoph Haberland, Haluk Karaca and Mohammad Elahinia. “The influence of heat treatment on the thermomechanical response of Ni-rich NiTi alloys manufactured by selective laser melting”. In: *Journal of Alloys and Compounds* 677 (2016), pp. 204–210. DOI: https://doi.org/10.1016/j.jallcom.2016.03.161.

[55] Soheil Saedi, Ali Sadi Turabi, Mohsen Taheri Andani, Narges Shayesteh Moghaddam, Mohammad Elahinia and Haluk Ersin Karaca. “Texture, aging, and superelasticity of selective laser melting fabricated Ni-rich NiTi alloys”. In: *Materials Science and Engineering: A* 686 (2017), pp. 1–10. DOI: https://doi.org/10.1016/j.msea.2017.01.008.

[56] S. Anand Kumar and R.V.S. Prasad. “Basic principles of additive manufacturing: Different additive manufacturing technologies”. In: *Additive manufacturing*. Elsevier, 2021, pp. 17–35. DOI: https://doi.org/10.1016/B978-0-12-822056-6.00012-6.

[57] Narges Shayesteh Moghaddam, Soheil Saedi, Amirhesam Amerinatanzi, Alejandro Hinojos, Ali Ramazani, Julia Kundin, Michael J. Mills, Haluk Karaca and Mohammad Elahinia. “Achieving superelasticity in additively manufactured NiTi in compression without post-process heat treatment”. In: *Scientific reports* 9.1 (2019), p. 41. DOI: https://doi.org/10.1038/s41598-018-36641-4.

[58] Mostafa Amirjan and Hassan Sakiani. “Effect of scanning strategy and speed on the microstructure and mechanical properties of selective laser melted IN718 nickel-based superalloy”. In: *The International Journal of Advanced Manufacturing Technology* 103 (2019), pp. 1769–1780. DOI: https://doi-org.tudelft.idm.oclc.org/10.1007/s00170-019-03545-0.

[59] Lore Thijs, Bey Vrancken, Jean-Pierre Kruth and Jan Van Humbeeck. “The influence of process parameters and scanning strategy on the texture in Ti6Al4V part produced by selective laser melting”. In: *Advanced Materials, Processes and Applications for Additive Manufacturing* 1 (2013), pp. 21–28.

[60] Fabian Geiger, Karsten Kunze and Thomas Etter. “Tailoring the texture of IN738LC processed by selective laser melting (SLM) by specific scanning strategies”. In: *Materials Science and Engineering: A* 661 (2016), pp. 240–246. DOI: https://doi.org/10.1016/j.msea.2016.03.036.

[61] Keyvan Safaei, Nasrin Taheri Andani, Mohammadreza Nematollahi, Othmane Benafan, Behrang Poorganji and Mohammad Elahinia. “The Build Orientation Dependency of NiTi Shape Memory Alloy Processed by Laser Powder Bed Fusion”. In: *Shape Memory and Superelasticity* 8.4 (2022), pp. 265–276. DOI: https://doi.org/10.1007/s40830-022-00389-8.

[62] Tomoyuki Kakeshita, Takashi Fukuda, Avadh Saxena and Antoni Planes. *Disorder and strain-induced complexity in functional materials*. Vol. 148. Springer Science & Business Media, 2011. DOI: https://doi.org/10.1007/978-3-642-20943-7.

[63] S.W. Robertson, A.R. Pelton and R.O. Ritchie. “Mechanical fatigue and fracture of Nitinol”. In: *International Materials Reviews* 57.1 (2012), pp. 1–37. DOI: https://doi-org.tudelft.idm.oclc.org/10.1179/1743280411Y.0000000009.

[64] Yong Liu, Zeliang Xie and Jan Van Humbeeck. “Cyclic deformation of NiTi shape memory alloys”. In: *Materials Science and Engineering: A* 273 (1999), pp. 673–678. DOI: https://doi.org/10.1016/S0921-5093(99)00347-0.

[65] Huseyin Sehitoglu, Robert Anderson, Ibrahim Karaman, Ken Gall and Yuriy Chumlyakov. “Cyclic deformation behavior of single crystal NiTi”. In: *Materials Science and Engineering: A* 314.1-2 (2001), pp. 67–74. DOI: https://doi.org/10.1016/S0921-5093(00)01924-9.

[66] A.R. Pelton. “Nitinol fatigue: a review of microstructures and mechanisms”. In: *Journal of Materials Engineering and Performance* 20 (2011), pp. 613–617. DOI: https://doi-org.tudelft.idm.oclc.org/10.1007/s11665-011-9864-9.

[67] P. Sedmák, P. Šittner, J. Pilch and C. Curfs. “Instability of cyclic superelastic deformation of NiTi investigated by synchrotron X-ray diffraction”. In: *Acta Materialia* 94 (2015), pp. 257–270. DOI: https://doi.org/10.1016/j.actamat.2015.04.039.

[68] Ken Gall, H. Sehitoglu, Yu I. Chumlyakov and I.V. Kireeva. “Tension–compression asymmetry of the stress–strain response in aged single crystal and polycrystalline NiTi”. In: *Acta Materialia* 47.4 (1999), pp. 1203–1217. DOI: https://doi.org/10.1016/S1359-6454(98)00432-7.

[69] Lianfeng Wang, Xiaohui Jiang, Yihong Zhu, Zishan Ding, Xiaogang Zhu, Jing Sun and Biao Yan. “Investigation of performance and residual stress generation of AlSi10Mg processed by selective laser melting”. In: *Advances in Materials Science and Engineering* 2018 (2018), pp. 1–12. DOI: https://doi.org/10.1155/2018/7814039.

A

Differential Scanning Calorimetry

The following tables contain the phase transformation temperatures for the second and the last cycles of the DSC measurements for all samples. Additionally, the thermal hysteresis values are given, wherever possible.

Table A.1: Phase transformation temperatures and thermal hysteresis for sample 0. All values in °C.

Heating, $M \rightarrow A$				Cooling, $A \rightarrow M$				Thermal Hysteresis
Cycle	A_s	A_f	A_p	Cycle	M_s	M_f	M_p	
2	-25.7	9.4	-3.8	2	-17.6	-65.9	-41.1	37
16	-29.4	4.1	-9.0	16	-30.2	-	-53.1	44

Table A.2: Phase transformation temperatures and thermal hysteresis for sample 90. All values in °C.

Heating, $M \rightarrow A$				Cooling, $A \rightarrow M$				Thermal Hysteresis
Cycle	A_s	A_f	A_p	Cycle	M_s	M_f	M_p	
2	-8.5	24.5	9.5	2	0.4	-43.6	-20.5	11
16	-13.4	20.4	4.9	16	-7.6	-54.6	-32.6	28

Table A.3: Phase transformation temperatures and thermal hysteresis for sample 30. All values in °C.

Heating, $M \rightarrow A$				Cooling, $A \rightarrow M$				Thermal Hysteresis
Cycle	A_s	A_f	A_p	Cycle	M_s	M_f	M_p	
2	-49.1	-1.0	-25.5	2	-	-	-	N/A
16	-48.0	-3.3	-27.6	16	-	-	-	N/A

Table A.4: Phase transformation temperatures and thermal hysteresis for sample 67. All values in °C.

Heating, $M \rightarrow A$				Cooling, $A \rightarrow M$				Thermal Hysteresis
Cycle	A_s	A_f	A_p	Cycle	M_s	M_f	M_p	
2	-39.4	0.8	-18.3	2	-10.0	-	-	N/A
16	-40.3	-2.5	-20.2	16	-	-	-	N/A

Table A.5: Phase transformation temperatures and thermal hysteresis for sample island_67. All values in °C.

Heating, $M \rightarrow A$				Cooling, $A \rightarrow M$				Thermal Hysteresis
Cycle	A_s	A_f	A_p	Cycle	M_s	M_f	M_p	
2	-32.2	11.7	-7.9	2	-11.5	-	-40.5	33
16	-32.8	9.3	-9.6	16	-20.7	-	-55.2	46

Table A.6: Phase transformation temperatures and thermal hysteresis for sample HLP_67. All values in °C.

Heating, $M \rightarrow A$				Cooling, $A \rightarrow M$				Thermal Hysteresis
Cycle	A_s	A_f	A_p	Cycle	M_s	M_f	M_p	
2	-	17.5	-24.1	2	-	-	-	N/A
16	-	17.2	-12.0	16	-	-	-	N/A

B

Scanning Electron Microscopy - Energy Dispersive X-Ray Spectroscopy

The following tables contain the full results for the Ti and Ni contents as measured by SEM-EDS for all samples.

Table B.1: Titanium and Nickel content measured by SEM-EDS for sample 0. All values in at.%.

Measurement	Titanium	Nickel
1	49.39	50.61
2	49.40	50.60
3	49.33	50.67

Table B.2: Titanium and Nickel content measured by SEM-EDS for sample 90. All values in at.%.

Measurement	Titanium	Nickel
1	49.11	50.89
2	49.91	50.09
3	49.11	50.89

Table B.3: Titanium and Nickel content measured by SEM-EDS for sample 30. All values in at.%.

Measurement	Titanium	Nickel
1	49.48	50.52
2	49.37	50.63
3	49.46	50.54

Table B.4: Titanium and Nickel content measured by SEM-EDS for sample 67. All values in at.%.

Measurement	Titanium	Nickel
1	49.07	50.93
2	49.20	50.80
3	49.25	50.75

Table B.5: Titanium and Nickel content measured by SEM-EDS for sample island_67. All values in at.%.

Measurement	Titanium	Nickel
1	49.26	50.74
2	49.14	50.86
3	49.19	50.81

Table B.6: Titanium and Nickel content measured by SEM-EDS for sample HLP_67. All values in at.%.

Measurement	Titanium	Nickel
1	48.73	51.27
2	48.86	51.14
3	48.90	51.1

C

Cyclic Axial Compression Test for Superelasticity

The following figures present the superelastic responses measured for the second specimen tested for each of the samples 0, 90, 30, 67 and island_67. Where applicable, both the HT and the LT tests are given.

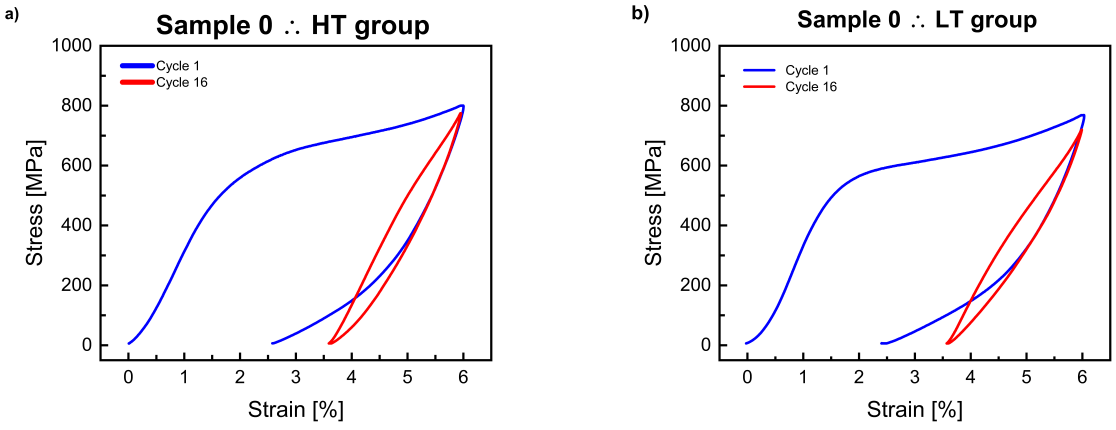


Figure C.1: Superelastic response for specimen no 2 of sample 0,***a)*** for the HT test and ***b)*** for the LT test.

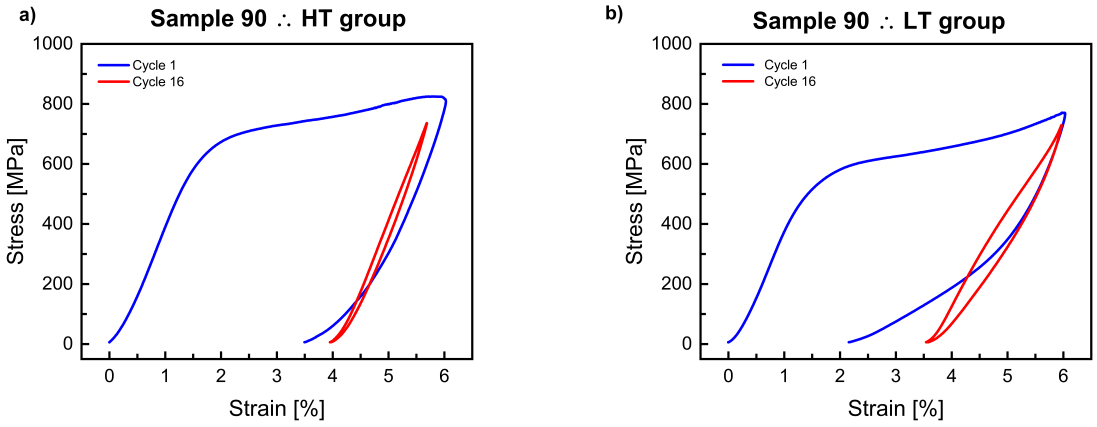


Figure C.2: Superelastic response for specimen no 2 of sample 90,***a)*** for the HT test and ***b)*** for the LT test.

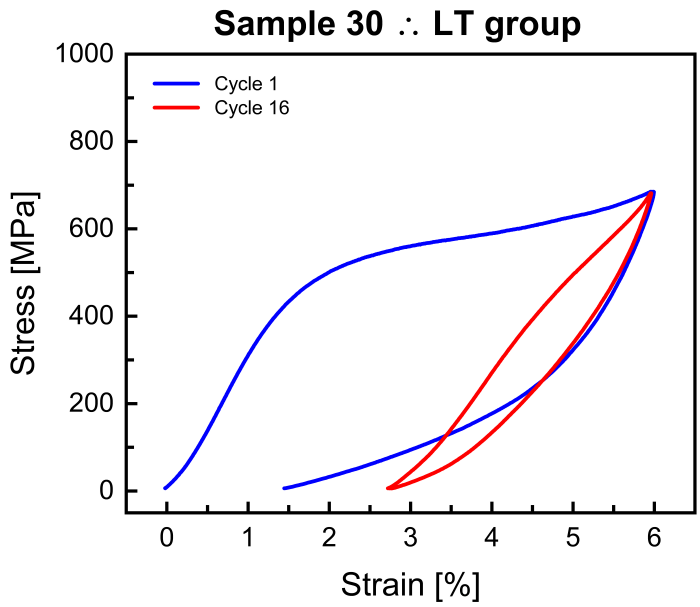


Figure C.3: Superelastic response for specimen no 2 of sample 30 for the LT test.

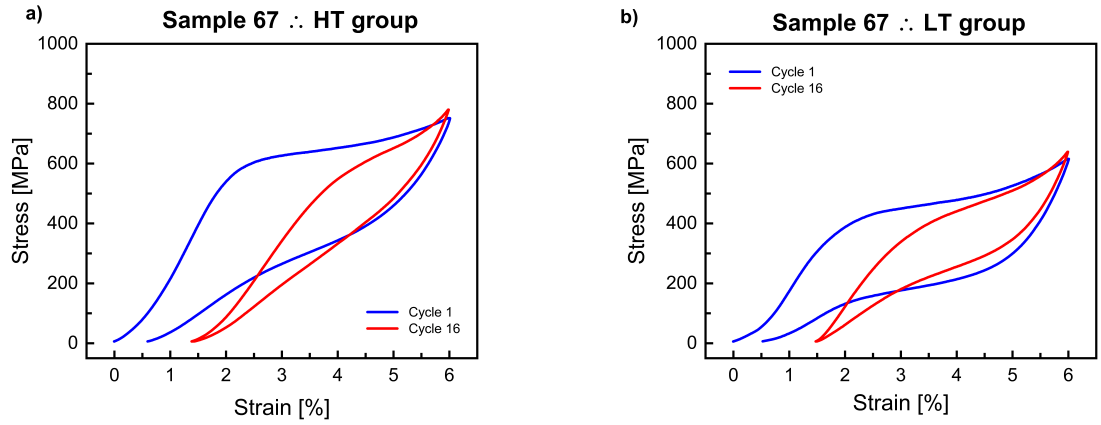


Figure C.4: Superelastic response for specimen no 2 of sample 67,***a)*** for the HT test and ***b)*** for the LT test.

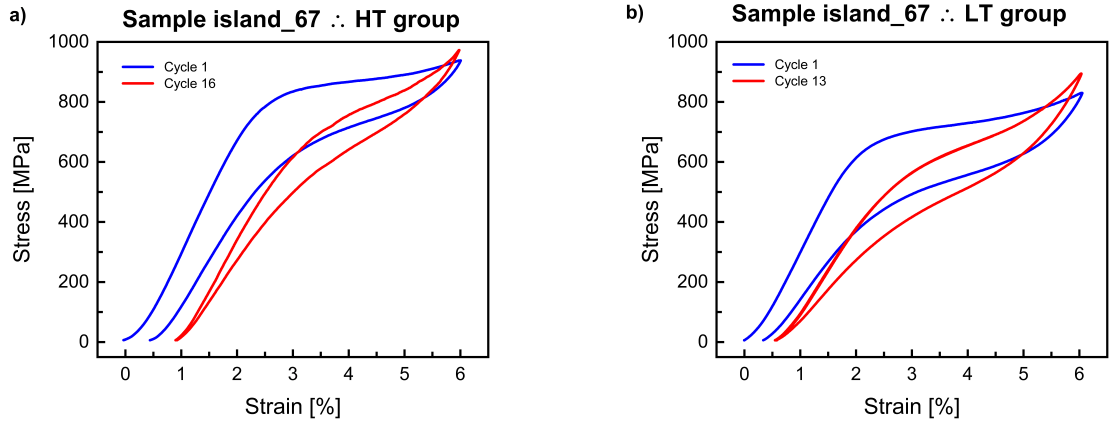


Figure C.5: Superelastic response for specimen no 2 of sample island_67,***a)*** for the HT test and ***b)*** for the LT test.